ISSN 1997-1397 (Print)
ISSN 2313-6022 (Online)

Журнал Сибирского федерального университета

Математика и физика

Journal of Siberian Federal University

Mathematics & Physics

2026 19 (2)

ISSN 1997-1397
(Print)

ISSN 2313-6022
(Online)

2026 19 (2)

ЖУРНАЛ СИБИРСКОГО ФЕДЕРАЛЬНОГО УНИВЕРСИТЕТА
Математика и Физика

JOURNAL OF SIBERIAN FEDERAL UNIVERSITY
Mathematics & Physics

Издание индексируется Scopus (Elsevier), Emerging Sources Citation Index (WoS, Clarivate Analytics), Российским индексом научного цитирования (НЭБ), представлено в международных и российских информационных базах: Ulrich's periodicals directiory, ProQuest, EBSCO (США), Google Scholar, MathNet.ru, КиберЛенинке.

Включено в список Высшей аттестационной комиссии «Рецензируемые научные издания, входящие в международные реферативные базы данных и системы цитирования».

Все статьи представлены в открытом доступе http://journal.sfu-kras.ru/en/series/mathematics_physics.

Журнал Сибирского федерального университета.
Математика и физика.
Journal of Siberian Federal University. Mathematics & Physics.

Учредитель: Федеральное государственное автономное образовательное учреждение высшего образования "Сибирский федеральный университет"(СФУ)
Главный редактор: А.М. Кытманов. Редакторы: В.Е. Зализняк, А.В. Щуплев.
Компьютерная верстка: Г.В. Хрусталева.
№ 2 от 26.04.2026. Индекс: 42327. Тираж: 1000 экз. Свободная цена
Адрес редакции и издателя: 660041 г. Красноярск, пр. Свободный, 82, стр. 24, оф. 117.
Отпечатано в типографии Издательства БИК СФУ
660041 г. Красноярск, пр. Свободный, 82.
Свидетельство о регистрации СМИ ПИ № ФС 77-28724 от 29.06.2007 г.,
выданное Федеральной службой по надзору в сфере массовых коммуникаций, связи и охраны культурного наследия
http://journal.sfu-kras.ru
Подписано в печать 15.04.26. Формат 84×108/16. Усл.печ. л. 12,0.
Уч.-изд. л. 11,8. Бумага тип. Печать офсетная.
Тираж 1000 экз. Заказ 25229
Возрастная маркировка в соответствии с Федеральным законом № 436-ФЗ:16+

CONTENTS

СОДЕРЖАНИЕ

EDN: MGJAZB
УДК 517.9

On the Joint Motion Stability of Two Ideal Fluid Layers

Viktor K. Andreev*
Institute of Computational Modelling SB RAS
Krasnoyarsk, Russian Federation

Received 10.06.2025, received in revised form 05.10.2025, accepted 07.12.2025

Abstract. The small perturbations evolution of two layers joint motion of ideal incompressible fluids on a solid substrate is studied. It is shown that the linearized problem in Lagrangian coordinates allows for the separation of variables. A system of amplitude equations is obtained, which contains two Weber numbers, the ratio of densities and initial layer thicknesses, as well as dimensionless wave numbers. The presented results of the asymptotic and numerical analysis of the amplitude equations indicate the stability of the layers motion.

Keywords: ideal fluid, free surface, interface, linear stability.

Citation: V.K. Andreev, On the Joint Motion Stability of Two Ideal Fluid Layers, J. Sib. Fed. Univ. Math. Phys., 2026, 19(2), 149–154. EDN: MGJAZB.

1. Description of the basic flow

Consider the joint unsteady motion of two immiscible layers of ideal fluids with densities ρ_1 and ρ_2. Let l_{10} and l_{20} be the corresponding layer thicknesses at the initial time. Then the formulas

$$u_j = \frac{kx}{1+kt}\,, \quad v_j = -\frac{ky}{1+kt}\,, \quad k = \text{const} > 0, \quad j = 1, 2,$$

$$p_1 = \frac{k^2}{(1+kt)^2}\,\left[\rho_2 l_2^2(t) + (\rho_1 - \rho_2) l_1^2(t) - \rho_1 y^2\right], \quad 0 \leqslant y \leqslant l_1(t), \tag{1}$$

$$p_2 = \frac{\rho_2 k^2}{(1+kt)^2}\,\left[l_2^2(t) - y^2\right], \quad l_1(t) \leqslant y \leqslant l_2(t)$$

describe the specified two-dimensional motion in the layers $|x| < \infty$, $0 \leqslant y \leqslant l_{10}(1+kt)^{-1} \equiv l_1(t)$ for $j = 1$ and $l_1(t) \leqslant y \leqslant l_{20}(1+kt)^{-1} \equiv l_2(t)$ for $j = 2$. Here, the line $y = 0$ is a fixed, impermeable solid wall; the line $y = l_1(t)$ is the interface, and on it $p_1 = p_2$, while the line $y = l_2(t)$ is the free surface, with the pressure on it being zero. As time increases, the layers thicknesses tend to zero as $l_{j0}(kt)^{-1}$. Note that the flow domain can be considered finite; for example, at $t = 0$, the lines $x = 0$ and $x = \xi_0$ can be taken as a solid walls. For $t > 0$, the wall $x = 0$ remains fixed, while the other moves according to the law $x(t) = \xi_0(1+kt)$. A uniform stretching of the layers occurs with velocity $k\xi_0$. The motion defined by formulas (1) is a potential. Since the free surface and the interface are flat and the contact angles are $\pi/2$, capillary forces do not affect this motion. It is this motion that will be investigated for linear stability hereafter.

*andr@icm.krasn.ru

2. Linearized problem

As a rule, the theoretical study of fluid motions with free boundaries is conveniently carried out in Lagrangian coordinates, see, for example, [1,2]. In our case, we introduce Lagrangian coordinates ξ, η such that $x = (1+kt)\xi$, $y = (1+kt)^{-1}\eta$. For $j = 1$, we have $0 \leqslant \xi \leqslant \xi_0$, $0 \leqslant \eta \leqslant l_{10}$, and for $j = 2$ — $0 \leqslant \xi \leqslant \xi_0$, $l_{10} \leqslant \eta \leqslant l_{20}$. Assuming the perturbations are also potential, we use the equations from [1], where the pressures perturbations in the layers are $\mathcal{P}^j = -\rho_j \Psi^j_t$, and the velocities are $\mathbf{U}^j = M^{*-1}\nabla\Psi^j$, $M^* = diag(1+kt, (1+kt)^{-1})$, $j = 1, 2$. After some transformations, we arrive to the following problem: the potentials $\Psi^j(\xi,\eta,t)$ satisfy the equations

$$\Psi^j_{\xi\,\xi} + (1+kt)^4 \Psi^j_{\eta\,\eta} = 0 \tag{2}$$

in the domains $0 \leqslant \xi \leqslant \xi_0$, $0 \leqslant \eta \leqslant l_{10}$ for $j = 1$, and $0 \leqslant \xi \leqslant \xi_0$, $l_{10} \leqslant \eta \leqslant l_{20}$ for $j = 2$.

On the free surface $\eta = l_{20}$:

$$\rho_2 \Psi^2_t(\xi, l_{20}, t) = -\frac{2\rho_2 k^2 l_{20}}{(1+kt)^3}\, R^2(\xi,t) + \frac{\sigma_2}{(1+kt)^2}\, R^2_{\xi\,\xi}(\xi,t), \tag{3}$$

$$0 \leqslant \xi \leqslant \xi_0, \quad t > 0.$$

On the interface $\eta = l_{10}$:

$$\Psi^1_\eta(\xi, l_{10}, t) = \Psi^2_\eta(\xi, l_{10}, t),$$

$$\rho_2 \Psi^2_t(\xi, l_{10}, t) - \rho_1 \Psi^1_t(\xi, l_{10}, t) + \frac{2k^2 l_{10}}{(1+kt)^3}\,(\rho_2 - \rho_1) R^1(\xi,t) = \tag{4}$$

$$= \frac{\sigma_1}{(1+kt)^2}\, R^1_{\xi\,\xi}(\xi,t), \quad 0 \leqslant \xi \leqslant \xi_0, \quad t > 0.$$

On the solid walls $\xi = 0$, $\xi = \xi_0$, $\eta = 0$ we have

$$R^1(0,t) = R^2(0,t) = 0, \quad R^1(\xi_0,t) = R^2(\xi_0,t) = 0, \quad \Psi^1_\eta(\xi,0,t) = 0. \tag{5}$$

The functions $R^j(\xi,t)$ are the normal components of the perturbation vectors [1], related to the potentials Ψ^j by the equalities

$$R^j(\xi,t) = \frac{1}{1+kt}\int_0^t (1+kt)^2 \Psi^j_\eta(\xi, l_{j0}, t)\, dt, \;\; j = 1,2, \quad 0 \leqslant \xi \leqslant \xi_0, \;\; t \geqslant 0. \tag{6}$$

In equations (3), (4), the quantities σ_1, σ_2 are the surface tension coefficients.

Now conditions (5) can be rewritten in terms of the potentials:

$$\Psi^j_\eta(0, l_{j0}, t) = 0, \quad \Psi^j_\eta(\xi_0, l_{j0}, t) = 0, \quad \Psi^1_\eta(\xi, 0, t) = 0, \quad j = 1,2. \tag{7}$$

The initial data must be added to the formulated problem

$$\Psi^j(\xi,\eta,0) = \Psi^j_0(\xi,\eta), \quad \Delta\Psi^j_0 = 0, \quad j = 1,2, \tag{8}$$

as well as the compatibility conditions

$$\Psi^1_{0\eta}(\xi, l_{10}) = \Psi^2_{0\eta}(\xi, l_{10}), \;\; \Psi^1_{0\eta}(\xi, 0) = 0, \;\; \Psi^j_{0\eta}(0, l_{j0}) = 0, \;\; \Psi^j_{0\eta}(\xi_0, l_{j0}) = 0. \tag{9}$$

3. Amplitude equations

In problem (2)–(9), the variables ξ and (η, t) are separable. Taking into account the boundary conditions on the solid walls, (5) or (7), we seek the solution in the form of Fourier series:

$$\Psi^j(\xi,\eta,t)=\sum_{n=1}^{\infty}A_n^j(\eta,t)\sin\left(\frac{n\pi\xi}{\xi_0}\right),\ R^j(\xi,t)=\sum_{n=1}^{\infty}N_n^j(t)\sin\left(\frac{n\pi\xi}{\xi_0}\right). \tag{10}$$

From the first condition (4) and the last one (5), we obtain the representations:

$$\begin{gathered}A_n^1(\eta,t)=C_{1n}(t)\mathrm{ch}\left[\frac{n\pi\eta}{\xi_0(1+kt)^2}\right],\quad 0<\eta<l_{10};\\ A_n^2(\eta,t)=C_{2n}(t)\mathrm{sh}\left[\frac{n\pi\eta}{\xi_0(1+kt)^2}\right]+C_{3n}(t)\mathrm{ch}\left[\frac{n\pi\eta}{\xi_0(1+kt)^2}\right]\end{gathered} \tag{11}$$

and the relation

$$C_{3n}(t)=C_{1n}(t)-C_{2n}(t)\mathrm{cth}\left[\frac{n\pi l_{10}}{\xi_0(1+kt)^2}\right]. \tag{12}$$

The dynamic conditions (3) and the second one (4) yield the relations ($\rho=\rho_1/\rho_2$)

$$\begin{gathered}A_{nt}^2(l_{20},t)+\left[\frac{2k^2l_{20}}{(1+kt)^3}+\frac{n^2\pi^2\sigma_2}{\xi_0^2\rho_2(1+kt)^2}\right]N_n^2(t)=0,\\ A_{nt}^2(l_{10},t)-\rho A_{nt}^1(l_{10},t)+\left[\frac{2k^2l_{10}(1-\rho)}{(1+kt)^3}+\frac{n^2\pi^2\sigma_1}{\xi_0^2\rho_2(1+kt)^2}\right]N_n^1(t)=0.\end{gathered} \tag{13}$$

Henceforth, let $\tau=1+kt$, $\tau\geqslant 1$, and, moreover, we will restrict ourselves to a single harmonic by fixing n. We introduce new unknown functions

$$y_1=\frac{A_n^1(l_{10},\tau)}{kl_{10}^2},\quad y_2=\frac{A_n^2(l_{20},\tau)}{kl_{10}^2},\quad y_3=\frac{\tau N_n^1(\tau)}{l_{10}},\quad y_4=\frac{\tau N_n^2(\tau)}{l_{10}}. \tag{14}$$

Computing $A_{n\eta}^1(l_{10},\tau)$, $A_{n\eta}^2(l_{20},\tau)$ from (11) and using equalities (6) and conditions (13), after transformations we obtain the system of amplitude equations (the prime here denotes differentiation with respect to τ)

$$\begin{gathered}y_1'=\left[2\left(\frac{1}{\rho}-1\right)\frac{1}{\tau^4}+\frac{n_1^2\mathrm{We}_1}{\rho\tau^3}\right]y^3-\frac{q(\tau)}{\rho}\,y_4,\\ y_2'=-q(\tau)y_4,\quad q(\tau)=\frac{2}{l_0\tau^4}+\frac{n_1^2\mathrm{We}_2}{\tau^3},\quad y_3'=n_1\mathrm{th}\frac{n_1}{\tau^2}\,y_1,\\ y_4'=\frac{n_1\mathrm{th}(n_1/\tau^2)}{\mathrm{ch}[(n_1/\tau^2)(1/l_0-1)]}\,y_1+n_1\mathrm{th}[(n_1/\tau^2)(1/l_0-1)]y_2.\end{gathered} \tag{15}$$

The initial data for system (15) follow from (6), (8), (10), (11):

$$y_1=y_{10},\quad y_2(1)=y_{20},\quad y_3(1)=y_4(1)=0. \tag{16}$$

Here and then notations are used in system (15): $\rho=\rho_1/\rho_2$; $l_0=l_{10}/l_{20}$; $n_1=\pi l_{10}n/\xi_0$ is the dimensionless wavenumber; $\mathrm{We}_j=\sigma_j/(k^2\rho_j l_{10}^3)$ are the Weber numbers; y_{j0} are the

perturbations of the velocity amplitudes at the interface and the free surface at the initial time $t = 0$ ($\tau = 1$).

The initial data (16) correspond to non-zero velocity perturbations at the free surface and the interface. A different type of perturbation is associated with a change in the initial domains [1]. In this case, the system of amplitude equations (15) remains unchanged with a different set of initial data

$$y_1(1) = y_2(1) = 0, \quad y_3(1) = y_{30}, \quad y_4(1) = y_{40}. \tag{17}$$

In conclusion of this section, we present the asymptotic behavior of system (15) for $\tau \to \infty$ and $l_0 = 1$. We will use the results of the monograph [3]. It is easy to show that $y_3' \sim y_4'$ for $\tau \to \infty$. Then for $\tau \gg 1$ $y_1(\tau)$ is a solution of the equation $(\tau^4 y_1')' + 2n_1^2\tau^{-2}y_1 = 0$. Hence [3],

$$y_1 \sim C_1 + C_2\tau^{-3}, \quad \tau \to \infty,$$

$$y_3 \sim -n_1^2\left(\frac{C_1}{\tau} + \frac{C_2}{4\tau^4}\right) + C_4, \quad y_4 \sim -n_1^2\left(\frac{C_1}{\tau} + \frac{C_2}{4\tau^4}\right) + C_3 \tag{18}$$

with constants C_j, $j = 1, ..., 4$.

The asymptotics (18) hold in the absence of surface forces $\mathrm{We}_j = 0$, $j = 1, 2$. Otherwise, for $\tau \gg 1$, the function $y_1(\tau)$ is a solution of the equation

$$(\tau^3 y_1')' + \frac{n_1^2}{\rho\tau^2}\big(\mathrm{We}_2 - \mathrm{We}_1\big)y_1 = 0,$$

so that [3] $y_1 \sim C_1 + C_2/\tau^2$, $\tau \to \infty$. Since $y_3' \sim y_4'$, we easily find

$$y_3 \sim C_3 - n_1^2\left(\frac{C_1}{\tau} + \frac{C_2}{3\tau^3}\right), \quad y_4 \sim C_4 + y_3, \quad \tau \to \infty.$$

According to the substitution (14), the amplitudes of the normal perturbations of the interface and the free surface tend to zero by the same laws:

$$N^j(\tau) \sim \frac{C_{2+j}}{\tau}, \quad \tau \to \infty, \quad j = 1, 2. \tag{19}$$

Therefore, the basic motion described by equations (1) is stable according to the linear approximation.

4. Some numerical results

The numerical solution of the Cauchy problems for the system of ODEs (15) was performed in the Maple environment using the Runge–Kutta–Fehlberg method.

Fig. 1 shows the evolution of the amplitudes $N^1(\tau)$, $N^2(\tau)$ in the absence of surface forces. The modulus of the amplitude increases with the dimensionless wavenumber n_1. Note that the curves for $N^j(\tau)$, $j = 1, 2$, "merge" for such parameter values.

Fig. 2 illustrates $N^1(\tau)$, $N^2(\tau)$ as functions of the change in l — the ratio of the initial layer thicknesses. Finally, Fig. 3 shows the behavior of $N^1(\tau)$, $N^2(\tau)$ depending on the Weber number We_2. As it increases, oscillations arise with amplitudes many times larger than those in Figs. 1 and 2.

In conclusion, we note that for $\tau \gg 1$, the behavior of the perturbation amplitudes follows the asymptotics (19). This confirms the stability of the basic motion (1). As $\tau \to \infty$, the fluids

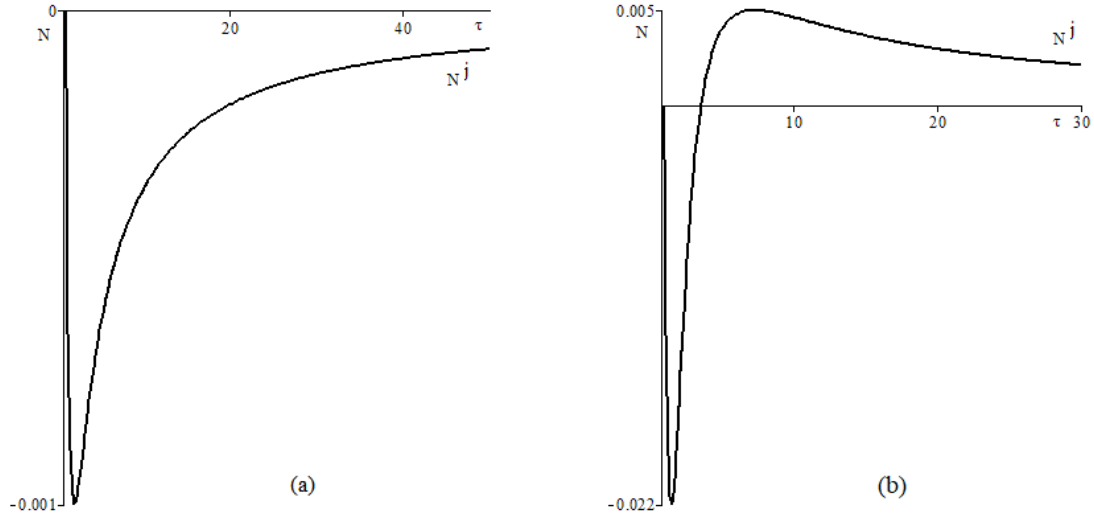

Fig. 1. Behavior of the perturbation amplitudes of the interface $N^1(\tau), N^2(\tau)$ for We1 $= 0$, We2 $= 0$, $\rho = 0.5$, $l = 1$, $y_{10} = -1$, $y_{20} = 1$, $y_{30} = y_{40} = 0$ and $n_1 = 0.5$ (a), $n_1 = 10$ (b)

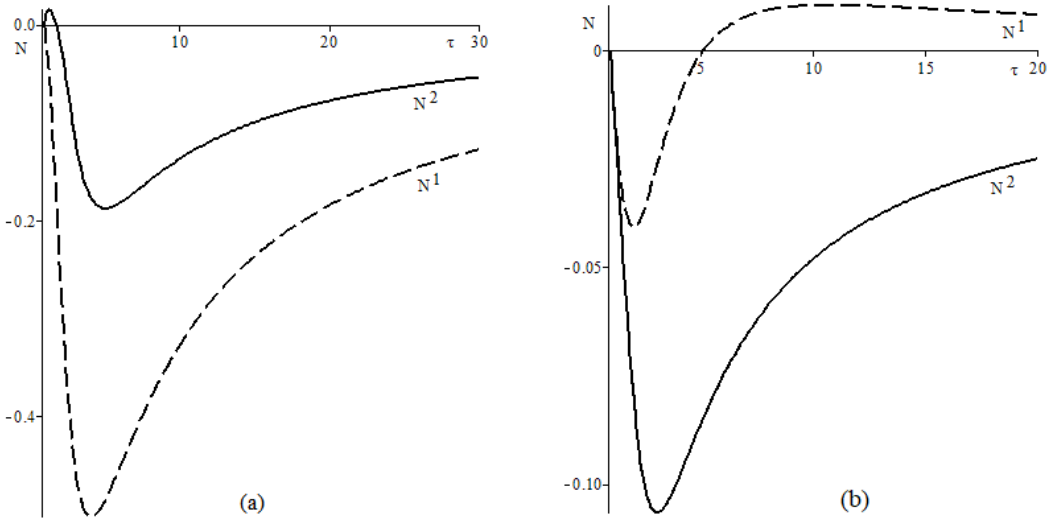

Fig. 2. Behavior of the perturbation amplitudes of the interface $N^1(\tau), N^2(\tau)$ for We1 $= 0$, We2 $= 0$, $\rho = 0.5$, $n_1 = 10$, $y_{10} = -1$, $y_{20} = 1$, $y_{30} = y_{40} = 0$ and $l = 0.5$ (a), $l = 2$ (b)

are "pressed" against the solid wall $y = 0$ ($\eta = 0$), which stabilizes the free surface and the interface.

This work is supported by the Krasnoyarsk Mathematical Center and financed by the Ministry of Science and Higher Education of the Russian Federation in the framework of the establishment and development of regional Centers for Mathematics Research and Education (Agreement No. 075–02–2025–1606).

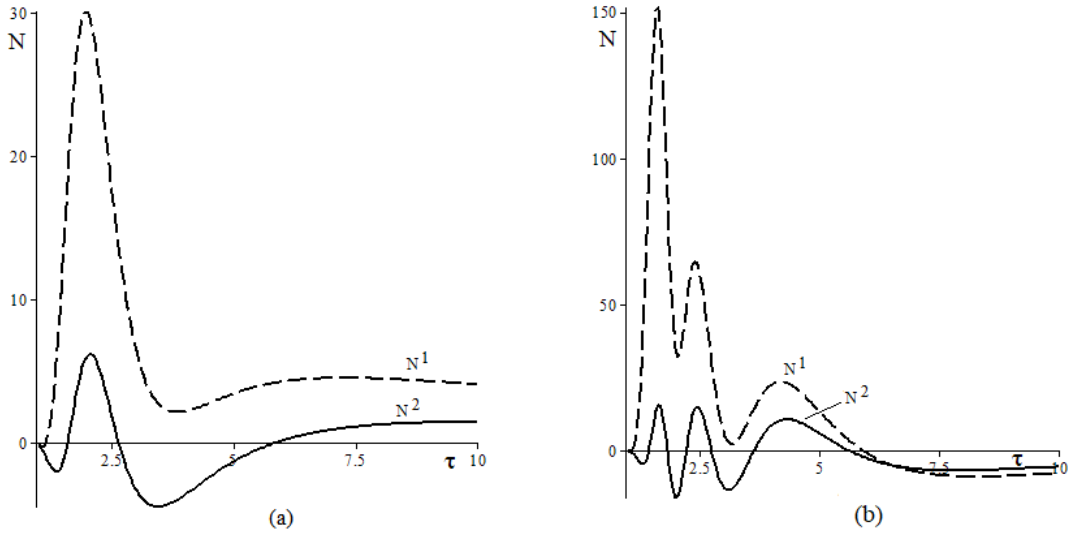

Fig. 3. Behavior of the perturbation amplitudes of the interface $N^1(\tau), N^2(\tau)$ for We1 $= 0$, $\rho = 0.5$, $n_1 = 10$, $l = 2$, $y_{10} = -1$, $y_{20} = 1$, $y_{30} = y_{40} = 0$ and $\mathrm{We}_2 = 2$ (a), $\mathrm{We}_2 = 5$ (b)

References

[1] V.K.Andreev, Stability of Unsteady Fluid Motions with a Free Boundary, Nauka, Novosibirsk, 1992 (in Russian).

[2] A.A.Abrashkin, E.I.Yakubovich, Vortex Dynamics in Lagrangian Description, Fizmatlit, Moscow, 2006 (in Russian).

[3] M.V.Fedoryuk, Asymptotic Methods for Linear Ordinary Differential Equations, Nauka, Moscow, 1983 (in Russian).

Об устойчивости совместного движения двух слоев идеальных жидкостей

Виктор К. Андреев
Институт вычислительного моделирования СО РАН
Красноярск, Российская Федерация

Аннотация. Изучается эволюция малых возмущений совместного движения двух слоев идеальных несжимаемых жидкостей на твердой подложке. Показано, что линеаризованная задача в лагранжевых координатах допускает разделение переменных. Получена система амплитудных уравнений, содержащая два числа Вебера, отношение плотностей и начальных толщин слоев, а также безразмерных волновых чисел. Приведенные результаты асимптотического и численного анализа амплитудных уравнений указывают на устойчивость движения слоёв.

Ключевые слова: идеальная жидкость, свободная граница, поверхность раздела, устойчивость по линейному приближению.

EDN: MECGDI
УДК 539.3

Elastoplastic Twisting of Rolled Section Rods Reinforced with Elastic Fibres

Olga N. Cherepanova*
Institute of Mathematics and Fundamental Informatics
Siberian Federal University
Krasnoyarsk, Russian Federation
Irina L. Savostyanova†
Scientific and Educational Center of the Institute of Space Research and High Technologies
Reshetnev Siberian State University of Science and Technology
Krasnoyarsk, Russian Federation
Sergei I. Senashov‡
Denis O. Evtikhov§
Reshetnev Siberian State University of Science and Technology
Krasnoyarsk, Russian Federation

Received 01.08.2025, received in revised form 05.10.2025, accepted 01.12.2025

Abstract. Formulas for calculating at any point the stress state of binding material of rods reinforced with elastic fibres are presented in this paper. The proposed solution method is called "conservation laws of differential equations". It allows one to construct an elastic-plastic boundary in a twisted rod and thereby evaluate its bearing capacity. The obtained relations provide the basis for developing computer programs that allow one to find the elastic-plastic boundary of the rod under study. As an example results of calculations for rods of the "H-beam" type profile are presented for various values of the torque parameter a and parameter λ.

Keywords: conservation laws, elastic-plastic boundary, rod torsion, composite materials.

Citation: O.N. Cherepanova, I.L. Savostyanova, S.I. Senashov, D.O. Evtikhov, Elastoplastic Twisting of Rolled Section Rods Reinforced with Elastic Fibres, J. Sib. Fed. Univ. Math. Phys., 2026, 19(2), 155–161. EDN: MECGDI.

Introduction

Rolled section rods are widely used in industry and construction. Let us consider some types of section rods.

Round section is one of the most used rolled sections. It takes up a considerable share of the total production volume. Round sections are used both for reinforcement or construction and as raw material pieces for lathe machining in various facilities.

Square section rods are used more frequently as raw material pieces for machine-building facilities. They are used in many products from fastening elements to components of jet engines. Also, They are used in construction for building frameworks, fences, and other metal structures.

*cheronik@mail.ru
†ruppa@inbox.ru https://orcid.org/0000-0002-9675-7109
‡sen@mail.sibsau.ru
§devtikhov@yandex.ru

Angle beam with "Γ-shape" has high strength with relatively low weight. It is a basic element in construction of framed and trussed structures, including supports of water towers, booms of column cranes, and electric power lines.

"Π-shape" section beam is used as supporting element in construction and heavy machine building. It is suited for building floor framings, stairs, elements of construction and special-purpose machinery. It can have straight and sloping flanges.

T-section beam and double T-section beam ("H-shape" beam) are used mainly in construction and heavy machine building. The presence of strengthening rib provides the profile with extra strength. That is why it withstands bending loads well. Double T-section beam can have parallel or sloping flanges.

Z-section beam was developed specially for railway carriage building industry. It is widely used in production of flat-cars and semi-railcars.

C-section beam is similar to channel bar in terms of its purpose. It is also used in construction and installation of various structures.

Channel-bar is used for building metal structures, various frameworks, supports, masts and floor framings. Also, they are used for making gates, fences, and fence doors.

Round pipes are used for making pipeline systems of various scales and purposes, for example, main pipelines, gas lines, domestic heating systems, water supply, sewage. In special cases pipes can be used as supporting elements in installations of special complexity.

Flat blank of metal is used virtually in all production and construction fields. In addition, it is used in parts of motor vehicles, tools, cases of various mechanisms and assembly units.

Recently, rolled section rods reinforced with elastic fibres are gaining acceptance. They possess a number of advantages over metal rods. As a rule, they weigh less and reinforcement allows them to withstand more loads before destruction than their metal analogues. At present, there are virtually no established methods of calculating their load-carrying capacity. The results of this paper will make a certain contribution to creating the appropriate calculation methods.

For quite some time now, equations of elasticity and plasticity are studied with the use of symmetries [1]. It was shown that symmetries allow one to build the exact solutions of these equations, some of which can be used for solving the boundary value problems. More detailed study of differential equations have shown that conservation laws are more suited for solving boundary value problems. They were used for solving boundary value problems for two-dimensional equations of plasticity [2,3,4]. It was shown that conservation laws are more suited for solving boundary value problems than the point symmetries [5]. This is explained by the fact that the symmetries are local in nature but conservation laws are global. Conservation laws were used for solving the elastoplastic problems of rod twisting and cantilever bending, and for solving elastoplastic problems for plates of finite sizes weakened by holes. Conservation laws were also used for solving boundary value problems for composite materials [6].

A method of constructing the elastoplastic boundary in twisted rolled section rods reinforced with elastic fibres is proposed in this study. This method allows one to evaluate the load-carrying capacity of such rods.

1. Problem setting

Let us consider elastoplastic twisting of a rolled section rod under the influence of torque. It is assumed that rod is reinforced with elastic fibres. The boundary of the contact layers is located along z axis. The lateral boundary of the rod is free from strains but the boundary is

in plastic state. Strain tensor components at a point are calculated with the help of contour integrals deduced from conservation laws formulated on the lateral boundary and the boundary of fibres. Further, the second strain tensor invariant is compared with yield limit. If yield limit is reached at some point then plastic state occurs at this point otherwise there is elastic state. This allows one to determine the boundary between plastic and elastic areas. This procedure provides a way to calculate elastoplastic boundaries for rods of basic rolled sections. One should note that boundary value problems for elastoplastic twisting of isotropic rods and elastic media for bodies of finite sizes were solved with the help of conservation laws.

Let us consider a rectilineal rod made of an elastoplastic material reinforced with elastic n fibres.

Matrix of the rod has elasticity modulus G and yield limit at pure shear k.The fibres are located along the rod in random order, and they are parallel to z axis. Each fibre has round cross-section, and its centre is located at the point with coordinates (x_i, y_i). Radius of fibre is equal to R, and elasticity modulus is G_i. The yield limit of the fibres exceeds the yield limit of the matrix. Tangential stress between the fibre and the matrix is equal to $\tau < k$.

The given process is described by the equilibrium equation

$$\frac{\partial \tau_{xz}}{\partial x} + \frac{\partial \tau_{yz}}{\partial y} = 0 \tag{1}$$

and by equation of strain compatibility

$$\frac{\partial \tau_{xz}}{\partial y} = \frac{\partial \tau_{yz}}{\partial x}. \tag{2}$$

The lateral surface of the rod is free from stresses, and it is in plastic state

$$\tau_{xz} n_0 + \tau_{yz} m_0 = 0, \quad \tau_{xz}^2 + \tau_{yz}^2 = k^2,$$

where n_0, m_0 are components of the vector normal to the lateral surface which can be written as

$$\tau_{xz} = \mp mk, \quad \tau_{yz} = \pm nk. \tag{3}$$

On the boundary between the fibre and the matrix the following conditions

$$\tau_{xz} m_i - \tau_{yz} n_i = \tau, \quad \tau_{xz}^2 + \tau_{yz}^2 = k^2,$$

are formulated, where n_i, m_i are components of the vector normal to the lateral surface of i fibre which are written in the form

$$\tau_{xz} = m\tau \pm n\sqrt{k^2 - \tau^2}, \quad \tau_{yz} = n\tau \pm m\sqrt{k^2 - \tau^2}. \tag{4}$$

Further, the upper sign is selected in relations (3)—(4).

2. Conservation laws for equations (1)-(2)

For convenience of further calculations, let us introduce the following notations

$$\tau_{xz} = u, \quad \tau_{yz} = v.$$

Then problem (1)–(4) is written as

$$F_1 = u_x + v_y = 0, \quad F_2 = u_y - v_x = 0. \tag{5}$$

Conditions on the lateral surface are

$$u = \mp mk, \quad v = \pm nk,$$

and conditions on the boundary of the fibre and the matrix are

$$u = m\tau \pm n\sqrt{k^2 - \tau^2}, \quad v = n\tau \pm m\sqrt{k^2 - \tau^2}.$$

Definition 1. *Conservation law for system of equations (5) is expressed in the following form*

$$A_x(x, y, u, v) + B_y(x, y, u, v) = \omega_1 F_1 + \omega_2 F_2, \tag{6}$$

where ω_1, ω_2 are some linear operators that are not simultaneously identically zero.

Let us assume that

$$A = \alpha^1 u + \beta^1 v + \gamma^1, \quad B = \alpha^2 u + \beta^2 v + \gamma^2, \tag{7}$$

where $\alpha^{i1}, \beta^i, \gamma^i$ are functions of only x and y.
Inserting (7) into (6), one can obtain

$$\alpha^1_x + \alpha^2_y = 0, \quad \beta^1_x + \beta^2_y = 0, \quad \alpha^1 = \omega_1,$$
$$\beta^1 = -\omega_2, \quad \alpha^2 = \omega_2, \quad \beta^2 = \omega_1, \quad \gamma^1_x + \gamma^2_y = 0.$$

It follows that

$$\alpha^1_x - \beta^1_y = 0, \quad \beta^1_x + \alpha^1_y = 0, \quad \gamma^1_x + \gamma^2_y = 0. \tag{8}$$

Let us consider two solutions for system of equations (8):
1.

$$\alpha^1 = \frac{x - x_0}{(x - x_0)^2 + (y - y_0)^2}, \quad \beta^1 = -\frac{y - y_0}{(x - x_0)^2 + (y - y_0)^2}, \tag{9}$$

2.

$$\alpha^1 = \frac{y - y_0}{(x - x_0)^2 + (y - y_0)^2}, \quad \beta^1 = \frac{x - x_0}{(x - x_0)^2 + (y - y_0)^2}, \ \gamma^1 = 0, \ \gamma^2 = 0, \tag{10}$$

where x_0, y_0 are constants.

3. Calculating stress condition at point x_0, y_0

Let us assume that x_0, y_0 is an arbitrary point that belongs to the bonding material. It is also assumed that at this point the conserved current has singularity of the form (9) or (10) (see Fig. 1). Then it follows from (6) that

$$\iint\limits_S (A_x + B_y)dxdy = \oint\limits_{\Gamma_0} dy - Bdx - \sum_{i=1}^{n} \oint\limits_{\Gamma_i} Ady - Bdx - \oint\limits_{\varepsilon} Ady - Bdx = 0 \tag{11}$$

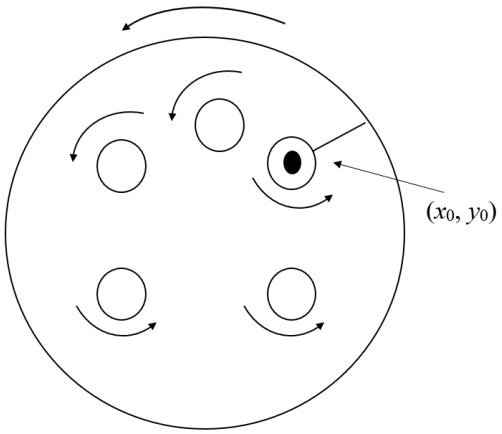

Fig. 1. Rod's cross-section

Let us consider solution (9) and assume that $x - x_0 = \varepsilon os\phi$, $y - y_0 = \varepsilon \sin\phi$. Then taking into account (9), one can obtain from (11) for $\varepsilon \to 0$ that

$$
\begin{aligned}
2\pi\tau_{xz}(x_0,y_0) = \oint_{\Gamma_0} &\left(m_0 k \frac{x-x_0}{(x-x_0)^2+(y-y_0)^2} - n_0 k \frac{y-y_0}{(x-x_0)^2+(y-y_0)^2} \right) dy - \\
-&\left(m_0 k \frac{y-y_0}{(x-x_0)^2+(y-y_0)^2} + n_0 k \frac{x-x_0}{(x-x_0)^2+(y-y)^2} \right) dx + \\
+\sum_{i=1}^{n} \oint_{\Gamma_i} &\left(\frac{(m_i\tau + n_i\sqrt{k^2-\tau^2})(x-x_0)}{(x-x_0)^2+(y-y_0)^2} - n_0 k \frac{(-n_i\tau + m_i\sqrt{k^2-\tau^2})(y-y_0)}{(x-x_0)^2+(y-y_0)^2} \right) dy - \\
-&\left(m_i\tau + n_i\sqrt{k^2-\tau^2} \frac{y-y_0}{(x-x_0)^2+(y-y_0)^2} + n_i\tau + m_i\sqrt{k^2-\tau^2} \frac{x-x_0}{(x-x_0)^2+(y-y)^2} \right) dx,
\end{aligned}
\tag{12}
$$

$$
\begin{aligned}
2\pi\tau_{yz}(x_0,y_0) = \oint_{\Gamma_0} &\left(m_0 k \frac{y-y_0}{(x-x_0)^2+(y-y_0)^2} + n_0 k \frac{x-x_0}{(x-x_0)^2+(y-y_0)^2} \right) dy - \\
-&\left(- m_0 k \frac{x-x_0}{(x-x_0)^2+(y-y_0)^2} + n_0 k \frac{y-y_0}{(x-x_0)^2+(y-y_0)^2} \right) dx + \\
+\sum_{i=1}^{n} \oint_{\Gamma_i} &\left(\frac{(m_i\tau + n_i\sqrt{k^2-\tau^2})(y-y_0)}{(x-x_0)^2+(y-y_0)^2} + n_0 k \frac{(-n_i\tau + m_i\sqrt{k^2-\tau^2})(x-x_0)}{(x-x_0)^2+(y-y_0)^2} \right) dy - \\
-&\left(- \left(m_i\tau + n_i\sqrt{k^2-\tau^2}\right) \frac{x-x_0}{(x-x_0)^2+(y-y_0)^2} + \right. \\
&\left. + n_i\tau + m_i\sqrt{k^2-\tau^2} \frac{y-y_0}{(x-x_0)^2+(y-y)^2} \right) dx.
\end{aligned}
\tag{13}
$$

Expressions (12) and (13) allow us to calculate the stress condition at any point of the bonding material. Those points where $\tau_{xz}^2 + \tau_{yz}^2 = k^2$ are in plastic state. The remaining points of the medium and the fibre remain in elastic state. The proposed method allows us to construct the elastoplastic boundary in the twisted rod, and to evaluate its load-carrying capacity.

Let us use these formulas to construct the elastoplastic boundary for rolled section rods.

4. Construction of elastic-plastic boundary for a rolled profile rod

Computer programs in the Maple environment was developed [7]. The calculation results are presented below. The change in the elastic-plastic boundaries of the rolled "H-shaped" section with the change in the value of the torque parameter a is shown in Fig. 2. The radius of the reinforcing fibre is equal to 0.5 in these figures. The areas that are marked in red are the plastic areas in these figures. The areas that are marked in green are the elastic areas.

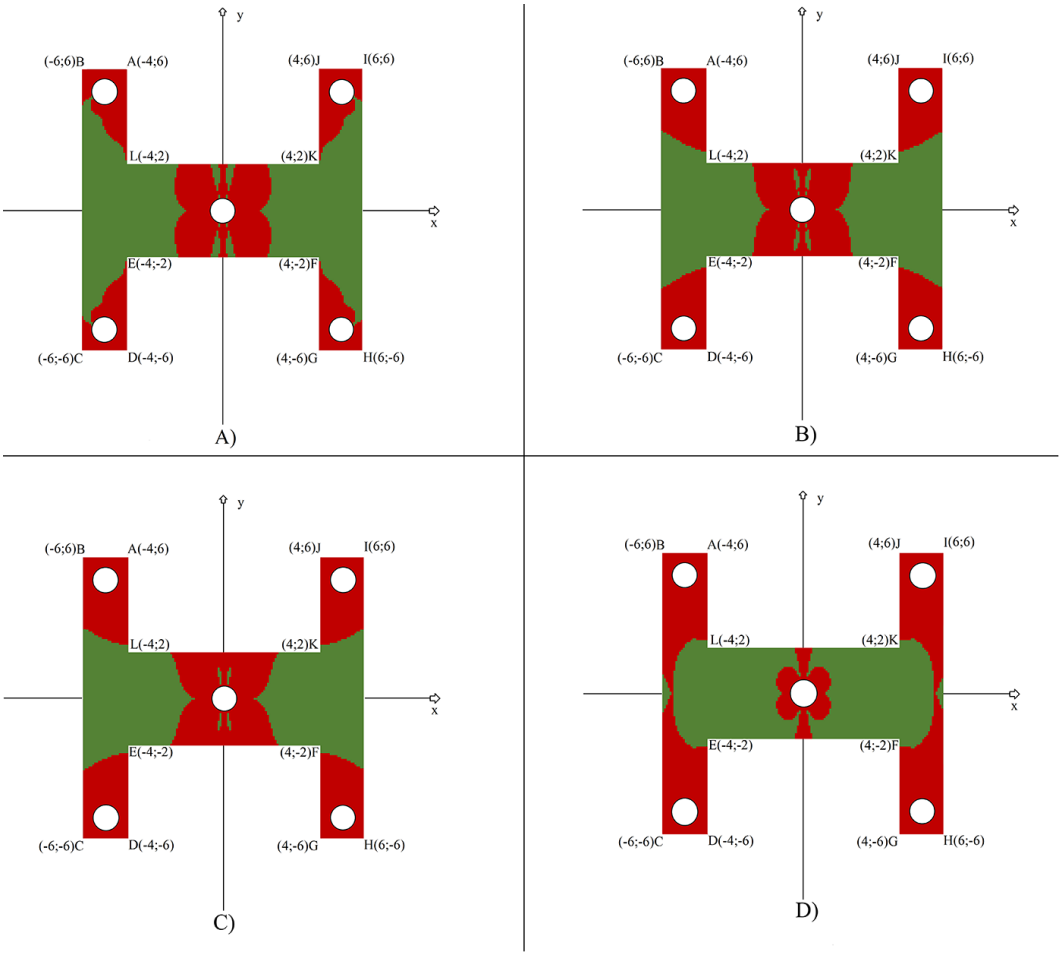

Fig. 2. The elastic-plastic boundary of the "H-shaped" section for various values of the torsional parameter a; A) $a = -0.6$, B) $a = -1$, C) $a = -1.6$, D) $a = -3$

Conclusion

The paper presents formulas that allow one to calculate the stress state at any point in the bonding material of rods reinforced with elastic fibres. The proposed method, called "conservation laws of differential equations", allows one to construct elastic-plastic boundary in a torsionally loaded rod and assess its load-bearing capacity. The formulas obtained with the use of conservation laws provide the basis for creating computer programs. They enable to deter-

mine the elastic-plastic boundary of the studied rod. The results of application of the developed computer program to the "H-shaped" section rod for various values of the torque parameter a and parameter λ are presented.

References

[1] B.D.Annin, V.O.Bytev, S.I.Senashov, Group properties of the equations of elasticity and plasticity, Novosibirsk: Siberian Branch of the USSR Academy of Sciences, 1983 (in Russian).

[2] S.I.Senashov, O.N.Cherepanova, A.V.Kondrin, On the elastic-plastic torsion of a rod, *Vestnik SibGAU*, **49**(2013), no. 3, 100 (in Russian). DOI:10.17516/1997-1397-2015-8-3-343-351

[3] S.I.Senashov, O.V.Gomonova, A.N.Yakhno, Mathematical issues of two-dimensional equations of ideal plasticity, Krasnoyarsk: SSib. gos. aerokosmich. Un., 2012 (in Russian).

[4] S.I.Senashov, I.L.Savostyanova, Elasto-plasticity and conservation laws Krasnoyars, Reshetnev University, 2023 (in Russian).

[5] L.V.Ovsyannikov, Group analysis of differential equations, Moscow, Nauka, 1978 (in Russian).

[6] S.I.Senashov, I.L.Savostyanova, The stress state of the composite console, *Composites and nanostructures*, **16**(2024), no. 1, 56 (in Russian). DOI: 10.36236/1999-7590-2024-16-1-56-61

[7] D.O.Evtikhov, I.L.Savostyanova, S.I,Senashov, O.N.Cherepanova, Construction of the Elastic-Plastic Boundary of a Twisted H-Beam Reinforced with Elastic Fibers, Certificate of Registration of a Computer Program **RU 2025614229**(20.02.2025), Application no. 2025612437.

Упруго-пластическое кручение стержней прокатного профиля, армированных упругими волокнами

Ольга Н. Черепанова
Сибирский федеральный университет
Красноярск, Российская Федерация
Ирина Л. Савостьянова
Сергей И. Сенашов
Денис О. Евтихов
Сибирский государственный университет науки и технологий имени академика М. Ф.Ѓешетнева
Красноярск, Российская Федерация

Аннотация. В статье приведены формулы, которые позволяют вычислить напряженное состояние в любой точке связующего материала стрежней, армированных упругими волокнами и подвергающихся кручению. Предложенный метод решения, который называется «законы сохранения дифференциальных уравнений», позволяет построить упруго-пластическую границу в скручиваемом стержне и тем самым оценить его несущую способность. Формулы, которые были выведены с помощью законов сохранения, стали основой создания программ для ЭВМ, позволяющих найти упруго-пластические границы исследуемых стержней. В заключение статьи приведены результаты работы программы для ЭВМ с различными значениями крутящего параметра a и параметра λ для стержней прокатного профиля типа «двутавр».

Ключевые слова: законы сохранения, упруго-пластическая граница, кручение стрежней, композиционные материалы.

EDN: HTICJO
УДК 536.24, 537.84

Numerical Investigation of Electrovortex Flows Induced by a Low Frequency Alternating Current

Pavel I. Polyakov*
Igor O. Teplyakov†
Laboratory 10.2
Joint Institute of High Temperatures RAS
Moscow, Russian Federation
Stepan M. Yudin‡
Institute of Thermal and Nuclear Power Engineering
National Research University «MPEI»
Moscow, Russian Federation

Received 22.05.2025, received in revised form 24.06.2025, accepted 27.11.2025

Abstract. In current paper we present numerical evaluations of electrovortex flows in a melt of In-Ga-Sn. A hemispherical copper container is filled with the melt. The flows were induced by applying low frequency (0.1–20 Hz) alternating current. Velocity, temperature, and mass concentration of the same melt admixture were obtained. An influence on the motion and heat transfer by the sinusoidal current was demonstrated.

Keywords: electrovortex flows, magnetohydrodynamics, numerical modelling.

Citation: P.I. Polyakov, I.O. Teplyakov, S.M. Yudin, Numerical Investigation of Electrovortex Flows Induced by a Low Frequency Alternating Current, J. Sib. Fed. Univ. Math. Phys., 2026, 19(2), 162–174. EDN: HTICJO.

Introduction

Electrovortex flows (hence in the text: EVFs) has a significance matter in such industrial areas as metal remelting, electrical welding, blanket liquid metal cooling systems in fusion reactors, breeder nuclear reactors, and promising liquid-metal batteries. In metallurgical furnaces knowledge of the vortex topology is important in view of output metal quality; purity and crystal grid structure are important factors for manufacturing end products. In this case mass transfer plays important role in research field of electrically induced flows. Our paper is tied with electroslag and electric-arc furnaces, however we don't consider our results as a direct simulation of any metallurgical setup.

The EVFs are generated by Lorentz forces $\mathbf{F}_\mathrm{L}$ in a liquid medium. Non-uniform distributed electrical current $\mathbf{j}$ that flows through the liquid metal medium and any non-parallel to the current magnetic field with induction $\mathbf{B}$ cause Lorentz force to appear: $\mathbf{F}_\mathrm{L} = \mathbf{j} \times \mathbf{B}$. Magnetic fields could be internal (self-induced by the current) and external (e.g., Earth's magnetic field). Non-uniformity of the current flow guarantees existence of non-zero curl of Lorentz force (rot),

*paul.ingvarsson@yandex.ru https://orcid.org/0009-0005-7124-332X
†igor.teplyakov@mail.ru https://orcid.org/0000-0002-2355-1935
‡yudin_uchebnaya@mail.ru https://orcid.org/0009-0007-8902-9561

which is needed to rotate the fluid in an enclosed geometry; in such conditions potential force, e.g. gravity, is not able to move the medium particles anywhere.

Studies of the EVFs trace to the paper written by S. Lundquist [1], where the author considered semi-infinite space filled with electrical conducting fluid, whither vertical external current is conducted through a point on a surface. Further works by Shercliff [2], Sozou [3, 4], Ajayi [5], Andrews [6], Davidson [7], Shatrov and Gerbeth [8] are devoted to theoretical description and numerical evaluation of the EVFs in hemispherical containers induced by a direct current with absence of an external magnetic field. Moreover, in the Soviet journal «Magnitnaya Gidrodinamika» numerous important papers [9–12] were published in the theme of EVFs. The pioneering experimental investigations of vortices induced by currents were performed in [14] in the Institute of Physics at Salaspils, Latvian SSR. Main equations and results are summarized in the [15] monograph. The idea and general scheme of the experiments were later adopted by JIHT RAS, where series of numerical and experimental works were carried [16–19]. In [20] it was shown, that external magnetic field of induction approximately 10^{-5} T significant swirl flow appears. Numerical investigations with cylindrical and hemisperical geometries with presence of vertical external magnetic fields with various inductions ($10^{-6} \dots 10^{-1}$ T) provided by Kharicha and his research group [21, 22] were performed to find fluid patterns and map them. In the last mentioned papers it was shown that vortex structure dramatically changes with increasing the external magnetic field.

Despite presence of plenty valuable proceedings in the EVFs, alternating current gained virtually little attention. The doctoral thesis [23] by A. Chudnovsky contains one section devoted to an effect of an alternating current on liquid metal EVF between two semi-infinite conductive plates. It was theoretically demonstrated that enlarging value of the current frequency leads to flattening of the cross-section velocity profile.

The importance of investigation on the EVFs induced by an alternating current heads from the paper [24] and doctoral thesis [25], in which reported that output quality of metal, produced in AC electrometallurgical furnaces, is better than that of DC units. However, these publications deal with the EVFs very little; conclusions there were made on basis of material science methods without deep understanding of internal fluid flow structure.

In our paper computations of the EVFs induced by an alternating current with absence of any external magnetic field in a hemispherical geometry are presented. Velocity, temperature, and mass concentration fields were calculated and are presented here with various diagrams.

1. Problem statement

1.1. Computational domain

In our investigation the EVFs were calculated in a 2D, axisymmetrical domain that represents experimental setup used in [26]. On the Fig. 1 the domain is drawn. Here, the melt *1* is located in the copper cylindrical container *3* that has the hemispherical cavity with radius $r_{\text{out}} = 94$ mm. The upper conductor *2* made of copper or steel is situated upon the open surface of the melt, whereas only spherical ending with radius $r_{\text{in}} = 2.5$ mm is deepened in the fluid. Around the electrical setup an air is modelled to provide a region to set room temperature and availability of heat transfer from the setup to an external medium.

The current terminals are B_1 and B_2 that are connected to an external source of sinusoidal current and ground respectively.

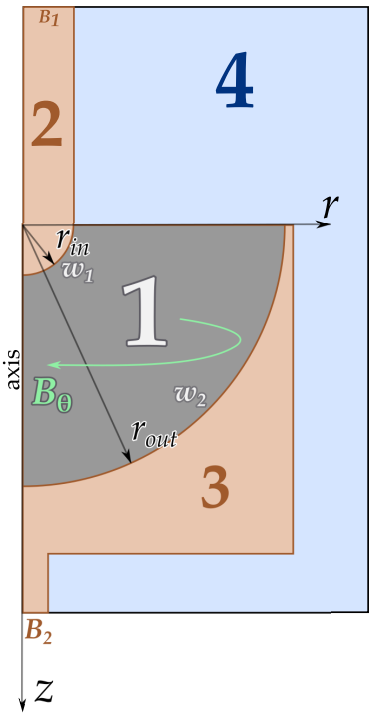

Fig. 1. The computational domain

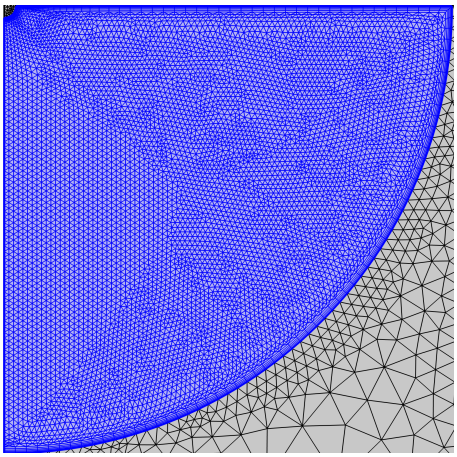

Fig. 2. The grid of the problem

For computations the finite-volume method is used. The method is realized in COMSOL 6.1 Multiphysics code. A grid of the domain is presented in Fig. 2; it has 17,922 cells, including a majority of triangle elements and quadrangle boundary layers near walls and the open surface. Linear dimensions of the elements in the volume vary from 0.0036 to 1.21 mm. In the electrodes the grid has coarser quality with dimensions up to 10 mm in account of the fact that there are only electromagnetic equations are solved.

Properties of the melt were taken from the experimental investigation conducted by Plevachuk et al [27]. The In-Ga-Sn euthectic composition is considered in account of two factors: the first one is experimental setup that contains this melt as working fluid; the second — its availability, relatively low melt temperature (283.7 K), and non-toxicity to researchers in comparison with mercury. Used empirical relations for the properties are listed in the following Tab. 1.:

Table 1. Properties of the In-Ga-Sn, taken from [27]

Property	Expression
Electrical conductivity, S/cm	$\sigma(T) = \sigma_0 - 49.8(T - T_m) + 0.0476(T - T_m)^2$
Thermal conductivity, W/(m·K)	$\lambda_0 + 0.0614(T - T_m) + 4.9 \cdot 10^{-5}(T - T_m)^2$
Viscosity, mPa·s	$\eta(T) = \eta_0 \exp(E/RT)$
Density, g/cm^3	$\rho = \rho_0 + \mathrm{d}\rho/\,\mathrm{d}t(T - T_m)$

In the table above, $\sigma_0 = 33170$ S/m; $T_m = 283.7$ K is the melting temperature; $\lambda_0 = 23.4$ W/(m·K); $R = 8.3144$ J/(mol·K) is the specific gas constant; $\eta_0 = 0.4352$ mPa·s; $\rho_0 = 6.58$ g/cm^{-3} and $E = 3904$ J/mol are fitting parameters. Although specific heat capacitance c_p of the melt wasn't considered in the mentioned paper, the constant value of 296 J/(kg·K) was used; it had been described in [28].

1.2. Governing equations

The electrovortex flows are multidisciplinary phenomena; they are described by coupled hydrodynamics and electromagnetics equations. In our investigeation heat and mass transfer equations were also evaluated.

There is a list of assumptions chosen to calculate the EVFs:

1. Electromagnetic field equations are considered with low frequency approximation to avoid displacement field consideration;
2. Physical properties of the melt are non-isothermal;
3. Air movement and melt's open surface deformation are not considered;
4. Free charges in the melt are absent;
5. All the setup is non-magnetic: $\mu = 1$.

The liquid metal medium of In-Ga-Sn is considered as incompressible, viscous fluid with properties depended on temperature. Therefore further motion equation is used in the calculations:

$$\rho(T)\left[\frac{\partial \mathbf{u}}{\partial t} + (\mathbf{u}\cdot\nabla)\mathbf{u}\right] = -\nabla p + \nabla\left[\eta(T)\nabla\mathbf{u}\right] + \mathbf{F}_{\mathrm{L}}, \tag{1}$$

where ρ — density, kg/m^3; T — temperature, K; $\mathbf{u}$ — velocity, m/s; t — time, s; p — pressure, Pa; η — dynamic viscosity, Pa/s. From the experiments mentioned above it's known that the EVFs are turbulent therefore $k-\omega$ — model of a turbulence is used.

On account of considering the medium as continuous, the mass conservation equation in the following form is used:

$$\nabla(\rho(T)\mathbf{u}) = 0. \tag{2}$$

Heat transfer is considered to investigate its effect on velocity fields of the flows; its equation is following:

$$\rho(T)c_p(T)\left(\frac{\partial T}{\partial t} + \mathbf{u}\cdot\nabla T\right) = \nabla\cdot(\lambda(T)\nabla T) + q_V, \tag{3}$$

where c_p — heat capacity at constant pressure, J/(kg·K); λ — thermal conductivity, W/(m·K); q_V — a volumetric source of a heat. The primary source of heat is Joule's heating process which is described as:

$$q_V = |\mathbf{j}^2|/\sigma(T), \tag{4}$$

where σ — electrical conductivity, A/m^2.

As mentioned in the Introduction, the EVFs source of motion is the electromagnetic force $\mathbf{F}_{\mathrm{L}}$, therefore the following set of equations that descrives electric and magnetic fields has to be introduced:

$$\nabla\cdot\mathbf{j} = 0; \tag{5a}$$

$$\mathbf{j} = \frac{1}{\mu_0}\nabla\times\mathbf{B}; \tag{5b}$$

$$\nabla\times\mathbf{A} = \mathbf{B}; \tag{5c}$$

$$-\nabla\Phi - \frac{\partial\mathbf{A}}{\partial t} = \mathbf{E}; \tag{5d}$$

$$\mathbf{j} = \sigma(T)(\mathbf{E} + \mathbf{u}\times\mathbf{B}). \tag{5e}$$

Here $\mu_0 \approx 1.26 \cdot 10^{-6}$ N/A^2 — the vacuum magnetic permeability; $\mathbf{A}$ — magnetic vector potential, Wb/m; Φ — electrical potential, V; $\mathbf{E}$ — electric field, V/m. The equation (5a) represents the conservation law of charges in the considered medium. Maxwell's equation in general form and magnetic vector potential representations are described by (5b)–(5d). The last expression (5e) is Ohm's law in general form with effect of the velocity field $\mathbf{u}$ on the current $\mathbf{j}$.

Lorentz's force $\mathbf{F}_\mathrm{L}$ couples hydrodynamics and electromagnetic fields; the following equation sets the force:

$$\mathbf{F}_\mathrm{L} = \mathbf{j} \times \mathbf{B}. \tag{6}$$

Mass transfer calculation is intended to investigate mixing quality. In this article neutral admixture method is used: in small area of a computational domain working fluid is marked as admixture, while all other properties are the same. The following expression describes the mixing process:

$$\frac{\partial C}{\partial t} + \mathbf{u} \cdot \nabla C = D \Delta C, \tag{7}$$

here C — concentration, mol/m^3; D — self-diffusivity coefficient (equals to 5×10^{-9} m^2/s for the In-Ga-Sn melt).

Governing equations and the domain were defined therefore it's necesserarily to define boundary and initial conditions shown in the Tab. 2.

Table 2. Boundary conditions. Here, f is the current frequency, Hz; $\mathbf{q}$ is a heat flow, W/m.

Boundary	Hydrodynamics	Electromagnetics	Thermal
MELT			
Inner wall	$\mathbf{u} = 0$	E/M-continuity	Heat from upper conductor
Outer wall	$\mathbf{u} = 0$	E/M-continuity	Heat to container
Open surface	$u_n = 0$	E/M-continuity	Room air heat exchange
UPPER CONDUCTOR			
Upper border	N/A	$\mathbf{j} = j_0 \cos(2\pi f t)$	$\mathbf{q} = 0$
Outer wall	N/A	E/M-continuity	Room air heat exchange
Spherical ending	N/A	E/M-continuity	Heat to melt
CONTAINER			
Spherical wall	N/A	E/M-continuity	Heat from melt
Outer walls	N/A	E/M-continuity	Room air heat exchange
Lower border	N/A	$\Phi = 0$	$\mathbf{q} = 0$
AIR			
Walls/open surface	N/A	E/M-continuity	Heat exchange with setup
Outer boundaries	N/A	$\mathbf{A} = 0$	$\mathbf{q} = 0$

1.3. Mass transfer problem additions

For the mass transfer problem some modifications in the domain were made. In the melt zone a square with 10×10 mm linear dimensions was situated. The upper edge is located on the depth of 35 mm from the open surface of the melt, while one of the vertical sides is placed onto symmetry axis. In this small region the same In-Ga-Sn melt is mapped, however here there is a mark of concentration, while in the remaining zone such mark is absent. Marking of the neutral admixture is made by setting non-zero concentration value.

2. Results

2.1. Calculation approach

To compute the EVFs in the problem stated above the following scheme was used. Firstly, electromagnetic equations (5a)–(5e) are solved, which result in the magnetic field **B** and current density **j**. Secondly, heat exchange is computed, as electromagnetic heating can be included in a solution. The next stage is calculating hydrodynamics in the domain; the Lorentz force and physical properties are available. Finally, mass transfer equation is solved.

In total, 40 regimes were solved. Total current in the upper electrode along with its frequency, and upper electrode's material were varied. Current values were 250, 500, 750, and 1000 A; frequencies: 0.5, 1, 5, 10, and 20 Hz. Upper electrode's material was either copper or steel. Each regime was solved for time length of 100 electrical periods (1/Hz) to calculate stabilized behavior of the vortices.

2.2. Velocity fields

As mentioned in the Introduction, a flow structure is of the great importance in the investigation. On the Fig. 3 four EVF formation stages are shown. The subfigure (*a*) depicts jet initiation under the upper electrode, which forms a small counter-vortex (seen at (*b*)) that downs to the bottom of hemispherical container (*c*) and finally merges into a single EVF (*d*). Such flow structure is the same to that can be seen when the electric current is direct.

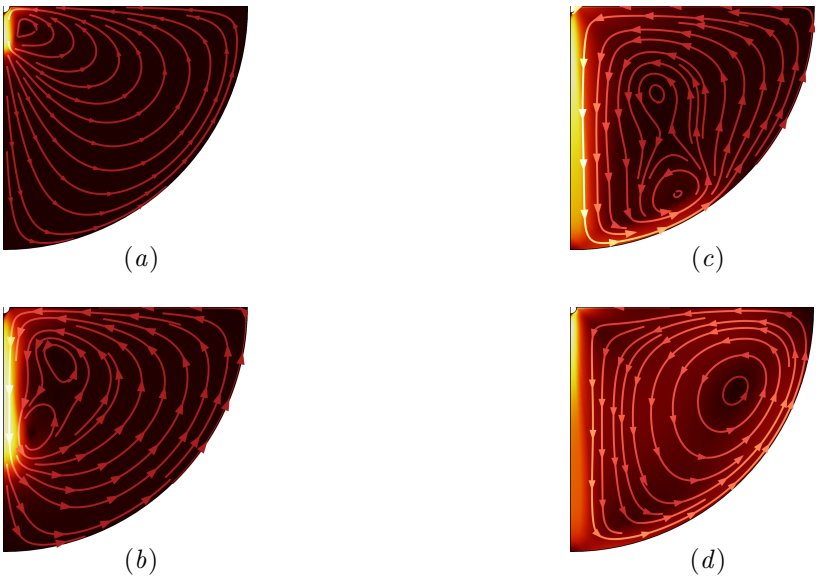

Fig. 3. An electrovortex flow formation

The main distinction between AC and DC induced EVFs is a jet pulsation in the former case. These pulsations can be represented by axial velocity diagrams like shown in Figs. 4 and 5. On the subplots axial velocities on four depths (10, 30, 50, and 70 mm) are shown. These depth values are chosen in account of forecoming experimental tests. The points of consideration are situated on the symmetry axis. Two distinct variants of representation were made: with fixed

frequency (Fig. 4) and fixed electric current (Fig. 5). The pale thin lines are real-time values of the velocities that have distinctive oscillation behavior, while thick lines represent mean values.

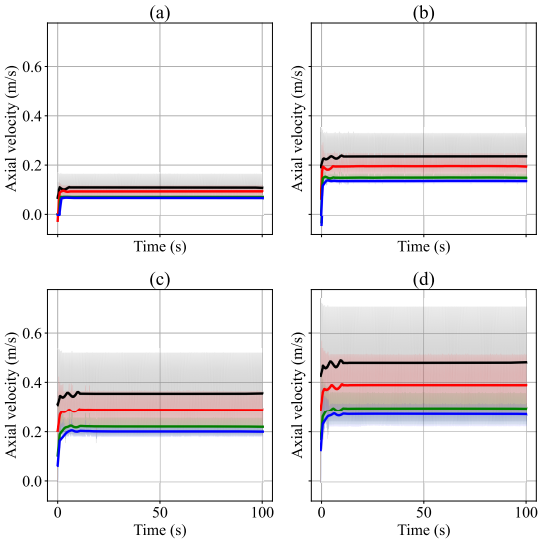

Fig. 4. Axial velocity. Frequency, Hz: 1. Current, A: (*a*) 250, (*b*) 500, (*c*) 750, (*d*) 1000. The upper electrode is made of steel

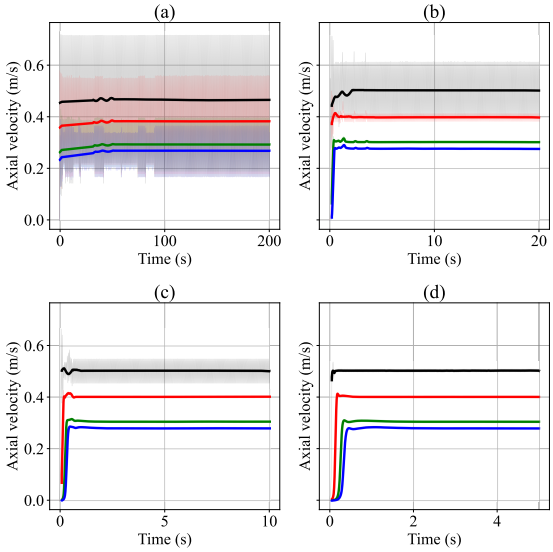

Fig. 5. Axial velocity. Current, A: 1000. Frequency, Hz: (*a*) 0.5, (*b*) 5, (*c*) 10, (*d*) 20. The upper electrode is made of steel

The following colors are used: black for 10 mm depth, red: 30 mm, green: 50 mm, and blue: 70 mm

From the velocity plots two important conclusions can be derived. The first one is that the higher the current the greater oscillations and mean velocities are. Such behavior is simple to be predicted. The second one is that amplifying frequency leads to abating the oscillation amplituides but not the mean velocity values, which stay virtually the same.

Oscillation behavior of axial velocity profiles on the symmetry axis is presented in Fig. 6. In these plots four lines are depicted; each one corresponds to an immediate time period of stabilized oscillations. Black color is used for the time when oscillating electromagnetic force has its maximum, while red for the minimum one. Blue and green are used for intermediate (around a half) positions in time between maximum and minimum and vice versa respectively. Such flattening of the velocity profiles was predicted in doctoral thesis by Chudnovksy [23].

2.3. Temperature fields

Temperatures in the EVFs distribute from the upper electrode with thermal conductivity, and heated zones are concentrated in the jet.Heat data on the axis were collected and are shown of Figs. 7 and 8, which are calculated in the same conditions as velocities are.

The following phenomena could be seen from plots metioned above. Increasing the current with fixed frequency leads to mean temperatures and their oscillations augmenting and furthermore slight positive slope appearing. In contrast, increasing the frequncy with constant current diminishes temperature and its oscillations. The latter phenomenon is known effect caused by an AC Joule's heating.

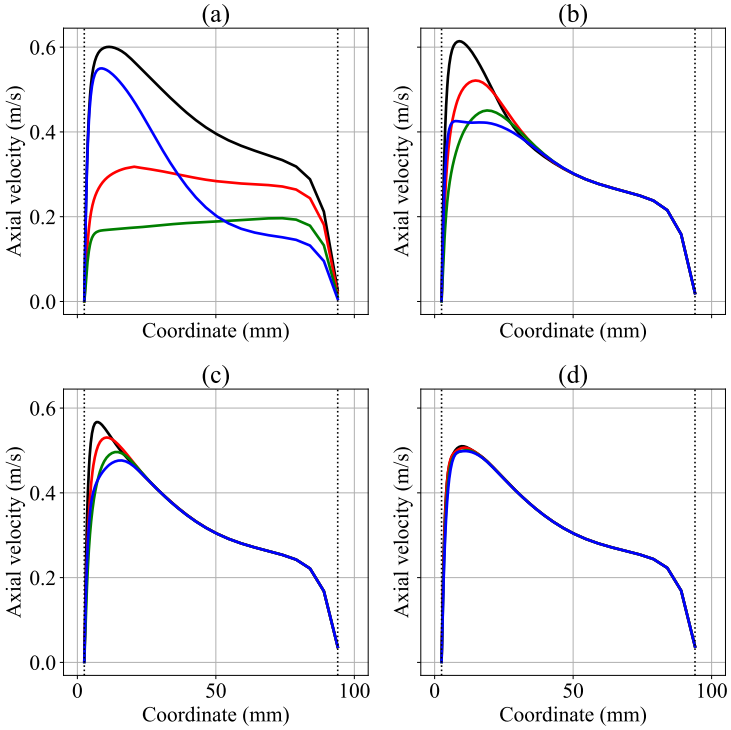

Fig. 6. Axial velocity profiles at current of 1000 A. Frequencies, Hz: (*a*) 0.5, (*b*) 5, (*c*) 10, and (*d*) 20. The upper electrode is made of steel

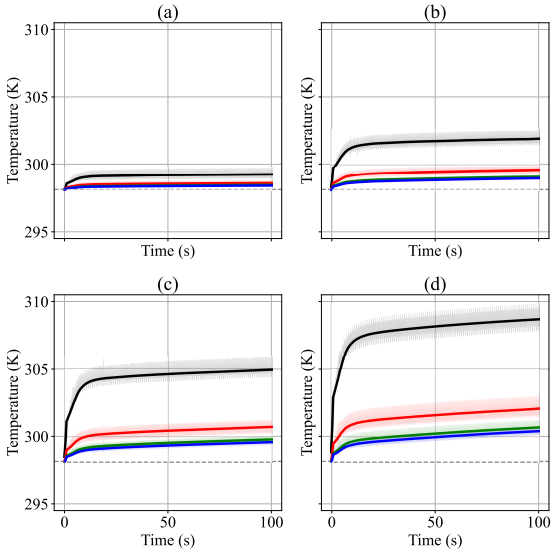

Fig. 7. Temperature on the symmetry axis. Frequency, Hz: 1. Current, A: (*a*) 250, (*b*) 500, (*c*) 750, (*d*) 1000. The upper electrode is made of steel

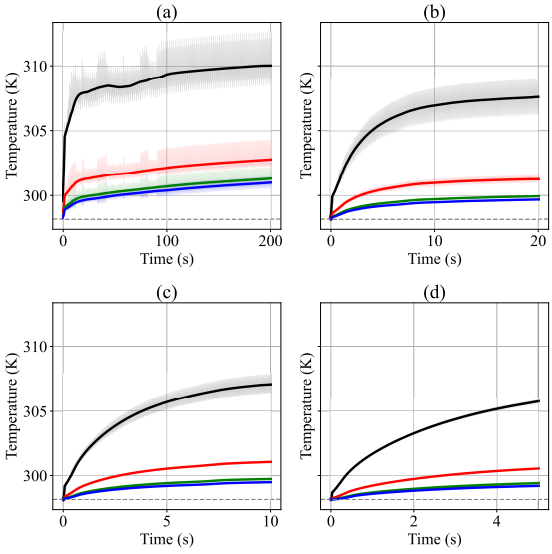

Fig. 8. Temperature on the symmetry axis. Current, A: 1000. Frequency, Hz: (*a*) 0.5, (*b*) 5, (*c*) 10, (*d*) 20. The upper electrode is made of steel

2.4. Temperature influence on the electrovortex flows

To catch effects on the fluid flows caused by heating in the upper electrode, two series of simulations were provided. In these series material of the upper electrode was changing between copper and steel, which properties are defined in COMSOL 6.1. Due to the fact that steel has lesser electrical conductivity than copper, more heat is generated in it. Electrical conductivity common values are approximately 60 MS/m for copper and 1.5 MS/m for steel, therefore accroding to (4) a difference around of one order should be considered in heat generation.

In the Fig. 9 two plots are presented. The left one depicts axial velocity on the 10 mm depth, while the right one — temperature in the same point. Red line represents copper electrode case, black — steel one. As seen here, when the upper conductor has copper properties, the temperature increases at about 1 K, while oscillations are little. Changing material to a steel leads to significant increase of temperature; at the computational finish the difference between room temperature and the point's one is around 10 K. However the axial velocity decreases in such conditions.

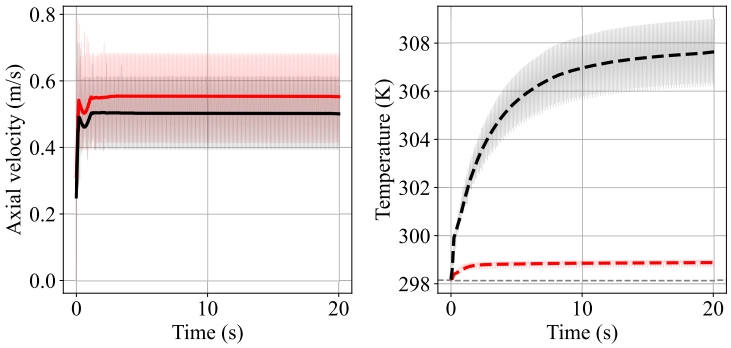

Fig. 9. Effects of the upper electrode material changing. In this case current is 1000 A, frequency is 5 Hz

2.5. Mixing results

The neutral admixture method was used to evaluate mixing quality in the hemisphere under an AC induction. Following criterion was introduced to make an attempt of evaluation:

$$\zeta = 1 - \frac{C_{\max} - \overline{C}}{C_{\max}}, \tag{8}$$

here $C_{\max}$ is a maximal concentration, mol/m^3; $\overline{C}$ is an average concentration, mol/m^3. In the Fig. 10 the diagram of the ζ criterion is shown. The lowest rate of mixing has a regime with the lowest current frequency (red in the plot). Increasing frequency leads to enhancing mixing parameter, to values resemble that of direct current (black in the plot).

Conclusion

In our paper a number of numerical computations of the electrovortex flows were carried out in the hemispherical geometry under an AC induction; the external magnetic field and other external forces are absent. Velocity and temperature fields, as well as mass transfer evaluations were acquired in the computations. The simulation included electromagnetic equations along with

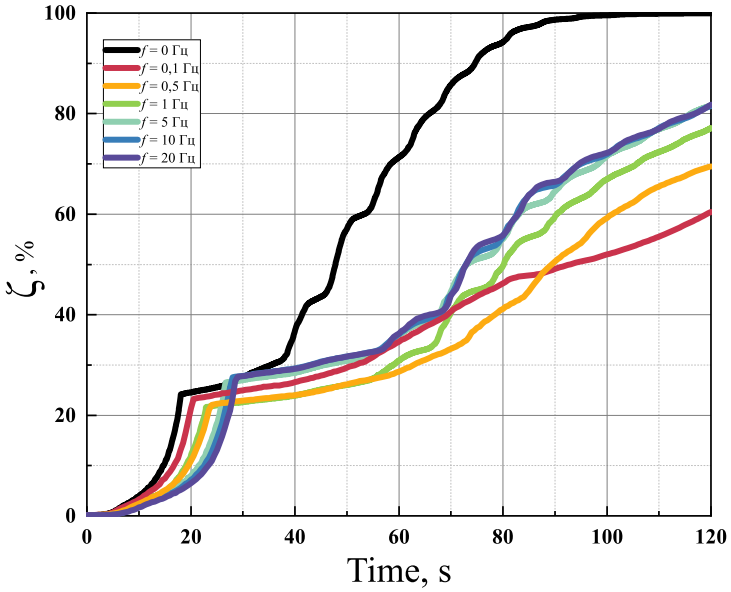

Fig. 10. Effects of the upper electrode material changing. In this case current is 1000 A, frequency is 5 Hz

hydrodynamics expressions with non-isothermal physical properties, consequently heat transfer was calculated.

From the results discussed above following summary could be formulated:

- Flow structure of an AC-induced EVFs is the same as of DC-induced ones, except jet pulsation;
- Increasing the current leads to enlarging values of both axial velocities and temperatures. The phenomenon is similar to that during applying a corresponding DC;
- Temperature and velocity oscillations are diminished when frequency amplifies; mean values of velocity are not affected, however of temperature are;
- Axial velocity profiles flattening is appeared during amplifying the current frequency;
- When more heat is generated by the upper conductor, the axial velocity depresses;
- According to the ζ parameter the fastest mixing is possible when the current frequency increases.

The AC induced EVFs description given here is incomplete. In future works it's necessary to introduce a vertical external magnetic field to take into account, e.g. Earth's magnetic field. In addition, we have to carry out experimental tests and theoretical surveys on this theme. Forecoming investigations will be devoted to a flow structure mapping as was done with DC induced EVFs in papers by [20–22]. Thorough experiments and theoretical expressions will make able to predict liquid metal flows in hemispherical geometry which is resemble to real-world applications — electrometallurgical furnaces. However for each concise problem it's necessary to simulate corresponding case, but our works are valuable source of calculation methodics.

The work is done with support by the Ministry of Science and Higher Education of the Russian Federation (State assignment no. 075-00269-25-00).

References

[1] S.Lundquist, On the hydromagnetic viscous flow generated by a diverging current, *Ark. Fys.*, **40**(1969), no. 5, 85–95.

[2] J.A.Shercliff, Fluid motions due to an electric current source, *J. Fluid Mech.*, **40**(1970), part 2, 241–250.

[3] C.Sozou, On fluid motions induced by an electric current source, *J. Fluid Mech.*, **46**(1971), part 1, 25–32.

[4] C.Sozou, W.M.Pickering, Magnetohydrodynamic flow due to the discharge of an electric current in a hemispherical container, *J. Fluid Mech.*, **73**(1976), part 4, 641–650.

[5] O.O.Ajayi, C.Sozou, W.M.Pickering, Nonlinear fluid motions in a container due to the discharge of an electric current, *J. Fluid Mech.*, **148**(1984), 285–300.

[6] J.G.Andrews, R.E.Craine, Fluid flow in a hemisphere induced by a distributed source of current, *J. Fluid Mech.*, **84**(1978), part 2, 281–290.

[7] P.A.Davidson, D.Kinnear, R.J.Lingwood, et al., The role of Ekman pumping and the dominance of swirl in confined flows driven by Lorentz forces, *Eur. J. Mech. B/Fluids*, **18**(1999), 693–711. DOI: 10.1016/S0997-7546(99)00106-5

[8] V.Shatrov, G.Gerbeth, Stability of the electrically induced flow between two hemispherical electrodes, *Magnetohydrodynamics*, **48**(2012), no. 3, 469–483. DOI: 10.22364/mhd.48.3.1

[9] R.P.Millere, V.I.Sharamkin, E.V.Shcherbinin, Effect of a longitudinal magnetic field on electrically driven rotational flow in a cylindrical vessel, *Magnitnaya Gidrodinamika*, **16**(1982), no. 1, 81–85 (in Russian).

[10] V.V.Bojarevich, R.P.Millere, Amplification of azimuthal rotation in a meridional electric vortex flow in a hemisphere, *Magnitnaya Gidrodinamika*, **18**(1982), no. 4, 51–56 (in Russian).

[11] V.Kh.Vlasyuk, V.I.Sharamkin, Effect of a vertical magnetic field on heat and mass transfer in a parabolic liquid-metal bath with current, *Magnitnaya Gidrodinamika*, **23** (1987), no. 2, 112–118 (in Russian).

[12] V.Kh.Vlasyuk, Electrovortex flows in vessels of various depths, *Magnitnaya Gidrodinamika*, **25**(1989), no. 2, 63–68 (in Russian).

[13] I.E.Butsenieks, Ya.Yu.Kopman, V.I.Sharamkin, et al., Experimental study of MHD processes in electric-slag welding, *Magnitnaya Gidrodinamika*, **11**(1975), no. 3, 143–148 (in Russian).

[14] V.G.Zhilin, Yu.P.Ivochkin, A.A.Oksman, et al., An experimental investigation of the velocity field in an axisymmetric electrovortical flow in a cylindrical container, *Magnitnaya Gidrodinamika*, **22**(1986), no. 3, 110–116 (in Russian).

[15] V.V.Bojarevich, Ja.Zh.Frejbergs, Je.I.Shilova, et al., Electrovortex flows, Riga: Zinātne, 1985 (in Russian).

[16] V.G.Zhilin, Yu.P.Ivochkin, V.S.Igumnov, A.A.Oksman, Experimental investigation of the electrovortex flows in the hemispherical volume, *Teplofizika Vysokih Temperatur*, **33**(1995), no. 1, 3–6 (in Russian).

[17] V.G.Zhilin, Yu.P.Ivochkin, I.O.Teplyakov, To the question on a swirl of axisymmetrical electovortex flows, *Teplofizika Vysokih Temperatur*, **47**(2011), no. 6, 957 (in Russian).

[18] Yu.P.Ivochkin, I.O.Teplyakov, A.A.Guseva, Yu.N.Tokarev, The numerical and experimental investigation of a structure of a swirled electrovortex flow, *Teplovyye protsessy v tehnike*, (2012), no. 8, 345–352 (in Russian).

[19] Yu.P.Ivochkin, I.O.Teplyakov, D.A.Vinogradov, About different approximations in the electrovortex flow simulation, *Software of systems in the industrial and social fields*, **7**(2019), no. 1, 18–23 (in Russian).

[20] D.A.Vinogradov, Yu.P.Ivochkin, I.O.Teplyakov, Effect of the Earth's Magnetic Field on the Electric-Vortex-Flow Structure, *Doklady Physics*, **63**(2018), no. 11, 447–450. DOI: S1028335818110046

[21] A.Kharicha, M.Al-Nasser, H.Barati, et al., Tornados and cyclones driven by Magnetohydrodynamic forces, *European Journal of Mechanics - B/Fluids*, **94**(2022), 90–105. DOI: 10.1016/j.euromechflu.2022.02.001

[22] M.Al-Nasser, E.Karimi-Sibaki, M.Wu, et al., 3D Modelling of Electro Vortex Flow Inside Liquid Metal and Effect of External Magnetic Fields, *IOP Conf. Ser.: Mater. Sci. Eng.*, **1309**(2024), 012004. DOI: 10.1088/1757-899X/1309/1/012004

[23] A.Yu.Chudnovskiy, Modelling of hydrodynamics processes in current conducting melts in electrical setups, Doctoral thesis. Riga: Institute of Physics, Academy of Sciences of Latvian SSR, 1988 (in Russian).

[24] A.V.Dub, V.S.Dub, Yu.N.Kriger, et al., Electroslag remelting — an approach to enhance quality and properties of responsible hardware in modern mechanical engineering. Technical claims and new solutions, *Tyazhyoloye mashinostroyeniye*, (2012), issue 6, 3–6 (in Russian).

[25] S.M.Nekhamin, Creation and introduction power effective arc and slag electrical furnace complexes with using direct current and low-frequency current, Doctoral thesis. Moscow: National Research University «MPEI», 2015 (in Russian).

[26] I.O.Teplyakov, The investigation of liquid metal electrovortex flow structure in the hemispherical cavity, Candidate thesis. Moscow: JIHT RAS, 2015 (in Russian).

[27] Yu.Plevachuk, V.Sklyarchuk, S.Eckert, et al., Thermophysical Properties of the Liquid Ga–In–Sn Eutectic Alloy, *Journal of Chemical & Engineering Data*, **59**(2014), no. 3, 757–763. DOI: 10.1021/je400882q

[28] V.Ya.Prokhorenko, Ye.A.Ratushnyak, B.I.Stadnyk, et al., Physical properties of thermometrical melt In-Ga-Sn, *Teplofizika Vysokih Temperatur*, **2**(1970), no. 8, 374–378.

Численное исследование электровихревых течений, индуцируемых переменным током низкой частоты

Павел И. Поляков
Игорь О. Тепляков
Лаборатория 10.2
Объединённый институт высоких температур РАН
Москва, Российская Федерация
Степан М. Юдин
Институт тепловой и атомной энергетики Национальный исследовательский университет «МЭИ»
Москва, Российская Федерация

Аннотация. Представлены результаты численного расчета электровихревых течений в расплаве In-Ga-Sn, индуцированных синусоидальным током низкой частоты (0.1–20 Гц), в полусферическом медном сосуде. Получены значения полей скорости и температур расплава. Показан характер влияния частоты синусоидального тока на движение и теплопередачу в жидком металле.

Ключевые слова: электровихревые течения, магнитная гидродинамика, численное моделирование.

EDN: MKFWBS
УДК 531

Relationship Between the Structural Organization and Young's Modulus of Tetrachiral Metamaterial

Linar R. Akhmetshin*
Institute of Strength Physics and Materials Science SB RAS
Tomsk, Russian Federation

Received 10.06.2025, received in revised form 05.10.2025, accepted 07.12.2025

Abstract. With the advent of a new class of materials—metamaterials—mathematical modeling has become an indispensable tool. Its application significantly accelerates the acquisition of new knowledge, as well as broadens the understanding of the deformation mechanisms in metamaterials. Typically, metamaterials are designed and optimized under the assumption of idealized geometry; however, this study develops an approach based on topological transformations. The subject of investigation is the unit cell of a metamaterial with a tetrachiral structure. The case of sequential transformation of the walls of a cubic cell, specifically the change in chirality, is considered. Despite a minor difference in porosity (0.4%), a substantial change in the effective Young's modulus (59.7%) was observed. It has been demonstrated that a 50% transformation of the unit cell can result in a 148% increase in the effective Young's modulus compared to a regular unit cell. A correlation between stiffness and the loading-twist coupling effect of the cell induced by the chiral structure was established.

Keywords: mechanical metamaterial, tension-torsion coupling, compression-torsion properties, effective Young's modulus, deformation mechanism, FEA simulation, architected cellular metamaterials, microstructure-property relationship.

Citation: L.R. Akhmetshin, Relationship Between the Structural Organization and Young's Modulus of Tetrachiral Metamaterial, J. Sib. Fed. Univ. Math. Phys., 2026, 19(2), 175–184. EDN: MKFWBS.

Introduction

The advancement of materials science and manufacturing technologies has fostered the emergence of a new research direction – the study of metamaterials [1]. Metamaterials are characterized by properties that depend less on the chemical composition of the base material and more on the artificially engineered structure. It can be posited that metamaterials reside at the intersection of materials science and structural engineering. Essentially, mechanical metamaterials are assemblies constructed from discrete blocks (unit cells) or elements [2–4]. Their design and optimization generally assume ideal geometry and a homogeneous base material [5]. The base material can vary-plastics, metals, wood, among others-depending on the fabrication method and intended application. Consequently, an alternative paradigm has supplanted the classical approach to materials development. The classical paradigm focuses on refining the chemical composition of materials [6, 7], whereas the alternative paradigm embraces fundamentally different strategies.

In crystalline materials, unit cells consist of atoms or ions; conversely, metamaterials are composed of much larger cells, several orders of magnitude greater than atomic dimensions [8]. When numerous such elements are present, the structure may be treated as an effective continuum [9]. By carefully tuning the geometry, size, shape and arrangement of structures in mechanical metamaterials, their deformation behavior and properties can be controlled [10, 11].

*Akhmetshin.lr@gmail.com https://orcid.org/0000-0002-9926-6567

The term "metamaterial" is applied when a medium exhibits effective properties unattainable in conventional materials [12]. For chiral metamaterials, a distinctive feature is the twisting deformation observed under uniaxial loading [13]. Chirality refers to the property of an object being non-superimposable on its mirror image. Chiral metamaterials, like other mechanical metamaterials, have demonstrated significant potential across a broad range of applications, including energy-absorbing structures [14, 15], vibration isolation systems [16, 17], and flexible electronics [18]. This capability arises from their porous framework, which efficiently redistributes stresses.

The overwhelming majority of studied metamaterials are fabricated from polymers, as they generally exhibit the capacity to withstand large deformations [19, 20]. However, it is important to keep in mind that polymers may exhibit viscoelastic properties, which will affect the overall mechanical characteristics [21]. For practical applications, the load-bearing capacity of polymers is often insufficient. Therefore, metals or ceramics must sometimes be employed to fabricate metamaterials [22]. Innovative strategies have been employed to find a compromise between different properties of the final sample. One such strategy involves the introduction of additional stiffening ribs [23] or the incorporation of soft fillers [24] to achieve the desired mechanical performance.

Another approach is the topological transformation of the structure. A. S. Meeussen et al., drawing an analogy with ferromagnetic and antiferromagnetic binary spin interactions, proposed a method for identifying and analyzing mechanical defects in two- and three-dimensional metamaterial cells of arbitrary geometry [25]. From the perspective of mechanical properties, the introduction of topological defects enables control over the behavior of such metamaterials [26, 27]. Purposeful structural design allows for the creation of materials with optimized mechanical and novel functional properties [28]. Nevertheless, the role of topological transformations in the properties of metamaterials remains insufficiently explored.

The metamaterial structure is meticulously designed during the prototyping phase. Subsequently, the model can be employed for mathematical modeling, which serves as an essential tool in the research and development of new metamaterials. Modeling minimizes production and testing costs. When describing a metamaterial as an effective medium with averaged properties, approaches from composite mechanics based on homogenization theory for heterogeneous materials with periodic or random structures are applicable [29].

This article aims to fill the gap in research concerning the influence of topological defects on the stiffness of metamaterials. A topological defect is defined as a topological transformation. The metamaterial with a tetrachiral structure has been selected as the object of study. Translation: In this context, a topological transformation entails a change in the chirality of any wall of the unit cell. The focus is on its unit cell, which is cubic and contains one ring with four ligaments on each wall. The connection between walls is made through ligaments at the vertices of the unit cell.

1. Materials and methods

This study focuses on a tetrachiral metamaterial. The tetrachiral structure consists of a ring and four ligaments tangentially connected to the ring. This structure is defined by five parameters: l — the length of the structure, i.e., the distance between two vertices; h — the thickness of the structure; t — the width of the ligament; r_2 — the outer radius of the ring; and r_1 — the inner radius of the ring. The thickness of the structure emerges during the extrusion process, resulting in a two-dimensional tetrachiral structure and subsequently a two-dimensional metamaterial. In this study, the parameters of the tetrachiral structure are related to the size of the unit cell as follows: 1 (l/l), 0.1 (h/l), 0.1 (t/l), 0.35 (r_2/l), 0.25 (r_1/l). The spatial (topological) arrangement of the two-dimensional structures in three-dimensional space enables

the creation of the unit cell of the metamaterial (Fig. 1a). Here, a three-dimensional tetrachiral metamaterial with a regular cubic shape is considered. The unit cell is the smallest repeating volume of the cellular material, composed of deliberately designed geometric elements, and serves as the basis for the creation of the chiral metamaterial. To form the unit cell, a three-dimensional figure must be constructed from two-dimensional tetrachiral elements. In our case, this figure is a cube. When the cubic cell is unfolded onto a plane, a left-handed chirality direction can be observed.

Uniaxial compression of the unit cell is investigated. Three loading schemes are implemented, corresponding to each of the three orthogonal axes. Boundary conditions for the vertical axis are described as follows (Fig. 1b):
- The bottom wall $S(\text{bot}) = \{x, y, z\}$ is rigidly fixed, which means displacement constraints along the three coordinate axes are applied: $u = U_{1|S(bot)}$, $U_1 = 0$ mm;
- The top wall $S(\text{top}) = \{x, y, z\}$ is uniformly loaded along the Y-axis: $u = U_{2|S(top)}$, $U_2 = 1.5$ mm;
- The lateral walls $S(\text{oth}) = \{x, y, z\}$ are free from external loads.

The problem was solved numerically, simulating quasi-static compression of the modeled tetrachiral metamaterial samples. The deformation behavior of the samples was studied using the finite element method. Tetrahedral finite elements were used in the three-dimensional models. To ensure mesh-independent results, a mesh convergence analysis was performed, resulting in an average element size of 1 mm for the simulations (Fig. 1c). An elastic material model was adopted for the analysis, with the following material properties: Young's modulus $E = 2.6$ GPa and Poisson's ratio $\nu = 0.4$. To account for geometric nonlinearity, a large displacement theory module was employed in the model.

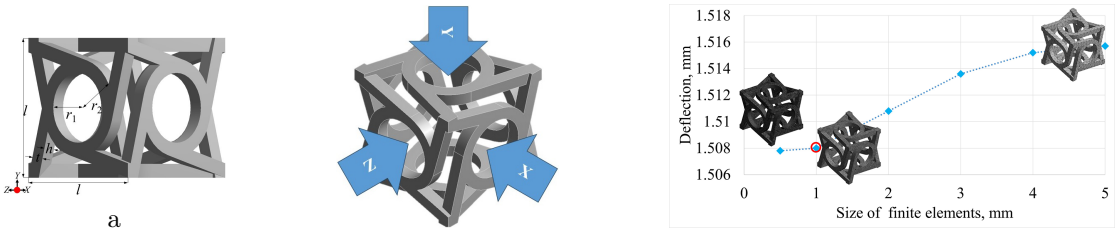

a b c

Fig. 1. Preparation for mathematical modeling: (a) creation of the cubic cell with tetrachiral structure, (b) application of boundary conditions, (c) mesh convergence analysis

The subject of this study is structural transformations. The work considers a unit cell not only with a regular arrangement of tetrachiral structures but also with structural transformations. In the cell with a regular arrangement, the tetrachiral structures are oriented in the same direction. Structural transformations, in this context, refer to changes in the chirality (ω_i) of one or more tetrachiral structures (Fig. 2). These transformations are performed while preserving the original geometry; for example, ω_3 indicates that three structures have been transformed. It should be understood that ω_3 represents the midpoint of possible structural transformations. Further changes lead to pairwise symmetry: ω_0 and ω_6, ω_1 and ω_5, ω_2 and ω_4. Thus, ω_6, like ω_0, can also be considered a cell with a regular structure.

2. Results and discussion

The transformation of a single structure, namely the change in chirality, leads to a new configuration of the unit cell. First, the porosity variation of cells with different structural

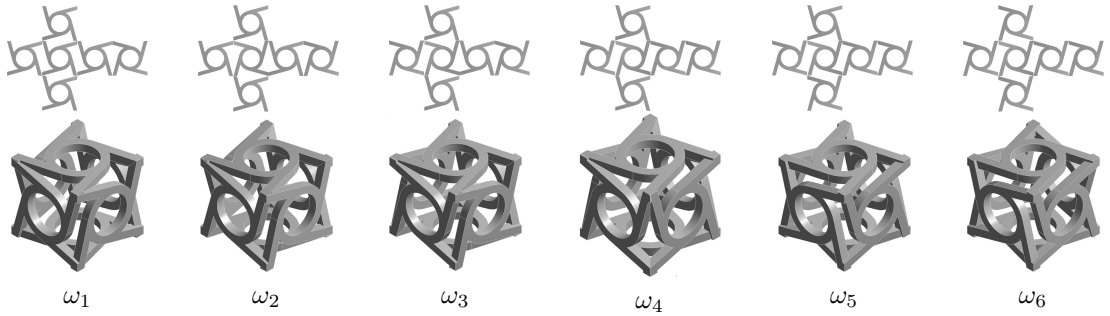

Fig. 2. Stepwise scheme (left to right) of chirality direction changes in the unit cell: one wall, two walls, three walls, four walls, five walls, and six walls

transformations is examined. For this, the following formula was used:

$$P = \frac{V_{con} - V_{bm}}{V_{con}} \times 100\%. \tag{1}$$

Here V_{con} is the volume of the cell assuming it is a continuum material (volume of base material plus pore space), and V_{bm} is the volume of the base material in the metamaterial framework.

As shown in Fig. 3, the porosity changes insignificantly, by approximately 0.36%. The graph is symmetric with respect to the third transformation because the cell contains three structures with right-handed chirality and three with left-handed chirality. The extreme values coincide because all six tetrachiral structures have switched from right-handed to left-handed chirality.

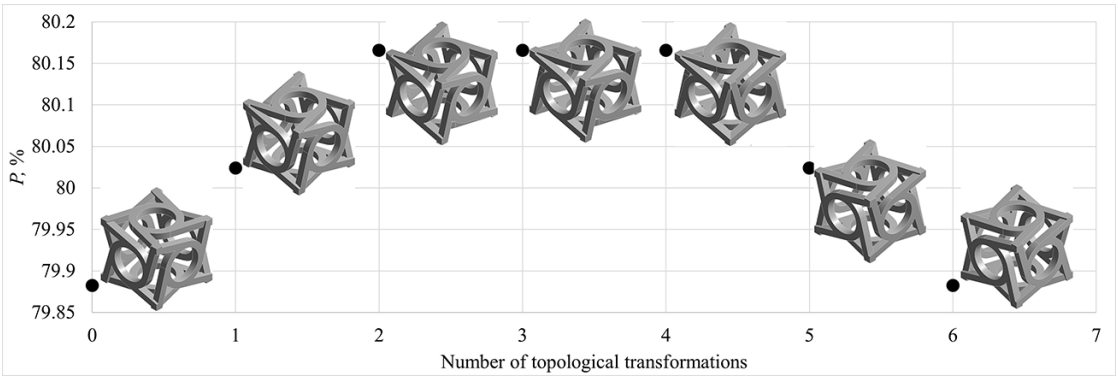

Fig. 3. Graph of porosity variation during structural transformations of the metamaterial's unit cell

The uniaxial loading process of the tetrachiral metamaterial's unit cell can be schematically described as follows:
- A displacement is applied to the upper wall, which moves along the OY axis toward the fixed lower wall;
- The force generated by the displacement of the upper wall is transmitted to the lateral walls, which deform. The deformation of the lateral walls includes rotating of tetrachiral structures, bending of ligaments, and changes in the ring shape;
- The rotating structures on the lateral walls affect both the lower and upper walls.

The lower wall is rigidly fixed, and the force required to deform the cell is calculated. This

force F is then converted into the effective Young's modulus using the formula:

$$E_{eff} = \frac{Fl}{S\Delta l}. \tag{2}$$

Here F is the reaction force at the fixed wall, S is the cross-sectional area of the cubic cell, Δl is the displacement after longitudinal compression by 3%. The rotating of the four lateral walls causes a rotation of the upper wall of the metamaterial cell. The twisting angle can be calculated by the formula:

$$\alpha_y = \frac{180}{\pi} \arcsin \frac{2x}{l}. \tag{3}$$

Here the subscript y indicates the loading axis, $\frac{180}{\pi}$ converts radians to degrees, and x denotes displacement from the original position along the OX axis. As seen from the formula, the twisting depends solely on the displacement. Therefore, comparison of results can be conducted based on displacements [30, 31].

In a regular unit cell under uniaxial loading along any of the three orthogonal axes, the final deformed shape remains the same. The values of the effective Young's modulus also do not change. This result is achieved due to the topologically rational arrangement of the tetrachiral structures. Disruption of the regularity of the structures within the cell leads to a different deformed shape, and this change varies depending on the loading direction. Therefore, the response of cells with such structural transformations was studied under compression along the three orthogonal loading axes (Fig. 4). Similar to porosity, the graph of E_{eff} versus the number of structural transformations is symmetric: 1) results for E_x are mirrored around ω_3, and 2) results for E_z are symmetric to those for E_y. The highest value obtained in this study is 57.3 MPa, which is 45.4 times lower than the Young's modulus of the base material.

Let us first consider the case of loading along the OX axis (purple markers). The effective Young's modulus values for the regular cell (ω_0) and the cell with six structural transformations (ω_6) are both 23.11 MPa. Upon transition to (ω_1), this value increases by 34%. Structural transformation (ω_2) results in an additional 67% increase. The value of E_{ω_0} differs from E_{ω_3} by 148%. Due to the symmetry of the values, the remainder of the graph does not require description. Thus, by increasing the number of structural transformations, the stiffness of the unit cell can be tuned. The highest value is achieved with an equal number of structures having opposite chirality directions.

Let us consider the case of loading along the OZ axis (blue markers). Structural transformations still lead to an increase in the effective Young's modulus. Transformation (ω_1) resulted in a 34% increase. Similarly, ω_2 provides an additional 67% increase, which represents the highest point for this case. A cell with three tetrachiral structures oriented left-handed and three oriented right-handed reduced this maximum by 17%. Subsequent transformation ω_4 did not produce significant changes. Structural transformations ω_5 and ω_6 further decreased the effective Young's modulus by 22% and 48%, respectively.

The final case is loading along the OY axis (dark blue markers). As mentioned earlier, the results for this case are symmetric to those for the OZ axis.

According to Ashby [32], cellular structures can be theoretically characterized using their relative density. Accordingly, the theoretical elastic modulus (E_{thr}) can be averaged and calculated using the following formula for a cellular metamaterial exhibiting bending-dominated behavior:

$$E_{thr} \approx E_{bm}\rho_r^2 = 0.1(GPa), \tag{4}$$

where E = 2.6 GPa is the Young's modulus of the base material, and $\rho_r = \frac{mV_{bm}}{mV_{con}} = \frac{24970}{125000} = 0.2$ is the relative density. Here V_{bm} is the volume of the base material, and $V_{con} = 3l$ is the continuum volume of the unit cell. The obtained theoretical value is 26 times lower than the

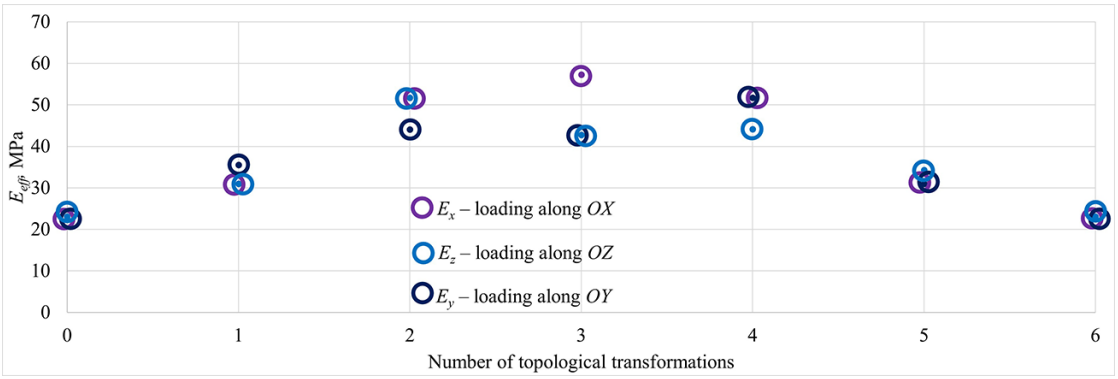

Fig. 4. Graph illustrating the relationship between the effective Young's modulus and the structural organization of the metamaterial's unit cell

Young's modulus of the base material and 1.7 times higher than the maximum effective Young's modulus observed. Ashby himself suggested that the proportionality coefficient equals 1 but did not insist on this. Most likely, such discrepancy is related to the shape of the cellular structure or the high porosity percentage [33].

Despite minor differences in the porosity of the cells, variations in the effective Young's modulus have been observed. This phenomenon may be related to the cell's internal structure or the nontrivial mechanical response of the tetrachiral metamaterial cell (Fig. 5). To demonstrate the influence of the cell's structure, attention should be paid to the contact areas between the tetrachiral structures (highlighted in red, Fig. 5a, b). The contacting elements in the cubic cells are the ligaments of the tetrachiral structure. In the ω_0 cell, these are the ends of the ligaments, whereas in the ω_3 cell, some parts of the ligaments are in contact. It was found that the larger the contacting area, the more difficult it is to deform the cells. It is also clear that this factor is challenging to quantify and directly affects the twisting behavior. Separating the influence of structural organization and twisting is important, as the latter also contributes significantly.

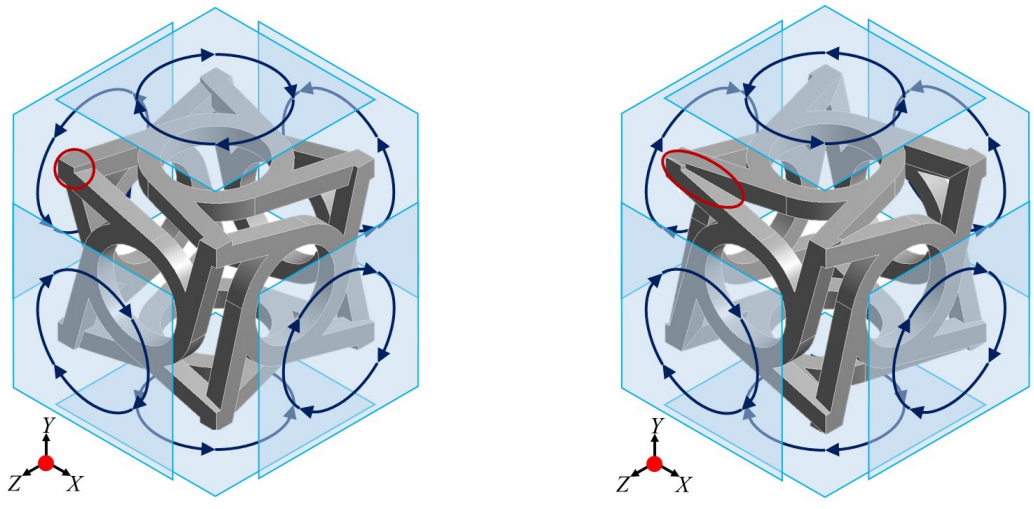

a b

Fig. 5. Schematic of the rotation of tetrachiral structures in unit cells ω_0 and ω_3 with indication of contact areas between cube walls

To clarify this, the maximum displacement values in ω_0 and ω_3 (Tab. 1) were analyzed and compared with the effective modulus E_{eff}. It is evident that in ω_0, displacement values are consistent, which is not the case for ω_3. The ω_3 cell exhibits a considerable spread of values depending on the loading axis. On average, displacement values in ω_3 are smaller than in ω_0, while E_{eff} is higher. This suggests that the deformation mechanisms in the sample hinder compression. For instance, some walls rotate in the opposite direction, thereby generating additional resistance.

Consider loading along the OX axis. In the regular cell (Fig. 5a), four structures in the XY and XZ planes induce rotation of the structure in the YZ plane. The cell twisting is directed oppositely, despite the chirality indicating the opposite rotation direction. In the ω_3 cell, two structures are oriented in one direction and two in the other, thus impeding twisting. This explains the reduced displacement in the XZ plane. Correspondingly, E_{eff} increases to the highest value among those considered. Taken together, these observations indicate a direct correlation between the loading-twist coupling effect and the effective Young's modulus.

Table 1. Displacement values for ω_0 and ω_3

Loading	ω_0	ω_3
	$x_{max}/z_{max}/y_{max}$	$x_{max}/z_{max}/y_{max}$
along X	–/1.51/1.51	–/0.64/0.79
along Y	1.51/1.51/–	1.63/2.49/–
along Z	1.51/–/1.51	1.62/–/0.36

An open question remains beyond the scope of this study: the extent of the influence of structural transformations during various non-sequential modifications of the cubic cell.

Conclusion

This study investigated the properties of an unit cell with a tetrachiral structure. The results were obtained using mathematical modeling. Uniaxial loading was applied along three orthogonal axes, and seven structural organizations of the cell were considered. Structural transformations refer to changes in the chirality of the cell walls. An unit cell in which all tetrachiral structures share the same chirality direction is referred to as regular.

The study revealed variations in the effective Young's modulus depending on the structural organization of the unit cell. Sequential structural transformations of the cell lead to an increase in the effective Young's modulus. The cell with 50% of its structures transformed exhibited the highest effective Young's modulus value of 57.3 MPa. The constructed graph revealed symmetry in the values for certain loading cases and structural transformations. The theoretical value of Young's modulus was obtained, which is 1.7 times greater than the obtained effective value.

A correlation between the effective Young's modulus and the loading-twist coupling effect of the tetrachiral structure was established. It was shown that some structural transformations reduce the twisting angle of the cell compared to the regular cell, resulting in an increased effective Young's modulus. Additionally, the consideration of contact area was proposed when analyzing the effective Young's modulus.

Structural transformations significantly influence the properties and mechanical behavior of the metamaterial, as demonstrated by the example of the unit cell with a tetrachiral structure. The key factor governing the stiffness of a unit cell in a tetrachiral metamaterial is the degree of suppression of twisting response achieved through the symmetric arrangement of structures with differing chirality.

This work was carried out within the state assignment no. FWRW-2026-0007 of the Ministry of Science and Higher Education of the Russian Federation.

References

[1] M.Y.Khalid, Z.U.Arif, A.Tariq, M.Hossain, R.Umer, M.Bodaghi, 3D printing of active mechanical metamaterials: A critical review, *Mater. Des.*, **246**(2024), 113305. DOI: 10.1016/j.matdes.2024.113305

[2] A.Sangsefidi, J.Kadkhodapour, A.P.Anaraki, S.Dibajian, S.Schmauder, Enhanced energy harvesting by devices with the metamaterial substrate, *Phys. Mesomech*, **25**(2022), is. 4, 106–121. DOI: 10.1134/S1029959922060091

[3] L.R.Akhmetshin, I.Yu.Smolin, Analysis of some methods of integration of cells in a mechanical metamaterial, *Vestnik Tomskogo gosudarstvennogo universiteta. Matematika i mekhanika – Tomsk State University Journal of Mathematics and Mechanics*, (2022) is. 77, 27–37. DOI: 10.17223/19988621/77/3

[4] L.Akhmetshin, I.Smolin, Characterization of a chiral metamaterial depending on the type of connection between unit cells, *Proc. Inst. Mech. Eng. C: J. Mech. Eng. Sci.*, **236**(2022), is. 19, 10214–10220. DOI: 10.1177/09544062221101832

[5] B.C.White, A.Garland, B.L.Boyce, Topological homogenization of metamaterial variability, *Mater. Today*, **53**(2022), 16–26. DOI: 10.1016/j.mattod.2022.01.021

[6] E.Davoodi, M.Hossein, M.A.Sadat, et al., Additively manufactured metallic biomaterials, *Bioact. Mater.*, **15**(2022), 214–249. DOI: 10.1016/j.bioactmat.2021.12.027

[7] R.Rahmani, N.Kamboj, M.Brojan, M.Antonov, K.G.Prashanth, Hybrid metal-ceramic biomaterials fabricated through powder bed fusion and powder metallurgy for improved impact resistance of craniofacial implants, *Materialia*, **24**(2022), 101465. DOI: 10.1016/j.mtla.2022.101465

[8] X.Yu, J.Zhou, H.Liang, Z.Jiang, L.Wu, Mechanical metamaterials associated with stiffness, rigidity and compressibility: A brief review, *Prog. Mater. Sci.*, **94**(2018), 114–173. DOI: 10.1016/j.pmatsci.2017.12.003

[9] X.Zhang, Y.Wu, Effective medium theory for anisotropic metamaterials, *Sci. Rep.*, **5**(2015), is. 1, 7892. DOI: 10.1038/srep07892

[10] Y.Gu, Z.Wei, G.Wei, Z.You, J.Ma, Y.Chen, Kirigami-Inspired Three-Dimensional Metamaterials with Programmable Isotropic and Orthotropic Thermal Expansion, *Adv. Mater.*, **36**(2024), is. 50, 2411232. DOI: 10.1002/adma.202411232

[11] X.Wang, L.Zhendong, D.Junjie, G.Tianyu, et al., Unprecedented Strength Enhancement Observed in Interpenetrating Phase Composites of Aperiodic Lattice Metamaterials, *Adv. Funct. Materials*, **35**(2025), is. 1, 2406890. DOI: 10.1002/adfm.202406890

[12] B.E.Jenett, Discrete mechanical metamaterials, Massachusetts Institute of Technology, School of Architecture and Planning, Program in Media Arts and Sciences, USA, 2020. [Online: https://hdl.handle.net/1721.1/130610]

[13] M.-H.Fu, B.-B.Zheng, W.-H.Li, A novel chiral three-dimensional material with negative Poisson's ratio and the equivalent elastic parameters, *Comp. Struct.*, **176**(2017), 442–448. DOI: 10.1016/j.compstruct.2017.05.027

[14] P.Wang, Y.Fan, Zh.Bailin, et al., Breaking the Tradeoffs between Different Mechanical Properties in Bioinspired Hierarchical Lattice Metamaterials, *Adv. Funct. Materials*, **33**(2023), is. 45, 2305978. DOI: 10.1002/adfm.202305978

[15] Y.Nian, S.Wan, M.Avcar, R.Yue, M.Li, 3D printing functionally graded metamaterial structure: Design, fabrication, reinforcement, optimization, *Int. J. Mech. Sci.*, **258**(2023), 108580. DOI: 10.1016/j.ijmecsci.2023.108580

[16] W.Liu, S.Janbaz, D.Dykstra, B.Ennis, C.Coulais, Harnessing plasticity in sequential metamaterials for ideal shock absorption, *Nature*, **634**(2024), is. 8035, 842–847. DOI: 10.1038/s41586-024-08037-0

[17] C.Zeng, L.Liwu, H.Yunqiang, Zh.Wei, X.Xiaozhou, L.Yanju, L.Jinsong, Stair?Stepping Mechanical Metamaterials with Programmable Load Plateaus, *Adv. Funct. Materials*, **34**(2024), is. 49, 2408887. DOI: 10.1002/adfm.202408887

[18] J.K.Choe, Y.Jiyoon, J.Hanhyeok, et al., Digital Mechanical Metamaterial: Encoding Mechanical Information with Graphical Stiffness Pattern for Adaptive Soft Machines, *Adv. Mater.*, **36**(2024), is. 4, 2304302. DOI: 10.1002/adma.202304302

[19] M.F.Berwind, A.Kamas, C.Eberl, A Hierarchical Programmable Mechanical Metamaterial Unit Cell Showing Metastable Shape Memory, *Adv. Eng. Mater.*, **20**(2018), is. 11, 1800771. DOI: 10.1002/adem.201800771

[20] C.El-Helou, R.L.Harne, Exploiting Functionally Graded Elastomeric Materials to Program Collapse and Mechanical Properties, *Adv. Eng. Mater.*, **21**(2019), is. 12, 1900807. DOI: 10.1002/adem.201900807

[21] D.M.J.Dykstra, J.Busink, B.Ennis, C.Coulais, Viscoelastic Snapping Metamaterials, *J. Appl. Mech.*, **86**(2019), is. 11, 111012. DOI: 10.1115/1.4044036

[22] S.C.L.Fischer, L.Hillen, C.Eberl, Mechanical Metamaterials on the Way from Laboratory Scale to Industrial Applications: Challenges for Characterization and Scalability, *Materials*, **13**(2020), is. 16, 3605. DOI: 10.3390/ma13163605

[23] J.Zhang, G.Lu, Z.You, Large deformation and energy absorption of additively manufactured auxetic materials and structures: A review, *Compos. B. Eng.*, **201**(2020), 108340. DOI: 10.1016/j.compositesb.2020.108340

[24] L.Du, S.Wei, G.Han, J.Hongxing, Zh.Qiuting, L.Mingjie, X.Ye, Mechanically Programmable Composite Metamaterials with Switchable Positive/Negative Poisson's Ratio, *Adv. Funct. Materials*, **34**(2024), is. 22, 2314123. DOI: 10.1002/adfm.202314123

[25] A.S.Meeussen, E.C.Oğuz, Y.Shokef, M.V Hecke, Topological defects produce exotic mechanics in complex metamaterials, *Nat. Phys.*, **16**(2020), is. 3, 307–311. DOI: 10.1038/s41567-019-0763-6

[26] A.S.Meeussen, E.C.Oğuz, M.V.Hecke, Y.Shokef, Response evolution of mechanical metamaterials under architectural transformations, *New J. Phys.*, **22**(2020), is. 2, 023030. DOI: 10.1088/1367-2630/ab69b5

[27] L.R.Akhmetshin, I.Yu. molin, The influence of the structural organization of chiral metamaterials on their physical and mechanical characteristics, *PNRPU Mechanics Bulletin*, (2023) is. 5, 17–25. DOI: 10.15593/perm.mech/2023.5.02

[28] S.Bonfanti, R.Guerra, M.Zaiser, S.Zapperi, Digital strategies for structured and architected materials design, *APL Materials*, **9**(2021), is. 2, 020904. DOI: 10.1063/5.0026817

[29] W. Xia, E. Oterkus, S. Oterkus, 3-Dimensional Bond-Based Peridynamic Representative Volume Element Homogenization, *Phys. Mesomech.*, **24**(2021), is. 5, 541–547. DOI: 10.1134/S1029959921050052

[30] H.Wang, C.Zhang, Q.-H.Qin, Y.Bai, Tunable compression-torsion coupling effect in novel cylindrical tubular metamaterial architected with boomerang-shaped tetrachiral elements, *Mater. Today Commun.*, **31**(2022), 103483. DOI: 10.1016/j.mtcomm.2022.103483

[31] L.R.Akhmetshin, I.Yu.Smolin, Effect of the type of unit cell connection in a metamaterial on its programmable behavior, *Nano Sci. Technol. Int. J.*, **14**(2023), is. 3, 63–71. DOI: 10.1615/NanoSciTechnolIntJ.2022044662

[32] M.F.Ashby, The properties of foams and lattices, *Phil. Trans. R. Soc. A.*, **364**(2006), is. 1838, 15–30. DOI: 10.1098/rsta.2005.1678

[33] C.T.Wanniarachchi, A.Arjunan, A.Baroutaji, M.Singh, Mechanical performance of additively manufactured cobalt-chromium-molybdenum auxetic meta-biomaterial bone scaffolds, *J. Mech. Behav. Biomed. Mater.*, **134**(2022), 105409. DOI: 10.1016/j.jmbbm.2022.105409

Связь структурной организации тетрахирального метаматериала с модулем Юнга

Линар Р. Ахметшин
Институт физики прочности и материаловедения СО РАН
Томск, Российская Федерация

Аннотация. С появлением нового типа материалов – метаматериалов, актуальным инструментом становится математическое моделирование. Его применение значительно ускоряет получение новых сведений, а также расширяет понимание механизмов деформирования метаматериалов. Чаще всего метаматериалы проектируются, оптимизируются в предположении идеальной геометрии, но в данной работе развивается подход топологических преобразований. В качестве объекта исследований рассматривается элементарная ячейка метаматериала с тетрахиральной структурой. Рассмотрен случай последовательного преобразования граней кубической ячейки — изменение хиральности. При незначительном отличии пористости (0,4%) наблюдалось значительное изменение эффективного модуля Юнга (59,7%). Показано, что при преобразовании ячейки на 50% эффективный модуль Юнга может быть увеличен на 148% по сравнению с регулярной ячейкой. Установлена связь между жесткостью, вращением ячейки, вызванным хиральной структурой.

Ключевые слова: механический метаматериал, связь растяжения-скручивания, свойство сжатие-скручивание, эффективный модуль Юнга, механизм деформации, метод конечных элементов, ячеистый метаматериал, связь микроструктуры и свойств.

EDN: OBOYXB
УДК 517.10

Kurepa's Function and Some Relations to Statistical Mechanics

Nicola Fabiano*
Vinca Institute of Nuclear Sciences
Belgrade, Serbia
University of Belgrade
Belgrade, Serbia
Stojan Radenović†
University of Belgrade
Belgrade, Serbia
Vuk Stojiljković‡
University of Novi Sad
Novi Sad, Serbia
Mathematical Grammar School
Belgrade, Serbia

Received 20.11.2025, received in revised form 19.01.2026, accepted 07.02.2026

Abstract. Starting from Kurepa's function and the hypothesis of divisibility to Gamma function, their thermodinamical analogies are constructed and their properties are compared to the one found for Riemann's Zeta function.

Keywords: Kurepa's function, Kurepa's conjecture, zeta function, quantum mechanics, partition function.

Citation: N. Fabiano, S. Radenović, V. Stojiljković, Kurepa's Function and some Relations to Statistical Mechanics, J. Sib. Fed. Univ. Math. Phys., 2026, 19(2), 185–191.
EDN: OBOYXB.

1. Kurepa's function and its properties

More than half a century ago Kurepa introduced the left factorial or Kurepa function [9–14]

$$K(n) = \sum_{k=0}^{n-1} k! = \sum_{k=0}^{n-1} \Gamma(k+1) \tag{1}$$

and extended it to the complex domain

$$K(z) = \int_0^{+\infty} e^{-t} \frac{t^z - 1}{t-1} dt\,.$$

He set forward some properties and relations to the Gamma function, like

$$\lim_{x\to+\infty} \frac{\Gamma(x)}{K(x)} = 1$$

*Corresponding author: nicola.fabiano@gmail.com https://orcid.org/0000-0003-1645-2071
†radens@beotel.net https://orcid.org/0000-0001-8254-6688
‡vuk.stojiljkovic999@gmail.com https://orcid.org/0000-0002-4244-4342

whose simplified proofs and more details could be found in [4]. Other properties recently discovered are in [3,5,17], which have plenty of references therein on the subject. The Gamma function has the definition [18,20]

$$\Gamma(z) = \int_0^{+\infty} e^{-t} t^{z-1} dt \;\text{ for } \mathrm{Re}(z) > 1\,.$$

Kurepa gave a hypothesis on $K(n)$ [4] in this and some other equivalent forms

$$\gcd(K(n), \Gamma(n+1)) = 2, \;\text{ for } n \geqslant 2\,, \tag{2}$$

where gcd means greatest common divisor. Some examples:

$$\gcd(K(2), \Gamma(2+1)) = \gcd(2,2) = 2\,,$$

$$\gcd(K(5), \Gamma(5+1)) = \gcd(34,120) = 2\,,$$

$$\gcd(K(9), \Gamma(9+1)) = \gcd(46234,362880) = 2\,,$$

$$\gcd(K(23), \Gamma(23+1)) = \gcd(1177652997443428940314, 25852016738884976640000) = 2\,.$$

This essentially states that $K(n)$ and $n!$ are coprime, except for the number 2. The hypothesis has yet to be proven (in 2024), although there are hints and empirical evidence of numerical simulations up to the value of $n < 2^{34}$ that confirm his hypothesis.

2. Energy levels

Consider the Schrödinger equation

$$H = -\hbar \left(\frac{d}{dx}\right)^2 + V(x)\,, \tag{3}$$

where eigenvalues of energy are found by finding solutions to the eigenstates problem

$$\left[-\hbar \left(\frac{d}{dx}\right)^2 + V(x)\right]\psi(x) = E\psi(x).$$

Those solutions depend on a quantum number k: E_k and $\psi_k(x)$, with its energy levels E_k, while eigenvectors ψ_k give the probability of finding a particle in the position x, $P(x) = |\psi(x)|^2$.

In the canonical ensemble, the partition function, which describes statistical properties of a system at thermodinamical equilibrium, is given by the expression

$$Z = \sum_k \exp(-\beta E_k), \tag{4}$$

where E_k is the energy level of the microstate k, β is the inverse of the temperature.

Our aim is to find all energy levels of systems that have as partition function Kurepa's function and Gamma function [3,4]. Previously, in [8] and later in [1] this has been done assuming the partition function to be Riemann's zeta function (see for instance [2]), that is

$$Z_{Riemann} = \zeta(s) = \sum_{k=1}^{+\infty} \frac{1}{k^s}\,. \tag{5}$$

This lead to the discovery of Riemann's gas or so called primon gas, formed of non interacting particles.

Another particular example is the hydrogen gas [6], which has the peculiarity of an infinite partition function.

2.1. Kurepa's gas

Comparing Kurepa's function to partition function, the result is given by:

$$Z_{Kurepa} = K(n) = \sum_{k=0}^{n-1} k! = \sum_{k=0}^{n-1} \exp(-\beta E_k)\,. \tag{6}$$

In order to find E_k we take the log termwise:

$$\ln k! = -\beta E_k\,.$$

For large k an excellent asymptotic expression for $\ln k!$ is given by Ramanujan's formula [20]

$$\ln k! \sim k\ln k - k + \frac{1}{6}\ln\left(8k^3 + 4k^2 + k + \frac{1}{30}\right) + \frac{1}{2}\ln\pi \tag{7}$$

therefore,

$$\ln k! \sim k(\ln k - 1) = -\beta E_k\ ,$$

leading to the energy level

$$E_k = -\frac{1}{\beta}\ln k! \sim -\frac{1}{\beta}k(\ln k - 1)\,. \tag{8}$$

2.2. Gamma function's gas

Proceeding in the same manner of Kurepa's gas, the partition function is:

$$Z_{Gamma} = \Gamma(n+1) = n! = \sum_{k=1}^{n} \exp(-\beta E_k)\,. \tag{9}$$

In order to compare terwise the two expressions, we need to select the kth term on both sides using the derivative of Gamma function, given by:

$$\Gamma(z)' = \Gamma(z)\psi^0(z)\ ,$$

$\psi^0(z) = \dfrac{d}{dz}\ln\Gamma(z)$ is the logarithmic derivative of $\Gamma(z)$ [18, 20]. For $k \in \mathbb{N}$,

$$\Gamma(k+1)' = k!\left(-\gamma + \sum_{i=1}^{k}\frac{1}{i}\right) = k!(-\gamma + H(k))\ , \tag{10}$$

where γ is the Euler–Mascheroni constant, $H(k) = \sum\limits_{i=1}^{k}\dfrac{1}{i}$ is the harmonic number [16, 19]. For $k = 10^4$, the error of the estimate is already smaller than $4.03 \times 10^{-3}\%$, and goes quickly to 0 with increasing k.

Comparing termwise equation (10):

$$k!(-\gamma + H(k)) = \exp(-\beta E_k)\ ,$$

providing the expression for energy level

$$E_k = -\frac{1}{\beta}\left[\ln k! + \ln(H(k) - \gamma)\right]\ .$$

For large k the asymptotic expression of harmonic numbers is

$$H(k) \sim \ln k + \gamma \, ,$$

therefore, the energy level for large k is given by

$$E_k \sim -\frac{1}{\beta} \left[k(\ln k - 1) + \ln(\ln k) \right] \tag{11}$$

that grows faster with k than the expression obtained for Kurepa's gas.

2.3. Riemann's gas

Proceeding in the same manner as shown before, for the partition function of (5),

$$Z_{Riemann} = \sum_{k=1}^{+\infty} \frac{1}{k^s} = \sum_{k=1}^{+\infty} \exp(-s \ln k) = \sum_{k=1}^{+\infty} \exp(-\beta E_k) \tag{12}$$

is provided the energy level E_k without approximations for large k:

$$E_k = \frac{s}{\beta} \ln k = C \ln k \, . \tag{13}$$

3. Monotonic energy

Consider the expression [7] for the inverse function of the potential $V(x)$ of Schrödinger's equation (3)

$$x(V) = 2 \int_0^V \frac{dk}{dE} \frac{1}{[2m(V-E)]^{1/2}} dE, \tag{14}$$

where (dk/dE) is the density of energy eigenvalues function. Applying this formula to (8) the density of eigenvalues for Kurepa's gas is given by

$$k = -\frac{E}{W\left(-\frac{E}{e}\right)}, \tag{15}$$

where W is the Lambert function that gives the principal solution for w in the equation $z = w \exp(w)$ [15]. Plugging this solution back in equation (14), the result

$$x(V) = 2 \int_0^V \frac{1}{\left[1 + W\left(-\frac{x}{e}\right)\right]} \frac{1}{[2m(V-E)]^{1/2}} dE \tag{16}$$

cannot be expressed in terms of elementary functions. The same applies to the statistics derived from Gamma function gas.

Equation (14) suggests the following theorem.

Theorem 1. *Suppose that the energy levels E are given by a monotonic function in the variable k. Then, the potential energy V is monotonic in x.*

Proof. Assume for simplicity that $\dfrac{dE}{dk} > 0$. It follows that $\dfrac{dE}{dk} = E'(k)$, or $\dfrac{1}{E'(k)} = \dfrac{dk}{dE} > 0$. So the density of energy eigenvalues $\dfrac{dk}{dE}$ is again positive, and in this case increasing as a function of E. The other function integrand of (14) is again positive, $\dfrac{1}{[2m(V-E)]^{1/2}} > 0$, therefore the result of the integral, $x(V)$, is a strictly increasing function of V. Its inverse, $V(x)$, the potential energy, is also a strictly increasing function of x. □

Corollary 1. *Suppose there are two thermodinamical systems with two different energy levels,* $E_1(k)$ *and* $E_2(k)$*. If* $\frac{dE_1}{dk} > \frac{dE_2}{dk}$*, then also their correspondent potential energies are ordered,* $\frac{dV_1}{dx} > \frac{dV_2}{dx}$*, and the converse is also true.*

Referring to Table 1 of [7], the relation of growth of energy with respect to quantum number and a power law potential could be read from the proportionality equations

$$E_k \propto k^a \text{ equals } V(x) \propto x^{\left(\frac{2a}{2-a}\right)} , \tag{17}$$

where k, a are real numbers and $k > 0$, $a < 2$, x is the position of the particle subject to the potential $V(x)$, and the symbol $\propto$ means "proportional to". For power law potentials that have known explicit solutions, the equality ranges from the energy of Coulomb potential $\frac{1}{x}$ and $E_k \propto k^{-2}$, to the harmonic oscillator x^2 and $E_k \propto k$. Equation (17) shows that an energy value of $E_k \propto k^2$ is obtained from an infinite barrier of potential.

Equation (17) illustrates in a simple manner the results of Theorem 1. Starting from Kurepa's gas, the behaviour of the energy eigenvalues (8) translates to a potential energy $V(x)$ being steeper than a parabola. In this case the interaction between gas particles is stronger than the one given by the harmonic oscillator.

For Gamma function gas, formula (11) shows than the rising of energy eigenvalues with increasing quantum number k is even larger than the case of Kurepa's gas, implying that the potential energy $V(x)$ is even stronger than the previous case. This fact is essentially due to the presence of the supplementary term of the harmonic number $H(k)$, leading to a gas particle interactions similar to an anharmonic oscillator, that has a potential with a further term larger than x^2.

For comparison, Riemann's gas has no particle interactions, as shown in formula (13). It could be seen from the fact that the energy levels $\ln k$ are essentially indistinguishable from a tiny power k^ε, thus the potential energy has the same behaviour, $V(x) \propto x^\varepsilon$, having a constant value for $\varepsilon \to 0$.

References

[1] J.G.Dueñas, N.F.Svaiter, Thermodynamics of the bosonic randomized Riemann gas, *Journal of Physics. A. Mathematical and Theoretica*, **48**(2015), no. 31, 315201. DOI: 10.1088/1751-8113/48/31/315201

[2] N.Fabiano, Zeta function and some of its properties, *Military Bulletin*, **68**(2020), no. 4, 895–906. DOI: 10.5937/vojtehg68-28535

[3] N.Fabiano, M.Gardašević-Filipovi c, N.Mirkov, V.Todorčevi c, S.Radenovi c, On the Distribution of Kurepa's Function, *Axioms*, **11**(2022), no. 8, 388.

[4] N.Fabiano, N.Mirkov, Z.D.Mitrović, and Stojan Radenović. On some new observations on Kurepa's left factorial, *Mathematical Analysis and its Contemporary Applications*, **4**(2022), no. 3, 1–8.

[5] N.Fabiano, N.Mirkov, Z.D.Mitrović, Stojan Radenović, 2023 World Scientific Publishing Company. Advances In Number Theory And Applied Analysis, 2023.

[6] N.Fabiano, S.Radenović, Some remarks on an alternative approach for boltzmann distribution of hydrogen atoms, *Bulletin of Natural Sciences Research*, **10**(2020), no. 1, 69–71. DOI: 10.5937/univtho10-26075

[7] N.Fabiano, S.Radenović, On scaling of Schrödinger equation and some results for heavy quarks mesons, *Bulletin of Natural Sciences Research*, **11**(2021), no. 1, 49–53. DOI: 10.5937/bnsr11-31433

[8] B.Julia, Statistical theory of numbers. In Number theory and physics (Les Houches, 1989), Volume 47 of Springer Proc. Phys., Springer, Berlin, 1990, 276–293.

[9] D.Kurepa, Factorials of cardinal numbers and trees, *Journal of Mathematical-Physical Astronomy. Society of Mathematicians and Physicists of Croatia. Series II*, **19**(1964), 7–21.

[10] D.Kurepa, On the left factorial function $!n$, *Mathematica Balkanica*, **1**(1971), 147–153.

[11] D.Kurepa. Left factorial function in complex domain, *Mathematica Balkanica*, **3**(1973), 297–307.

[12] D.Kurepa, On some new left factorial propositions, *Mathematica Balkanica*, **4**(1974), 383–386.

[13] D.Kurepa, Selected papers of Đuro Kurepa. Edited and with commentaries by Aleksandar Ivić, Zlatko Mamuzić, Žarko Mijajlović and Stevo Todorčević, Mathematical Institute SANU, Belgrade, 1996.

[14] D.R.Kurepa, Right and left factorials, *Boll. Un. Mat. Ital.*, **9**(1974), no. 4, (suppl, suppl. fa) 171–189.

[15] I.Mezö, The Lambert W function: its generalizations and applications. Chapman and Hall/CRC, 2022.

[16] A.S.Olaikhan, An Introduction to the harmonic series and logarithmic integrals: for high school students up to researchers. Amazon Digital Services LLC-KDP Print US, 2021.

[17] A.Petojević, S.Gordić, M.Mandić, M.G.Ranitović, New equivalents of Kurepa's hypothesis for left factorial, *Axioms*, **12**(2023), no. 8, 785. DOI: 10.3390/axioms12080785

[18] H.M.Srivastava, J.Choi, Series associated with the Zeta and related functions. Kluwer Academic Publishers, 2001.

[19] V.Stojiljković, N.Fabiano, V.S.Čavič, Harmonic series with polyloga-rhythmic functions, *Military Bulletin*, **70**(2022), no, 1, 43–61.

[20] E.T.Whittaker, G.N.Watson, A Course of Modern Analysis, Cambridge University Press, 5 edition, 2021.

Функция Курепы и некоторые связи со статистической механикой

Никола Фабиано
Институт ядерных наук им. Винчи
Белград, Сербия
Белградский университет
Белград, Сербия
Стоян Раденович
Белградский университет
Белград, Сербия
Вук Стойликович
Университет Нови-Сада
Нови-Сад, Сербия
Математическая гимназия
Белград, Сербия

Аннотация. Исходя из функции Курепы и гипотезы делимости на гамма-функцию, строятся их термодинамические аналоги, и их свойства сравниваются со свойствами дзета-функции Римана.

Ключевые слова: функция Курепы, гипотеза Курепы, дзета-функция, квантовая механика, функция разделения.

EDN: NNIORD
УДК 517.55 + 512.7

Limit-sets of the Discriminant Locus for a System of Algebraic Equations

Irina A. Antipova*
Semyon Yu. Chuvashov†
Siberian Federal University
Krasnoyarsk, Russian Federation

Received 10.09.2025, received in revised form 20.10.2025, accepted 07.12.2025

Abstract. We consider a system of n trinomial algebraic equations in n unknowns, where the exponents of the monomials in each equation are fixed while all the coefficients vary. The discriminant locus of such a system is defined to be the closure of the set of all coefficients for which the system has multiple roots with non-zero coordinates. We study the limit-sets of the discriminant hypersurface which are given by truncation polynomials of the discriminant on faces of its Newton polytope. The limit-sets are characterized in terms of the discriminants of systems of lower dimension.

Keywords: system of algebraic equations, discriminant, Newton polytope, truncation of the polynomial, discriminant locus, parametrization.

Citation: I.A. Antipova, S.Yu. Chuvashov, Limit-sets of the Discriminant Locus for a System of Algebraic Equations, J. Sib. Fed. Univ. Math. Phys., 2026, 19(2), 192–202. EDN: NNIORD.

1. Introduction and preliminaries

In paper [1], George M. Bergman studied "the behavior at infinity" of an algebraic variety $V \subset (\mathbb{C} \setminus \{0\})^n$, and introduced the concept of the logarithmic limit-set of the variety as a subset of the unit sphere $S^{n-1} \subset \mathbb{R}^n$, considering the limit values of the ratios $\log|x_1| : \ldots : \log|x_n|$, where $x = (x_1, \ldots, x_n) \in V$. If V is a hypersurface defined by a polynomial P, then the logarithmic limit-set of V is the intersection of the sphere S^{n-1} with the set of faces of the normal fan for the Newton polytope of the polynomial P.

In this paper, we consider the limit positions of the discriminant hypersurface of a system of algebraic equations with a fixed support and variable coefficients. Our approach is based on the parametrization of the discriminant locus of a system of n Laurent polynomials in n unknowns, introduced and studied in detail in [2]. As a result, the limit positions of the discriminant hypersurface are characterized in terms of parametrizations for discriminant loci of systems of lower dimension.

We consider the following system of n trinomial algebraic equations

$$Q_i := y^{\omega^{(i)}} + x^{(i)} y^{\lambda^{(i)}} - 1 = 0, \ i = 1, \ldots, n \tag{1}$$

with unknowns $y = (y_1, \ldots, y_n) \in (\mathbb{C} \setminus \{0\})^n$, variable complex coefficients $x = \left(x^{(1)}, \ldots, x^{(n)}\right)$, in which $y^{\omega^{(i)}}$, $y^{\lambda^{(i)}}$ are monomials of $y_1, \ldots, y_n$ with integer exponents. The set of coefficients

*iantipova@sfu-kras.ru https://orcid.org/0000-0003-1382-0799
†simontahkraa@gmail.com https://orcid.org/0009-0001-2344-7185

of system (1) runs through the vector space $\mathbb{C}_x^n$. It is assumed that the matrix ω, composed of vector columns $\omega^{(i)}$, is non-degenerate. A trinomial system in which all monomials have independent variable coefficients can be reduced to form (1) using monomial transformations of the coefficients due to the property of polyhomogeneity of its solution. The procedure for dehomogenizing the system is detailed in [2].

Let us denote by ∇° a subset of $\mathbb{C}_x^n$ of all coefficients $x = (x^{(i)})$, for which the polynomial mapping $Q := (Q_1, \ldots, Q_n)$ has multiple zeros in the complex algebraic torus $(\mathbb{C} \setminus \{0\})^n$, that is,

$$\nabla^\circ = \{x \in \mathbb{C}_x^n : Q_1(y^0) = \ldots = Q_n(y^0) = \frac{\partial Q}{\partial y}(y^0) = 0,\ y^0 \in (\mathbb{C} \setminus \{0\})^n\},$$

where $\dfrac{\partial Q}{\partial y}$ is the Jacobian of the mapping Q.

Definition 1. *The discriminant locus ∇ of the system* (1) *is defined to be the closure of ∇° in the space of coefficients. If ∇ is a hypersurface, then its defining polynomial $\Delta(x)$ is said to be the discriminant of the system* (1).

This approach to defining the discriminant of a polynomial system was proposed in [2] as an extension of the concept of the A-discriminant developed by I. Gelfand, A. Zelevinsky and M. Kapranov, in their monograph [3, Ch. 9]. In parallel, this theory was extended to polynomial systems in papers by A. Esterov and co-authors (see, for example, [4]). Hereinafter we will denote the discriminant locus and the discriminant of the system (1) by ∇_n and $\Delta_n(x)$, respectively, emphasising the number of equations in the system and the dimension of the coefficient space with the index n.

This paper studies limit positions of the discriminant set ∇_n in the toric compactification of the space $(\mathbb{C} \setminus \{0\})^n$ associated with the Newton polytope of the discriminant $\Delta_n(x)$. Recall that the Newton polytope $\mathcal{N}_{\Delta_n}$ of the polynomial $\Delta_n(x)$ is the convex hull (in the space $\mathbb{R}^n$) of its support. Each monomial $x^\alpha = x_1^{\alpha_1} \cdot \ldots \cdot x_n^{\alpha_n}$ can be visualized as a point $\alpha = (\alpha_1, \ldots, a_n)$ of the lattice $\mathbb{Z}^n$. The support of a polynomial is defined to be the set of all exponents of its monomials with non-zero coefficients. The limit positions of the ∇_n are determined by truncations of the discriminant $\Delta_n(x)$ to the faces of the Newton polytope $\mathcal{N}_{\Delta_n}$.

Definition 2. *The truncation of the polynomial $\Delta_n(x)$ to the face h of the polytope $\mathcal{N}_{\Delta_n}$ is defined to be the sum of all monomials of $\Delta_n(x)$ whose exponents belong to h.*

It is known that the Newton polytope of the discriminant of an algebraic equation of degree m is combinatorially equivalent to an $(m-1)$-dimensional cube [3, Ch. 12]. For example, for the quartic equation

$$y^4 + a_3y^3 + a_2y^2 + a_1y - 1 = 0 \tag{2}$$

the Newton polytope of its discriminant is a hexagon in $\mathbb{R}^3$. The discriminant itself has the following form:

$$\begin{aligned}\Delta = 256 - 192a_1a_3 - 128a_2^2 + 144a_2a_3^2 - 4a_1^2a_2^3 - 4a_2^3a_3^2 + 144a_1^2a_2 - 6a_1^2a_3^2 + \\ +16a_2^4 - 27a_1^4 - 27a_3^4 - 80a_1a_2^2a_3 + 18a_1a_2a_3^3 + 18a_1^3a_2a_3 + a_1^2a_2^2a_3^2.\end{aligned} \tag{3}$$

The truncations of the discriminant can be factorized into products of discriminants of lower-degree equations. For example, one of the faces of the Newton polytope of polynomial (3) is a parallelogram. Its truncation admits a representation as

$$\Delta|_h = 16a_2^4 + a_1^2a_2^2a_3^2 - 4a_2^3a_3^2 - 4a_1^2a_2^3 = a^2(a_1^2 - 4a_2)(a_3^2 - 4a_2). \tag{4}$$

The binomials in parentheses on the right-hand side in (4) are discriminants of the semi-reduced quadratic equations:

$$a_2y^2 + a_1y + 1 = 0 \ \text{ and } \ y^2 + a_3y + a_2 = 0$$

respectively. E. Mikhalkin, V. Stepanenko and A. Tsikh in [5] developed a new approach to proving factorization identities for truncations of the classical discriminant. This method provides a more elementary alternative to the intricate A-determinant theory employed in the original proof [3, Ch. 10].

The combinatorial properties of the Newton polytope associated with a polynomial system remain largely unexplored. Some observation are available in [6,7]. In this paper, we extend the study of the limit-sets of the discriminant hypersurface of a system of trinomials, initiated in [8]. Let us consider the system of the following form

$$\tilde{Q}_i := y_i + x^{(i)}y^{\varphi^{(i)}} - 1 = 0, \ i = 1, \dots, n, \tag{5}$$

where $\varphi^{(i)} \in \mathbb{Z}^n_+$. It can be derived from (1) by monomial transformation of coordinates. The construction presented below can be implemented for systems of a more general form, but will require cumbersome calculations.

Let us introduce the matrix Φ, whose columns are exponents $\varphi^{(1)}, \dots, \varphi^{(n)}$ of system (5), as well as the matrix $\tilde{\Phi} := \Phi - E_n$, where E_n is the identity matrix. Rows of matrices Φ and $\tilde{\Phi}$ are denoted by $\varphi_1, \dots \varphi_n$ and $\tilde{\varphi}_1, \dots, \tilde{\varphi}_n$ respectively. We assume that both Φ and $\tilde{\Phi}$ contain no zero entries. This ensures the discriminant locus is a hypersurface [2].

We assume that the Newton polytope of the discriminant of (5) has two families of hyperfaces $h_1, \dots, h_n$ and $\tilde{h}_1, \dots, \tilde{h}_n$ with outward normals $\varphi_1, \dots, \varphi_n$ and $-\tilde{\varphi}_1, \dots, -\tilde{\varphi}_n$ respectively (see [6]). Let us fix an ordered set $J := \{j_1, \dots, j_p\} \subset \{1, \dots, n\}$. We suppose that the intersections of hyperfaces $h_{j_1} \cap \dots \cap h_{j_p}$ and $\tilde{h}_{j_1} \cap \dots \cap \tilde{h}_{j_p}$ form the faces of codimension p. Let us denote them by h_J and $\tilde{h}_J$ respectively. The rows $\varphi_j, j \in J$ and $\tilde{\varphi}_j, j \in J$ form $p \times n$ matrices Φ_J and $\tilde{\Phi}_J$. We suppose that columns of matrices Φ_J and $\tilde{\Phi}_J$ indexed by $j \in J$ form minors δ and $\tilde{\delta}$ that are not equal to zero.

Theorem 1. *A. The zero locus of the truncation $\{\Delta_n(x)|_{h_J} = 0\} \subset \mathbb{C}^n_x$ admits a parametrization of the form*

$$x^{\boldsymbol{e}_k} = \left(z^{(k)}(t)\right)^{\delta}, \quad t \in \mathbb{CP}^{n-p-1}, \ k = 1, \dots, n-p.$$

Here, the vectors $\boldsymbol{e}_k \in \mathbb{Z}^n$ form the basis of the kernel of the linear mapping defined by the matrix Φ_J, and $z^{(k)}(t)$ are coordinates of the mapping (14) that defines the discriminant locus of the system of $n-p$ trinomials.

B. The zero locus of the truncation $\{\Delta_n(x)|_{\tilde{h}_J} = 0\} \subset \mathbb{C}^n_x$ admits a parametrization of the form

$$x^{\tilde{\boldsymbol{e}}_k} = \left(\tilde{z}^{(k)}(t)\right)^{\tilde{\delta}}, \quad t \in \mathbb{CP}^{n-p-1}, \ k = 1, \dots, n-p.$$

Here, the vectors $\tilde{\boldsymbol{e}}_k \in \mathbb{Z}^n$ form the basis of the kernel of the linear mapping defined by the matrix $\tilde{\Phi}_J$, and $\tilde{z}^{(k)}(t)$ are coordinates of the mapping (15) that defines the discriminant locus of the system of $n-p$ trinomials.

The proof of the theorem is given in Section 3.

2. Parametrization and tropicalization of the discriminant locus

In order to prove Theorem 1 we need the parametrization of the homogenized discriminant locus of a system of n trinomials with n unknowns. In addition to the space of coefficients $\mathbb{C}_x^n$ we introduce the space $\mathbb{C}_s^n$ with variables $s = (s^{(1)}, \dots, s^{(n)})$. We will treat s as homogeneous coordinates for $\mathbb{CP}_s^{n-1}$. The support of system (1) is given by the block matrix $(\omega|\Lambda)$, composed of vector columns $\omega^{(i)}$ and $\lambda^{(i)}$ respectively. The parametrization is written in terms of the elements of the matrices $\Psi := \omega^{-1}\Lambda$ and $\tilde{\Psi} := \Psi - E_n$, where ω^{-1} is the inverse matrix to ω.

Let us consider an algebraic multivalued mapping $x = x(s)$ from the projective space $\mathbb{CP}_s^{n-1}$ to the coefficient space $\mathbb{C}_x^n$ with coordinates

$$x^{(i)} = -\frac{s^{(i)}}{\langle\tilde{\psi}_i, s\rangle}\prod_{k=1}^{n}\left(\frac{\langle\tilde{\psi}_k, s\rangle}{\langle\psi_k, s\rangle}\right)^{\psi_k^{(i)}}, \ i = 1, \dots, n. \tag{6}$$

Here, the angle brackets denote the dot product of vectors, ψ_k and $\tilde{\psi}_k$ are the rows of matrices Ψ and $\tilde{\Psi}$ respectively. The mapping (6) parametrizes the discriminant locus of system (1). The number of branches in (6) is equal to the absolute value of the determinant $|\omega|$, but some branches may coincide. If the discriminant locus of the system (1) is an irreducible hypersurface depending on all variables, then the mapping (6) parametrizes it with multiplicity equal to the index $|\mathbb{Z}^n : L|$ of the sublattice $L \subset \mathbb{Z}^n$, generated by columns of the matrix $(\omega|\Lambda)$, and appears to be the inverse of the logarithmic Gauss mapping [2].

If matrices Ψ and $\tilde{\Psi}$ are integer, then coordinates of the parametrization (6) are Laurent monomials of linear forms, consequently the general combinatorial construction of tropicalization of algebraic varieties proposed in [9] is applicable. In this situation, the tropical fan is encoded by the pair of block matrices:

$$U_{3n\times n} = \left(-E_n|\Psi^T|\tilde{\Psi}^T\right)^T, \quad V_{n\times 3n} = \left(E_n| - \Psi^T|\tilde{\Psi}^T\right). \tag{7}$$

The rows of the matrix U define $3n$ linear forms, while the rows of the matrix V define n Laurent monomials that appear in (6). According to [9, Theorem 3.1], the tropicalization of the variety ∇ is a polyhedral fan $\mathrm{trop}(\nabla)$, which is the image of the Bergman fan $\mathcal{B}(M)$ of the matroid M associated with the matrix U under the linear mapping V. The Bergman fan is a geometric model of the matroid M which tropicalizes the linear subspace given by the mapping $s \to Us$ (see [10,13]). The structure of the tropical fan leads to factorization identities for the discriminant truncations (see the example in Section 4).

3. Truncations of the discriminant

We examine the faces h_J and $\tilde{h}_J$ of the Newton polytope N_{Δ_n} corresponding to the set J. We will focus on the case of h_J; the case for $\tilde{h}_J$ is similar. The normal subspace to the face h_J is generated by the vectors $\varphi_{j_1}, \dots, \varphi_{j_p}$. We denote it by $F_J^{\perp}$. We consider the sublattice $B := \mathbb{Z}^n \cap F_J^{\perp} \subset \mathbb{Z}^n$. of rank p and choose a basis $\beta_1, \dots, \beta_p$ in B. Let β be the $p \times n$ matrix with rows $\beta_1, \dots, \beta_p$. We denote the columns of this matrix by $\beta^{(1)}, \dots, \beta^{(n)}$.

In the complex algebraic torus $(\mathbb{C} \setminus \{0\})^n$, we consider the complex p-dimensional torus $x = \tau^{\beta}, \tau = (\tau_1, \dots, \tau_p) \in (\mathbb{C} \setminus \{0\})^p$, where τ^{β} denotes the monomial mapping with coordinates

$$x^{(j)} = \tau^{\beta^{(j)}}, \ j = 1, \dots, n.$$

The relationship between the discriminant $\Delta_n(x)$ and its truncation on the face h_J can be established using the function

$$H_J(\tau, x) := \tau_1^{d_1} \dots \tau_p^{d_p} \cdot \Delta_n \left(\frac{x^{(1)}}{\tau^{\beta^{(1)}}}, \dots, \frac{x^{(n)}}{\tau^{\beta^{(n)}}} \right), \tag{8}$$

where d_i is the weighted degree of Δ_n relative to the weight β_i, defined as the maximum of all dot products $\langle \alpha, \beta_i \rangle$, being taken over all exponents α of monomials in $\Delta_n(x)$.

Lemma 1. *The function $H_J(\tau, x)$ is a homogenization of the discriminant of system (5) with respect to the weights $\beta_1, \dots, \beta_p$. Furthermore, it satisfies the property*

$$H_J(\tau, x) \underset{\tau \to 0}{\longrightarrow} \Delta_n(x)|_{h_J}. \tag{9}$$

Proof of Lemma 1. The weighted degree, with respect to the weight β_i, of any monomial in $\Delta_n(x)$ that does not belong to the truncation on the face h_J is strictly less than d_i. Therefore, in the limit (9) all monomials will disappear, except for those whose exponents lie on the face h_J. This completes the proof of Lemma 1. □

A similar statement holds for the truncation of the discriminant on the face $\tilde{h}_J$ and the corresponding dehomogenization function.

Next, within the ordered set $I = \{i_1, \dots, i_{n-p}\} := \{1, \dots, n\} \setminus J$, we fix the element i_k. We then define the determinants $\delta^{[l]}$ and $\tilde{\delta}^{[l]}$, $l = 1, \dots, p$, obtained by replacing in δ ($\tilde{\delta}$) the j_l-th column of the matrix Φ_J ($\tilde{\Phi}_J$) with the i_k-th column. Let us introduce the vectors

$$\boldsymbol{e}_k = \delta e_{i_k} - \sum_{l=1}^{p} \delta^{[l]} e_{j_l}, \quad \tilde{\boldsymbol{e}}_k = \tilde{\delta} e_{i_k} - \sum_{l=1}^{p} \tilde{\delta}^{[l]} e_{j_l}, \quad k = 1, \dots, n-p, \tag{10}$$

here, $e_1, \dots, e_n$ is a standard basis in $\mathbb{R}^n$.

Lemma 2. *The vectors $\boldsymbol{e}_k$ (respectively, $\tilde{\boldsymbol{e}}_k$) form a basis for the kernel of the linear mapping defined by the matrix Φ_J (respectively, $\tilde{\Phi}_J$).*

Proof of Lemma 2. A direct verification shows that the vectors $\boldsymbol{e}_k$ and $\tilde{\boldsymbol{e}}_k$ are orthogonal to the rows of the matrices Φ_J and $\tilde{\Phi}_J$ respectively. □

Note, however, that the vectors $\boldsymbol{e}_k$ may not span the lattice among the columns of the matrix Φ_J. The same statement holds to the vectors $\tilde{\boldsymbol{e}}_k$ with respect to the matrix $\tilde{\Phi}_J$.

Proof of Theorem 1. We consider a multivalued algebraic mapping with coordinates

$$x^{(i)} = -\frac{s^{(i)}}{\langle \tilde{\varphi}_i, s \rangle} \prod_{k=1}^{n} \left(\frac{\langle \tilde{\varphi}_k, s \rangle}{\langle \varphi_k, s \rangle} \right)^{\varphi_k^{(i)}}, \ i = 1, \dots, n, \tag{11}$$

which parametrizes the discriminant locus of system (5). The mapping (11) is defined in the domain

$$S = \{ s \in \mathbb{CP}^{n-1} : \langle \varphi_1, s \rangle \cdot \ldots \cdot \langle \varphi_n, s \rangle \neq 0 \}.$$

To describe the values of the mapping (11) on the entire space $\mathbb{CP}^{n-1}$, we will treat it as a "correspondence" according to the terminology of [11]. Specifically, we consider the set $\pi(Z) \subset \mathbb{C}_x^n$, defined as the image of the projection $\pi : \mathbb{CP}_s^{n-1} \to \mathbb{C}_x^n$ applied to the algebraic set

$$Z = \left\{ (s, x) \in \mathbb{CP}_s^{n-1} \times \mathbb{C}_x^n : x^{(i)} \prod_{k=1}^{n} \langle \varphi_k, s \rangle^{\varphi_k^{(i)}} + s^{(i)} \prod_{k=1}^{n} \langle \tilde{\varphi}_k, s \rangle^{\tilde{\varphi}_k^{(i)}} = 0, i = 1, \dots, n \right\}.$$

Next, we consider the sets

$$W_\tau := \{x \in \mathbb{C}^n : H_J(\tau, x) = 0\},\ \tau \neq 0.$$

According to (11), they admit the parametrization

$$x^{(i)} = -\tau^{\beta^{(i)}} \frac{s^{(i)}}{\langle\tilde{\varphi}_i, s\rangle} \prod_{k=1}^{n} \left(\frac{\langle\tilde{\varphi}_k, s\rangle}{\langle\varphi_k, s\rangle}\right)^{\varphi_k^{(i)}},\ i = 1, \ldots, n. \tag{12}$$

Then, we define the plane

$$\sigma_J := \{s \in \mathbb{CP}_s^{n-1} : \langle\varphi_j, s\rangle = 0, j \in J\}.$$

For all linear forms $\langle\varphi_{i_r}, s\rangle, i_r \in I$ we calculate the restrictions to the plane σ_J as follows

$$\langle\varphi_{i_r}, s\rangle|_{\sigma_J} = \langle\theta_r, s'\rangle,$$

here $s' = (s^{(i_1)} : \ldots : s^{(i_{n-p})})$ and $\theta_r := (\langle\varphi_{i_r}, \boldsymbol{e}_1\rangle, \ldots, \langle\varphi_{i_r}, \boldsymbol{e}_{n-p}\rangle)$. Henceforth, we denote the vector $t = (t^{(1)}, \ldots, t^{(n-p)})$ by s'. We take the restrictions of monomials $x^{\boldsymbol{e}_k}$ on σ_J, thereby eliminating the parameters $\tau = (\tau_1, \ldots, \tau_p)$ from (12). As a result, we obtain:

$$x^{\boldsymbol{e}_k}|_{\sigma_J} = \left(-\frac{\delta t^{(k)}}{\langle\tilde{\theta}_k, t\rangle}\right)^{\delta} \prod_{r=1}^{n-p} \left(\frac{\langle\tilde{\theta}_r, t\rangle}{\langle\theta_r, t\rangle}\right)^{\theta_r^{(k)}},\quad k = 1, \ldots, n-p. \tag{13}$$

The mapping

$$H : \mathbb{CP}_t^{n-p-1} \to \mathbb{C}_z^{n-p}$$

with coordinates

$$z^{(k)} = -\frac{\delta t^{(k)}}{\langle\tilde{\theta}_k, t\rangle} \prod_{r=1}^{n-p} \left(\frac{\langle\tilde{\theta}_r, t\rangle}{\langle\theta_r, t\rangle}\right)^{\frac{\theta_r^{(k)}}{\delta}},\quad k = 1, \ldots, n-p \tag{14}$$

parametrizes the discriminant locus ∇_{n-p} of the system of $n-p$ trinomial equations, whose support is given by the block matrix $(\delta E_{n-p}|\Theta)$, where $\Theta := (\theta_r^{(k)})$. Thus, the limit set of the discriminant locus ∇_n, associated with the face h_J of the Newton polytope of the discriminant of system (5), is given by the relations

$$x^{\boldsymbol{e}_k} = \left(z^{(k)}\right)^{\delta},\ k = 1, \ldots, n-p,$$

where $z = \left(z^{(k)}\right) \in \nabla_{n-p}$. This completes the proof of the Part A of Theorem 1.

Next, we note that the mapping (11), which parametrizes the discriminant locus of system (5), can be rewritten as

$$x^{(i)} = -\frac{s^{(i)}}{\langle\varphi_i, s\rangle} \prod_{k=1}^{n} \left(\frac{\langle\varphi_k, s\rangle}{\langle\tilde{\varphi}_k, s\rangle}\right)^{\tilde{\varphi}_k^{(i)}},\ i = 1, \ldots, n.$$

Consequently, the proof of the part B of Theorem 1 follows the same pattern. The limit set of the discriminant locus ∇_n, associated with the face $\tilde{h}_J$ of the Newton polytope of the discriminant of system (5), is given by the relations

$$x^{\tilde{\boldsymbol{e}}_k} = \left(\tilde{z}^{(k)}\right)^{\tilde{\delta}},\ k = 1, \ldots, n-p,$$

where

$$\tilde{z}^{(k)} = -\frac{\tilde{\delta} t^{(k)}}{\langle \tilde{\varkappa}_k, t\rangle} \prod_{r=1}^{n-p} \left(\frac{\langle \tilde{\varkappa}_r, t\rangle}{\langle \varkappa_r, t\rangle} \right)^{\frac{\varkappa_r^{(k)}}{\tilde{\delta}}}, \ k = 1, \ldots, n-p, \tag{15}$$

and $\varkappa_r := (\langle \varphi_{i_r}, \tilde{\boldsymbol{e}}_1\rangle, \ldots, \langle \varphi_{i_r}, \tilde{\boldsymbol{e}}_{n-p}\rangle)$. The mapping

$$\tilde{H} : \mathbb{CP}^{n-p-1}_t \to \mathbb{C}^{n-p}_{\tilde{z}}$$

with coordinates (15) parametrizes the discriminant locus ∇_{n-p} of the system of $n-p$ trinomial equations, whose support is given by the matrix $(\tilde{\delta} E_{n-p}|K)$, where $K := (\varkappa_r^{(k)})$. This completes the proof of Theorem 1. □

4. Example

We consider the system of equations

$$\begin{cases} y_1 + a y_1^3 y_2 y_3 - 1 = 0, \\ y_2 + b y_1 y_2^3 y_3 - 1 = 0, \\ y_3 + c y_1 y_2 y_3^3 - 1 = 0, \end{cases} \tag{16}$$

with unknowns $y := (y_1, y_2, y_3) \in (\mathbb{C} \setminus \{0\})^3$ and variable complex coefficients (a, b, c). The support of the system is given by the matrix

$$(E_3|\Phi) = \left(\begin{array}{ccc|ccc} 1 & 0 & 0 & 3 & 1 & 1 \\ 0 & 1 & 0 & 1 & 3 & 1 \\ 0 & 0 & 1 & 1 & 1 & 3 \end{array} \right).$$

Columns of this matrix span the lattice $\mathbb{Z}^3$. Since the matrices Φ and $\tilde{\Phi}$ have no zero entries, the discriminant locus ∇_3 of system (16) is a hypersurface. The rational mapping $\mathbb{CP}^2_s \to \mathbb{C}^3_{a,b,c}$, given by the formulae

$$\begin{aligned} a &= \frac{-s^{(1)}}{2s^{(1)} + s^{(2)} + s^{(3)}} \left(\frac{2s^{(1)} + s^{(2)} + s^{(3)}}{3s^{(1)} + s^{(2)} + s^{(3)}} \right)^3 \left(\frac{s^{(1)} + 2s^{(2)} + s^{(3)}}{s^{(1)} + 3s^{(2)} + s^{(3)}} \right) \left(\frac{s^{(1)} + s^{(2)} + 2s^{(3)}}{s^{(1)} + s^{(2)} + 3s^{(3)}} \right), \\ b &= \frac{-s^{(2)}}{s^{(1)} + 2s^{(2)} + s^{(3)}} \left(\frac{2s^{(1)} + s^{(2)} + s^{(3)}}{3s^{(1)} + s^{(2)} + s^{(3)}} \right) \left(\frac{s^{(1)} + 2s^{(2)} + s^{(3)}}{s^{(1)} + 3s^{(2)} + s^{(3)}} \right)^3 \left(\frac{s^{(1)} + s^{(2)} + 2s^{(3)}}{s^{(1)} + s^{(2)} + 3s^{(3)}} \right), \\ c &= \frac{-s^{(3)}}{s^{(1)} + s^{(2)} + 2s^{(3)}} \left(\frac{2s^{(1)} + s^{(2)} + s^{(3)}}{3s^{(1)} + s^{(2)} + s^{(3)}} \right) \left(\frac{s^{(1)} + 2s^{(2)} + s^{(3)}}{s^{(1)} + 3s^{(2)} + s^{(3)}} \right) \left(\frac{s^{(1)} + s^{(2)} + 2s^{(3)}}{s^{(1)} + s^{(2)} + 3s^{(3)}} \right)^3 \end{aligned} \tag{17}$$

parametrizes the discriminant locus with multiplicity 1. Here, $s = (s^{(1)}, s^{(2)}, s^{(3)}) \in \mathbb{C}^3$ are homogeneous coordinates in $\mathbb{CP}^2_s$.

Calculations performed in Sage CAS [12] show that the discriminant $\Delta_3(a, b, c)$ of system (16) contains 611 monomials. The Newton polytope $\mathcal{N}_{\Delta_3}$ has 24 facets, 57 edges, and 35 vertices.

Let us use this example to illustrate Theorem 1. We consider the set $J = \{1\} \subset \{1, 2, 3\}$, which defines the facet h_1 with the outward normal $\varphi_1 = (3, 1, 1)$. The truncation of the discriminant $\Delta_3(a, b, c)$ on the h_1 has the form:

$$\Delta_3(a,b,c)|_{h_1} = a^8\cdot(1048576000000000000000000000b^8c^8 - 250482492702720000000000ab^9c^4 +$$
$$+ 52401285365760000000000000ab^8c^5 - 335145861120000000000000ab^7c^6 - 335145861120000000000000ab^6c^7 +$$
$$+ 52401285365760000000000000ab^5c^8 - 250482492702720000000000ab^4c^9 + 14958734309808773529 6a^2b^{10} -$$
$$- 2597002484341800960a^2b^9c - 2553418530611527680a^2b^8c^2 - 249666909820157952 0a^2b^7c^3 -$$
$$- 12621395262144144998 40a^2b^6c^4 + 32234780523789633454 08a^2b^5c^5 - 12621395262144144998 40a^2b^4c^6 -$$
$$- 249666909820157952 0a^2b^3c^7 - 2553418530611527680a^2b^2c^8 - 2597002484341800960a^2bc^9 +$$
$$+ 14958734309808773529 6a^2c^{10} + 752295975321600000a^3b^7 - 365699432448000000a^3b^6c -$$
$$- 2111794585600000a^3b^5c^2 - 2121708288000000a^3b^4c^3 - 2121708288000000a^3b^3c^4 -$$
$$- 2111794585600000a^3b^2c^5 - 365699432448000000a^3bc^6 +$$
$$+ 752295975321600000a^3c^7 + 217145126953125a^4b^2c^2).$$

The polynomial in parentheses in (4) is irreducible. According to Theorem 1, the set $\{\Delta_3(a,b,c)|_{h_1} = 0\}$ admits the parametrization

$$a^{-1}b^3 = (u(t))^3, \quad a^{-1}c^3 = (v(t))^3,$$

here $t \in \mathbb{CP}^1$, and

$$u(t) = \frac{-t^{(1)}}{7t^{(1)}+2t^{(2)}}\left(\frac{7t^{(1)}+2t^{(2)}}{8t^{(1)}+2t^{(2)}}\right)^8\left(\frac{2t^{(1)}+7t^{(2)}}{2t^{(1)}+8t^{(2)}}\right)^2,$$
$$v(t) = \frac{-t^{(2)}}{2t^{(1)}+7t^{(2)}}\left(\frac{7t^{(1)}+2t^{(2)}}{8t^{(1)}+2t^{(2)}}\right)^2\left(\frac{2t^{(1)}+7t^{(2)}}{2t^{(1)}+8t^{(2)}}\right)^8.$$

The mapping $(u(t),v(t)) : \mathbb{CP}^1_t \to \mathbb{C}^2_{u,v}$ defines the discriminant locus of the system of two equations

$$\begin{cases} y_1^3 + uy_1^8y_2^2 - 1 = 0, \\ y_2^3 + vy_1^2y_2^8 - 1 = 0. \end{cases} \tag{18}$$

The discriminant of system (18) is as follows

$$\Delta_2(u,v) = 1048576000000000000000000\,u^8v^8 - 250482492702720000000000\,u^9v^4 +$$
$$+ 52401285365760000000000\,u^8v^5 - 335145861120000000000\,u^7v^6 - 335145861120000000000\,u^6v^7 +$$
$$+ 52401285365760000000000\,u^5v^8 - 250482492702720000000000\,u^4v^9 + 14958734309808773529 6\,u^{10} -$$
$$- 2597002484341800960\,u^9v - 2553418530611527680\,u^8v^2 - 249666909820157952 0\,u^7v^3 -$$
$$- 12621395262144144998 40\,u^6v^4 + 32234780523789633454 08\,u^5v^5 - 12621395262144144998 40\,u^4v^6 -$$
$$- 249666909820157952 0\,u^3v^7 - 2553418530611527680\,u^2v^8 - 2597002484341800960\,uv^9 +$$
$$+ 14958734309808773529 6\,v^{10} + 752295975321600000\,u^7 - 365699432448000000\,u^6v -$$
$$- 2111794585600000\,u^5v^2 - 2121708288000000\,u^4v^3 - 2121708288000000\,u^3v^4 -$$
$$-2111794585600000\,u^2v^5 - 365699432448000000\,uv^6 + 752295975321600000\,v^7 + 217145126953125\,u^2v^2.$$

The composition of $\Delta_2(u,v)$ with monomials $u = a^{-1/3}b,\ v = a^{-1/3}c$ yields the truncation $\Delta_3(a,b,c)|_{h_1}$, up to a monomial factor.

We now consider the edge $h_{1,2} := h_1 \cap h_2$. The normal space to the $h_{1,2}$ is formed by vectors $\varphi_1 = (3,1,1)$ and $\varphi_2 = (1,3,1)$. The truncation of the discriminant $\Delta_3(a,b,c)$ to the $h_{1,2}$ is as follows

$$\Delta_3(a,b,c)|_{h_{1,2}} = 1099511627776\cdot a^8\cdot b^8\cdot(9765625c^4 - 11664ab)^2, \tag{19}$$

here the polynomial in parentheses is irreducible and can be represented as

$$(5^5)^2c^4 - (2^2 3^3)^2 ab. \tag{20}$$

By Theorem 1, in the coordinates $u = a^{-1/4}b^{-1/4}c$ the zero set of the polynomial (20) is the discriminant locus of the trinomial equation

$$y^4 + uy^{10} - 1 = 0.$$

It consists of the two points $u = \pm\dfrac{2 \cdot 3^{3/2}}{5^{5/2}}$.

Theorem 1 does not characterize all faces of the Newton polytope. The tropical fan provides a more complete description of the faces of $\mathcal{N}_{\Delta_n}$ and the factorization of their truncations.

Let us construct the tropicalization $\mathrm{trop}(\nabla_3)$ of the discriminant hypersurface $\nabla_3 \subset \mathbb{C}^3_{a,b,c}$, given by the mapping (17). According to the general construction [9, Theorem 3.1], the mapping (17) is encoded by a pair of matrices:

$$U = \begin{pmatrix} -1 & 0 & 0 \\ 0 & -1 & 0 \\ 0 & 0 & -1 \\ 3 & 1 & 1 \\ 1 & 3 & 1 \\ 1 & 1 & 3 \\ 2 & 1 & 1 \\ 1 & 2 & 1 \\ 1 & 1 & 2 \end{pmatrix} \quad \text{and} \quad V = \begin{pmatrix} 1 & 0 & 0 & -3 & -1 & -1 & 2 & 1 & 1 \\ 0 & 1 & 0 & -1 & -3 & -1 & 1 & 2 & 1 \\ 0 & 0 & 1 & -1 & -1 & -3 & 1 & 1 & 2 \end{pmatrix}.$$

Let $E = \{1, 2, \ldots, 9\}$ be the row index for the matrix U. We consider the matroid M defined on the ground set E. Then we construct the Bergman fan $\mathcal{B}(M)$ of the matroid M (also known as the associated tropical linear space). In this example, it is a two-dimensional fan in $\mathbb{R}^9/\mathbb{R}\mathbf{1}$, constructed from nested chains of proper closed flats of the matroid M. The list of proper flats is as follows

$$(1), (2), (3), (4), (5), (6), (7), (8), (9);$$
$$(1,2), (1,3), (1,5), (1,6), (1,4,7), (1,8), (1,9), (2,3), (2,4), (2,6),$$
$$(2,7), (2,5,8), (2,9), (3,4), (3,5), (3,7), (3,8), (3,6,9), (4,5), (4,6),$$
$$(4,8), (4,9), (5,6), (5,7), (5,9), (6,7), (6,8), (7,8), (7,9), (8,9).$$

We refer the reader to [10, 13] for the technique of constructing Bergman fans.

The image of the Bergman fan $\mathcal{B}(M)$ under the linear mapping V is a two-dimensional fan that is the tropicalization $\mathrm{trop}(\nabla_3)$ of the discriminant hypersurface ∇_3. The constructed tropical fan shows that the Newton polytope indeed has 24 facets. Only 9 facets are explicitly predicted by the parametrization (17). Their outward normals are as follows

$$\begin{array}{lll} \mu^{(1)} = (-1,0,0), & \mu^{(4)} = (3,1,1), & \mu^{(7)} = (-2,-1,-1), \\ \mu^{(2)} = (0,-1,0), & \mu^{(5)} = (1,3,1), & \mu^{(8)} = (-1,-2,-1), \\ \mu^{(3)} = (0,0,-1), & \mu^{(6)} = (1,1,3), & \mu^{(9)} = (-1,-1,-2). \end{array} \tag{21}$$

The fifteen "hidden" normals are formed by the intersection of the cones of the fan $\mathrm{trop}(\nabla_3)$. Their complete list is as follows

$$\begin{array}{lll} \mu^{(10)} = (-2,-1,-2), & \mu^{(11)} = (-2,-2,-1), & \mu^{(12)} = (-1,-2,-2), \\ \mu^{(13)} = (-4,-2,-9), & \mu^{(14)} = (-2,0,-5), & \mu^{(15)} = (-5,0,-2), \\ \mu^{(16)} = (-9,-2,-4), & \mu^{(17)} = (-9,-4,-2), & \mu^{(18)} = (-5,-2,-0), \\ \mu^{(19)} = (-2,-5,-0), & \mu^{(20)} = (-4,-9,-2), & \mu^{(21)} = (-2,-9,-4), \\ \mu^{(22)} = (0,-5,-2), & \mu^{(23)} = (0,-2,-5), & \mu^{(24)} = (-2,-4,-9). \end{array}$$

To see how these vectors arise, consider the normal vector $\mu^{(12)}$. The cone C_1, constructed from flags $\mathcal{F}_1 = \{(3) \subset (3,8)\}$ and $\mathcal{F}_2 = \{(8) \subset (3,8)\}$, intersects the cone C_2, which is built from flags $\mathcal{F}_3 = \{(2) \subset (2,9)\}$ and $\mathcal{F}_4 = \{(9) \subset (2,9)\}$. Their intersection is the ray $\mathbb{R}_{\geqslant}(1,2,2)^T$.

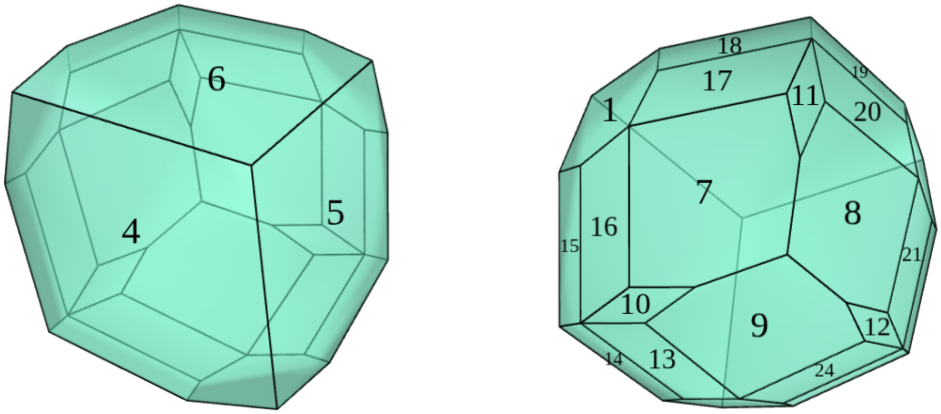

Fig. 1. Two views of the Newton polytope $\mathcal{N}_{\Delta_3}$

Constructing the polytope $\mathcal{N}_{\Delta_3}$ (see Fig.1) as the convex hull of the exponent vectors of the monomials in the discriminant $\Delta_3(a,b,c)$ reveals that all its "hidden" facets are parallelograms. This observation is consistent with the fact that all truncations on "hidden" facets factorize (up to monomial) into products of discriminants of trinomial equations. Furthermore, these factors can be recovered from the matroid M. For example, the truncation on the facet with the normal $\mu^{(12)} = (1,2,2)$ admit the representation:

$$3294172 \cdot a^7 \cdot b^2 \cdot c^2 \cdot (3125a^2 + 108c) \cdot (3125a^2 + 108b).$$

The binomial factors in parentheses originate from truncations on the edges of facets associated with the flats (3) and (8), and (2) and (9), respectively.

The research is supported by grant of the Russian Science Foundation (project 24-21-00217).

References

[1] G.M.Bergman, The logarithmic limit-set of an algebraic variety, *Trans. Amer. Math. Soc.*, **157**(1971), 459–469.

[2] I.A.Antipova, A.K.Tsikh, The discriminant locus of a system of n Laurent polynomials in n variables, *Izvestiya: Mathematics*, **76**(2012), Issue 5, 881–906. DOI: 10.1070/IM2012v076n05ABEH002608

[3] I.M.Gelfand, M.M.Kapranov, A.V.Zelevinsky, Discriminants, Resultants, and Multidimensional Determinants, Birkhauser 1994.

[4] A.Esterov, The discriminant of a system of equations, *Advances in Mathematics*, **245**(2013), 534–572. DOI: 10.1016/j.aim.2013.06.027

[5] E.Mikhalkin, V.Stepanenko, A.Tsikh, Blow-ups for the Horn-Kapranov parametrization of the classical discriminant, In: P. Exner et al. (eds.), Partial Differential Equations, Spectral Theory, and Mathematical Physics. The Ari Laptev Anniversary Volume, EMS Series of Congress Reports, EMS Publishing House, **18**(2021), 315–329.

[6] I.A.Antipova, E.A.Kleshkova, On facets of the Newton polytope for the discriminant of the polynomial system, *Sib. electron. math. Izv.*, **18**(2021), no. 2, 1180-1188. DOI: 10.33048/semi.2021.18.089

[7] E.Cattani, M.A.Cueto, A.Dickenstein, S.Di Rocco, B.Sturmfels, Mixed discriminants, *Math. Z.*, **274**(2013), no. 3, 761–778.

[8] I.A.Antipova, E.A.Kleshkova, Parametrizations of limit positions for the discriminant locus of a trinomial system, *J. Sib. Fed. Univ. Math. Phys.*, **16**(2023), no. 3, 318–329. edn: MNWSFN

[9] A.Dickenstein, E.M.Feichtner, B.Sturmfels, Tropical discriminants, *J. Amer. Math. Soc.*, **20**(2007), 1111–1133.

[10] F.Ardila-Mantilla, The geometry of geometries: matroid theory, old and new, Proc. Int. Cong. Math., Vol. 6, 2022.

[11] D.Mumford, Algebraic Geometry I: Complex Projective Varieties, Springer Science & Business Media, 1995.

[12] SageMath, the Sage Mathematics Software System (Version 9.5), The Sage Developers, 2022, https://www.sagemath.org.

[13] D.Maclagan, B.Sturmfels, Introduction to Tropical Geometry, Graduate Studies in Mathematics, Amer. Math. Soc., Vol. 161, Providence, RI, 2015.

Предельные положения дискриминантного множества системы алгебраических уравнений

Ирина А. Антипова
Семен Ю. Чувашов
Сибирский федеральный университет
Красноярск, Российская Федерация

Аннотация. Рассматривается система n триномиальных алгебраических уравнений от n неизвестных. Показатели мономов в каждом уравнении фиксированы, а коэффициенты — переменные. Дискриминантное множество системы определяется как замыкание множества всех коэффициентов системы, при которых она имеет кратные корни с ненулевыми координатами. Исследуются предельные положения дискриминантной гиперповерхности системы, которые определяются срезками дискриминанта на грани его многогранника Ньютона. Дана характеристика предельных положений в терминах дискриминантных множеств систем меньшей размерности.

Ключевые слова: система алгебраических уравнений, дискриминант, многогранник Ньютона, срезка, дискриминантное множество, параметризация.

EDN: MLITLS
УДК 517

Characterizations of Lindelöfness in Primal Topological Spaces

Abdo Qahis*
Department of Mathematics
College of Arts and Sciences
Najran university
Saudi Arabia

Received 10.09.2025, received in revised form 23.10.2025, accepted 07.12.2025

Abstract. In [2], the author introduced the notion of $\mathcal{P}$-compactness via the primal structure. This paper extends that work by defining and exploring $\mathcal{P}$-Lindelöfness in primal topological spaces, establishing its main properties and providing some results as natural generalizations of covering properties within the primal framework.

Keywords: primal, primal topological space, $\mathcal{P}$-Lindelöfness.

Citation: A. Qahis, Characterizations of Lindelöfness in Primal Topological Spaces, J. Sib. Fed. Univ. Math. Phys., 2026, 19(2), 203–213. EDN: MLITLS.

1. Introduction and preliminaries

The incorporation of algebraic structures such as grills, ideals, and filters has significantly enriched the study of topology, see [6–11]. In this direction, *et al.* [12] introduced the concept of a primal topological space ($\mathcal{P}$TS), which has become a useful framework for extending classical topological concepts. A space $(X, \mathcal{T}))$ equipped with a primal structure $\mathcal{P}$ on X is called a *primal topological space* and is denoted by $(X, \mathcal{T}, \mathcal{P})$ [12]. Several authors have explored fundamental properties such as $\mathcal{P}$-regularity, $\mathcal{P}$-Hausdorffness and $\mathcal{P}$-normality, see [1, 3–5, 13].

In 2024, Ohud Alghamdi introduced the notion of $\mathcal{P}$-compactness in primal spaces as follows: A $\mathcal{P}$TS $(X, \mathcal{T}, \mathcal{P})$ is said to be *$\mathcal{P}$-compact* [2] if every open cover $\mathcal{U}$ of X has a finite subfamily $\mathcal{U}_0 \subseteq \mathcal{U}$ such that

$$\bigcup \mathcal{U}_0 \notin \mathcal{P}.$$

A subset $A \subseteq X$ is a *$\mathcal{P}$-compact subspace of X* if, for every open cover $\mathcal{U}$ of A, there exists a finite subfamily $\mathcal{U}_0 \subseteq \mathcal{U}$ satisfying

$$X \setminus \left(A \setminus \bigcup \mathcal{U}_0\right) \notin \mathcal{P}.$$

Motivated by this extension of compactness, the present paper introduces and investigates the concept of $\mathcal{P}$-Lindelöfness within the framework of primal topological spaces. The primary goal of this study is to is to establish its fundamental properties, explore its relationship with $\mathcal{P}$-compactness, and demonstrate how it provides a broader and more flexible understanding of covering properties within the primal framework.

In this work, We denote by $(X, \mathcal{T}, \mathcal{P})$ a primal topological space and refer to it as ($\mathcal{P}$TS). For any subset $A \subseteq X$, its closure is written as $Cl(A)$. The symbol $\mathbb{N}$ denotes the set of natural numbers, and 2^X denotes the power set of X.

*cahis82@gmail.com https://orcid.org/0000-0003-3174-8516

Definition 1.1 ([12]). *Let X denote a nonempty set. We call a family $\mathcal{P}$ of subsets of X a* primal collection *on X if the following conditions are satisfied.*

(1) $X \notin \mathcal{P}$;

(2) whenever $H \in \mathcal{P}$ and $G \subseteq H$, then $G \in \mathcal{P}$;

(3) for any subsets $H, G \subseteq X$, if $H \cap G \in \mathcal{P}$, then $H \in \mathcal{P}$ or $G \in \mathcal{P}$.

Corollary 1.2 ([12]). *For a nonempty set X, a subfamily $\mathcal{P} \subseteq 2^X$ constitutes* primal collection *on X is characterized by the following:*

(1) $X \notin \mathcal{P}$;

(2) $H \notin \mathcal{P}$ and $H \subseteq G$ imply $G \notin \mathcal{P}$;

(3) $H, G \notin \mathcal{P}$ imply $H \cap G \notin \mathcal{P}$.

Definition 1.3 ([2]). *Let $(X, \mathcal{T}, \mathcal{P})$ be a $\mathcal{P}TS$. For any subset $A \subseteq X$, we define:*

*(1) The set A is called $\mathcal{P}_g$-*closed *if, for every open set $U \in \mathcal{T}$ such that $(X \setminus A) \cup U = X \setminus (A \setminus U)$, the condition $X \setminus (A \setminus U) \notin \mathcal{P}$ implies that $\mathrm{Cl}(A) \subseteq U$.*

*(2) The set A is called g-*closed *whenever $\mathrm{Cl}(A) \subseteq U$ for every open set U of X with $A \subseteq U$.*

Lemma 1.4 ([2]). *Let $f : (X, \mathcal{T}) \to (Y, \sigma)$ be a bijection. Then the following properties are satisfied:*

(1) If $\mathcal{P}$ a primal collection on X, then the family $f(\mathcal{P}) = \{ f(V) : V \in \mathcal{P} \}$ forms a primal collection on Y.

(2) If $\mathcal{K}$ represents a primal collection on Y, then the family $f^{-1}(\mathcal{K}) = \{ f^{-1}(B) : B \in \mathcal{K} \}$ constitutes a primal collection on X.

Lemma 1.5 ([2]). *Let $(X, \mathcal{T}, \mathcal{P})$ be a $\mathcal{P}TS$. Consider a function $f : (X, \mathcal{T}, \mathcal{P}) \to (Y, \sigma)$ and define $\mathcal{K}_{\mathcal{P}} = \{ B \subseteq Y : f^{-1}(B) \in \mathcal{P} \}$. Then the following statements hold:*

(1) The collection $\mathcal{K}_{\mathcal{P}}$ constitutes a primal collection on Y;

(2) When f is one-to-one, it follows that $\mathcal{P} \subseteq f^{-1}(\mathcal{K}_{\mathcal{P}})$;

(3) When f is onto, we have $\mathcal{K}_{\mathcal{P}} \subseteq f(\mathcal{P})$;

(4) When f is a bijection, then $\mathcal{K}_{\mathcal{P}} = f(\mathcal{P})$.

2. On $\mathcal{P}$-Lindelöfness spaces

Definition 2.1. *Let $(X, \mathcal{T}, \mathcal{P})$ be a $\mathcal{P}TS$. The space $(X, \mathcal{T}, \mathcal{P})$ is said to be a* primal Lindelöf space *(or $\mathcal{P}$-Lindelöf space) if for each open cover $\{V_\alpha : \alpha \in \Lambda\}$ of X, there exists a countable set $\Lambda_0 \subseteq \Lambda$ satisfying $\bigcup_{\alpha \in \Lambda_0} V_\alpha \notin \mathcal{P}$. Furthermore, for a subset $A \subseteq X$, we say that A is a $\mathcal{P}$-Lindelöf subspace of X if, whenever $\{V_\alpha : \alpha \in \Lambda\}$ is an open cover of A, there exists a countable set $\Lambda_0 \subseteq \Lambda$ such that $X \setminus \left[A \setminus \bigcup_{\alpha \in \Lambda_0} V_\alpha \right] \notin \mathcal{P}$.*

Theorem 2.2. *Let $(X, \mathcal{T}, \mathcal{P})$ be a $\mathcal{P}TS$ and let $A \subseteq X$. If A is Lindelöf as a subspace of X, then A is $\mathcal{P}$-Lindelöf as a subspace of X.*

Proof. Let $\{V_\alpha : \alpha \in \Lambda\}$ be an open cover of A. Since A is a Lindelöf subspace of X, there exists a countable subfamily $\{V_\alpha : \alpha \in \Lambda_0\}$, with $\Lambda_0 \subseteq \Lambda$, such that

$$A \subseteq \bigcup_{\alpha\in\Lambda_0} V_\alpha.$$

It follows that

$$X \setminus \left[A \setminus \bigcup_{\alpha\in\Lambda_0} V_\alpha\right] = X \notin \mathcal{P}.$$

Hence, A is a $\mathcal{P}$-Lindelöf subspace of X. □

Remark 2.3. *Let $(X, \tau, \mathcal{P})$ be a $\mathcal{P}TS$. If $\mathcal{P} = 2^X \setminus \{X\}$, then one can easily verify that the concept of a Lindelöf space coincides with that of a $\mathcal{P}$-Lindelöf space.*

The converse of Theorem 2.2 fails in general, which can be seen from the next example

Example 2.4. *Consider $(\mathbb{R}, \mathcal{T}, \mathcal{P})$, where it represents a $\mathcal{P}TS$. determined in the following:*

$$\mathcal{T} = \{\emptyset\} \cup \{V \subseteq \mathbb{R} : 0 \in V\}, \quad \mathcal{P} = \{V \subseteq \mathbb{R} : 0 \notin V\}.$$

Let $\{V_\alpha : \alpha \in \Lambda\}$ be any open cover of the interval $[0, 1]$ such that $V_\alpha \neq \emptyset$ for every $\alpha \in \Lambda$. Consider a countable subfamily $\Lambda_0 = \{V_i : i \in \mathbb{N}\} \subseteq \{V_\alpha : \alpha \in \Lambda\}$. Then,

$$0 \in \mathbb{R} \setminus \left([0, 1] \setminus \bigcup_{i=1}^{\infty} V_i\right),$$

which implies that

$$\mathbb{R} \setminus \left([0, 1] \setminus \bigcup_{i=1}^{\infty} V_i\right) \notin \mathcal{P}.$$

Hence, $[0, 1]$ is a $\mathcal{P}$-Lindelöf subspace of X. Note that $[0, 1]$ is not Lindelöf. In fact, the family $\mathcal{U} = \{\{x, 0\} : x \in [0, 1]\}$ is an open cover of $[0, 1]$, but it admits no countable subcover.

The following example demonstrates that a $\mathcal{P}$-Lindelöf space is not necessarily $\mathcal{P}$-compact.

Example 2.5. *Consider the primal topological space $(\mathbb{R}, \mathcal{U}, \mathcal{P})$ defined as follows:*

$$\mathcal{U} = \{\, A \subseteq \mathbb{R} \mid A = \varnothing \text{ or for every } y \in A, \text{ there exist real numbers } p < q \text{ such that } y \in (p, q) \subseteq A \,\}.$$

and $\mathcal{P} = 2^{\mathbb{R}} \setminus \{\mathbb{R}\}$. Now let $\{V_\alpha\}_{\alpha\in\Lambda}$ be a any open cover of $\mathbb{R}$. Then there exits countable $\Lambda_0 \subseteq \Lambda$ such $\bigcup_{\alpha\in\Lambda_0} V_\alpha = \mathbb{R} \notin \mathcal{P}$.

Now consider the family Let $\mathcal{V} = \{\, W_n = (-n, n) \,:\, n \in \mathbb{N} \,\}$, where $\mathcal{V} \subseteq \mathcal{U}$. Clearly,

$$\bigcup_{n\in\mathbb{N}} W_n = \mathbb{R} \notin \mathcal{P}.$$

Take the finite subfamily $\mathcal{V}_0 = \{W_i = (-i, i) : i \leqslant m,\ i, m \in \mathbb{N}\} \subseteq \mathcal{V}$. Then $\bigcup_{i\leqslant m} W_i = (-m, m) \in \mathcal{P}$, it follows that $(\mathbb{R}, \mathcal{U}, \mathcal{P})$ fails to be $\mathcal{P}$-compact.

Theorem 2.6. *Every closed subspace of a $\mathcal{P}$-Lindelöf space is also $\mathcal{P}$-Lindelöf.*

Proof. Let $(X, \mathcal{T}, \mathcal{P})$ be a $\mathcal{P}$-Lindelöf space and let $F \subseteq X$ be a closed subspace. Suppose that $\mathcal{U} = \{V_\alpha : \alpha \in \Lambda\}$ is an open cover of F. Then the collection $\mathcal{U} \cup \{X \setminus F\}$ forms an open cover of X. Since X is $\mathcal{P}$-Lindelöf , there exists a countable subfamily

$$\Lambda_0 = \{V_i : i \in \mathbb{N}\} \subseteq \{X \setminus F\} \cup \{V_\alpha : \alpha \in \Lambda\}$$

such that

$$\bigcup_{i \in \mathbb{N}} V_i \notin \mathcal{P}.$$

Consequently, we obtain

$$X \setminus \Big[F \setminus \bigcup_{i \in \mathbb{N}} V_i\Big] \notin \mathcal{P},$$

which shows that F is itself a $\mathcal{P}$-Lindelöf subspace of X. □

A subspace of X that is not closed may fail to be $\mathcal{P}$-Lindelöfness, as this example demonstrates.

Example 2.7. *Consider the $\mathcal{P}TS$ $(\mathbb{R}, \mathcal{T}, \mathcal{P})$ defined as follows:*

$$\mathcal{T} = \big\{ U \subseteq \mathbb{R} : \sqrt{2} \notin U \text{ or } \mathbb{R} \setminus U \text{ is finite} \big\},$$

and

$$\mathcal{P} = \big\{ U \subseteq \mathbb{R} \mid \mathbb{R} \setminus U \text{ is infinite} \big\}, \quad \text{see Example 2,3 [2].}$$

Let $\mathcal{U} = \{V_\alpha : \alpha \in \Lambda\}$ be an open cover of $\mathbb{R}$. Since $\sqrt{2} \in V_\beta$ for some $\beta \in \Lambda$, it follows that $\mathbb{R} \setminus V_\beta$ is finite. Define $\mathcal{U}_0 = \{V_\beta\} \subseteq \mathcal{U}$. Because $V_\beta \notin \mathcal{P}$, we conclude that $\mathbb{R}$ is a $\mathcal{P}$ -Lindelöf space.

Now consider the subspace $X = \mathbb{R} \setminus \{\sqrt{2}\}$. We claim that X is not $\mathcal{P}$-Lindelöf. In fact, let

$$\mathcal{V} = \{\{x\} : x \in X\}$$

be the open cover of X consisting of singletons. For every countable subfamily $\{\{x_i\} : i \in \mathbb{N}\}$, we have

$$\bigcup_{i \in \mathbb{N}} \{x_i\} \in \mathcal{P}.$$

Hence X is not $\mathcal{P}$-Lindelöf.

Observe also that $X = \mathbb{R} \setminus \{\sqrt{2}\}$ forms a discrete subspace of $\mathbb{R}$, but it is not a closed subset.

A subset W of a topological space (X, τ) is said to be *ω-open* [14] if and only if there exists an open set $U \in \tau$ such that $U \setminus W$ is countable. The collection of all ω-open sets forms a topology on X that is finer than τ.

The following theorem establishes a relationship between a cover consisting of ω-open sets and the concept of $\mathcal{P}$-Lindelöf .

Theorem 2.8. *Let $(X, \mathcal{T}, \mathcal{P})$ be a $\mathcal{P}TS$ and let $A \subseteq X$. Then the following statements are equivalent.*

(1) A is a $\mathcal{P}$-Lindelöf subspace of X;

(2) For every ω-open cover $\mathcal{U}$ of A, there exists a countable subfamily $\mathcal{U}_0 \subseteq \mathcal{U}$ such that $X \setminus (A \setminus \bigcup \mathcal{U}_0) \notin \mathcal{P}$.

Proof. (1) $\Rightarrow$ (2): Suppose that A is a $\mathcal{P}$-Lindelöf subspace of X, and let $\mathcal{U} = \{W_\alpha : \alpha \in \Lambda\}$ be an arbitrary ω-open cover of A.

For each $x \in A$, there exists some $\alpha(x) \in \Lambda$ such that $x \in W_{\alpha(x)}$. Since $W_{\alpha(x)}$ is ω-open, there exists an open set $V_{\alpha(x)}$ such that

$$x \in V_{\alpha(x)} \quad \text{and} \quad V_{\alpha(x)} \setminus W_{\alpha(x)} \text{ is countable.}$$

Thus, the family $\{V_{\alpha(x)} : x \in A\}$ is an open cover of A. Because A is $\mathcal{P}$-Lindelöf, there exists a countable subfamily $\{V_{\alpha(x_i)} : i \in \mathbb{N}\}$ such that

$$X \setminus \Big[A \setminus \Big(\bigcup_{i\in\mathbb{N}} V_{\alpha(x_i)}\Big)\Big] \notin \mathcal{P}.$$

Now, observe that

$$X \setminus \Big[A \setminus \Big(\bigcup_{i\in\mathbb{N}} V_{\alpha(x_i)}\Big)\Big] \subseteq X \setminus \Big[A \setminus \bigcup_{i\in\mathbb{N}} \Big((V_{\alpha(x_i)} \setminus W_{\alpha(x_i)}) \bigcup W_{\alpha(x_i)}\Big)\Big].$$

Equivalently,

$$X \setminus \Big[A \setminus \Big(\bigcup_{i\in\mathbb{N}} V_{\alpha(x_i)}\Big)\Big] \subseteq X \setminus \Big[A \setminus \Big(\bigcup_{i\in\mathbb{N}} (V_{\alpha(x_i)} \setminus W_{\alpha(x_i)} \cap A) \bigcup (\bigcup_{i\in\mathbb{N}} W_{\alpha(x_i)})\Big)\Big]$$

For each $i \in \mathbb{N}$, the set $(V_{\alpha(x_i)} \setminus W_{\alpha(x_i)}) \cap A$ is countable. Hence, there exists a countable subset $\Lambda_{\alpha(x_i)} \subseteq \Lambda$ such that

$$(V_{\alpha(x_i)} \setminus W_{\alpha(x_i)}) \cap A \ \subseteq \ \bigcup\{W_\alpha : \alpha \in \Lambda_{\alpha(x_i)}\}.$$

Therefore,

$$\begin{aligned} A\setminus\Big[\Big(\bigcup_{i\in\mathbb{N}} \Big(\bigcup\{W_\alpha : \alpha \in \Lambda_{\alpha(x_i)}\}\Big)\Big) \bigcup \Big(\bigcup_{i\in\mathbb{N}} W_{\alpha(x_i)}\Big)\Big] \\ \subseteq A \setminus \Big[\Big(\bigcup_{i\in\mathbb{N}} ((V_{\alpha(x_i)} \setminus W_{\alpha(x_i)}) \cap A)\Big) \bigcup \Big(\bigcup_{i\in\mathbb{N}} W_{\alpha(x_i)}\Big)\Big] \\ \subseteq A \setminus \Big(\bigcup_{i\in\mathbb{N}} V_{\alpha(x_i)}\Big) \end{aligned}$$

This yields

$$X \setminus \Big[A \setminus \Big(\bigcup_{i\in\mathbb{N}} V_{\alpha(x_i)}\Big)\Big] \subseteq X \setminus \Big[A \setminus \Big[\Big(\bigcup_{i\in\mathbb{N}} \Big(\bigcup\{W_\alpha : \alpha \in \Lambda_{\alpha(x_i)}\}\Big)\Big) \bigcup \Big(\bigcup_{i\in\mathbb{N}} W_{\alpha(x_i)}\Big)\Big]\Big].$$

Consequently

$$X \setminus \Big[A \setminus \Big[\Big(\bigcup_{i\in\mathbb{N}} \Big(\bigcup\{W_\alpha : \alpha \in \Lambda_{\alpha(x_i)}\}\Big)\Big) \bigcup \Big(\bigcup_{i\in\mathbb{N}} W_{\alpha(x_i)}\Big)\Big]\Big] \notin \mathcal{P}.$$

(2) $\Rightarrow$ (1): Since every open set is also ω-open, the conclusion follows immediately. □

Corollary 2.9. *A $\mathcal{P}TS$ $(X, \tau, \mathcal{P})$ is said to be $\mathcal{P}$-Lindelöf precisely when, for any ω-open covering $\mathcal{U}$ of X, there exists a countable subcollection $\mathcal{U}_0 \subseteq \mathcal{U}$ satisfying $\bigcup\mathcal{U}_0 \notin \mathcal{P}$.*

Theorem 2.10. *Let $(X, \mathcal{T}, \mathcal{P})$ be a $\mathcal{P}TS$ and let $A \subseteq X$. The following statements are equivalent.*

(1) A is a $\mathcal{P}$-Lindelöf subspace of X;

(2) For every family $\{F_\alpha\}_{\alpha\in\Lambda}$ of closed subsets of X satisfying $A\bigcap\big(\bigcap_{\alpha\in\Lambda}F_\alpha\big)=\varnothing$, there exists a countable subfamily $\{F_\alpha\}_{\alpha\in\Lambda_0}$, with $\Lambda_0\subseteq\Lambda$, such that $(X\setminus A)\bigcup\big[\bigcup_{\alpha\in\Lambda_0}(X\setminus F_\alpha)\big]\notin\mathcal{P}$.

Proof. (1) $\Rightarrow$ (2): Let $\{F_\alpha:\alpha\in\Lambda\}$ be a family of closed subsets of X such that $A\bigcap\big(\bigcap_{\alpha\in\Lambda}F_\alpha\big)=\emptyset$. Then we obtain

$$A\subseteq X\setminus\bigcap_{\alpha\in\Lambda}F_\alpha=\bigcup_{\alpha\in\Lambda}(X\setminus F_\alpha).$$

Since each $X\setminus F_\alpha$ is open in X and A is a $\mathcal{P}$-Lindelöf subspace of X, there exists a countable subset $\Lambda_0\subseteq\Lambda$ such that

$$X\setminus\Big[A\setminus\Big(\bigcup_{\alpha\in\Lambda_0}(X\setminus F_\alpha)\Big)\Big]\notin\mathcal{P}.$$

Now we observe that

$$\begin{aligned}(X\setminus A)\bigcup\Big(\bigcup_{\alpha\in\Lambda_0}(X\setminus F_\alpha)\Big)&=X\bigcap\Big[(X\setminus A)\bigcup\Big(\bigcup_{\alpha\in\Lambda_0}(X\setminus F_\alpha)\Big)\Big]\\&=X\setminus\Big[A\bigcap\Big(\bigcap_{\alpha\in\Lambda_0}F_\alpha\Big)\Big]\\&=X\setminus\Big[A\setminus\bigcup_{\alpha\in\Lambda_0}(X\setminus F_\alpha)\Big]\notin\mathcal{P}.\end{aligned}$$

(2) $\Rightarrow$ (1): Let $\{V_\alpha:\alpha\in\Lambda\}$ be an open cover of A. Then

$$A\bigcap\Big(X\setminus\bigcup_{\alpha\in\Lambda}V_\alpha\Big)=A\bigcap\Big(\bigcap_{\alpha\in\Lambda}(X\setminus V_\alpha)\Big)=\emptyset.$$

Since $X\setminus V_\alpha$ is closed for each $\alpha\in\Lambda$, condition (2) ensures that there exists a countable subset $\Lambda_0\subseteq\Lambda$ such that

$$(X\setminus A)\bigcup\Big(\bigcup_{\alpha\in\Lambda_0}V_\alpha\Big)\notin\mathcal{P}.$$

Equivalently,

$$(X\setminus A)\bigcup\Big(\bigcup_{\alpha\in\Lambda_0}V_\alpha\Big)=X\setminus\Big[A\setminus\bigcup_{\alpha\in\Lambda_0}V_\alpha\Big]\notin\mathcal{P}.$$

Hence, A is a $\mathcal{P}$-Lindelöf subspace of X. □

In particular, taking $A=X$ in the above Theorem 2.10, yields the following corollary.

Corollary 2.11. *Let $(X,\mathcal{T},\mathcal{P})$ be a $\mathcal{P}TS$, and let $\{F_\alpha\}_{\alpha\in\Lambda}$ be a family of closed subsets of X such that $\bigcap_{\alpha\in\Lambda}F_\alpha=\varnothing$. Then X is a $\mathcal{P}$-Lindelöf space if and only if there is a countable subfamily $\{F_\alpha\}_{\alpha\in\Lambda_0}$ with $\Lambda_0\subseteq\Lambda$ such that*

$$\bigcup_{\alpha\in\Lambda_0}(X\setminus F_\alpha)\notin\mathcal{P}.$$

Theorem 2.12. *Let $(X,\mathcal{T},\mathcal{P})$ be a $\mathcal{P}TS$. If G and H are $\mathcal{P}$-Lindelöf subspaces of X, then their union $G\cup H$ is also a $\mathcal{P}$-Lindelöf subspace of X.*

Proof. Consider an open cover $\{W_\alpha:\alpha\in\Lambda\}$ of $G\cup H$. Since G is a $\mathcal{P}$-Lindelöf subspace of X, there exists a countable subfamily $\Lambda_0\subseteq\Lambda$ such that

$$X\setminus\Big(G\setminus\bigcup_{\alpha\in\Lambda_0}W_\alpha\Big)\notin\mathcal{P}.$$

Similarly, as H is also $\mathcal{P}$-Lindelöf, we can choose a countable subfamily $\Lambda_1 \subseteq \Lambda$ satisfying

$$X \setminus \Big(H \setminus \bigcup_{\alpha \in \Lambda_1} W_\alpha \Big) \notin \mathcal{P}.$$

Now, consider $\Lambda_0 \cup \Lambda_1$, which is still countable. For this family we have

$$X \setminus \Big[(G \cup H) \setminus \bigcup_{\alpha \in \Lambda_0 \cup \Lambda_1} W_\alpha \Big] \notin \mathcal{P}.$$

Thus, the union $G \cup H$ is covered by a countable subcollection of $\{W_\alpha : \alpha \in \Lambda\}$ in the sense of $\mathcal{P}$-Lindelöf. Therefore, $G \cup H$ is a $\mathcal{P}$-Lindelöf subspace of X. □

Theorem 2.13. *Let $(X, \mathcal{T}, \mathcal{P})$ be a $\mathcal{P}TS$ and let $G, H \subseteq X$. If G is a $\mathcal{P}$-Lindelöf subspace of X and H is closed in X, then the intersection $G \cap H$ is also a $\mathcal{P}$-Lindelöf subspace of X.*

Proof. Consider an open cover $\{W_\alpha : \alpha \in \Lambda\}$ of $G \cap H$. Define

$$\mathcal{U} = \{W_\alpha : \alpha \in \Lambda\} \cup \{X \setminus H\}.$$

Clearly, $\mathcal{U}$ forms an open cover of G. Since G is $\mathcal{P}$-Lindelöf, there is a countable subfamily $\{W_\alpha : \alpha \in \Lambda_0\}$ such that

$$X \setminus \Big[G \setminus \bigcup_{\alpha \in \Lambda_0} W_\alpha \Big] \notin \mathcal{P}.$$

Notice that

$$X \setminus \Big[G \setminus \bigcup_{\alpha \in \Lambda_0} W_\alpha \Big] \subseteq X \setminus \Big[(G \cap H) \setminus \Big(\bigcup_{\alpha \in \Lambda_0} W_\alpha \Big) \Big].$$

Hence,

$$X \setminus \Big[(G \cap H) \setminus \Big(\bigcup_{\alpha \in \Lambda_0} W_\alpha \Big) \Big] \notin \mathcal{P}.$$

This shows that $G \cap H$ is a $\mathcal{P}$-Lindelöf subspace of X. □

Theorem 2.14. *Let $(X, \mathcal{T}, \mathcal{P})$ be a $\mathcal{P}TS$, and let $, G, H \subseteq X$ satisfy $G \subseteq H \subseteq \mathrm{Cl}(G)$. Then the following statements are true:*

(1) Suppose $G \subseteq X$ is $\mathcal{P}$-Lindelö and $\mathcal{P}_g$-closed. Then the subspace $H \subseteq X$ is Lindelöf.

(1) Suppose $H \subseteq X$ is $\mathcal{P}$-Lindelöf and $G \subseteq X$ is g-closed. Then G is a $\mathcal{P}$-Lindelöf subspace of X.

Proof. (1) Assume that G is both a $\mathcal{P}$-Lindelöf subspace of X and $\mathcal{P}_g$-closed. Let $\{W_\alpha : \alpha \in \Lambda\}$ be an arbitrary open cover of H. Clearly, $\{W_\alpha : \alpha \in \Lambda\}$ also serves as an open cover of G.

Since G is $\mathcal{P}$-Lindelöf, there exists a countable index set $\Lambda_0 \subseteq \Lambda$ such that

$$X \setminus \Big(G \setminus \bigcup_{\alpha \in \Lambda_0} W_\alpha \Big) \notin \mathcal{P}.$$

Because G is $\mathcal{P}_g$-closed, this condition implies

$$Cl(G) \subseteq \bigcup_{\alpha \in \Lambda_0} W_\alpha.$$

Hence,

$$H \subseteq \bigcup_{\alpha \in \Lambda_0} W_\alpha,$$

which shows that H is $\mathcal{P}$-Lindelöf subspace of X.

(2) Now assume that H is a $\mathcal{P}$-Lindelöf subspace of X, and suppose G is g-closed. Let $\{W_\alpha : \alpha \in \Lambda\}$ be an open cover of G. Since G is g-closed, we have

$$Cl(G) \subseteq \bigcup_{\alpha\in\Lambda} W_\alpha,$$

and because $H \subseteq Cl(G)$, it follows that

$$H \subseteq \bigcup_{\alpha\in\Lambda} W_\alpha.$$

As H is a $\mathcal{P}$-Lindelöf, there exists a countable subfamily indexed by $\Lambda_0 \subseteq \Lambda$ such that

$$X \setminus \Big(H \setminus \bigcup_{\alpha\in\Lambda_0} W_\alpha\Big) \notin \mathcal{P}.$$

Notice that

$$X \setminus \Big(H \setminus \bigcup_{\alpha\in\Lambda_0} W_\alpha\Big) \subseteq X \setminus \Big(G \setminus \bigcup_{\alpha\in\Lambda_0} W_\alpha\Big).$$

Therefore,

$$X \setminus \Big(G \setminus \bigcup_{\alpha\in\Lambda_0} W_\alpha\Big) \notin \mathcal{P}.$$

This proves that G is $\mathcal{P}$-Lindelöf in X. □

Corollary 2.15. *Let $(X, \mathcal{T}, \mathcal{P})$ be a $\mathcal{P}$TS. For subsets $G, H \subseteq X$ with $G \subseteq H \subseteq \mathrm{Cl}(G)$, if G is $\mathcal{P}_g$-closed, then G is $\mathcal{P}$-Lindelöf subspace of X if and only if H is $\mathcal{P}$-Lindelöf subspace of X.*

Theorem 2.16. *Let $(X, \mathcal{T}, \mathcal{P}_1)$ and $(X, \mathcal{T}, \mathcal{P}_2)$ be $\mathcal{P}$TSs, and let $A \subseteq X$. Then A is both a $\mathcal{P}_1$-Lindelöf subspace of X and a $\mathcal{P}_2$-Lindelöf subspace of X if and only if A is a $(\mathcal{P}_1 \cup \mathcal{P}_2)$-Lindelöf subspace of X.*

Proof. $\Rightarrow$ Suppose that A is both a $\mathcal{P}_1$-Lindelöf subspace and a $\mathcal{P}_2$-Lindelöf subspace of X. Let $\mathcal{U} = \{U_\alpha : \alpha \in \Lambda\}$ be an arbitrary open cover of A in X. Since A is $\mathcal{P}_1$-Lindelöf, there exists a countable subfamily $\{U_\alpha : \alpha \in \Lambda_1\} \subseteq \mathcal{U}$ such that

$$X \setminus \Big[A \setminus \bigcup_{\alpha\in\Lambda_1} U_\alpha\Big] \notin \mathcal{P}_1.$$

Similarly, since A is $\mathcal{P}_2$-Lindelöf, there exists a countable subfamily $\{U_\alpha : \alpha \in \Lambda_2\} \subseteq \mathcal{U}$ such that

$$X \setminus \Big[A \setminus \bigcup_{\alpha\in\Lambda_2} U_\alpha\Big] \notin \mathcal{P}_2.$$

Let $\Lambda_0 = \Lambda_1 \cup \Lambda_2$. Then Λ_0 is countable, and we have

$$X \setminus \Big[A \setminus \bigcup_{\alpha\in\Lambda_0} U_\alpha\Big] \notin \mathcal{P}_1 \cup \mathcal{P}_2.$$

Hence, A is a $(\mathcal{P}_1 \cup \mathcal{P}_2)$-Lindelöf subspace of X.

$\Leftarrow$ Conversely, assume that A is a $(\mathcal{P}_1 \cup \mathcal{P}_2)$-Lindelöf subspace of X. Let $\mathcal{U} = \{U_\alpha : \alpha \in \Lambda\}$ be an arbitrary open cover of A in X. Then there exists a countable subfamily $\{U_\alpha : \alpha \in \Lambda_0\} \subseteq \mathcal{U}$ such that

$$X \setminus \Big[A \setminus \bigcup_{\alpha\in\Lambda_0} U_\alpha\Big] \notin \mathcal{P}_1 \cup \mathcal{P}_2.$$

This means that

$$X \setminus \Big[A \setminus \bigcup_{\alpha\in\Lambda_0} U_\alpha\Big] \notin \mathcal{P}_1 \quad \text{and} \quad X \setminus \Big[A \setminus \Big(\bigcup_{\alpha\in\Lambda_0} U_\alpha\Big)\Big] \notin \mathcal{P}_2.$$

Hence, A is both a $\mathcal{P}_1$-Lindelöf and a $\mathcal{P}_2$-Lindelöf subspace of X. □

Theorem 2.17. *Let $f : (X, \mathcal{T}, \mathcal{P}) \to (Y, \sigma, f(\mathcal{P}))$ be a continuous surjection. If $A \subseteq X$ is $\mathcal{P}$-Lindelöf, then its image $f(A) \subseteq Y$ is also $\mathcal{P}$-Lindelöf.*

Proof. Let $\{V_\alpha : \alpha \in \Lambda\}$ be an open cover of $f(A)$. Since f is continuous, the family $\{f^{-1}(V_\alpha) : \alpha \in \Lambda\}$ forms an open cover of $f^{-1}(f(A))$. As $A \subseteq f^{-1}(f(A))$, it follows that $\{f^{-1}(V_\alpha) : \alpha \in \Lambda\}$ is also an open cover of A.

Because A is $\mathcal{P}$-Lindelöf, there exists a countable subfamily indexed by $\Lambda_0 \subseteq \Lambda$ such that

$$X \setminus \Big[A \setminus \bigcup_{\alpha\in\Lambda_0} f^{-1}(V_\alpha)\Big] \notin \mathcal{P}.$$

Applying f, we obtain

$$f(X) \setminus \Big[f(A) \setminus f\Big(f^{-1}\Big(\bigcup_{\alpha\in\Lambda_0} V_\alpha\Big)\Big)\Big] \notin f(\mathcal{P}).$$

Since f is surjective, this reduces to

$$Y \setminus \Big[f(A) \setminus \bigcup_{\alpha\in\Lambda_0} V_\alpha\Big] \notin f(\mathcal{P}).$$

Thus $f(A)$ is an $\mathcal{P}$-Lindelöf subspace of Y. □

Corollary 2.18. *Let $f : (X, \mathcal{T}, \mathcal{P}) \to (Y, \sigma, f(\mathcal{P}))$ be a continuous surjective function. If $(X, \mathcal{T}, \mathcal{P})$ is a $\mathcal{P}$-Lindelöf space, then $(Y, \sigma, f(\mathcal{P}))$ is also a $\mathcal{P}$-Lindelöf space.*

Theorem 2.19. *Let $f : (X, \mathcal{T}, \mathcal{P}) \to (Y, \sigma, f(\mathcal{P}))$ be an injective and continuous function. If A is a $\mathcal{P}$-Lindelöf subspace of X, then $f(A)$ is a $\mathcal{P}$-Lindelöf subspace of Y.*

Proof. Let $\{V_\alpha : \alpha \in \Lambda\}$ be an open cover of $f(A)$ in Y. For each $x \in A$, there exists $\alpha(x) \in \Lambda$ such that $f(x) \in V_{\alpha(x)}$. Since f is continuous, for every $x \in A$ there is an open set $U_x \in \mathcal{T}$ with $x \in U_x$ such that

$$f(U_x) \subseteq V_{\alpha(x)}.$$

Hence, the family $\{U_x : x \in A\}$ forms an open cover of A in X.

Because A is $\mathcal{P}$-Lindelöf, there exists a countable subset $A_0 \subseteq A$ such that

$$X \setminus \Big[A \setminus \bigcup_{x\in A_0} U_x\Big] \notin \mathcal{P}.$$

Since $U_x \subseteq f^{-1}(V_{\alpha(x)})$ for each $x \in A$, we have

$$A \setminus \bigcup_{x\in A_0} U_x \supseteq A \setminus \bigcup_{x\in A_0} f^{-1}(V_{\alpha(x)}).$$

It follows that

$$X \setminus \Big[A \setminus \bigcup_{x\in A_0} U_x\Big] \subseteq X \setminus \Big[A \setminus \bigcup_{x\in A_0} f^{-1}(V_{\alpha(x)})\Big].$$

Hence,

$$X \setminus \Big[A \setminus \bigcup_{x\in A_0} f^{-1}(V_{\alpha(x)})\Big] \notin \mathcal{P}.$$

Applying f, we obtain

$$f(X) \setminus \Big[f(A) \setminus f\big(f^{-1}(\textstyle\bigcup_{x\in A_0} V_{\alpha(x)})\big)\Big] \notin f(\mathcal{P}).$$

Since f is injective, it follows that

$$f\big(f^{-1}(\textstyle\bigcup_{x\in A_0} V_{\alpha(x)})\big) = \Big(\bigcup_{x\in A_0} V_{\alpha(x)}\Big) \bigcap f(X).$$

It follows that,

$$f(X) \setminus \Big[f(A) \setminus \textstyle\bigcup_{x\in A_0} V_{\alpha(x)}\Big] \notin f(\mathcal{P}).$$

and hence

$$Y \setminus \Big[f(A) \setminus \textstyle\bigcup_{x\in A_0} V_{\alpha(x)}\Big] \notin f(\mathcal{P}).$$

This shows that $f(A)$ is a $\mathcal{P}$-Lindelöf subspace of Y. □

Theorem 2.20. *Let $f : (X, \mathcal{T}, \mathcal{P}) \to (Y, \sigma, \mathcal{K}_{\mathcal{P}})$ be a bijective continuous function. Then, for any 'P-Lindelöf subspace A of X, the set $f(A)$ is $\mathcal{K}_{\mathcal{P}}$-Lindelöf in Y.*

Proof. The proof follows directly from Lemma 1.4, Lemma 1.5, and the corresponding Theorem 2.19. □

Corollary 2.21. *Let $f : (X, \mathcal{T}, \mathcal{P}) \to (Y, \sigma, \mathcal{K}_{\mathcal{P}})$ be a bijective continuous function. If $(X, \mathcal{T}, \mathcal{P})$ is $\mathcal{P}$-Lindelöf, then $(Y, \sigma, \mathcal{K}_{\mathcal{P}})$ is $\mathcal{K}_{\mathcal{P}}$-Lindelöf.*

Conclusion

This study extends the classical notion ofLindelöfness to the framework of primal topological spaces by introducing and analyzing the concept of $\mathcal{P}$-Lindelöf . We established main properties distinguishing it from the classical case, showing that every Lindelöf space is $\mathcal{P}$-Lindelöf f, though not conversely, and that the property is preserved under closed subspaces and continuous mappings.

Additionally, $\mathcal{P}$-Lindelöfness was characterized using ω-open covers, linking primal and classical topological refinements. These findings demonstrate that $\mathcal{P}$Lindelöfness generalizes Lindelöfness while maintaining structural coherence within the primal framework, providing a foundation for future studies on related properties such as $\mathcal{P}$-paracompactness and $\mathcal{P}$-paraLLindelöfness

References

[1] O.Alghamdi, A.Al-Omari, M.H.Alqahtani, Novel operators in the frame of primal topological spaces, *AIMS Mathematics*, **9**(2024), 25792–25808. DOI: 10.3934/math.20241260.

[2] O.Alghamdi, On the compactness via primal topological spaces, *AIMS Mathematics*, **9**(2024), 32124–32137. DOI: 10.3934/math.20241542.

[3] A.Al-Omari, O.Alghamdi, Regularity and normality on primal spaces, *AIMS Mathematics*, **9**(2024), 7662–7672. DOI: 10.3934/math.2024372.

[4] A.Al-Omari, M.H.Alqahtani, Primal structure with closure operators and their applications, *Mathematics*, **11**(2023), 4946.

[5] H.Al-Saadi, H.Al-Malki, Categories of open sets in generalized primal topological spaces, *Mathematics*, **12**(2024), 207.

[6] G.Choquet, Sur les notions de filtre et de grille, *Comptes Rendus de l'Académie des Sciences, Paris*, **224**(1947), 171–173.

[7] D.Jankovic, T.R.Hamlet, New topologies from old via ideals, *American Mathematical Monthly*, **97**(1990), 295–310. DOI: 10.2307/2324512.

[8] K.Kuratowski, *Topology*. Elsevier, Netherlands, 1966. DOI: 10.1016/C2013-0-11022-7.

[9] S.Modak, Grill-filter space, *Journal of the Indian Mathematical Society*, **80**(2013), 313–320.

[10] B.Roy, M.N.Mukherjee, On a type of compactness via grills, *Matematicki Vesnik*, **59**(2007), 113–120.

[11] R.Vaidyanathaswamy, The localization theory in set-topology, *Proceedings of the Indian Academy of Sciences*, **20**(1944), 51–61.

[12] S.Acharjee, M.Özköc, F.Y.Issaka, Primal topological spaces. DOI: 10.48550/arXiv.2209.12676.

[13] A.Al-Omari, S.Acharjee, M.Özköc, A new operator of primal topological spaces. DOI: 10.48550/arXiv.2210.17278.

[14] H.Z.Hdeib, ω-closed mappings, *Revista Colombiana de Matematicas*, **16**(1982), 65–78.

Характеристики линделефности в первичных топологических пространствах

Абдо Кахис
Математический факультет
Колледж искусств и наук
Университет Наджрана
Саудовская Аравия

Аннотация. В работе [2] автор ввел понятие $\mathcal{P}$-компактности через первичную структуру. Данная статья расширяет эту работу, определяя и исследуя $\mathcal{P}$-линделевскую компактность в первичных топологических пространствах, устанавливая ее основные свойства и предоставляя некоторые результаты в качестве естественных обобщений свойств покрытия в рамках первичной структуры.

Ключевые слова: первичное, первичное топологическое пространство, $\mathcal{P}$-Линделевство.

EDN: NZDRNR
УДК 531.131.1

On the Analityc Definition of the Separation Point of a Freely Rolling Down Body

Sophie B. Bogdanova*
Sergey O. Gladkov†
Moscow Aviation Institute
(National Research University)
Moscow, Russian Federation

Received 19.09.2025, received in revised form 24.10.2025, accepted 07.12.2025

Abstract. Movement of a freely rolling body along a chute with a given curve configuration is considered in the paper. The detachment condition is obtained with the use of the method of moving basis. The separation point is found from obtained equations in cases where the curve is given parametrically and in Cartesian and polar coordinates. The implementation of the proposed method is illustrated for some particular curves.

Keywords: natural basis of a curve, curvature of a curve, equation of motion, ellipse, Archimedes' spiral.

Citation: S.B. Bogdanova, S.O. Gladkov, On the Analityc Definition of the Separation Point of a Freely Rolling Down Body, J. Sib. Fed. Univ. Math. Phys., 2026, 19(2), 214–222. EDN: NZDRNR.

Introduction

The problem of the detachment of a point body rolling down a curve under the action of gravity is solved in this paper. The solution of this problem is known for a special case of circle [1]. However, literature review has shown that in general formulation this problem is not solved [2–4].

In order to solve it the method of the natural basis is used [5, 9]. The method consists of the tangent ort $\boldsymbol{\tau}$ pointed in the direction of body motion and the normal ort $\mathbf{n}$ pointed in the direction of concavity of the curve. The basis vectors are connected by well-known relation

$$\begin{cases} \dfrac{d\boldsymbol{\tau}}{ds} = K\mathbf{n}, \\ \dfrac{d\mathbf{n}}{ds} = -K\boldsymbol{\tau}, \end{cases}$$

where curvature of the curve is $K = \dfrac{|y''|}{\left(1+y'^2\right)^{\frac{3}{2}}} \geqslant 0$ [10, 11] (see Figs. 1, 2).

1. The detachment condition

Let us write down the basic equation of motion

$$m\mathbf{a} = \mathbf{N} + \mathbf{mg}$$

*sonjaf@list.ru https://orcid.org/0000-0001-8503-1794
†sglad51@mail.ru https://orcid.org/0000-0002-2755-9133

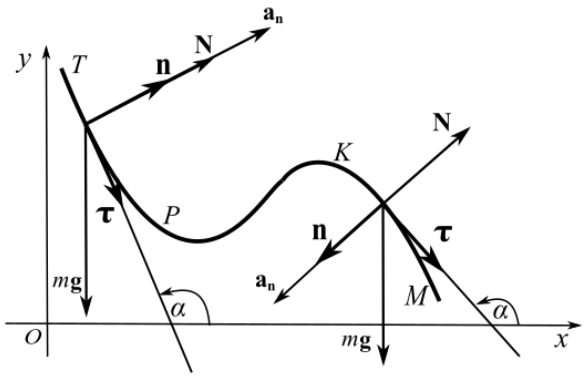

Fig. 1. The distribution of forces in various parts of the curve

for a body of mass m moving from right to left (Fig.1). Force $F = N + mg$ in projections on the axis $\mathbf{n}$ is

$$\begin{cases} m\,|\mathbf{a_n}| = |\mathbf{N}| - |\mathbf{pr_n}\, m\mathbf{g}| & \text{in the area of convexity } TP, \\ m\,|\mathbf{a_n}| = -\,|\mathbf{N}| + |\mathbf{pr_n}\, m\mathbf{g}| & \text{in the area of concavity } KM, \end{cases}$$

where $\mathbf{a_n} = K\mathbf{v^2 n}$ is the centripetal acceleration of the body. As a result the system is rewritten in the form

$$\begin{cases} K\mathbf{v^2} = \dfrac{|\mathbf{N}|}{m} + g\cos\alpha & \text{in the area of convexity } TP, \\ K\mathbf{v^2} = -\dfrac{|\mathbf{N}|}{m} - g\cos\alpha & \text{in the area of concavity } KM. \end{cases} \tag{1}$$

The separation of the body from the gutter is described by the condition $\mathbf{N} = \mathbf{0}$. It means that separation in the convex region TP must be determined by a contradictory relation

$$Kv^2 = g\cos\alpha, \tag{2}$$

since the right hand side of the equation is negative due to condition $\cos\alpha < 0$ (Fig. 1) but the left part is positive. This means that separation of the body on a convex (or straight) section of the gutter is impossible. Separation of a rolling body in a concave area MK is quite possible. It follows from the lower equation (1)

$$Kv^2 = -g\cos\alpha, \tag{3}$$

where both parts of the equation are always positive (Fig. 1). Of course if it turns out that $\dfrac{Kv^2}{g} > 1$ then the body stays in the trough but otherwise equation (3) is solvable. A similar analysis of Fig. 2 when the rolling occurs from right to left leads to the same result: the separation of the body is impossible on a convex or rectilinear section of the trough but it is possible on a concave section because $\cos\alpha > 0$ according to condition (1).

Summarizing equations (2) and (3) and using relation $v^2 = 2g\,(H - y)$, where H is the ordinate of the point from which the rolling of the body begins, one can obtain universal condition for the detachment of a body rolling down a chute under the action of gravity (friction is not taken into account):

$$2\,(H - y) = \frac{|\cos\alpha|}{K}. \tag{4}$$

Let us consider condition (4) when shape of the chute is given in various ways. When the shape of the chute is described in Cartesian coordinates as $y = y(x)$ then condition (4) is

$$2\,|y''|\,(H - y(x)) = 1 + y'^2. \tag{5}$$

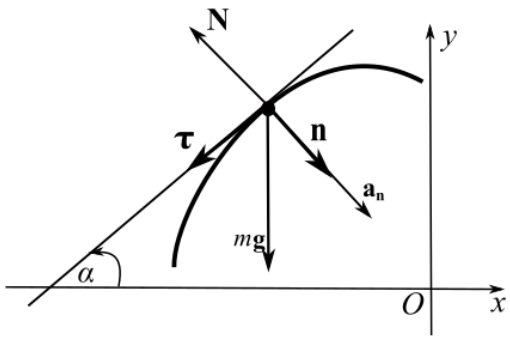

Fig. 2. Movement of the body from right to left

When the shape of the chute is described parametrically $x = x(t), y = y(t)$ then condition (4) is

$$2\left(H - y(t)\right) = \frac{|\dot{x}|\left(\dot{x}^2 + \dot{y}^2\right)}{|\dot{x}\ddot{y} - \dot{y}\ddot{x}|}. \tag{6}$$

When the shape of the chute is described in polar coordinate system $r = r(\varphi)$ then condition (4) takes the form

$$2\left(H - r\left(\varphi\right)\sin\varphi\right) = \left(r^2 + r'^2\right)\left|\frac{r'\cos\varphi - r\sin\varphi}{r^2 + 2r'^2 - r\,r''}\right|. \tag{7}$$

It is important to note that all three relations are ordinary differential equations. They should be solved with respect to x, t or φ since the shape of the chute is considered to be given. Summarizing all the above, one have to

1. establish the fundamental solvability of these equations that means the existence of a separation point.

2. find a solution of these equations.

Let us consider some specific examples for equations (5)–(7).

2. Finding separation points on curves given in Cartesian coordinates

Using equation (5), it was shown [12] that among the family of curves $y = 1 - x^n,\ n \in R$, $x \in [0; 1]$ the earliest separation of the body rolling from the top $(0; 1)$ can occur only at $n = 4.19$. This value is the minimum of function $x(n) = \frac{1}{\sqrt[2n-2]{n^2 - 2n}},\ n \in R$, and the point of separation is equal to 0.7065.

Consider another example of application of equation (5). Let us find the shape of a concave curve providing the normal force to the body rolling down from left to right at each point of the curve is equal to zero. Let us use condition (5) and projection of the equation of motion $m\mathbf{a} = \mathbf{F}$ on axis $\boldsymbol{\tau}$:

$$\begin{cases} \dot{v} = g\sin\alpha, \\ v^2 K = g\left|\cos\alpha\right|. \end{cases} \tag{8}$$

According to the definition of curvature, one can write

$$K = \left|\frac{d\alpha}{ds}\right| = \left|\frac{\frac{d\alpha}{dt}}{\frac{ds}{dt}}\right| = \left|\frac{d\alpha}{v \cdot dt}\right| = \left|\frac{\dot{\alpha}}{v}\right|,$$

where $\dot{\alpha} < 0$ and $\cos\alpha < 0$ due to given above assumptions. Division of the first equation (8) by the second gives

$$\frac{dv}{v} = \frac{\sin\alpha}{\cos\alpha} d\alpha.$$

Then it follows that

$$v = \frac{C}{\cos\alpha}, \quad C < 0.$$

It is logical to assume that at the initial moment of time $v_0(\pi) = -C$. Then

$$v = -\frac{v_0}{\cos\alpha}.$$

Let us differentiate this equation in time. Using the first equation (8), one can find

$$\dot{v} = g\sin\alpha = -v_0 \cdot \frac{\sin\alpha}{\cos\alpha} \cdot \dot{\alpha}.$$

Then $\mathrm{tg}\alpha = -\frac{g}{v_0}t + \tilde{C}$. Assuming that $\alpha(0) = \pi$ and $\tilde{C} = 0$, finally one can write

$$\alpha(t) = \pi - \mathrm{arctg}\left(\frac{g}{v_0}t\right).$$

According to Fig. 3, it is clear that

$$\Delta s \cdot |\cos\alpha| = \Delta x > 0, \quad -\sin\alpha \cdot \Delta s = \Delta y < 0. \tag{9}$$

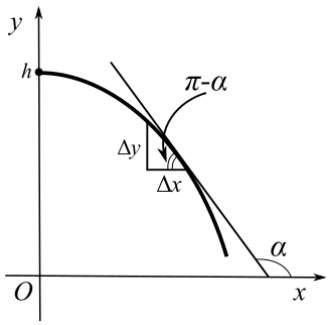

Fig. 3. Visual representation of inequalities (9).

Then

$$\begin{cases} \dot{x} = v \cdot |\cos\alpha|, \\ \dot{y} = -v \cdot \sin\alpha. \end{cases}$$

Substituting $v = -\frac{v_0}{\cos\alpha}$ in these equations, one can obtain

$$\begin{cases} \dot{x} = v_0, \\ \dot{y} = v_0 \cdot \mathrm{tg}\left(\pi - arctg\frac{gt}{v_0}\right) = -gt. \end{cases}$$

Taking into account the initial condition $y(0) = h$, one can find

$$y = -\frac{g}{2v_0^2}x^2 + h. \tag{10}$$

The obtained result means that body moving along a parabola is in close to zero gravity condition. It is used in parabolic flights to create weightlessness.

3. Finding separation points on parametrically defined curves

As a first example, let us find the point of detachment of a body rolling down from the top of a cycloid

$$\begin{cases} x = a\,(t - \sin t)\,, \\ y = a\,(1 - \cos t) \end{cases} \tag{11}$$

Let us substitute (11) into (6) and obtain after some transformations a surprisingly simple result: the breakaway points are determined by the roots of the equation which is clearly illustrated in Fig. 4.

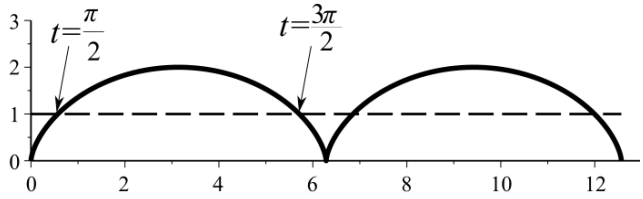

Fig. 4. Illustration of the points of detachment of the body from the cycloid.

Another illustrative case is associated with an ellipse the equation of which in parametric form is

$$\begin{cases} x = a\cos t, \\ y = b\sin t. \end{cases}$$

Condition (6) for the rolling of a body from the point $(0; b)$ leads to the trigonometric equation of the third degree

$$\left(a^2 - b^2\right)\sin^3 t + 3b^2\sin t - 2b^2 = 0. \tag{12}$$

Solution of equation (12) in the case $a = b$ leads to an obvious result $\sin t = \dfrac{2}{3}$ that coincides with the solution of the classical problem of body detachment from the circle of radius R [1]. Cubic equation (12) has two complex roots and real root:

$$\sin t = \left(\frac{b^2\left(\left(a^2 - b^2\right)^{\frac{3}{2}} + a^3 - b^2 a\right)}{\left(a^2 - b^2\right)^{\frac{5}{2}}}\right)^{\frac{1}{3}} - \frac{b^2}{\left(a^2 - b^2\right)\left(\dfrac{b^2\left(\left(a^2-b^2\right)^{\frac{3}{2}} + a^3 - b^2 a\right)}{\left(a^2-b^2\right)^{\frac{5}{2}}}\right)}. \tag{13}$$

Solution of this equation requires at least the fulfilment of the condition $0 < b < a$, i.e., $a = kb$, where $k > 1$. Let us substitute this relation in (13) and obtain after some transformations rather curious result

$$\sin t = \frac{\left(\sqrt{k^2 - 1} + k\right)^{\frac{2}{3}} - 1}{\left(\sqrt{k^2 - 1} + k\right)^{\frac{1}{3}}\sqrt{k^2 - 1}}. \tag{14}$$

The right-hand part of relation (14) is always less than one but greater than zero for $k > 1$. This follows from the limits $\lim\limits_{k\to 1} f(k) = \dfrac{2}{3}$ and $\lim\limits_{k\to\infty} f(k) = 0$. The graph of function $f(k) = \dfrac{\left(\sqrt{k^2-1}+k\right)^{\frac{2}{3}} - 1}{\left(\sqrt{k^2-1}+k\right)^{\frac{1}{3}}\sqrt{k^2-1}}$ is shown in Fig. 5.

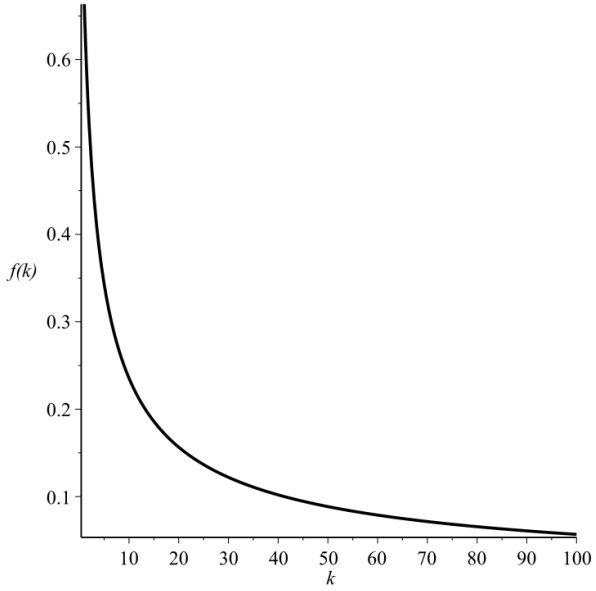

Fig. 5. Function $f(k) = \dfrac{\left(\sqrt{k^2-1}+k\right)^{\frac{2}{3}} - 1}{\left(\sqrt{k^2-1}+k\right)^{\frac{1}{3}}\sqrt{k^2-1}}$ at $k > 1$

This means that separation of the body from the chute in the form of an ellipse that freely moves down from the point $(0; b)$ is inevitable. The point of separation is determined by the solution of equations (13) or (14).

It follows from equation (14) that the value of the parameter t at which separation occurs is the same for each family of ellipses satisfying the condition $\dfrac{a}{b} = k$. That is the moment of time of the body's rolling off such ellipses is always the same.

4. Finding separation points on curves given in polar coordinates

Let us consider the spiral of Archimedes given by the relation $r = a\varphi,\ a > 0$ as an example. In this case expression (7) can be rewritten in the form

$$2\left(H_0 - \varphi\sin\varphi\right) = \left(1+\varphi^2\right)\left|\frac{\cos\varphi - \varphi\sin\varphi}{\varphi^2+2}\right|, \tag{15}$$

where $H_0 = \varphi_0\sin\varphi_0$ and the φ_0 is the polar angle at which the equilibrium point is located on a particular turn of the spiral. This point can be found from the solution of the following equation

$$\varphi = -\mathrm{tg}\varphi. \tag{16}$$

As an example, consider the first turn of the spiral for which $0 < \varphi < \pi$. The concave part of the curve is of interest, and it is clear that $\left|\frac{\cos\varphi - \varphi\sin\varphi}{\varphi^2+2}\right| = \frac{\varphi\sin\varphi - \cos\varphi}{\varphi^2+2}$). Fig. 6 shows the equilibrium point on the first turn of the spiral $r = \varphi$ for which the numerical solution of equation (16) is $\varphi = 2.028757838$.

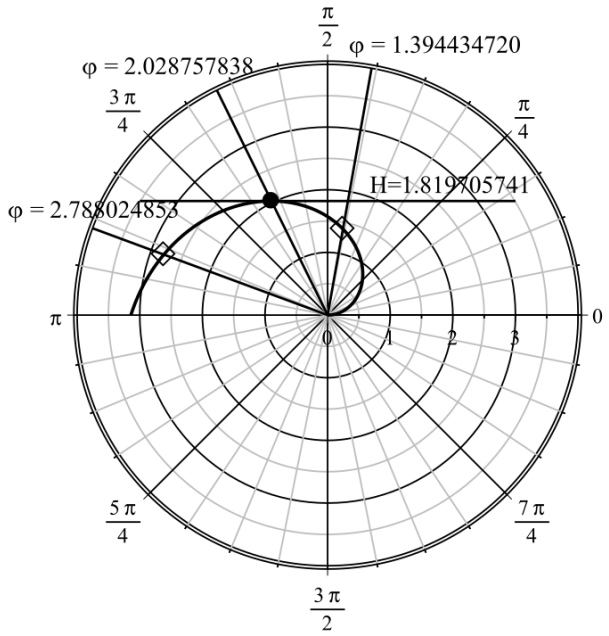

Fig. 6. Equilibrium point on the first turn of the spiral $r = \varphi$

It is clear that rolling from the highest point of the spiral is possible both from left to right and from right to left. Indeed, the numerical solution of the equation

$$2\left(H_0 - \varphi\sin\varphi\right) = \left(1+\varphi^2\right)\frac{\varphi\sin\varphi - \cos\varphi}{\varphi^2+2} \tag{17}$$

on the interval $(0;\pi)$ results in two values: $\varphi = 1.394434720$ and $\varphi = 2.788024853$ shown in Fig. 6. The problem of the points of equilibrium and separation points of the body can be solved in exactly the same way on subsequent turns of the spiral $r = \varphi$. Fig. 7 shows the points of equilibrium and points of detachment of the body on the first six turns of the spiral.

It follows from Fig.7 and equation (16) that equilibrium positions of the body asymptotically tends to the ray $\varphi = \dfrac{\pi}{2}$ with an increase in the number of the spiral turns (they are shown by filled circles). According to this picture, points of separation both on the left and on the right are located almost on a straight line (they are depicted by squares). Thus, it was found that approximate relation for the right-hand separation points has the form

$$y = 0.94x + 1.32,$$

and for the left-hand separation points it is

$$y = -0.88x - 1.4.$$

Taking into account the specifics of the geometry of the line in question, this result is quite expected.

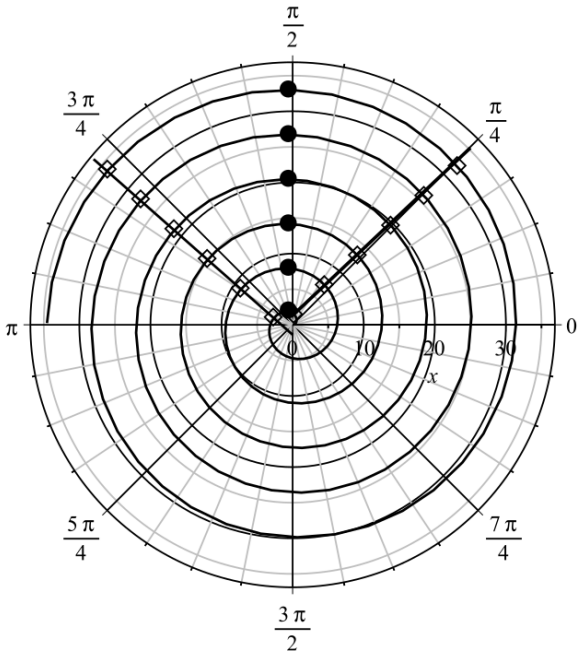

Fig. 7. Points of equilibrium and points of detachment of the body for the first six turns of the spiral

Conclusion

It is worth noting the following main results of this study:

1. A strict physical condition of detachment of a body rolling down a chute of a certain shape under the action of gravity was obtained.

2. Several examples related to the rolling of a body along known curves were considered. They are cycloid, ellipse and the spiral of Archimedes.

3. Equation of special curve that provides motion of a body under condition of permanent separation from the chute was proposed.

References

[1] I.E.Irodov, General Physics Problems: A Textbook for Universities (Zadachi po obshchey fizike: uchebnoye posobiye dlya vuzo), Moscow: Laboratoriya znaniy, 2023.

[2] I.S.Mamaev, T.B.Ivanova, The dynamics of rigid body whose sharp edge in contact with a inclined surface with dry friction, *Russian Journal of Nonlinear Dynamics*, **9**(2013), no. 3, 567–593.

[3] A.P.Ivanov, N.D.Shuvalov, T.B.Ivanova, On detachment conditions of a top on an absolutely rough support, *Vestnik Udmurtskogo universiteta. Matematika. Mekhanika. Komp'yuternyye nauki*, **3**(2012), 103–113.

[4] V.T.Grishakin, A.N.Kalinina, Influence of rolling resistance of the ball on its separation from the convex bearing surface, Proceedings of the Second International Conference with

the participation of young scientists and students "Science and Technology in the Road Industry", Moscow: MADI, 2022, 14–18.

[5] S.O.Gladkov, S.B.Bogdanova, On a strict mathematical definition of the brachistochrone's shape taking into account the thermal effect in the contact zone, University Proceedings. Volga region. Physical and Mathematical Sciences, vol. 1, 2025, 29–43.

[6] S.O.Gladkov, S.B.Bogdanova, On the trajectories of bodies in non-inertial reference frames. Part II, *Tomsk State University Journal of Mathematics and Mechanics*, **91**(2024), 51–60.

[7] S.O.Gladkov, S.B.Bogdanova., An Application of the Plane Curve's Standard Basis to a Certain Class of Problems from Classical Mechanics, *J. Sib. Fed. Univ. Math. Phys.*, **17**(2024), no. 4, 537–543. edn: YSEZDY

[8] S.O.Gladkov, S.B.Bogdanova, On the trajectories of bodies in non-inertial frames of reference, *Tomsk State University Journal of Mathematics and Mechanics*, **84**(2023), 68–80.

[9] S.O.Gladkov, S.B.Bogdanova, On the Issue of the Trajectory of a Freely Falling Body in Noninertial Frames of Reference, *Optics and Spectroscopy*, **131**(2023), no. 11, 1143–1147.

[10] A.P.Norden, Course in Differential Geometry, Moscow, State Publishing House of Physical and Mathematical Literature, 1958.

[11] S.P.Novikov, A.T.Fomenko, Elements of differential geometry and topology (Elementy differentsial'noy geometrii i topologii), Moscow, Nauka, 1987.

[12] S.O.Gladkov, S.B.Bogdanova, On the question of determining points of separation in the category of the curves $y = ax^n$, Proceedings of the XII All-Russian scientific conference with international participation "Mathematical modeling and boundary value problems", Samara, 2024, 49–52.

К вопросу аналитического определения точки отрыва свободно скатывающего тела

Софья Б. Богданова
Сергей О. Гладков
Московский авиационный институт (Национальный исследовательский университет)
Москва, Российская Федерация

Аннотация. Использование метода подвижного базиса позволяет получить условие отрыва тела, свободно скатывающего по желобу, имеющего форму заданной кривой. Из полученных уравнений найдена точка отрыва в случаях, когда кривая задана параметрически, а также в декартовых и полярных координатах. Для конкретно заданных кривых показано, как «работает» предложенный метод.

Ключевые слова: естественный базис кривой, кривизна кривой, уравнение движения, эллипс, спираль Архимеда.

EDN: QLEKCG
УДК 517.55+517.962.2

Vector Partition Functions in Summation Problems for Systems of Linear Equations of a Specific Form

Vladimir A. Uspensky*
Federal Research Center KSC SB RAS
Krasnoyarsk, Russian Federation
Siberian Federal University
Krasnoyarsk, Russian Federation

Received 10.09.2025, received in revised form 12.11.2025, accepted 17.12.2025

Abstract. We present a method for the efficient computation of weighted sums over the sets of nonnegative integer solutions to linear systems of a specific form. Our main result is an explicit formula that evaluates such sums through a discrete analogue of the Newton–Leibniz operator. This formula serves as a powerful tool for tackling combinatorial problems. To illustrate the effectiveness of our approach, we apply it to classical examples, including the problem of counting lucky tickets.

Keywords: vector partition functions, difference equations, summation of functions

Citation: V.A. Uspensky, Vector Partition Functions in Summation Problems for Systems of Linear Equations of a Specific Form, J. Sib. Fed. Univ. Math. Phys., 2026, 19(2), 223–230. EDN: QLEKCG.

This work is dedicated to the memory of my teacher, Professor Evgeniy Konstantinovich Leinartas (1954–2024), Doctor of Physical and Mathematical Sciences, a distinguished specialist in the theory of functions of several complex variables. His recent research, which applied complex analysis to the study of multidimensional difference equations, was a significant inspiration for this paper.

1. Preliminaries

Let $\mathbb{Z}^n = \mathbb{Z} \times \mathbb{Z} \times \cdots \times \mathbb{Z}$, where $\mathbb{Z}$ is the set of integers. Let us introduce integer vectors $a^j = (a_1^j, a_2^j, \ldots, a_m^j)$, where $j = 1, 2, \ldots, n$, and define the matrix $A = (a_i^j)_{m\times n}$, whose columns are given by $(a^j)^\top = (a_1^j, a_2^j, \ldots, a_m^j)^\top$, $j = 1, 2, \ldots, n$. Suppose the set

$$K = \{x \in \mathbb{R}^m \mid x = t_1 a^1 + \cdots + t_n a^n, t \in \mathbb{R}^n_{\geqslant}\}$$

is a pointed cone (i.e., one that does not contain any line). We denote by the same symbol the following lattice cone, which will be implied everywhere hereafter in the work:

$$K = \{x \in \mathbb{Z}^m \mid x = t_1 a^1 + \cdots + t_n a^n, t \in \mathbb{Z}^n_{\geqslant}\}.$$

Definition 1.1 ([1]). Consider a function $g : \mathbb{Z}^n_{\geqslant} \to \mathbb{C}$ and a point x from the lattice cone K. A sum of the form

$$P_A(x; g) = \sum_{At=x, t\in\mathbb{Z}^n_{\geqslant}} g(t) \tag{1}$$

is called a *vector partition function with weight* $g(t)$.

*ivladimir_1990year@mail.ru

We note that the vector partition functions with various weights $g(t)$ were considered in [2], a structure theorem for vector partition functions was presented in [3]. Its proof rests on a formula for counting lattice points in rational convex polytopes [4]. An effective algorithm for computing vector parition functions was developed in [5].

The projection operator π_i acts on a given function of several variables $g(t_1, \dots, t_n)$ as follows:

$$\pi_i g(t) = g(t_1, \dots, t_{i-1}, 0, t_{i+1}, \dots, t_n), \quad i = 1, \dots, n,$$

the shift operator δ_i increments the argument t_i by one, i.e.,

$$\delta_i g(t) = g(t_1, \dots, t_{i-1}, t_i + 1, t_{i+1}, \dots, t_n), \quad i = 1, \dots, n.$$

2. Main result

Consider the problem of summing the values of a function of several variables $g(t_1, \dots, t_n)$ over nonnegative integer points $(t_1, \dots, t_n)$ of the integer lattice that are solutions to a linear equation of the form:

$$a_2 \dots a_n t_1 + a_1 a_3 \dots a_n t_2 + \dots + a_1 \dots [k] \dots a_n t_k + \dots + a_1 \dots a_{n-1} t_n = a_1 \dots a_n x,$$

where t_i, $i = 1, \dots, n$, are nonnegative integers, x is a nonnegative integer, a_i are pairwise coprime nonnegative integers and the symbol $[k]$ means that the factor a_k is omitted from the product.

We consider a polynomial difference operator

$$W(\delta) = \prod_{1 \leqslant i < j \leqslant n} (\delta_j^{a_j} - \delta_i^{a_i}).$$

Definition 2.1 ([6, 7]). The operator

$$W_{NL}(\delta, \pi) = \prod_{1 \leqslant i < j \leqslant n} (\delta_j^{a_j} \pi_i - \delta_i^{a_i} \pi_j)$$

is called the discrete analog of the Newton-Leibniz operator.

Theorem 2.1. *Let $a_1, a_2, \dots, a_n$ be pairwise coprime nonnegative integers, and let x be a nonnegative integer. Let a function $g(t_1, \dots, t_n)$ be defined on $\mathbb{Z}^n_{\geqslant}$. If a function $f = f(t_1, \dots, t_n)$ is a discrete primitive of the function $g(t_1, \dots, t_n)$, i.e., $W(\delta) f(t_1, \dots, t_n) = g(t_1, \dots, t_n)$, then*

$$S(x) = \sum_{\sum_{k=1}^n a_1 \dots [k] \dots a_n t_k = a_1 \dots a_n x} g(t_1, \dots, t_n) = W_{NL}(\delta, \pi) f(a_1 x, a_2 x, \dots, a_n x).$$

Proof. We adapt the proof strategy from [6] as follows. Consider the sum $s_q(x)$ of the form

$$s_q(x) = \sum_{\sum_{k=1}^n a_1 \dots [k] \dots a_n t_k = a_1 \dots a_n x} q_1^{t_1} \dots q_n^{t_n}.$$

Rewriting the sum in a different form, we obtain:

$$s_q(x) = \sum_{|t| = x} q_1^{a_1 t_1} \dots q_n^{a_n t_n}.$$

Next, we derive an expression for computing $s_q(x)$. Finally, consider $H(z;q)$:

$$H(z;q) = \frac{1}{(1-q_1^{a_1}z)}\frac{1}{(1-q_2^{a_2}z)}\cdots\frac{1}{(1-q_n^{a_n}z)}.$$

Note that $H(z;q)$ can be represented in the following form:

$$H(z;q) = \sum_{x=0}^{\infty} s_q(x)z^x.$$

We denote

$$\Gamma = \left\{ z \in \mathbb{C}\colon |z| < \min_{1\leqslant k\leqslant n} \frac{1}{|q_k|^{a_k}} \right\},$$

then, using the residue theorem, we obtain

$$s_q(x) = \frac{1}{2\pi i}\int_{\Gamma}\frac{H(z;q)dz}{z^{x+1}} = -\sum_{k=1}^{n}\operatorname{res}_{z=\frac{1}{q_k^{a_k}}}\frac{H(z;q)}{z^{x+1}} = \sum_{k=1}^{n}\frac{q_k^{a_k(x+n-1)}}{\prod\limits_{i=1,i\neq k}^{n}(q_k^{a_k}-q_i^{a_i})}.$$

We introduce $W[k]$ as follows:

$$W(\delta[k]) = W[k] = \prod_{1\leqslant i<j\leqslant n, i,j\neq k}(\delta_j^{a_j}-\delta_i^{a_i}).$$

Proposition 2.1. The following assertion is true: □

$$W(\delta) = (-1)^{n-k}\prod_{i=1,i\neq k}^{n}(\delta_k^{a_k}-\delta_i^{a_i})W[k]. \tag{2}$$

Now we proceed to the calculation of the desired sum:

$$\begin{aligned}
S(x) &= \sum_{\sum_{k=1}^{n} a_1\ldots[k]\ldots a_n t_k = a_1\ldots a_n x} g(t_1,\ldots,t_n) = \\
&= \sum_{\sum_{k=1}^{n} a_1\ldots[k]\ldots a_n t_k = a_1\ldots a_n x} W(\delta)f(t_1,\ldots,t_n) = \\
&= \sum_{\sum_{k=1}^{n} a_1\ldots[k]\ldots a_n t_k = a_1\ldots a_n x} W(\delta)\delta^t f(0) = \\
&= \sum_{\sum_{k=1}^{n} a_1\ldots[k]\ldots a_n t_k = a_1\ldots a_n x} \delta_1^{t_1}\ldots\delta_n^{t_n}W(\delta)f(0) = \\
&= \sum_{|t|=x}\delta_1^{a_1t_1}\ldots\delta_n^{a_nt_n}W(\delta)f(0).
\end{aligned}$$

From the definition of the sum $s_q(x)$ and the formula for its computation, we obtain the following formula for $S(x)$:

$$S(x) = \sum_{k=1}^{n}\frac{\delta_k^{a_k(x+n-1)}}{\prod\limits_{i=1,i\neq k}^{n}(\delta_k^{a_k}-\delta_i^{a_i})}W(\delta)f(0).$$

Define

$$W_{NL}(\delta[k],\pi[k])=\begin{vmatrix} \pi_1^{n-1} & \dots & \delta_1^{a_1(n-2)}\pi_1 \\ \vdots & \ddots & \vdots \\ \pi_{k-1}^{n-1} & \dots & \delta_{k-1}^{a_{k-1}(n-2)}\pi_{k-1} \\ \pi_{k+1}^{n-1} & \dots & \delta_{k+1}^{a_{k+1}(n-2)}\pi_{k+1} \\ \vdots & \ddots & \vdots \\ \pi_n^{n-1} & \dots & \delta_n^{a_n(n-2)}\pi_n \end{vmatrix}.$$

Expanding $W(\delta)$ using (2) and substituting it into the previous equality yields:

$$\begin{aligned} S(x)&=\sum_{k=1}^{n}\frac{\delta_k^{a_k(x+n-1)}}{\prod\limits_{i=1,i\neq k}^{n}(\delta_k^{a_k}-\delta_i^{a_i})}(-1)^{n-k}\prod_{i=1,i\neq k}^{n}(\delta_k^{a_k}-\delta_i^{a_i})W[k]f(0)= \\ &=\sum_{k=1}^{n}(-1)^{n-k}\delta_k^{a_k(x+n-1)}W[k]f(0)= \\ &=\sum_{k=1}^{n}(-1)^{n-k}\delta_k^{a_k(n-1)}W[k]\delta_k^{a_kx}f(0). \end{aligned}$$

We now examine $W[k]\delta_k^{a_kx}f(0)$ separately:

$$\begin{aligned} W[k]\delta_k^{a_kx}f(0)&=\prod_{1\leqslant i<j\leqslant n,i,j\neq k}(\delta_j^{a_j}-\delta_i^{a_i})\delta_k^{a_kx}f(0)= \\ &=\prod_{1\leqslant i<j\leqslant n,i,j\neq k}(\delta_j^{a_j}\pi_i-\delta_i^{a_i}\pi_j)\pi_1\pi_2\dots[k]\dots\pi_nf(a_1x,a_2x,\dots,a_nx)= \\ &=W_{NL}(\delta[k],\pi[k])f(a_1x,a_2x,\dots,a_nx). \end{aligned}$$

Substituting the found expression into $S(x)$ yields

$$\begin{aligned} S(x)&=\sum_{k=1}^{n}(-1)^{n-k}\delta_k^{a_k(x+n-1)}W[k]f(0)= \\ &=\sum_{k=1}^{n}(-1)^{n-k}\delta_k^{a_k(n-1)}W_{NL}(\delta[k],\pi[k])f(a_1x,a_2x,\dots,a_nx). \end{aligned}$$

Using the form of $W_{NL}(\delta,\pi)$, we obtain the desired formula:

$$S(x)=W_{NL}(\delta,\pi)f(a_1x,a_2x,\dots,a_nx).$$

Let us consider a generalization to the case where the condition is given by a system of linear equations of the form considered earlier:

$$S(x)=\sum_{\substack{a_2^{(1)}\dots a_{k_1}^{(1)}t_1^{(1)}+\dots+a_1^{(1)}\dots a_{k_1-1}^{(1)}t_{k_1}^{(1)}=a_1^{(1)}\dots a_{k_1}^{(1)}x_1 \\ \dots \\ a_2^{(m)}\dots a_{k_m}^{(m)}t_1^{(m)}+\dots+a_1^{(m)}\dots a_{k_m-1}^{(m)}t_{k_m}^{(m)}=a_1^{(m)}\dots a_{k_m}^{(m)}x_m}} g\left(t^{(1)},\dots,t^{(m)}\right). \tag{3}$$

The coefficients $a_i^{(j)}$, $i=1,\dots,k_j$, $j=1,\dots,m$ in each individual row under the summation sign are nonnegative pairwise coprime integers, and $t^{(j)}=\left(t_1^{(j)},\dots,t_{k_j}^{(j)}\right)$. The operator $\delta_i^{(j)}$

acts on a function $g\left(t^{(1)},\dots,t^{(m)}\right)$, where $t^{(j)}=\left(t_1^{(j)},\dots,t_{k_j}^{(j)}\right)$, in the following way: $\delta_i^{(j)}g=g\left(t^{(1)},\dots,t_{i-1}^{(j)},t_i^{(j)}+1,t_{i+1}^{(j)},\dots,t^{(m)}\right)$. The operator $\pi_i^{(j)}$ is defined similarly.

We note that similar sums with linear constraints on the summation indices were considered in [8, 9] in the connection with the Hadamard product of power series [10].

Let us define $W(\delta)$ by

$$W(\delta)=\prod_{1\leqslant i<j\leqslant k_1}\left(\left(\delta_j^{(1)}\right)^{a_j^{(1)}}-\left(\delta_i^{(1)}\right)^{a_i^{(1)}}\right)\cdots\prod_{1\leqslant i<j\leqslant k_m}\left(\left(\delta_j^{(m)}\right)^{a_j^{(m)}}-\left(\delta_i^{(m)}\right)^{a_i^{(m)}}\right),$$

i. e., $W(\delta)=W(\delta^{(1)})\dots W(\delta^{(m)})$.

Definition 2.2. The operator

$$W_{NL}(\delta,\pi)=\prod_{1\leqslant s\leqslant m}\prod_{1\leqslant i<j\leqslant k_s}\left(\left(\delta_j^{(s)}\right)^{a_j^{(s)}}\pi_i-\left(\delta_i^{(s)}\right)^{a_i^{(s)}}\pi_j\right)$$

is called the discrete analog of the Newton–Leibniz operator. It can be written in the following form:

$$W_{NL}(\delta,\pi)=W_{NL}\left(\delta^{(1)},\pi^{(1)}\right)\dots W_{NL}\left(\delta^{(m)},\pi^{(m)}\right).$$

Theorem 2.2. *For each $j=1,\dots,m$ let pairwise coprime nonnegative integers $a_1^{(j)},\dots,a_{k_j}^{(j)}$ and nonnegative integers x_i, $i=1,\dots,m$ be given. Let a function $g=g\left(t^{(1)},\dots,t^{(m)}\right)$, where $t^{(i)}=\left(t_1^{(i)},\dots,t_{k_i}^{(i)}\right)$, be given. If a function $f=f\left(t^{(1)},\dots,t^{(m)}\right)$ is a discrete primitive of the function g, i.e., $W(\delta)f(t)=g(t)$, then*

$$S(x)=W_{NL}(\delta,\pi)\ f\left(t_1^{(1)},\dots,t_{k_1}^{(1)},\dots,t_1^{(m)},\dots,t_{k_m}^{(m)}\right)\Big|_{t_i^{(j)}=a_i^{(j)}x_j,i=1\dots k_j,j=1\dots m}.$$

Proof. For convenience, denote by T the set of nonnegative integer solutions of the system under the summation sign in (3). Since $Wf=g$, we have

$$\begin{aligned}S(x)&=\sum_{t\in T}W(\delta)f\left(t^{(1)},\dots,t^{(m)}\right)=\\&=\sum_{t\in T}W(\delta)\left(\delta^{(1)}\right)^{t^{(1)}}\dots\left(\delta^{(m)}\right)^{t^{(m)}}f(0)=\\&=\sum_{t\in T}\left(\delta^{(1)}\right)^{t^{(1)}}\dots\left(\delta^{(m)}\right)^{t^{(m)}}W(\delta)f(0)=\\&=\sum_{\substack{t_1^{(1)}+\dots+t_{k_1}^{(1)}=x_1\\\dots\\t_1^{(m)}+\dots+t_{k_m}^{(m)}=x_m}}\left(\delta^{(1)}\right)^{a^{(1)}t^{(1)}}\dots\left(\delta^{(m)}\right)^{a^{(m)}t^{(m)}}W(\delta)f(0).\end{aligned}$$

Applying the formula for $s_q(x)$ derived earlier, the last equality yields:

$$\prod_{i=1}^{m}\sum_{k=1}^{k_i}\frac{\left(\delta_k^{(i)}\right)^{a_k^{(i)}(x_i+k_i-1)}}{\prod\limits_{j=1,j\neq k}^{k_i}\left(\left(\delta_k^{(i)}\right)^{a_k^{(i)}}-\left(\delta_j^{(i)}\right)^{a_j^{(i)}}\right)}Wf(0)=$$

$$=\sum_{s_1=1}^{k_1}\cdots\sum_{s_m=1}^{k_m}\prod_{i=1}^{m}\frac{\left(\delta_{s_i}^{(i)}\right)^{a_{s_i}^{(i)}(x_i+k_i-1)}}{\prod\limits_{j=1,j\neq s_i}^{k_i}\left(\left(\delta_{s_i}^{(i)}\right)^{a_{s_i}^{(i)}}-\left(\delta_j^{(i)}\right)^{a_j^{(i)}}\right)}Wf(0).$$

Since $W(\delta)=W(\delta^{(1)})\dots W(\delta^{(m)})$, we obtain the following:

$$\sum_{s_1=1}^{k_1}\cdots\sum_{s_m=1}^{k_m}\prod_{i=1}^{m}\frac{\left(\delta_{s_i}^{(i)}\right)^{a_{s_i}^{(i)}(x_i+k_i-1)}}{L_i}(-1)^{k_i-s_i}L_iW(\delta^{(i)}[s_i])f(0)=$$

$$=\sum_{s_1=1}^{k_1}\cdots\sum_{s_m=1}^{k_m}\prod_{i=1}^{m}(-1)^{k_i-s_i}\left(\delta_{s_i}^{(i)}\right)^{a_{s_i}^{(i)}(k_i-1)}W(\delta^{(i)}[s_i])\left(\delta_{s_i}^{(i)}\right)^{a_{s_i}^{(i)}x_i}f(0),$$

where

$$L_i=\prod_{j=1,j\neq s_i}^{k_i}\left(\left(\delta_{s_i}^{(i)}\right)^{a_{s_i}^{(i)}}-\left(\delta_j^{(i)}\right)^{a_j^{(i)}}\right).$$

As in Theorem 2.1, we note that

$$W(\delta^{(1)}[s_1])\dots W(\delta^{(m)}[s_m])\left(\delta_{s_1}^{(1)}\right)^{a_{s_1}^{(1)}x_1}\dots\left(\delta_{s_m}^{(m)}\right)^{a_{s_m}^{(m)}x_m}f(0)=$$
$$=W_{NL}(\delta^{(1)}[s_1],\pi^{(1)}[s_1])\dots W_{NL}(\delta^{(m)}[s_m],\pi^{(m)}[s_m])f(ax),$$

where $f(ax)=f\left(a_1^{(1)}x_1,\dots,a_{k_1}^{(1)}x_1,\dots,a_1^{(m)}x_m,\dots,a_{k_m}^{(m)}x_m\right)$.

Substituting the resulting expression into the penultimate equality, we obtain the desired expression for our sum:

$$S(x)=W_{NL}(\delta,\pi)\ f\left(t_1^{(1)},\dots,t_{k_1}^{(1)},\dots,t_1^{(m)},\dots,t_{k_m}^{(m)}\right)\Big|_{t_i^{(j)}=a_i^{(j)}x_j,i=1\dots k_j,j=1\dots m}.$$

□

3. Examples

Example 3.1. Let us find

$$S(x_1,x_2)=\sum_{t_1^{(1)}+t_2^{(1)}+t_3^{(1)}=x_1,\ t_1^{(2)}+t_2^{(2)}+t_3^{(2)}=x_2}1.$$

The function f can be chosen as $f=\frac{1}{4}t_1^2t_2t_4^2t_5$, then

$$S(x_1,x_2)=\frac{(x_1^2+3x_1+2)(x_2^2+3x_2+2)}{4}.$$

Example 3.2. The result can be applied to the problem of enumerating lucky tickets, where a ticket is identified by a six-digit number and is considered lucky if the sum of the first three digits equals the sum of the last three digits. As a specific example, let us compute the number of tickets for which the sum of the first three digits equals 25.

$$P_{25} = \sum_{\substack{t_1^{(1)}+t_2^{(1)}+t_3^{(1)}=25 \\ t_1^{(2)}+t_2^{(2)}+t_3^{(3)}=25}} 1 - |A| \,. \tag{4}$$

In formula (4), A is the set of tuples $\left(t_1^{(1)}, \ldots, t_3^{(2)}\right)$ satisfying

$$t_1^{(1)} + t_2^{(1)} + t_3^{(1)} = t_1^{(2)} + t_2^{(2)} + t_3^{(2)} = 25,$$

with at least one $t_i^{(j)} \geqslant 10$.

We find the cardinality of A using the inclusion-exclusion principle:

$$|A| = \sum_{i=1}^{6} S(15, 25) - (6S(5, 25) + 9S(15, 15)) + 18S(5, 15) - 9S(5, 5),$$

where the values $S(x_1, x_2)$ are computed using the formula from the example above.

This research was supported by the Russian Science Foundation and Krasnoyarsk Regional Science Foundation, project no. 25-21-20076.

References

[1] A.P.Lyapin, S.Chandragiri, Generating functions for vector partition functions and a basic recurrence relation, *Journal of Difference Equations and Applications*, **25**(2019), no. 7, 1052–1061.

[2] M.Brion, M.Vergne, Residue formulae, vector partition functions and lattice points in rational polytopes, *J. American Math. Soc.*, **10**(1997), no. 4, 797–833.

[3] B.Sturmfels, On vector partition functions, *Journal of Combinatorial Theory. Series A*, **72**(1995), no. 3, 302–309.

[4] M.Beck, P.E.Gunnells, E.Materov, Weighted lattice point sums in lattice polytopes, unifying Dehn-Sommerville and Ehrhart-Macdonald, *Discrete Comput. Geom.*, **65**(2021), no. 2, 365–384. DOI: 10.1007/s00454-020-00175-2

[5] A.B.Leinartene, A.P.Lyapin, Applying Computer Algebra Systems to Study Chaundy-Bullard Identities for the Vector Partition Function with Weight, *Programming and Computer Software*, **50**(2024), no. 2, 176–179. DOI: 10.1134/S0361768824020105

[6] E.K.Leinartas, O.A.Shishkina, The Discrete Analog of the Newton-Leibniz Formula in the Problem of Summation over Simplex Lattice Points, *Journal of Siberian Federal University. Math. & Phys.*, **12**(2019), no. 4, 503–508. DOI: 10.17516/1997-1397-2019-12-4-503-508

[7] E.K.Leinartas, O.A.Shishkina, The Euler–Maclaurin Formula In The Problem Of Summation Over Lattice Points Of A Simplex, *J. Sib. Fed. Univ. Math. & Phys.*, **15**(2022), no. 1, 108–113. DOI: 10.17516/1997-1397-2022-15-1-1-6

[8] A.A.Grigoriev, E.K.Leinartas, A.P.Lyapin, Summation of functions and polynomial solutions to a multidimensional difference equation, *J. Sib. Fed. Univ. Math. & Phys.*, **16**(2023), no. 2, 153–161. edn: BBJNGZ

[9] E.K.Leinartas, Multidimensional Hadamard Composition And Sums With Linear Constraints On The Summation Indices, *Sib. Math. J.*, **30**(1989), 250–255.

[10] L.A.Aizenberg, E.K.Leinartas, Multidimensional Hadamard Composition And Szegö Kernels, *Sib. Math. J.*, **24**(1983), no. 3, 317–323.

Функции векторного разбиения в задачах суммирования для систем линейных уравнений определенного вида

Владимир А. Успенский
Федеральный исследовательский центр КНЦ СО РАН
Красноярск, Российская Федерация
Сибирский федеральный университет
Красноярск, Российская Федерация

Аннотация. Мы рассматриваем метод для эффективного вычисления взвешенных сумм по множествам неотрицательных целочисленных решений систем линейных уравнений специального вида. Нашим основным результатом является явная формула, которая вычисляет такие суммы путём введения дискретного аналога оператора Ньютона–Лейбница. Данная формула предоставляет мощный инструмент для решения комбинаторных задач. Мы демонстрируем эффективность нашего подхода, применяя его к классическим задачам, включая вычисление количества счастливых билетов.

Ключевые слова: функции векторного разбиения, разностные уравнения, суммирование функций.

Journal of Siberian Federal University. Mathematics & Physics 2026, 19(2), 231–247

EDN: WTAIQQ
УДК 512.554

Finite Quasifields with the Hall Condition

Olga V. Kravtsova*
Siberian Federal University
Krasnoyarsk, Russian Federation
Valeria S. Loginova†
Institute of Computational Modeling SB RAS
Krasnoyarsk, Russian Federation

Received 10.10.2025, received in revised form 17.11.2025, accepted 17.12.2025

Abstract. Since the beginning of the last century, non-associative algebraic systems have been used to coordinatize non-Desarguesian projective translation planes. Such systems as semifields and quasifields are now find application in cryptographic algorithm design. Hall quasifields were introduced in 1943 and were the first examples of non-distributive and non-associative quasifields. They are two-dimensional quasifields over the center, all non-central elements of which satisfy unique quadratic equation. The automorphism group acts transitively on non-central elements. Hall quasifields of the same order coordinatize the isomorphic translation planes, that is Hall planes. Increasing the dimension of the quasifield over the center, we obtain generalized quasifields with the Hall condition. Such a quasifield cannot be either a semifield or a near-field. More than one non-isomorphic quasifields with the Hall condition can correspond to one irreducible polynomial over a given field. The spread set method is used for reasoning and calculations. It allows to present the multiplication rule as a linear transformation and so to describe subfields and sub-quasifields, spectra and automorphisms. These structural questions with some solutions are naturally transferred from the two-dimensional case. Unlike Hall quasifields, a multidimensional quasifield with the Hall condition cannot be generated by a single element, this fact completes the results by M. Cordero and V. Jha (2009) on covering and primitivity. Presenting examples, the authors list all non-isomorphic quasifields of order 16 with the Hall condition and define their automorphism groups.

Keywords: Hall quasifield, quasifield with Hall condition, spread set, spectrum, automorphism, right-primitive quasifield.

Citation: O.V. Kravtsova, V.S. Loginova, Finite Quasifields with the Hall Condition, J. Sib. Fed. Univ. Math. Phys., 2026, 19(2), 231–247. EDN: WTAIQQ.

Introduction

To coordinatize the points and the lines in a finite projective plane, the elements of suitable set Q are usually used. The properties of the incidence relation allow to introduce two binary operation of addition and multiplication on Q. A classical Desarguesian projective plane is coordinatized by a skewfield, a translation plane by a quasifield. The concept of quasifield is obtained by excluding the associativity of multiplication and one of the distributive laws from the list of skewfield axioms.

*ol71@bk.ru https://orcid.org/0000-0002-6005-2393
†loginovavs011001@mail.ru

Definition 1. *An algebraic system $Q = (Q, +, \cdot)$ with two binary operations $+$ and $\cdot$ is called a right quasifield if*

1) $(Q, +)$ is an Abelian group;
2) $Q^* = (Q \setminus \{0\}, \cdot)$ is a loop;
3) the right distributive law holds, $(a + b)c = ac + bc$ $(a, b, c \in Q)$;
4) $a \cdot 0 = 0$ for all $a \in Q$;
5) the equation $xa = xb + c$ is uniquely solved for all $a, b, c \in Q$, $a \neq b$.

A left quasifield is defined analogously.

The first examples of non-trivial semifields not being fields were presented in 1906–1907 by L. E. Dickson [1], O. Veblen and J. Maclagan–Wedderburn. In the literature until 1975, the term «Veblen–Wedderburn systems» was usually used to refer to quasifields [3, 20.4]. Quasifields have anomalous properties compared to fields, but they are also widely used in projective geometry, coding theory, and combinatorics.

Definition 2. *A kernel of a right quasifield Q is the set of all elements $k \in Q$ satisfying the conditions:*

1) $k(a + b) = ka + kb$;
2) $k(ab) = (ka)b$ for all $a, b \in Q$.

A kernel of a quasifield is always a skewfield, hence it necessarily contains the prime subfield formed by integer multiples of identity. A quasifield can be considered as a vector space over its kernel [4, theorem 7.2]. Thus, a finite quasifield is of order p^m, where p is prime. It is clear that a quasifield of prime order p is the field; the minimal order of non-trivial quasifield is 9. We call a *center* of quasifield Q the subset of the kernel K whose elements commute with all elements from Q:

$$Z(Q) = \{z \in K \mid za = az \ \forall a \in Q\}.$$

A center of an arbitrary quasifield is not necessarily a subfield, see the examples of exceptional Zassenhaus near-fields [3].

A quasifield with two-sided distributivity is called a *semifield*. First examples of non-trivial finite semifields were shown by L. E. Dickson in 1906. A quasifield with associative multiplication is called (right or left) *near-field*. First examples of near-fields were constructed by L. E. Dickson in 1905 [5], all finite near-fields were completely classified by H. Zassenhaus in 1936 [6].

The first examples of finite quasifields that are neither semifields nor near-fields were presented by M. Hall [7] in 1943 (see also [3, 20.4]).

Let the polynomial $\varphi(x) = x^2 - rx - s$ be irreducible over $GF(q)$ ($q = p^n$, p is prime). A quasifield Q of order q^2 with the kernel $K \simeq GF(q)$ is called *Hall quasifield*, if K is the center of Q and each element of $Q \setminus K$ is a root of the polynomial $\varphi(x)$.

A finite Hall quasifield is a field iff it has order 4; it is a non-trivial near-field iff $K = GF(3)$ and $\varphi(x) = x^2 + 1$ [4, Lemma 9.2]. Hall quasifields over the same finite field K are *isotopic* and coordinatize isomorphic translation planes which are *Hall planes* [8, Theorems 3.2 and 4.2]. Thus, all three non-isomorphic Hall quasifields of order 9 are isotopic to the Dickson near-field of order 9. The properties of Hall planes are presented, for instance, in [9, Chapter 14].

Hall quasifields attract the attention of researchers by the possibility of applications and generalizations. G. Nagy identifies in [10] Hall quasifields that admit 2-transitive sets of even permutations. Y. Hiramine proposes [11] *a generalized Hall quasifield* Q with base 1, λ over kernel K, each element of which $\xi = a + b\lambda$ from $Q \setminus K$ satisfies the functional equation $\xi^2 - r(b)\xi - s(b) = 0$,

where r and s are mappings from K^* to K. M. Biliotti and co-authors in [9, 14.3.11] formulate the questions on the existence of infinite generalizations of Hall quasifields.

We can specify the examples of «near-Hall» quasifields not contained in any finite Hall quasifield. These are quasifields of order 16 whose spread sets were listed by U. Dempwolff while enumerating pairwise non-isomorphic translation planes of order 16 [12]. There are exactly 8 such planes: one Desarguesian, coordinatized by the field $GF(16)$, two are semifield planes, and five are coordinatized by non-isotopic quasifields. V. M. Levchuk and P. K. Stuckert in [13, Theorem 3.3] showed that each of Dempwolff quasifields Q_1, Q_3, Q_4 is a set-theoretic union of seven maximal subfields of order 4. These quasifields are not Hall quasifields, since they have dimension 4 over the center $\mathbb{Z}_2$, although all their non-central elements are the roots of the same polynomial $\varphi(x) = x^2 + x + 1$.

Changing the dimension of the quasifield over the kernel in the definition of Hall quasifield, we obtain a *quasifield with Hall condition*.

Definition 3. *Let Q be a right quasifield of order q^m with the kernel $K \simeq GF(q)$ ($q = p^n$, p is prime, $m > 2$). We say that Q is a quasifield with Hall condition if $Z(Q) = K$ and there exists an irreducible polynomial $\varphi(x) = x^2 - rx - s \in K[x]$ such that all elements of $Q \setminus K$ are the roots of $\varphi(x)$.*

Clearly, $m = 2$ gives the Hall quasifield definition. This paper solves structural problems for quasifields with Hall condition and lists all such quasifields of order 16 with their automorphism groups. An explicit example of the quasifields with the simple non-Abelian automorphism group $\mathrm{PSL}(2, 7)$ is given.

1. Structural questions for finite Hall quasifields

The following structural questions for finite semifields and quasifields have long been studied and were written by V. M. Levchuk in [14].

(A) *Enumerate maximal subfields and their possible orders.*
(B) *Find the finite quasifields Q with not-one-generated loop Q^*.*
(C) *What loop spectra Q^* of finite semifields and quasifields are possible?*
(D) *Find the automorphism group $\mathrm{Aut}\, Q$.*

In the previous paper [15], the authors solved (A)–(D) for finite Hall quasifields, listing known results with proving new ones. We summarize key results for comparison with the m-dimensional Hall condition case.

The spread set method is the primary investigation tool, for more details see [16].

Let $Q = (Q, +, \cdot)$ be a (right) quasifield of order q^m ($q = p^n$, p is prime) with the kernel $K \simeq GF(q)$. Then Q is a (left) vector space m-dimensional over K, and for fixed $u \in Q$, the right multiplication map $\rho_u : x \to xu$ is a linear transformation of Q (by the kernel definition). The set of all these transformations $\Sigma = \{\rho_u \mid u \in Q\}$ is called the *spread set* of Q. By definition, Σ contains zero and identity maps; the difference of any two distinct elements is invertible. The set of matrices

$$R = \{\theta(u) \mid u \in Q\} \subset GL_m(q) \cup \{0\}$$

for these linear transformations (in a fixed base) is also called the spread set.

Let Q be a right Hall quasifield of order q^2 with the kernel (center) $K \simeq GF(q)$ and associated polynomial $\varphi(x) = x^2 - rx - s$. We will write elements of Q as rows (x, y), $x, y \in K$, and choose

the base e_1, e_2 of the linear space Q, where $e_1 = 1$ is the quasifield identity, $e_2 \notin K$. The spread set matrices are [15]

$$\theta(x,y) = \begin{pmatrix} x & y \\ -y^{-1}\varphi(x) & r-x \end{pmatrix},\ y \neq 0, \qquad \theta(x,0) = \begin{pmatrix} x & 0 \\ 0 & x \end{pmatrix}, \tag{1}$$

the multiplication of row vectors is performed according to the rule

$$(u,v)\cdot(x,y) = (u,v)\theta(x,y), \qquad u,v,x,y \in K.$$

Note that the coordinate form of the multiplication record in a Hall quasifield Q with $e_1 = 1$ does not depend on the choice of the second base element. This is explaned by the transitivity of the group $Aut_K Q$ on $Q \setminus K$. The matrices $\theta(x,y)$ with $y \neq 0$ forms a conjugacy class in $GL_2(q)$ with characteristic polynomial $\varphi(x)$ [17].

Let P be the minimal subfield of K containing the coefficients r, s of the polynomial $\varphi(x)$, $|P| = p^t$. It is clear that $t \mid n$ and n/t is odd, otherwise K contains the splitting field of $\varphi(x)$. In particular, if $n = 2^k$, then $P = K$.

Theorem 1 ([15, Th. 1]). *The automorphism group $Aut\,Q$ of the Hall quasifield Q is of order $(q^2-q)n/t$, it consists of all semilinear transformations*

$$(x,y) \to (x^\sigma, y^\sigma)\begin{pmatrix} 1 & 0 \\ a & b \end{pmatrix}, \tag{2}$$

where $a, b \in K$, $b \neq 0$, $\sigma \in Aut_P K$. The kernel stabilizer $Aut_K Q$ is of order q^2-q, it consists of all linear transformations (2) *with $\sigma = 1$.*

Corollary 1 ([15, Cor. 2]). *Two Hall quasifields Q_1 and Q_2 of order q^2 with the center $K \simeq GF(q)$ and associated polynomials $\varphi_1(x) = x^2 - r_1 x - s_1$ and $\varphi_2(x) = x^2 - r_2 x - s_2$ are isomorphic iff there exists an automorphism σ of K such that $r_1^\sigma = r_2$, $s_1^\sigma = s_2$.*

Thus, to determine the number of pairwise non-isomorphic Hall quasifields of the same order, we must group the irreducible polynomials in $K[x]$ according to their coefficient field P. In particular, all Hall quasifields of order p^2 with different associated polinomials are pairwise non-isomorphic. In general case, the number of pairwise non-isomorphic Hall quasifields is at most $q(q-1)/2$.

Theorem 2 ([15, Th. 2]). *The center K of a finite Hall quasifield Q is its unique maximal subfield, except when $K \simeq GF(2^{2m+1})$ and $\varphi(x) = x^2 + x + 1$, where Q is the union of K and subfields of order 4.*

Non-associative multiplication in a quasifield leads to taking into account the order of brackets even when writing the product of identical factors.

Definition 4. *The right-ordered n-th degree of an element $a \in Q^*$ is defined inductively:*

$$a^{1)} = a, \quad a^{i+1)} = a^{i)} \cdot a, \quad i = 1, 2, \ldots.$$

The smallest integer m with the condition $a^{m)} = 1$ is called the right order of a, the set of right orders of all elements is the right spectrum of the loop Q^*.

Definition 5. *An element $a \in Q^*$ is called right-primitive if the multiplicative loop Q^* is exhausted by the right-ordered degrees of this element:*

$$Q^* = \{1, a, a^{2)}, a^{3)}, \ldots\}.$$

A quasifield Q containing a right-primitive element is also called right-primitive.

A left-ordered degree, left order, left spectrum, and left-primitive element are defined similarly. As proved in [14, Lemma 5], the right and left orders of an element do not exceed the order of the loop Q^*. More precisely [15, Pr. 2], the right order of an element a of a right quasifield divides the order of the matrix $\theta(a)$ of a spread set in the group $GL_m(q)$. Calculating the left order of an element in a right quasifield (and vice versa) is more complicated.

For a Hall quasifield Q, the transitivity of the automorphism group on $Q \setminus K$ implies that all non-central elements have the same right order and the same left order.

Theorem 3 ([15, Th. 5]). *The right spectrum of a Hall quasifield Q is $M \cup \{\mu\}$, where M is the set of all divisors of $q-1$, μ is a divisor of q^2-1 that does not divide $q-1$. Conversely, for any $M \cup \{\mu\}$ of the described form there exists a Hall quasifield with such a right spectrum. The left order of any non-central element in a Hall quasifield is three for $r = s$, four for $r = 0$, and more than four otherwise.*

In 1991, G. Wene conjectured [18]: *Any finite semifield is left-primitive or right-primitive.* This conjecture was disproved in 2004 by I. Rua, who presented a counterexample of order 32. This commutative *Knuth–Rua semifield* is neither right-primitive nor left-primitive. A second counterexample is the *Hentzel–Rua semifield* of order 64, constructed by [19] in 2007 (see also [14] for details).

M. Cordero and V. Jha studied [20] the primitivity problem for quasifields, focusing on the non-primitivity of Hall quasifields covered by proper subquasifields. Let Q be a finite quasifield with the set of proper subquasifields $\mathcal{Q} = \{Q_i \mid 1 \leqslant i \leqslant n\}$, such that $Q = \cup Q_i$. Then $\mathcal{Q}$ is a *covering* of Q, Q is a *quasifield admitting a covering*. Clearly, a quasifield with a covering is non-primitive. More precisely, any element $a \in Q$ is neither left- nor right-primitive.

Among finite Hall quasifields, some are coverable, others are right-primitive in the case when $P = K$ and $\varphi(x)$ is a primitive irreducible polynomial. For any $q = p^n$ there exist $\boldsymbol{\varphi}(q^2-1)/(2n)$ of right-primitive Hall quasifields of order q^2, where $\boldsymbol{\varphi}$ is the Euler function [15].

2. General results for quasifields with the Hall condition

Let Q be a right quasifield of order q^m with the Hall condition. Its kernel $K \simeq GF(q)$ coincides with the center, all elements of $Q \setminus K$ are roots of the irreducible polynomial $\varphi(x) = x^2 - rx - s \in K[x]$. Such Q admits a cover by Hall quasifields of order q^2.

Theorem 4. *A quasifield Q of order q^m with the Hall condition and kernel $K \simeq GF(q)$ is the union of isomorphic Hall quasifields of order q^2 intersecting on K.*

Proof. For any $a \in Q \setminus K$, consider the two-dimensional linear subspace $H_a = \{x + ya \mid x, y \in K\}$ and verify that it is closed under multiplication. Indeed, let $b, c \in H_a$, $b = x_1 + y_1 a$, $c = x_2 + y_2 a$, $x_i, y_i \in K$. If $y_1 = 0$, then $cb \in H_a$. For $y_1 \neq 0$, the vectors $1, b$ form a base of H_a, and $c = x_3 + y_3 b$. Then

$$cb = (x_3 + y_3 b)b = x_3 b + y_3 b^2 = x_3 b + y_3(rb + s) = y_3 s + (x_3 + y_3 r)b \in H_a.$$

Note that we do not directly simplify the product $(x_1 + y_1 a)(x_2 + y_2 a)$ due to only one-sided distributivity.

So, H_a is closed under addition and multiplication, it is a Hall quasifield of order q^2 with the center K and associated polynomial $\varphi(x)$. Now we choose $d \in Q \setminus H_a$, compose H_d and so on. All such Hall subquasifields H_a, $a \in Q \setminus K$, are isomorphic, since they have the same order

and are determined by the same quadratic polynomial. The number of such subquasifields is obviously

$$\frac{q^m - q}{q^2 - q} = 1 + q + q^2 + \cdots + q^{m-2}.$$

The theorem is proved. □

For $q = p = 2$, a special case arises when the covering is composed of subfields of order 4.

Corollary 2. *A quasifield Q of order 2^m with the Hall condition and with the kernel $K \simeq \mathbb{Z}_2$ and associated polynomial $\varphi(x) = x^2 + x + 1$ is the union of $2^{m-1} - 1$ subfields of order 4.*

Unlike Hall quasifields, several non-isomorphic quasifields may correspond to one polynomial $\varphi(x)$ for fixed q and m. This is confirmed by direct calculations even in the case of minimal order $|Q| = 16$ (see below) and is explained by the ambiguity of composing matrices of a spread set. Let us explain using the example $m = 4$. Consider the matrix $\theta(x, y, z, t)$ of a spread set for arbitrary $x, y, z, t \in K$. It is clear that for $y = z = t = 0$ we obtain the scalar matrix $\theta(x, 0, 0, 0) = xE$. In other cases, the vector (x, y, z, t) must be a root of the polynomial $\varphi(x)$:

$$(x, y, z, t)\theta(x, y, z, t) = r(x, y, z, t) + s(1, 0, 0, 0). \tag{3}$$

The matrix of a spread set is uniquely determined by its first row, i.e. the remaining elements are functions (polynomials) of the variables x, y, z, t:

$$\theta(x, y, z, t) = \begin{pmatrix} x & y & z & t \\ f_1 & f_2 & f_3 & f_4 \\ g_1 & g_2 & g_3 & g_4 \\ h_1 & h_2 & h_3 & h_4 \end{pmatrix},$$

here $f_i = f_i(x, y, z, t)$, $g_i = g_i(x, y, z, t)$, $h_i = h_i(x, y, z, t)$. Then from the equation (3) we get:

$$\begin{cases} yf_1 + zg_1 + th_1 = -\varphi(x), \\ yf_2 + zg_2 + th_2 = y(r - x), \\ yf_3 + zg_3 + th_3 = z(r - x), \\ yf_4 + zg_4 + th_4 = t(r - x). \end{cases}$$

From this system of $m = 4$ equations, $m^2 - m = 12$ functions f_i, g_i, h_i are not uniquely determined, as well as for other $m > 2$. For $m = 2$, that is, for the Hall quasifield, we have $m = m^2 - m = 2$, and the functions of the spread set are expressed uniquely.

We cannot yet propose a solution to the problem of the structure of the automorphism group of a quasifield with the Hall condition due to the existence of a large number of variants (see examples below), except for the following obvious fact. The group $Aut\, Q$ must permute the Hall subquasifields H_a, $a \in Q \setminus K$. A subgroup of $Aut\, Q$ that fixes the subquasifield H_a induces an automorphism group $Aut\, H_a$, whose structure and order are known, see Theorem 1.

Lemma 1. *Let Q be a quasifield of order q^m with the Hall condition, its center be $K \simeq GF(q)$, $P \simeq GF(p^t)$ be the coefficient subfield. Then the order of the automorphism group $Aut\, Q$ divides the number $\frac{n}{t}(q^2 - q) \cdot (1 + q + q^2 + \cdots + q^{m-2})!$*

The question **(A)** on maximal subfields is solved similarly to Hall quasifields.

Theorem 5. *Any subfield of a quasifield Q with the Hall condition is contained in one of its Hall subquasifields.*

Proof. Consider the centralizer of $a \in Q$: $C(a) = \{x \in Q \mid ax = xa\}$. The centralizer of the element a in the subquasifield H_a is equal to $K \cup \{a, r - a\}$, see [15]. We will show that no element $b \in Q \setminus H_a$ commutes with a. Let the first three base elements of the quasifield Q be 1, a, b (they are linearly independent). Consider the matrices of a spread set $\theta(a)$ and $\theta(b)$:

$$\theta(a) = \begin{pmatrix} 0 & 1 & 0 & \dots \\ s & r & 0 & \dots \\ \alpha & \beta & \gamma & \dots \\ \dots & \dots & \dots & \dots \end{pmatrix}, \qquad \theta(b) = \begin{pmatrix} 0 & 0 & 1 & \dots \\ \alpha & \beta & \gamma & \dots \\ s & 0 & r & \dots \\ \dots & \dots & \dots & \dots \end{pmatrix},$$

here $a^2 = s + ra$, $ba = ab = \alpha + \beta a + \gamma b + \dots$, $b^2 = s + rb$, the coefficients of the decomposition in the base are the corresponding rows of the matrices. By the definition of a spread set, the difference of these matrices must be non-singular, but

$$\det(\theta(a) - \theta(b)) = \begin{vmatrix} 0 & 1 & -1 & \dots \\ s-\alpha & r-\beta & -\gamma & \dots \\ \alpha - s & \beta & \gamma - r & \dots \\ \dots & \dots & \dots & \dots \end{vmatrix} = \begin{vmatrix} 0 & 1 & -1 & \dots \\ s-\alpha & r-\beta & -\gamma & \dots \\ 0 & r & -r & \dots \\ \dots & \dots & \dots & \dots \end{vmatrix} = 0.$$

The resulting contradiction shows that outside the subquasifield H_a there are no elements commuting with a. And like the case of Hall quasifield [15], the centralizer of an element $a \in Q \setminus K$ is $K \cup \{a, r - a\}$.

Now let F be a subfield of Q that is not completely contained in H_a. If $b \in F \setminus H_a$, then $ab = ba$ and $b \in C(a)$, then $b \in K$, that contradicts to the choice. □

Corollary 3. *The center K of a finite quasifield Q with the Hall condition is its unique maximal subfield, except when $K \simeq GF(2^{2k+1})$ and $\varphi(x) = x^2 + x + 1$, where Q is the union of K and subfields of order 4.*

The question of spectra is also solved similarly to the finite Hall quasifield, except that we cannot yet guarantee the existence of a Hall quasifield for any possible choice of kernel and associated polynomial.

Theorem 6. *The right spectrum of a quasifield Q with the Hall condition is $M \cup \{\mu\}$, where M is the set of all divisors of $q-1$, μ is a divisor of q^2-1 that does not divide $q-1$. The left order of any non-central element in a Hall quasifield is three for $r = s$, four for $r = 0$, and more than four otherwise.*

Here μ is the order of the root α of $\varphi(x)$ in the multiplicative group of the field $K(\alpha) \simeq GF(q^2)$, that is, μ is uniquely determined by $\varphi(x)$.

Since the degrees of any non-central element $a \in Q$ belong to the Hall subquasifield H_a, a quasifield Q with the Hall condition is not generated by one element. It is neither left- nor right-cyclic, since the base elements necessarily belong to different Hall subquasifields H_a.

Recall that *right-cyclic* is a quasifield Q of order q^m with the kernel $K \simeq GF(q)$, admitting a K-base $\{e,\ a,\ a^{2)}, \dots, a^{m-1)}\}$, composed of right-ordered degrees of some element $a \in Q$ (left-cyclic is defined similarly).

Theorem 7. *A finite m-dimensional quasifield with the Hall condition ($m > 2$) is not left- and right-primitive, left- and right-cyclic, and is not generated by one element.*

The following result bounds the dimension m of a quasifield with the Hall condition.

Theorem 8. *A finite quasifield with the Hall condition cannot have dimension 3 over its center.*

Proof. Let $|Q| = q^3$, $a \in Q \setminus K$, $A = \theta(a)$ is the corresponding matrix of a spread set, $A \in GL_3(q)$. Since $a \notin K$, then the matrix A is not scalar, its characteristic polynomial has degree three and is divisible by the minimal polynomial of A:

$$\det(A - \lambda E) = (\lambda^2 - r\lambda - s)(\lambda - \beta), \quad \beta \in K.$$

Let $b \in Q$ be an eigenvector of the linear transformation with the matrix A, corresponding to the eigenvalue $\lambda = \beta$:

$$bA = \beta b \Rightarrow ba = b\beta.$$

From the definition of a loop it follows that $a = \beta \in K$, we get a contradiction. □

A quasifield with the Hall condition is neither distributive nor associative.

Theorem 9. *A finite quasifield Q with the Hall condition of dimension $m > 2$ over the kernel is not a semifield.*

Proof. Let Q be a semifield with the Hall condition, $|Q| = |K|^m$, $m > 2$ (more precisely, $m > 3$). If $a \in Q \setminus K$, then $\varphi(a) = \varphi(a + 1) = 0$. Hence $a^2 - ra - s = 0$ and $(a + 1)^2 - r(a + 1) - s = 0$, $2a + 1 - r = 0$. If $p \neq 2$, then $a = (r - 1)/2 \in K$, it contradicts to the condition. Hence, only $p = 2$ and $r = 1$ are possible.

Since $m > 2$, there exist $a, b \in Q \setminus K$ such that $1, a, b$ is a linearly independent system over K. Then $\varphi(a) = \varphi(b) = \varphi(a + b) = 0$, whence $ab + ba = -s$.

The system $1, a, b + s$ is also linearly independent over K, therefore $a(b + s) + (b + s)a = -s$, $as = sa$. Further, from $a + s \notin K$ it follows $\varphi(a + s) = 0$, $s^2 - s = 0$, $s = 1$ ($s \neq 0$ due to the irreducibility of the polynomial $\varphi(x)$). Thus, $\varphi(x) = x^2 + x + 1$, $|K| = 2^{2k+1}$.

Since $m > 3$, the basis Q over K contains at least four linearly independent vectors. Let these be the vectors $1, a, b, c$. Then $a + b + c \notin K$, $\varphi(a + b + c) = 0$, $ab + ba = ac + ca = bc + cb = 1$:

$$(a + b + c)^2 + (a + b + c) + 1 =$$

$$= (a^2 + a + 1) + (b^2 + b + 1) + (c^2 + c + 1) + (ab + ba) + (ac + ca) + (bc + cb) =$$

$$= 1 + 1 + 1 \neq 0,$$

we obtain the contradiction that completes the proof of the theorem. □

Recall that there is one near-field among the Hall quasifields, it is Dickson near-field of order 9. The remaining near-fields of dimension 2 over the kernel do not satisfy the Hall condition: neither the seven exceptional Zassenhaus near-fields, nor the Dickson near-fields from the class $DF(q, 2)$, $q \neq 3$. We will show that the Dickson near-fields of dimension greater than 2 over the kernel also do not satisfy the Hall condition.

Theorem 10. *A finite quasifield Q with the Hall condition of dimension $m > 2$ over the kernel is not a near-field.*

Proof. Let $Q \in DF(q, m)$ be a Dickson near-field of dimension $m > 2$ over the center $K \simeq GF(q)$, $q = p^n$. Then (q, m) is a Dickson pair, i.e. all prime divisors of m divide $q-1$ and $m \not\equiv 0 \pmod 4$ for $q \equiv 3 \pmod 4$.

In accordance with the Dickson–Zassenhaus construction [3], we define a new multiplication $\circ$ on elements of $GF(q^m)$. Let z be a generator of the multiplicative group of the field. For any element $u = z^{km+j}$, the congruence

$$q^i \equiv 1 + j(q - 1) \pmod{m(q - 1)}$$

leads to the number $i \in \{0, 1, 2, \ldots, m-1\}$ and we set $w \circ u = u \cdot w^{q^i}$.

It is clear that for $j = 0$, that is, for $u \in \langle z^m \rangle$, we obtain $w \circ u = u \cdot w$ and, in particular, $u \circ u = u^2$ is a square in the field $GF(q^m)$. The subgroup $H = \langle z^m \rangle$ has the order $(q^m - 1)/m$ and contains more than two elements for any $m \geqslant 3$, which is easily verified by methods of calculus. This means that the quadratic equation $u \circ u - ru - s = 0$ will have more than two roots in the field $GF(q^m)$, among the elements of the set H, which is impossible. The theorem is proved. □

3. Quasifields of order 16 with the Hall condition

Let Q be a quasifield of order 16 with the Hall condition, 4-dimensional over the center $\mathbb{Z}_2$. Then any element $a \in Q$, not equal 0 or 1, has the minimal polynomial $\varphi(x) = x^2 + x + 1$, irreducible over the center, and a quasified Q is the union of seven subfields of order 4. The matrix $A = \theta(a)$ from the spread set $R \subset GL_4(2) \cup \{0\}$ has the minimal polynomial divisible to $\varphi(x)$ [21], so the normal diagonal form of the matrix $A - \lambda E$ must be $diag(1, 1, \varphi(\lambda), \varphi(\lambda))$ or $diag(1, 1, 1, \varphi^2(\lambda))$.

The square matrices of the same dimension are conjugated iff their characteristic matrices have the same normal diagonal form. Therefore, without loss of generality, we can assume that $R \setminus \{0, E\}$ contains in the union of two conjugacy classes $[A_1]$ and $[A_2]$, with the representatives

$$A_1 = \begin{pmatrix} 0 & 1 & 0 & 0 \\ 1 & 1 & 0 & 0 \\ 0 & 0 & 0 & 1 \\ 0 & 0 & 1 & 1 \end{pmatrix}, \quad A_2 = \begin{pmatrix} 0 & 1 & 0 & 0 \\ 1 & 1 & 0 & 0 \\ 1 & 0 & 0 & 1 \\ 0 & 1 & 1 & 1 \end{pmatrix}.$$

Direct computer calculations show the powers of these classes: $|[A_1]| = 112$ and $|[A_2]| = 1680$. Nevertheless, we must preserve in the class $[A_2]$ only the matrices A, where the first row $a = (a_{11}, a_{12}, a_{13}, a_{14})$ is the root of the polynomial $\varphi(x)$, that is with the condetion $a \cdot A + a + 1 = 0$. Here $1 = (1, 0, 0, 0) = e_1$ is the identity of a quasifield Q and the first base vector. The union of two conjugacy classes, with this restriction, contains 448 matrices. Divide all the matrices into subclasses numerated by the first row: M_{0001}, M_{0010}, M_{0011}, …, M_{1111}. Choose one matrix from every subclass, complete the matrices set by zero and identity matrices, and prove the definition of a spread set: any non-zero matrices difference must be non-degenerated. From the subclass M_{0100} we choose A_1 or A_2. Computer search of variants results in 100 spread sets from the class $[A_1]$, no one spread sets from the class $[A_2]$, and three spread sets from the union $[A_1] \cup [A_2]$.

It is known (for instance, [22]), that the isomorphism of the quasifields of the same order p^n is a linear map $\beta : u \to uB$ of n-dimensional vector space over $\mathbb{Z}_p$, it operates on the spread sets R and R' by conjugation:

$$B^{-1}\theta(u)B = \theta'(uB) \quad \forall u \in Q$$

(here $\theta(u) \in R$, $\theta'(uB) \in R'$). This linear map with the matrix B must transfer the identity of the first quasifield to the identity of the second quasifield, therefore the first row of the matrix B equals $(1, 0, 0, 0)$. Consider all such the matrices, we obtain the isomorphism classes and, simultaneously, we find the automorphism group of every quasifield.

To store information about the matrices $B \in GL_4(2)$ and quickly access them in programs,

we introduce the *binary number* of each matrix (see also [19]):

$$B = \begin{pmatrix} b_{11} & b_{12} & b_{13} & b_{14} \\ b_{21} & b_{22} & b_{23} & b_{24} \\ b_{31} & b_{32} & b_{33} & b_{34} \\ b_{41} & b_{42} & b_{43} & b_{44} \end{pmatrix} \Rightarrow$$

$$N(B) = 2^{15} \cdot b_{11} + 2^{14} \cdot b_{12} + 2^{13} \cdot b_{13} + 2^{12} \cdot b_{14} + 2^{11} \cdot b_{21} + \cdots + 2b_{43} + b_{44}.$$

So, for instance, the identity matrix E has the binary number 33825. The Tab. 1 contains the spread sets of all pairly non-isomorphic quasifields of order 16 with the Hall condition, defined by binary numbers of their matrices, without 0 and E.

Table 1. Spread sets of quasifields

Quasifield	Binary numbers of matrices from $R \setminus \{0, E\}$
Q_1	4713 9133 12773 19475 23223 27484 31178 40664 44934 48511 51250 54862 59387 62868
Q_2	4713 9133 12773 19475 23494 27003 31388 40792 44430 48887 51250 55231 58836 63050
Q_3	4713 9636 14686 19475 23494 25562 31388 38472 41349 48511 51250 57319 59387 65213
Q_4	4713 9636 15062 19475 21406 27484 31178 38472 41349 48887 51250 55231 61309 65003
Q_5	4713 10671 15062 19475 22506 27484 29109 38472 44430 48887 51250 54219 61309 62868
Q_6	6105 11686 14686 19475 21103 26036 31388 39912 41349 48887 51250 54219 61309 63050
Q_7	6905 11175 14686 19475 21103 25562 29109 38472 42892 46532 51250 56982 61309 65003
Q_8	7033 10671 15062 19475 22506 26036 30285 40792 44430 48887 51250 54219 57749 62060
Q_9	4729 9135 12758 19475 23271 27482 31165 40520 44940 48580 51250 54942 59381 62827
Q_{10}	6761 11181 14821 19475 21183 25556 29002 38488 42894 46583 51250 57030 61307 64924
Q_{11}	7161 10663 14942 19475 22378 26044 30405 40920 44422 48767 51250 54091 57757 62180

The spread sets of three quasifields Q_9, Q_{10} и Q_{11} contains two matrices 19475 (A_1) and 51250 ($A_1 + E$) from the class $[A_1]$, and other matrices from the class $[A_2]$. The first eight quasifieds has the spread set from $[A_1] \cup \{0, E\}$.

Now we consider the isomorphisms $\beta : Q_i \to Q_i$ and obtain the elements of the automorphism groups $Aut\, Q_i$. The Tab. 2 contains the binary numbers of matrices from automorphism groups.

The small orders of these groups allow us to recognize the groups by the spectrum, see Tab. 3.

Theorem 11. *There exists exactly 11 pairly non-isomorphic quasifields of order 16 with the Hall condition. They all are 4-dimensional over the center $\mathbb{Z}_2$ and they are the union of seven subfields of order 4. The automorphism groups of these quasifields are: S_3, S_4, A_4, $\mathbb{Z}_7 \leftthreetimes \mathbb{Z}_3$ and the simple non-Abelian group $PSL(2, 7)$.*

Table 2. Automorphism groups

Quasifield	$Aut\,Q_i$	Binary numbers of matrices from $Aut\,Q_i$
Q_1, Q_7, Q_9, Q_{10}, Q_{11}	S_4	33811 33825 33842 33887 33901 33918 33943 33957 33974 34011 34025 34042 35858 35875 35889 35930 35947 35961 35998 36015 36029 36054 36071 36085
Q_5	S_4	33353 33366 33463 33710 33737 33759 33825 33887 33974 34094 34119 34225 35382 35527 35545 35631 35662 35673 35889 36015 36054 36151 36257 36302
Q_2	S_3	33811 33825 33842 35858 35875 35889
Q_6	S_3	33825 33943 34042 35858 35961 36012
Q_3	$\mathbb{Z}_7 \leftthreetimes \mathbb{Z}_3$	33090 33149 33214 33300 33403 33517 33825 33918 34011 34738 34769 34788 35623 35661 35809 36119 36142 36276 36379 36423 36562
Q_4	A_4	33090 33300 33710 33825 34203 34509 35253 35555 35673 36054 36204 36410
Q_8	$PSL(2,7)$	33063 33086 33099 33106 33132 33141 33190 33215 33226 33235 33261 33268 33311 33333 33353 33366 33379 33404 33437 33463 33483 33492 33505 33534 33558 33581 33610 33628 33639 33649 33685 33710 33737 33759 33764 33778 33811 33825 33842 33887 33901 33918 33943 33957 33974 34011 34025 34042 34074 34094 34100 34119 34153 34163 34207 34219 34225 34242 34284 34294 34324 34347 34367 34373 34385 34426 34450 34477 34489 34499 34519 34556 34589 34596 34617 34630 34651 34658 34714 34723 34750 34753 34780 34789 35109 35133 35151 35159 35178 35186 35244 35252 35270 35294 35299 35323 35358 35382 35405 35411 35429 35451 35476 35516 35527 35545 35567 35569 35607 35631 35662 35673 35681 35702 35740 35748 35781 35794 35818 35837 35858 35875 35889 35930 35947 35961 35998 36015 36029 36054 36071 36085 36123 36140 36151 36163 36207 36212 36246 36257 36282 36302 36322 36345 36373 36393 36412 36417 36436 36477 36507 36519 36530 36559 36570 36595 36636 36646 36666 36674 36702 36708 36755 36777 36789 36813 36817 36843

Table 3. Number of automorphisms of order 2,3,4,7

Quasifield	$\lvert AutQ_i\rvert$	**2**	**3**	**4**	**7**	$AutQ_i$
Q_1, Q_5, Q_7, Q_9, Q_{10}, Q_{11}	24	9	8	6		S_4
Q_2, Q_6	6	3	2			S_3
Q_3	21		14		6	$\mathbb{Z}_7 \leftthreetimes \mathbb{Z}_3$
Q_4	12	3	8			A_4
Q_8	168	21	56	42	48	$PSL(2,7)$

Note that the computer result corresponds to the estimation of automorphism group order from Lemma 1: the order of $|Aut\,Q|$ must divide the number

$$\frac{n}{t}(q^2-q)\cdot(1+q+q^2+\cdots+q^{m-2})! = \frac{2}{2}(2^2-2)(1+2+2^2)! = 2\cdot 7!$$

Really, it holds for orders of all constructed automorphism groups $Aut\,Q_i$.

To investigate quasifields, it is useful to represent the matrix elements in the spread set by the functions (polynomials) of the first row elements as arguments. In the case of basic field $\mathbb{Z}_2$ these functions are Zhegalkin polynomials, which are easy to find by direct search or by the indefinite coefficients method. Thus, the functional record of the spread set matrices for the quasifield Q_5 is following:

$$\theta(x,y,z,t) = \begin{pmatrix} x & y & z & t \\ y+z+yz+yt & x+y+yz & t+yz & z+yt+zt \\ z+yz+yt & t+yz & x+z+t+yz & y+yt+zt \\ z+t & z & y+z & x+y+z+t \end{pmatrix} =$$

$$= x\begin{pmatrix}1&0&0&0\\0&1&0&0\\0&0&1&0\\0&0&0&1\end{pmatrix} + y\begin{pmatrix}0&1&0&0\\1&1&0&0\\0&0&0&1\\0&0&1&1\end{pmatrix} + z\begin{pmatrix}0&0&1&0\\1&0&0&1\\1&0&1&0\\1&1&1&1\end{pmatrix} + t\begin{pmatrix}0&0&0&1\\0&0&1&0\\0&1&1&0\\1&0&0&1\end{pmatrix} +$$

$$+yz\begin{pmatrix}0&0&0&0\\1&1&1&0\\1&1&1&0\\0&0&0&0\end{pmatrix} + yt\begin{pmatrix}0&0&0&0\\1&0&0&1\\1&0&0&1\\0&0&0&0\end{pmatrix} + zt\begin{pmatrix}0&0&0&0\\0&0&0&1\\0&0&0&1\\0&0&0&0\end{pmatrix}.$$

For compact record of the matrix polynomial $\theta(x,y,z,t)$, we replace each coefficient matrix with its binary number:

$$\theta(x,y,z,t) = x[33825] + y[19475] + z[10671] + t[4713] + yz[3808] + yt[2448] + zt[272].$$

Such the functional representation of the spread set for all quasifields is shown in the Tab. 4. Note that two first terms are $xE + yA_1$ throughout the table.

As it is proven in [15], three quasifields of order 16 with the Hall condition from the paper [13] are not contained as subquasifields in any finite Hall quasifield. Let prove this fact for all quasifields of order 16 with the Hall condition, without exact matrix representation of all 11 spread sets. Nevertheless, this proof is possible due to the unique irreducible quadratic polynomial over $\mathbb{Z}_2$, and it is difficult for another basic field, even in the case of the same dimension 4.

Theorem 12. *A quasifield of order 16 with the Hall condition is not contained in any finite Hall quasifield.*

Proof. Let Q be a quasifield of order 16 with the Hall condition, it is 4-dimensional over the center $\mathbb{Z}_2$. Let the vectors $e_1 = 1$, $e_2 = a = (0,1,0,0)$, $e_3 = b = (0,0,1,0)$, $e_4 = c = (0,0,0,1)$ form its base. Consider the correspondent matrices from the spread set:

$$\theta(a) = \begin{pmatrix}0&1&0&0\\1&1&0&0\\a_1&0&0&1\\0&a_1&1&1\end{pmatrix}, \quad \theta(b) = \begin{pmatrix}0&0&1&0\\b_1&b_2&b_3&b_4\\1&0&1&0\\b_5&b_6&b_7&b_8\end{pmatrix}, \quad \theta(c) = \begin{pmatrix}0&0&0&1\\c_1&c_2&c_3&c_4\\c_5&c_6&c_7&c_8\\1&0&0&1\end{pmatrix},$$

Table 4. Functional representation of spread sets

Quasifield	$\theta(x,y,z,t)$
Q_1	$x[33825]+y[19475]+z[9133]+t[4713]+xz[2058]+xt[2192]+$ $+yz[1250]+yt[1229]+zt[33]+xyz[140]+xyt[72]+xzt[2081]+yzt[1043]$
Q_2	$x[33825]+y[19475]+z[9133]+t[4713]+xz[2562]+xt[2320]+$ $+yz[1733]+yt[1468]+zt[33]+xyz[652]+xyt[328]+xzt[2081]+yzt[1043]$
Q_3	$x[33825]+y[19475]+z[9636]+t[4713]+yz[2669]+yt[1468]+zt[3731]$
Q_4	$x[33825]+y[19475]+z[9636]+t[4713]+yz[747]+yt[3556]+zt[3355]$
Q_5	$x[33825]+y[19475]+z[10671]+t[4713]+yz[3808]+yt[2448]+zt[272]$
Q_6	$x[33825]+y[19475]+z[11686]+t[6105]+xy[72]+xz[2568]+xt[400]+$ $+yz[64]+yt[3457]+zt[801]+xyz[1190]+xyt[3157]+xzt[803]+yzt[528]$
Q_7	$x[33825]+y[19475]+z[11175]+t[6905]+yz[512]+yt[256]+zt[2048]$
Q_8	$x[33825]+y[19475]+z[10671]+t[7033]+xy[196]+xz[2562]+yz[1638]+$ $+yt[289]+zt[3857]+xyz[3240]+xyt[2204]+xzt[394]+yzt[887]$
Q_9	$x[33825]+y[19475]+z[9135]+t[4729]+xz[2050]+xt[2064]+$ $+yz[1254]+yt[1165]+xyz[140]+xyt[72]+xzt[2081]+yzt[1043]$
Q_{10}	$x[33825]+y[19475]+z[11181]+t[6761]+xz[2050]+xt[2064]+$ $+yz[1130]+yt[1221]+zt[2081]+xyz[140]+xyt[72]+xzt[2081]+yzt[1043]$
Q_{11}	$x[33825]+y[19475]+z[10663]+t[7161]+yz[8]+yt[128]+zt[2048]$

$a_1, b_i, c_i \in \mathbb{Z}_2$. If $a_1 = 0$, then we have the matrix $\theta(a) = A_1$ with the minimal polynomial x^2+x+1, and the matrix $\theta(a) = A_2$ with the minimal polynomial $(x^2+x+1)^2$ in the case $a_1 = 1$.

If the Hall quasifield Q' of order 2^{2n} with the kernel $K \simeq GF(2^n)$ contains the subquasifield Q_0 of order 16 isomorphic to Q, then n is odd, $Q_0 \cap K = \{0,1\}$, $\varphi(x) = x^2+x+1$.

Let σ be an isomorphism from Q onto Q_0. Define the images of base elements 1, a, b, c in Q_0. It is clear that $1^\sigma = 1$ is the identity of the quasifield Q'. Choose the image of $a^\sigma = d \in Q' \setminus K$ as second base element of the Hall quasifield Q', which is considered as 2-dimensional vector space over K. Then $d \notin K$, otherwise the kernel K contains the subfield of order 4, and the polynomial $\varphi(x)$ is reducible over K; denote $d = a^\sigma = (0,1)$.

Calculate the products of base elements a and b in the quasifield Q:

$$ab = a\theta(b) = (b_1, b_2, b_3, b_4) = b_1 + b_2 a + b_3 b + b_4 c, \qquad ba = (a_1, 0, 0, 1) = a_1 + c.$$

If $b_4 = 0$, then $(b_3 + a)b = b_1 + b_2 a$. The elements $b_3 + a$ and $b_1 + b_2 a$ belong to subquasifield H_a in the quasifield Q, and so $b \in H_a$ due to closedness, and the linear dependence of 1, a, b contradicts the base choice. Thus, $b_4 = 1$.

Let $b^\sigma = (x,y) \in Q'$. If $y = 0$, then $b^\sigma \in K$, that contradicts the condition $\varphi(b^\sigma) = 0$. Therefore, $y \neq 0$ and from (1) we have

$$\theta'(b^\sigma) = \theta'(x,y) = \begin{pmatrix} x & y \\ -y^{-1}\varphi(x) & r-x \end{pmatrix} = \begin{pmatrix} x & y \\ y^{-1}(x^2+x+1) & 1+x \end{pmatrix}.$$

Find the image c^σ from the conditions $ab = b_1 + b_2a + b_3b + c$ and $ba = a_1 + c$:

$$\begin{aligned} c^\sigma &= a^\sigma b^\sigma + b_1 1^\sigma + b_2 a^\sigma + b_3 b^\sigma = (0,1)\theta'(x,y) + b_1(1,0) + b_2(0,1) + b_3(x,y) = \\ &= (y^{-1}(x^2+x+1) + b_1 + b_3 x, 1 + x + b_2 + b_3 y), \\ c^\sigma &= b^\sigma a^\sigma + a_1 1^\sigma = (x,y)\theta'(0,1) + a_1(1,0) = (y + a_1, x + y). \end{aligned}$$

Now we have the system of equations

$$\begin{cases} y^{-1}(x^2+x+1) + b_1 + b_3 x = y + a_1, \\ 1 + x + b_2 + b_3 y = x + y, \end{cases} \tag{4}$$

and from the second equation we obtain $(b_3+1)y = 1 + b_2$, and $y \in \mathbb{Z}_2$, $y = 1$, or $b_2 = b_3 = 1$. If $y = 1$, then we obtain $b^\sigma = x1 + d = x1 + a^\sigma$, $(a+b)^\sigma = x \in K$. Because $\varphi(a+b) = 0$ in Q, we see $\varphi(x) = 0$ in Q', the contradiction.

It remains to consider the case $b_2 = b_3 = 1$. As $ca = a_1 + b + c$, from the isomorphism we have $c^\sigma a^\sigma = a_1 a^\sigma + b^\sigma + c^\sigma$,

$$(y + a_1, x + y)\begin{pmatrix} 0 & 1 \\ 1 & 1 \end{pmatrix} = a_1(0,1) + (x,y) + (y + a_1, x + y) \Rightarrow a_1 = 0,\ c^\sigma = (y, x + y).$$

If $a_1 = 0$, then the minimal polynomial of the matrix $\theta(a)$ is $\lambda^2 + \lambda + 1$, and from the arbitrary of base elements choice it follows that the matrices $\theta(b)$ and $\theta(c)$ have the same minimal polynomial. Turning the matrix $\theta(b) - \lambda E$ to a normal diagonal form, we obtain

$$\begin{pmatrix} 1 & 0 & 0 & 0 \\ 0 & 1 & 0 & 0 \\ 0 & 0 & \lambda^2+\lambda+1 & 0 \\ 0 & 0 & t & \lambda^2+\lambda+1 \end{pmatrix},$$

where $t = b_7\lambda^2 + (b_5 + b_7 + 1)\lambda + (b_5 + b_1)$. It is possible only $t = 0$ or $t = \lambda^2 + \lambda + 1$, therefore $b_5 = 1$, $b_7 = b_1 + 1$. Note that the condition $\det(\theta(b) - \lambda E) = (\lambda^2 + \lambda + 1)^2$ leads to $b_4 = b_6 = 1$ and $b_8 = b_2 + 1 = 0$. The element b_1 is non-zero, because otherwise the matrix $\theta(a) + \theta(b)$ contains equal rows and is degenerate. Thus, $b_1 = 1$, $b_7 = 0$,

$$\theta(b) = \begin{pmatrix} 0 & 0 & 1 & 0 \\ 1 & 1 & 1 & 1 \\ 1 & 0 & 1 & 0 \\ 1 & 1 & 0 & 0 \end{pmatrix},$$

and the first equation from the system (4) become

$$x^2 + xy + y^2 + x + y + 1 = 0. \tag{5}$$

For the matrix $\theta(c)$, the characteristic polynomial is $(\lambda^2 + \lambda + 1)^2$, so $c_3 = c_6 = 1$ and $c_7 = c_2 + 1$. The minimal polynomial of the matrix

$$\theta(c) = \begin{pmatrix} 0 & 0 & 0 & 1 \\ c_1 & c_2 & 1 & c_4 \\ c_5 & 1 & c_2+1 & c_8 \\ 1 & 0 & 0 & 1 \end{pmatrix}$$

is $\lambda^2 + \lambda + 1$, and we have two possible cases:

$$(1)\ \begin{cases} c_5 = 0, \\ c_8 = c_1, \\ c_4 = c_1(1 + c_2), \end{cases} \qquad (2)\ \begin{cases} c_5 = 1, \\ c_8 = c_1 + c_2, \\ c_4 = c_1(1 + c_2) + 1. \end{cases}$$

Further we consider $ac = c_1 + c_2 a + b + c_4 c$ and $(ac)^\sigma$:

$$a^\sigma c^\sigma = (0,1) \begin{pmatrix} y & x+y \\ (x+y)^{-1}\varphi(y) & 1+y \end{pmatrix} = c_1(1,0) + c_2(0,1) + (x,y) + c_4(y, x+y),$$

$$\begin{cases} (x+y)^{-1}(y^2 + y + 1) = c_1 + x + c_4 y, \\ 1 + c_2 = c_4(x+y). \end{cases}$$

If $c_4 = 1$, then $x + y = 1$, and the first equation is $y^2 + y + 1 = c_1$, that leads to $c_1 = 1$, $y = 1$, $x = 0$, $b^\sigma = (x, y) = (0, 1) = a^\sigma$, it contradicts linear independence. Thus, $c_4 = 0$, $c_2 = 1$, and the case (1) is realized. The element c_1 is non-zero, because otherwise the matrix $\theta(a) + \theta(c)$ contains the equal rows and is degenerated:

$$\theta(a) + \theta(c) = \begin{pmatrix} 0 & 1 & 0 & 0 \\ 1 & 1 & 0 & 0 \\ 0 & 0 & 0 & 1 \\ 0 & 0 & 1 & 1 \end{pmatrix} + \begin{pmatrix} 0 & 0 & 0 & 1 \\ 0 & 1 & 1 & 0 \\ 0 & 1 & 0 & 0 \\ 1 & 0 & 0 & 1 \end{pmatrix} = \begin{pmatrix} 0 & 1 & 0 & 1 \\ 1 & 0 & 1 & 0 \\ 0 & 1 & 0 & 1 \\ 1 & 0 & 1 & 0 \end{pmatrix}.$$

Therefore, $c_1 = 1$, and the first equation leads to $x^2 + y^2 + x + xy + 1 = 0$, and from (5) we have $y = 0$, that is impossible. The resulting contradiction proves the theorem. □

Remark 1. *Note that the matrices $\theta(b)$ and $\theta(c)$ from this proof have the binary numbers 12204 and 7769 respectively. They are, together with the matrix $\theta(a) = A_1$, contained in eight spread sets from our 103 ones, obtained by direct computer calculations. Nevertheless, the quasifields with these spread sets are in three isomorphism classes of the power 7, 7 and 28, so, they are isomorphic to quasifields with another matrices $\theta(b)$ and $\theta(c)$. This result indirectly confirms the validity of the proved theorem.*

Conclusion

The enumeration problem for quasifield of order 16 with the Hall condition solved here is naturally generalized to the problem of constructing quasifields of another orders. We must note that even in the case of $|Q| = p^4$ and $p > 2$ the reasonings and calculations will become much more complicated, because in this case the minimal polynomial of a non-scalar matrix can be the product of two different irreducible polynomials $\varphi(x)\psi(x) \in \mathbb{Z}_p[x]$. The question of the existence of such quasifields remains open, as well as an estimate of their number.

Problems on the order and the quantity of subquasifields in Hall quasifields and in the quasifields with the Hall condition are of natural interest: *Can such a quasifield contain a subquasifield of a dimension greater than two over the kernel?*

The assumption of the existence of a non-Hall quasifield in a Hall quasifield does not contain obvious contradictions. It seems possible that an arbitrary subquasifield F of a Hall quasifild Q does not satisfy the Hall quasifield definition. Evidently, it may be in the case when the coefficients of the polynomial $\varphi(x)$ do not belong to the center of subquasifield F.

The authors hope for further development of the spread set method in relation to the objects described and for progress in solving the problems of classification of finite quasifields.

This work is supported by the Krasnoyarsk Mathematical Center and financed by the Ministry of Science and Higher Education of the Russian Federation (Agreement no. 075-02-2025-1790).

References

[1] L.E.Dickson, Linear algebras in which division is always uniquely possible, *Trans. Amer. Math. Soc.*, **7**(1906), no. 3, 370–390. DOI: 10.1090/S0002-9947-1906-1500755-5

[2] O.Veblen, J.H.Maclagan–Wedderburn, Non-Desarguesian and Non-Pascalian Geometries, *Trans. Amer. Math. Soc.*, **8**(1907), no. 3, 379–388. DOI: 10.1090/S0002-9947-1907-1500792-1

[3] M.Hall, The theory of groups, Chelsea Pub. Co, 1976.

[4] D.R.Hughes, F.C.Piper, Projective planes, Springer–Verlag, New–York Inc., 1973.

[5] L.E.Dickson, On finite algebras, Nachr. Akad. Wiss. Göttingen, Math.-Phys., Kl. II, 1905, 358–393.

[6] H.Zassenhaus, Uber endliche Fastkörper, *Abh. Math. Sem. Hamburg*, **11**(1936), 187–220. DOI: doi.org/10.1007/BF02940723

[7] M.Hall, Projective planes, *Trans. Amer. Math. Soc.*, **54**(1943), 229–277. DOI: 10.1090/S0002-9947-1943-0008892-4

[8] S.B.Nesbitt–Stobert, C.W.L.Garner, A direct proof that all Hall planes of the same finite order are isomorphic, *Riv. Mat. Univ. Parma*, **12**(1986), no. 4, 241–247.

[9] M.Biliotti, V.Jha, N.L.Johnson, Foundations of translation planes, *Marcel Dekker Inc., New York, Basel*, (2001).

[10] G.P.Nagy, Doubly transitive sete of even permutations, *Bul. Acad. Ştiinţe. Repub. Mold. Mat.*, **1**(2016), 78–82.

[11] Y.Hiramine, A generalization of Hall quasifields, *Osaka J. Math.*, **22**(1985), 61–69. DOI: 10.18910/7798

[12] U.Dempwolff, A.Reifart, The Classification of the translation planes of order 16, Part I, *Geom. Dedic.*, **15**(1983), 137–153.

[13] V.M.Levchuk, P.K.Shtukkert, Problems on structure for quasifields of orders 16 and 32, *Journal of Siberian Federal University. Mathematics & Physics*, **7**(2014), no. 3, 362–372.

[14] V.M.Levchuk, O.V.Kravtsova, Problems on structure of finite quasifields and projective translation planes, *Lobachevskii Journal of Mathematics*, **38**(2017), no. 4, 688–698. DOI: 10.1134/S1995080217040138

[15] O.V.Kravtsova, V.S.Loginova, Questions of the structure of finite Hall quasifields, *Trudy Inst. Mat. i Mekh. UrO RAN*, **30**(2024), no. 1, 128–141.

[16] O.V.Kravtsova, D.S.Skok, The spread set method for the construction of finite quasifields, *Trudy Inst. Mat. i Mekh. UrO RAN*, **28**(2022), no. 1, 164–181.

[17] H.Mäurer, Die affine Projektivitätengruppe der Hallebenen [The affine group of projectivities of the Hall planes], *Aequationes Math.*, **32**(1987), 271–273.

[18] G.P.Wene, On the multiplicative structure of finite division rings, *Aequationes Math.*, **41**(1991), 222–233. DOI: 10.1007/BF02227457

[19] I.R.Hentzel, I.F.Rúa, Primitivity of finite semifields with 64 and 81 elements, *International Journal of Algebra and Computation*, **17**(2007), no. 7, 1411–1429. DOI: 10.1142/S0218196707004220

[20] M.Cordero, V.Jha, On the multiplicative structure of quasifields and semifields: cyclic and acyclic loops, *Note di Matematica*, **29**(2009), no. 1, 45–59. DOI: 10.1285/i15900932v29n1supplp45

[21] O.V.Kravtsova, Minimal polynomials in finite semifields, *Journal of Siberian Federal University. Mathematics & Phisics*, **11**(2018), no. 5, 588–596. DOI: 10.17516/1997-1397-2018-11-5-588-596

[22] O.V.Kravtsova, On automorphisms of semifields and semifield planes, *Sib. Elect. Math. Rep.*, **13**(2016), 1300–1313.

Конечные квазиполя с условием Холла

Ольга В. Кравцова
Сибирский федеральный университет
Красноярск, Российская Федерация
Валерия С. Логинова
Институт вычислительного моделирования СО РАН
Красноярск, Российская Федерация

Аннотация. Для координатизации недезарговых проективных плоскостей трансляций с начала прошлого века применяют неассоциативные алгебраические системы: полуполя и квазиполя. Эти системы находят сейчас приложение и в разработке криптографических алгоритмов.

Квазиполя Холла были представлены в 1943 году и явились первым примером недистрибутивных и неассоциативных квазиполей. Это двумерные над центром квазиполя, все нецентральные элементы которых удовлетворяют одному квадратному уравнению. Группа автоморфизмов действует транзитивно на нецентральных элементах. Все квазиполя Холла одного порядка координатизируют одну плоскость трансляций – плоскость Холла.

Увеличивая размерность квазиполя над центром, получаем обобщенные квазиполя с условием Холла. Такое квазиполе не может быть ни полуполем, ни почти-полем. Одному неприводимому многочлену над данным полем может соответствовать несколько неизоморфных квазиполей с условием Холла.

Для исследования применяется метод регулярного множества, основанный на записи умножения как линейного преобразования. Решение некоторых структурных вопросов естественно переносится с двумерного случая: описаны подполя и спектры. В отличие от квазиполя Холла, многомерное квазиполе с условием Холла не может порождаться одним элементом, что дополняет результаты М. Кордеро и В. Джа 2009 г. о покрытии и примитивности.

Представляя примеры, авторы перечисляют все неизоморфные квазиполя порядка 16 с условием Холла и определяют их группы автоморфизмов.

Ключевые слова: квазиполе Холла, квазиполе с условием Холла, регулярное множество, спектр, автоморфизм, правопримитивное квазиполе.

EDN: TGWSLB
УДК 524.3

Charged Particles Finite Motion in Gutsunaev-Manko Spacetime

Sergei Ph. Tegai*
Ivan V. Kichigin†
Siberian Federal University
Krasnoyarsk, Russian Federation

Received 19.10.2025, received in revised form 26.11.2025, accepted 27.12.2025

Abstract. We study the motion of a charged particle in the Gutsunaev–Manko spacetime, which is an exact solution of the Einstein–Maxwell equations for a massive magnetic dipole. The problem is reduced to the motion in the two-dimensional effective potential. We find the circular orbits corresponding to potential stationary points not only within the equatorial plane but also under and above it. We show that the motion in the Gutsunaev–Manko spacetime retains such a property of the classical Størmer problem as the transition from periodic to quasi-periodic and chaotic trajectories. Furthermore, for certain parameter values, the Gutsunaev–Manko spacetime allows for the existence of families of periodic trajectories same as in the classical problem. However, for alternative parameter settings, the families of periodic orbits deviate noticeably from the classical ones.

Keywords: general relativity, Størmer problem, periodic orbits, chaotic motion

Citation: S.Ph. Tegai, I.V. Kichigin, Charged Particles Finite Motion in Gutsunaev–Manko Spacetime, J. Sib. Fed. Univ. Math. Phys., 2026, 19(2), 248–259. EDN: TGWSLB.

Introduction

Magnetostatic solutions of the Einstein–Maxwell field equations are of considerable interest due to their possible astrophysical applications. Plenty of such solutions have been found [1] mainly by generating them from stationary vacuum or electrovacuum solutions using the Bonnor theorems [2]. However, the physical properties of those spacetimes, such as the asymptotic behavior or the motion of the test objects have received limited attention so far.

Among numerous exact magnetostatic solutions, the ones that are most valuable from an astrophysical perspective satisfy two essential criteria simultaneously. First, the solution must reduce to Schwarzschild spacetime both at large distances from the source and in the absence of a magnetic field. Second, the magnetic field should exhibit dipole behavior if observed far enough from the center. Only such solutions can be interpreted as the exterior field of some massive object with the dipole magnetic moment. Gutsunaev and Manko [3] demonstrated that the solution they derived fulfills both of these requirements.

In this work, we study the trajectories of charged test particles in the Gutsunaev–Manko spacetime. This is actually a special case of the gravitational Størmer problem which has a long and extensive history since Pisacane [4] incorporated the Newtonian potential into analysis of the Van Allen radiation belts. The study of relativistic corrections for that problem was started

*tegai_s_f@inbox.ru https://orcid.org/0000-0002-4336-5646
†ivan.kichigin.krasnoy.98@mail.ru

by Prasanna and coworkers [5–8], who considered the motion of charged particles in the external dipole magnetic field in the background Schwarzschild and Kerr spacetimes. Later, Preti [9] and Bakala et al [10, 11] addressed various aspects of the same problem. The Paczyński–Wiita potential as the other background has been considered by Schovancová et al [12]. The study of the relativistic off-equatorial motion of charged particles has begun with the works of Prasanna and Sengupta [13] and has been continued by Kovar et al [14,15] who, among other results, confirmed the existence of circular halo orbits in the relativistic case of the Størmer problem. The external magnetic field utilized in the papers listed above doesn't make a contribution to gravity. The fully general relativistic approach, accounting for the distortion of spacetime by the energy of the magnetic field, was adopted by Kovar et al [16]. They considered the trajectories of charged particle in the Bonnor spacetime [17], which is the other exact solution of the Einstein–Maxwell equations.

A remarkable property of the Størmer problem is the existence of chaotic motion [18], [19]. This chaotic behaviour persists in the vicinity of strong gravitational fields. Nakamura and Ishizuka [21] verified this phenomenon in the context of the Kerr spacetime and Kovar et al [16] showed the same for the Bonnor spacetime. Thus, it is reasonable to anticipate the presence of chaotic motion in the Gutsunaev–Manko spacetime as well.

In this study, we consider the two aspects of the gravitational Størmer problem within the Gutsunaev–Manko spacetime. First is the existence and stability of circular orbits of charged test particles. Both the equatorial and halo orbits are treated. Second is the transition from regular to chaotic behavior of the trajectories with the change of the initial conditions.

Natural units with the speed of light c and gravitational constant G set to unity are used throughout the paper.

1. Gutsunaev–Manko solution

The line element $ds^2 = g_{\mu\nu}dx^\mu dx^\nu$ of a static axially symmetric spacetime can be written in the form

$$ds^2 = fdt^2 - \frac{k^2 e^{2\gamma}}{f}\left(x^2-y^2\right)\left(\frac{dx^2}{x^2-1}+\frac{dy^2}{1-y^2}\right) - \frac{k^2}{f}\left(x^2-1\right)\left(1-y^2\right)d\varphi^2, \tag{1}$$

where $f(x,y)$ and $\gamma(x,y)$ are functions dependent on the prolate ellipsoidal coordinates (x,y), and k is a constant. Gutsunaev and Manko [3] derived the following expressions for the metric functions:

$$f = \frac{1}{2}\sqrt{\frac{x-1}{x+1}}\left(\frac{n_-}{d_-}+\frac{n_+}{d_+}\right), \tag{2}$$

$$e^{2\gamma} = \frac{x^2-1}{x^2-y^2}\cdot\frac{\left(n_-d_+ + n_+d_-\right)^4}{\left(1+\alpha^2\right)^8\left(x^2-y^2\right)^8} \tag{3}$$

with auxiliary quantities defined as

$$n_\pm = x^2 - y^2 \pm 2\alpha y\sqrt{x^2-1} + \alpha^2\left(x+1\right)^2, \tag{4}$$

$$d_\pm = x^2 - y^2 \pm 2\alpha y\sqrt{x^2-1} + \alpha^2\left(x-1\right)^2. \tag{5}$$

These expressions provide a solution to the Einstein–Maxwell equations, modeling a massive magnetic dipole. The parameter of the solution α governs the value of the magnetic field. The

corresponding electromagnetic four-potential has only one non-zero component

$$A_\varphi = \frac{8k\alpha^3\left(y^2-1\right)\left[2\left(1+\alpha^2\right)x^3+\left(1-3\alpha^2\right)x^2+y^2+\alpha^2\right]}{\left(1+\alpha^2\right)\left(n_-d_+ + n_+d_-\right)}. \tag{6}$$

Looking at the behaviour of the metric functions and the four-potential at large distances from the source, Gutsunaev and Manko [3] demonstrated that the solution is asymptotically flat and the parameters k and α determine the mass m and the dipole moment μ of the central object by means of the expressions

$$m = k\frac{1-3\alpha^2}{1+\alpha^2}, \tag{7}$$

$$\frac{\mu}{m^2} = \frac{8\alpha^3}{\left(1-3\alpha^2\right)^2}. \tag{8}$$

An important property of the Gutsunev–Manko solution is that it continuously reduces to the Schwarzschild spacetime when the parameter α decreases from any value in the range $0 < \alpha < 1/\sqrt{3}$ down to zero.

The Schwarzschild coordinates (r, θ) are related to the prolate ellipsoidal coordinates (x, y) by the transformation $x = (r-m)/k$, $y = \cos\theta$. For illustration purposes, we utilize logarithmic scaling for the radial coordinate, setting $\rho = \ln r\cos\theta$ and $z = \ln r\sin\theta$.

As the only axially symmetric stationary black hole solution of Einstein–Maxwell equations is the Kerr–Newman solution, the Gutsunaev–Manko spacetime should somehow violate the conditions of the uniqueness theorem. Indeed, Karas and Vokrouhlický [22] demonstrated that the Gutsunaev–Manko solution is not free from singularities residing above the horizon $x = 1$. Specifically, both the metric function $f(x, y)$ and the Riemann tensor diverge at the surface generated by the rotation of the curves $d_\pm(x, y; \alpha) = 0$ around the symmetry axis. The two singularity curves start in points $(x = 1, y = \pm 1)$ and terminate again at $y = \pm 1$ but with $x > 1$. To interpret this solution as representing the exterior spacetime of a realistic astrophysical object carrying a magnetic moment, it is necessary to posit that the entire singularity is enveloped by the stellar surface.

2. The effective potential

The motion of a particle with specific charge q and four-velocity $u^\mu \equiv dx^\mu/ds$ is governed by the Lagrangian

$$\mathcal{L} = \frac{1}{2}g_{\mu\nu}u^\mu u^\nu + qA_\mu u^\mu. \tag{9}$$

Conservation laws corresponding to the cyclic coordinates t and φ are

$$E = \frac{\partial\mathcal{L}}{\partial u^t} = g_{tt}u^t, \tag{10}$$

$$L = -\frac{\partial\mathcal{L}}{\partial u^\varphi} = -g_{\varphi\varphi}u^\varphi - qA_\varphi. \tag{11}$$

Inserting these into the first integral $u_\mu u^\mu = 1$, we obtain the equation

$$-g_{tt}\left(g_{xx}\left(\frac{dx}{ds}\right)^2 + g_{yy}\left(\frac{dy}{ds}\right)^2\right) + g_{tt}\left(1 - \frac{\left(L+qA_\varphi\right)^2}{g_{\varphi\varphi}}\right) = E^2 \tag{12}$$

which corresponds to the motion of a particle in the two-dimensional effective potential

$$V_{eff}(x,y) = g_{tt}\left(1 - \frac{(L+qA_\varphi)^2}{g_{\varphi\varphi}}\right). \tag{13}$$

The potential remains unchanged under simultaneous sign reversals of L and q. Therefore, we will further consider only the positive specific charge q.

The shape of the effective potential (13) is primarily characterized by its stationary points. Every stationary point corresponds to a circular orbit. These orbits can occur either in equatorial plane or outside of it. In the latter case they are referred to as halo circular orbits. The number, type and stability of effective potential critical points depend on the values of the parameters L, q and α_0.

We first consider the parameter choice which yields a clearly distinguishable magnetic lobe so that we can relate the motion in the Gutsunaev–Manko spacetime with the classical Størmer problem. The case is shown in the Fig. 1. There are three equatorial potential wells separated by two barriers. The outermost potential well centers around a local minimum. The motion here is determined mainly by gravity because the magnetic field is of dipole nature and thus decays faster than gravitational. On the contrary, the trajectories in the intermediate lobe are much more affected by the Lorentz force exerted on the charged particle by the magnetic field. The lobe itself has a crescent form typical for Størmer problem. It is located around a saddle point called 'thalweg'. Its corresponding circular orbit is unstable to non-radial perturbations. No circular orbits exist in the innermost potential well adjacent to the horizon. All particles in that region inevitably fall into the horizon, demonstrating relativistic behaviour similar to the Schwarzschild trajectories falling to the singularity.

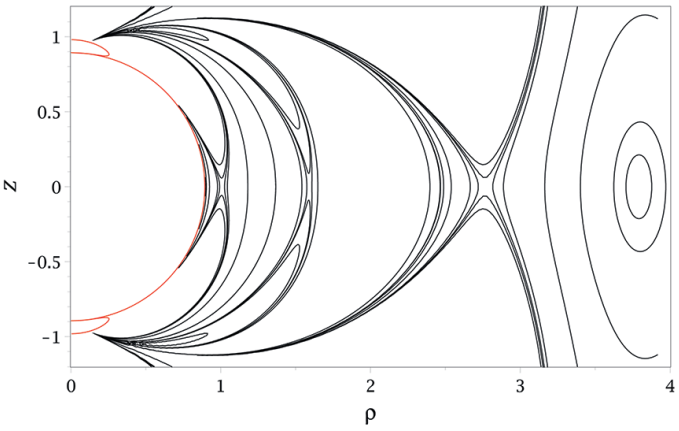

Fig. 1. The contour lines of the effective potential with the parameter values $\alpha_0 = \alpha_{max}/2$, $L = 8$, $q = 90$. The horizon and singularity are shown in dark red

The effective potential exhibits a stable halo circular orbit for the previously selected parameter values. This is illustrated in Fig. 1, where the location of the orbit above the equatorial plane can be clearly seen. These types of orbits were initially investigated by Kovář et al. [16] within the context of Bonnor spacetime, where such trajectories exist even for electrically neutral particles. In the Gutsunaev–Manko solution, the circular halo orbits are only possible for sufficiently large charges.

Varying the parameters L and q changes the number and character of effective potential stationary points both in and above the equatorial plane. Areas in the parameter space with different behaviour of effective potential are separated by its vanishing hessian lines and are shown in Fig. 2.

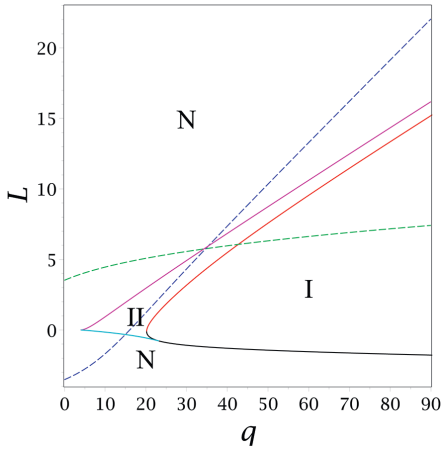

Fig. 2. The areas of the parameters q and L with different numbers of effective potential stationary points for $\alpha = 1/2\sqrt{3}$. Dashed lines indicate the vanishing Hessian in the equatorial plane. Solid lines correspond to vanishing Hessian outside the equatorial plane. There is only one singular point above the equatorial plane in the region I, there are two of them in region II and no halo circular orbits in the region N

Dashed lines denote the vanishing Hessian in the equatorial plane, dividing the parameter plane into four distinct regions. In the upper right part the potential exhibits two minima and two maxima in equatorial plane as in our starting choice described earlier. Conversely, the lower-left region shows no equatorial extrema. There is only one minimum and one maximum in equatorial plane in the remaining parts of the parameter plane. Innermost stable circular orbits (ISCO) with positive angular velocity lie on a green dashed line, while those with negative angular velocity follow a blue dashed line.

Solid lines in Fig. 2 delimit parameter values leading to different number of potential stationary points outside the equatorial plane. Only one stationary point exists above the equatorial plane in region I, necessarily being a minimum corresponding to a stable circular orbit. Two stationary points occur in region II, where the point farther from the equatorial plane remains a minimum while the closer one forms a saddle point. No halo circular orbits appear in region N. Due to the system's mirror symmetry, stationary points below the equatorial plane replicate those found above it. Although halo circular orbits characterized by negative L signs exist in regions I and II of Fig. 2, the particle on the halo circular orbit maintain positive angular velocity.

3. Periodic, quasi-periodic and chaotic motion

It is well established [18–20] that the Newtonian dynamics of a charged particle in a dipole magnetic field may display chaotic behavior. Consequently, analogous properties might reasonably be anticipated in the Gutsunaev–Manko spacetime. Periodic orbits play an essential role in analyzing such chaotic systems. We focus here specifically on simple periodic off-equatorial

trajectories possessing mirror symmetry with respect to equatorial plane.

In this section of the paper, we primarily investigate the parameter choice yielding distinctly separable magnetic and gravitational lobes. This case is is physically closest to the classical problem since the magnetic and gravitational components remain distinguishable.

To find periodic orbits, we initiate vertical upward launches of a particle from the equatorial plane. By adjusting the starting position x_0, we ensure that orbit returns to the initial point vertically from below. Continuous variations in particle energy E result in slight shifts of the starting location for periodic orbits, thereby generating families of simple periodic orbits.

We found that the Gutsunaev–Manko spacetime admits the same families of periodic oscillations observed in the classical problem of a charged particle revolving around a magnetic dipole. A classification scheme for these orbits was introduced by Markellos, Klimopoulos, and Halioulias [23]. Families of symmetric simple-periodic orbits are denoted as $f0, f1, \ldots$. The families are enumerated by their starting points located at the right boundary of the potential well as shown in Fig. 3. The difference from the classical problem is the existence of an $f0$ family branch in the gravitational well displayed in Fig. 3(b). The left branch of the $f0$ curve starts at the maximum of the effective potential ($\rho \approx 2.71$) in the equatorial plane, while its right branch begins at the minimum of the gravitational well at ($\rho \approx 3.79$). Increasing the specific charge q lowers the barrier between the magnetic and gravitational wells. When this barrier disappears, the two parts of the $f0$ family merge.

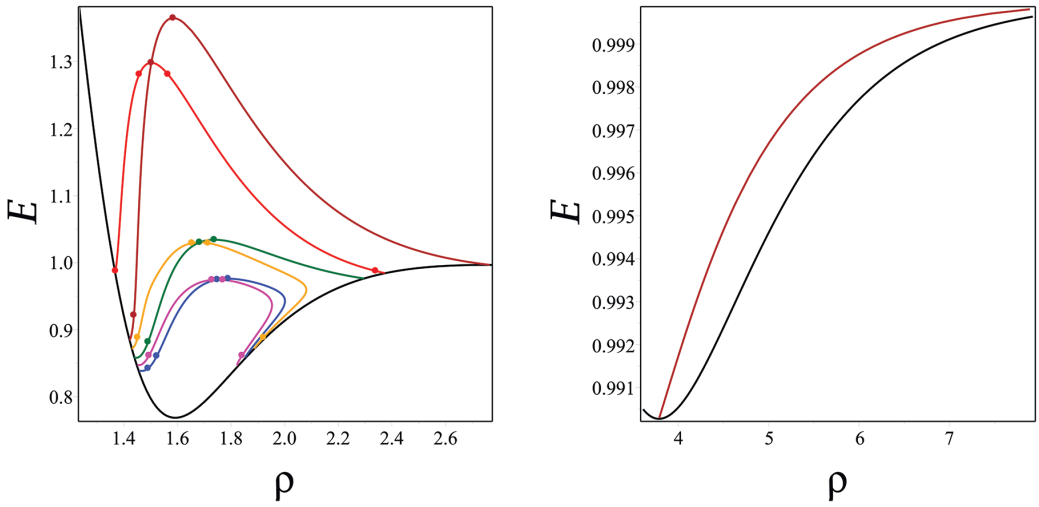

(a) (b)

Fig. 3. Families of symmetric periodic orbits in Gutsunaev–Manko space located in (a) magnetic lobe and (b) gravitational lobe. Colors assigned to orbit families are as follows: brown – $f0$, red – $f1$, green – $f2$, orange – $f3$, blue – $f4$, magenta – $f5$. Effective potential in equatorial plane is shown in black. Points mark transitions in stability of orbits. Parameter values are $\alpha_0 = \alpha_{max}/2$, $L = 8$ and $q = 90$

Typical forms of poloidal projections of the trajectories of the types $f0, f1, f2, f3, f4$ and $f5$ are presented in Fig. 4, as well as the projections of irregular trajectories, originate from different starting points.

Trajectory projections of even families $f0, f2, \ldots$ cross the equatorial plane at one point while trajectory projections of odd families $f1, f3, \ldots$ cross the equatorial plane at two different points.

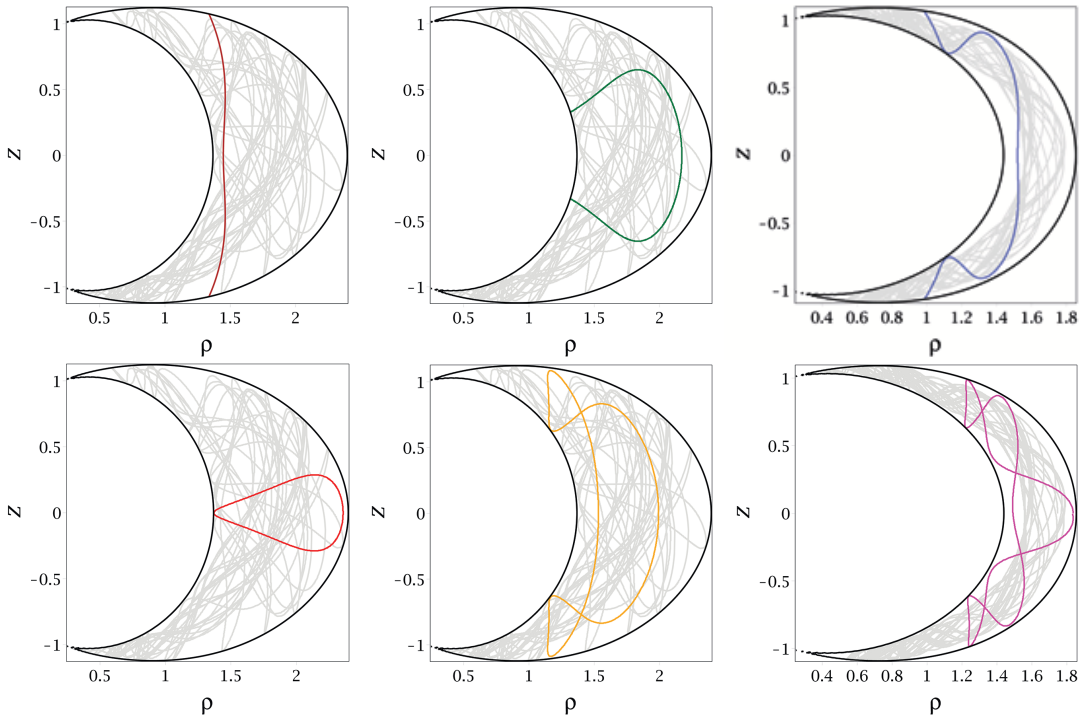

Fig. 4. Typical forms of poloidal projections for different families. Even curves $f0$, $f2$, $f4$ are shown in the top row using the same colors as in Fig. 3. Odd curves $f1$, $f3$, $f5$ are displayed in the second row. Chaotic trajectories of the same energy are depicted in gray. Parameter values used are $\alpha = 1/2\sqrt{3}$, $L = 8$ and $q = 90$. Energy $E = 0.986$ for $f0$, $f1$, $f2$ and $f3$, while $E = 0.858$ for $f4$ and $f5$

The families $f2n$ and $f2n+1$, $n = 0, 1, \ldots$ form a connected pair. Their curves intersect at the maximum of odd family.

Let Δx_0, Δu_0^x be small displacements of trajectory starting coordinate and velocity. These displacements induce subsequent small deviations Δx_1, Δu_1^x of coordinate and velocity of the trajectory next intersection with the equatorial plane. Then stability of orbits is governed by the following linear mapping, as discussed in [24]

$$\begin{pmatrix} \Delta x_1 \\ \Delta u_1^x \end{pmatrix} = \begin{pmatrix} a & b \\ c & d \end{pmatrix} \begin{pmatrix} \Delta x_0 \\ \Delta u_0^x \end{pmatrix}, \tag{14}$$

where a, b, c and d are the stability parameters of the solution given by the partial derivatives

$$a = \frac{\partial x_1}{\partial x_0}, \qquad b = \frac{\partial x_1}{\partial u_0^x}, \qquad c = \frac{\partial u_1^x}{\partial x_0}, \qquad d = \frac{\partial u_1^x}{\partial u_0^x}. \tag{15}$$

For orbits symmetrical with respect to the equatorial plane, the equality $a = d$ holds true [25]. The condition of orbits stability is $|a| = |d| < 1$. Pieces of curves close to their start at the right side of the effective potential exhibit instability. Changes in stability occur precisely when $|a| = |d| = 1$ and are indicated by points in Fig. 3. For instance, $f0$ family is unstable from its starting point at the potential maximum until its highest energy point. Subsequently, a stable

phase emerges until the curve intersects with the $f1$ trajectory. After that it becomes unstable again. Finally, stability restores at the leftmost section of $f0$ curve. The branch of the $f0$ family residing within the gravitational well maintains stability throughout.

Dynamical systems are commonly analyzed using Poincaré surfaces of section. In this study, we construct these surfaces by plotting the intersection points of trajectories with the equatorial plane. Details of the location and stability of periodic orbits obtained earlier in this section significantly aid this process. The resulting Poincaré maps corresponding to the same energy levels used in Fig. 4 are presented in Fig. 5 and Fig. 6.

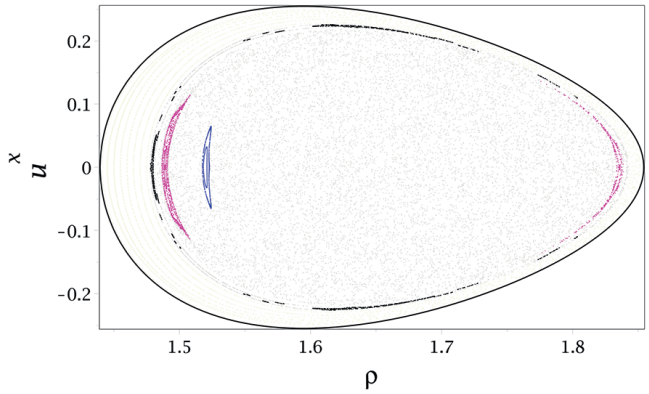

Fig. 5. The Poincaré map for parameter values $\alpha = 1/2\sqrt{3}$, $L = 8$, $q = 90$ and $E = 0.858$

The Poincaré section in Fig. 5 is constructed for energy $E = 0.858$. It includes two stability islands originating from the $f5$ family (shown in magenta) and one island stemming from the $f4$ family (blue). Additionally, a group of regular quasi-periodic curves surrounds the boundary of the Poincaré section (yellow). Curves in the vicinity of 3-periodic orbit are presented by three islands on the same section (black). Gray dots illustrate chaotic trajectories.

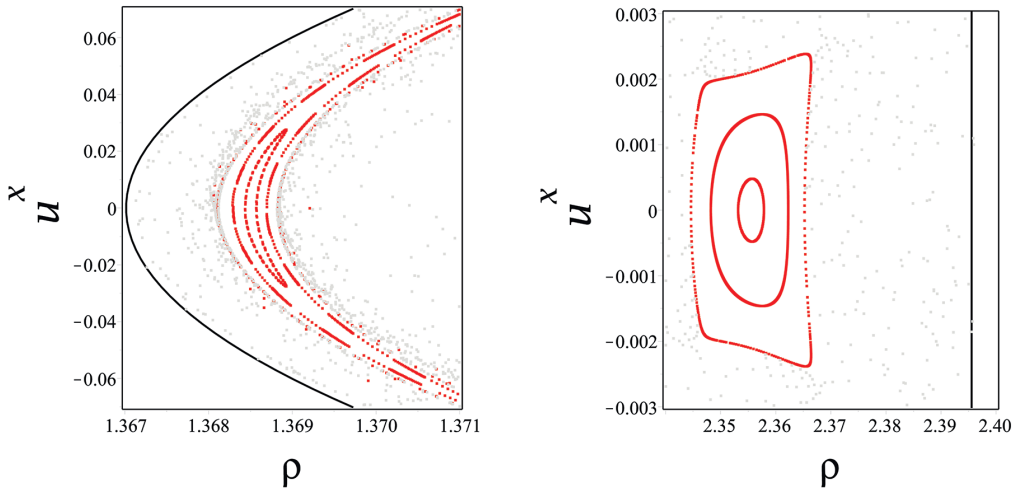

Fig. 6. The Poincaré map for parameter values $\alpha = 1/2\sqrt{3}$, $L = 8$, $q = 90$ and $E = 0.986$. Central part of the surface is omitted for clarity since we could not detect any islands of stability there

The Poincaré section in Fig. 6 represents the system at energy level $E = 0.986$. On this section, we observe only two stability islands belonging to the $f1$ family, located near the left and right edges of the section (colored red). The middle part of the section is removed because it consists solely of chaotic motion. As can be seen from Fig. 3, trajectories of the $f2$ and $f3$ families do exist for energy $E = 0.986$. Nevertheless, we don't observe them clearly on Poincaré surface of section because they produce chaotic motion due to their instability.

Conclusion

We have considered the motion of test charged particles in the Gutsunayev-Manko spacetime. This spacetime has been interpreted by its authors as the field of a massive magnetic dipole based on the asymptotic behavior of gravitational and electromagnetic potentials. Our results show that the Gutsunaev–Manko solution also bears other important properties of the gravitational Størmer problem. Firstly, it contains all the classes of periodic orbits introduced by Markellos [23]. Secondly, it allows the existence of halo circular orbits. And finally, the problem involves a transition from regular to chaotic motion of charged particles within the magnetic lobe of the effective potential.

The distinction between the relativistic problem and its classical counterpart arises from the presence of an additional potential well near the event horizon. This leads to the appearance of innermost stable circular orbits and finite trajectories falling into the horizon. Qualitatively, these trajectories resemble those in Schwarzschild spacetime. However, the innermost stable circular orbits appear in pairs. One orbit for particles moving with positive angular velocity and another for particles with negative angular velocity.

Other possible differences involve the behaviour of off-equatorial periodic orbits with the change of parameters. This is illustrated in Fig. 7. The families exhibited in Fig. 7(a) correspond to a point in parameters space characterized by two extrema of the effective potential in the equatorial plane, located to the right of the blue dashed line in Fig. 2. Whereas Fig. 7(b) portrays families corresponding to a different point in parameter space with no stationary points existing in the equatorial plane and two stationary points outside it.

First of all, the curves $f0$, $f1$ do not intersect the boundary of the potential well, but rather approach asymptotically towards the line $E = 1$ (see Fig. 7). In these situations, Markellos' classification method fails because the starting points of families are missing from the right boundary of the potential well. To address this issue, we distinguish odd curves by number of loops in their poloidal projections and determine types of even orbits based on intersection with odd family curves. However this classification can be uncertain because for some parameters values the number of $f1$ curves can be greater than one (Fig. 7(a)) and the curve of even family can intersect with both $f1$ and $f3$ (Fig. 7(b)).

Furthermore, if the stationary point of the potential represents a two-dimensional minimum, an even-type curve will emerge from it (as seen in Fig. 3(b) and Fig. 7(a)). Also off-equatorial periodic orbits exist even in the absence of circular orbits in the equatorial plane (Fig. 7(b)).

The obtained picture of families of symmetric periodic orbits in the Gutsunaev–Manko spacetime shows that these families, for certain particle parameters values, exhibit noticeable differences compared to the classical problem of charged particle motion in the field of a point magnetic dipole [23]. One reason behind these qualitative disparities in the behaviour of the curves arises from distinctions in the number and type of singular points of the effective potential.

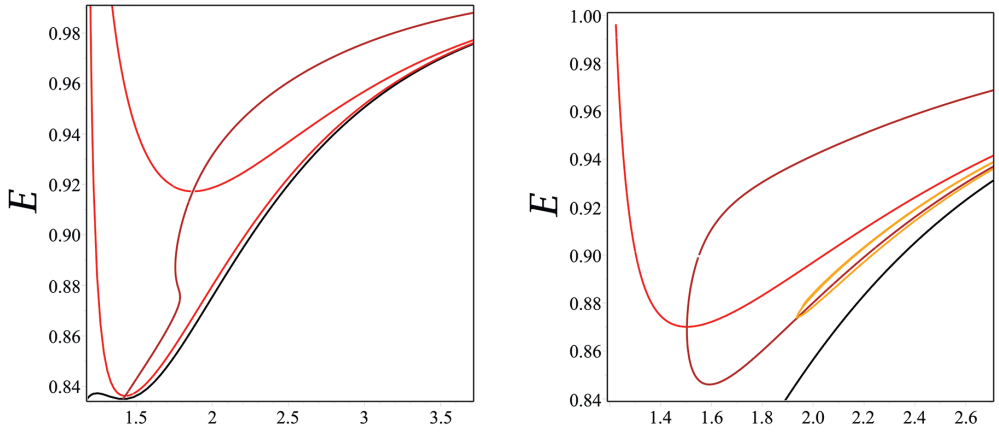

(a) (b)

Fig. 7. Families of symmetric periodic motion of a charged particle in Gutsunaev–Manko solution. The figures are given for parameter values: (a) $q = 13$, $L = -1$ and (b) $q = 12$, $L = -0.1$. Colors of curves are: $f0$ – brown, $f1$ – red, $f3$ – orange and effective potential is black

References

[1] H.Stephani, D.Kramer, M.MacCallum, C.Hoenselaers, E.Herlt, Exact Solutions of Einstein's Field Equations, Cambridge, U.K.: Cambridge University Press, 2003.

[2] W.B.Bonnor, Static magnetic fields in general relativity, *Proc. Phys. Soc. Lond. A*, **67**(1954), 225.

W.B.Bonnor, Exact solutions of the Einstein–Maxwell equations, *Z. Phys.*, **161**(1961), 439.

[3] Ts.I.Gutsunaev, V.S.Manko, On a family of solutions of the Einstein–Maxwell equations, *Gen. Rel. Grav.*, **20**(1988), 327.

[4] V.L.Pisacane Particle motion in the equatorial plane, *AIAA Journal*, **2**(1964), 1361.

[5] A.R.Prasanna, R.K.Varma, Charged particle trajectories in a magnetic field on a curved space-time, *Pramana*, **8**(1977), 229.

[6] A.R.Prasanna, C.V.Vishveshwara, Charged particle motion in an electromagnetic field on Kerr background geometry, *Pramana*, **11**(1978), 359.

[7] A.R.Prasanna, D.K.Chakraborty, Charged particle orbits in Kerr geometry with electromagnetic fields as viewed from locally non-rotating frames, *Pramana*, **14**(1980), 113.

[8] A.R.Prasanna, General-relativistic analysis of charged-particle motion in electromagnetic fields surrounding black holes, *Rev. del. Nuovo Cimento*, **3**(1980), 11.

[9] G.Preti, On charged particle orbits in dipole magnetic fields around Schwarzschild black holes, *Class. Quant. Grav.*, **21**(2004), 3433. DOI: 10.1088/0264-9381/21/14/008

[10] P.Bakala, E.Šrámková, Z.Stuchlík, G.Török, On magnetic-field-induced non-geodesic corrections to relativistic orbital and epicyclic frequencies, *Class. Quant. Grav.*, **27**(2010), 045001. DOI: 10.1088/0264-9381/27/4/045001

[11] P.Bakala, M.Urbanec, E.Šrámková, Z.Stuchlík, G.Török, On magnetic-field-induced corrections to the orbital and epicyclic frequencies: paper II. Slowly rotating magnetized neutron stars, *Class. Quant. Grav*, **29**(2012), 065012. DOI: 10.1017/S1743921312019539

[12] J.Schovancová, L.Šubr, V.Karas, Z.Stuchlík, J.Kovář, Some aspects of the Störmer problem within strong gravitational fields, Proc. RAGtime 6/7: Workshops on Black Holes and Neutron Stars (Silesian University in Opava, Czech Republic, 16–18/18–20 September 2004/2005), 2005, 157.

[13] A.R.Prasanna, S.Sengupta, Charged particle trajectories in the presence of a toroidal magnetic field on a Schwarzschild background, *Phys. Lett.* A, **193** (1994), 25.

[14] J.Kovář, Z.Stuchlík, V.Karas, Off-equatorial orbits in strong gravitational fields near compact objects, *Class. Quant. Grav.*, **25** (2008), 095011. DOI: 10.1088/0264-9381/25/9/095011

[15] J. Kovář, O.Kopáček, V.Karas, Z.Stuchlík, Off-equatorial orbits in strong gravitational fields near compact objects—II: halo motion around magnetic compact stars and magnetized black holes, *Class. Quant. Grav.*, **27**(2010), 135006. DOI: 10.1088/0264-9381/27/13/135006

[16] J.Kovář, O.Kopáček, V.Karas, Y.Kojima, Regular and chaotic orbits near a massive magnetic dipole, *Class. Quant. Grav.*, **30**(2013), 025010. DOI: 10.1088/0264-9381/30/2/025010

[17] W.B.Bonnor, An exact solution of the Einstein–Maxwell equations referring to a magnetic dipole, *Z. Phys.*, **190**(1966), 444.

[18] A.J.Dragt, Trapped orbits in a magnetic dipole field, *Reviews of Geophysics*, **3** (1965), 255.

[19] O.F.A.de Bonfim, D.J.Griffiths, S.Hinkley, Chaotic and hyperchaotic motion of a charged particle in a magnetic dipole field, *Int. J. Bifurcation and Chaos*, **10**(2000), 265. DOI: 10.1142/S0218127400000177

[20] R.Liu, S.Liua, F.Zhub, Q.Chen, Y.He, C.Cai, Orbits of charged particles trapped in a dipole magnetic field, *Chaos*, **32**(2022), 043104. DOI: 10.1063/5.0086161

[21] Y.Nakamura, T.Ishizuka, *Motion of a charged particle around a black hole permeated by magnetic field and its chaotic characters*, *Astrophys. Space Sci.*, **210**(1993), 105.

[22] V.Karas, D.Vokrouhlický, New exact solutions of the Einstein–Maxwell solutions, *Bull. Astron. Inst. Czechosl.*, **42**(1991), 247.

[23] V.V.Markellos, S.Klimopoulos, A.A.Halioulias, Periodic motions in the meridian plane of a magnetic dipole, I, *Celest. Mech.*, **17**(1978), 215.

[24] V.V.Markellos, On the stability parameters of periodic solutions, *Astrophys. Space Sci.*, **43**(1976), 449.

[25] G.H.Darwin, Periodic orbits and miscellaneous papers, *Cambridge University Press*, **4**(1911), 57.

Финитное движение заряженных частиц в пространстве Гуцунаева-Манько

Сергей Ф. Тегай
Иван В. Кичигин
Сибирский федеральный университет
Красноярск, Российская Федерация

Аннотация. Мы рассматриваем движение заряженных частиц в пространстве Гуцунаева–Манько, которое представляет собой точное решение уравнений Эйнштейна–Максвелла для массивного магнитного диполя. Задача сводится к исследованию движения в двумерном эффективном потенциале. Мы находим круговые орбиты, соответствующие стационарным точкам потенциала, как в экваториальной плоскости, так и вне ее. Мы демонстрируем, что движение в пространстве Гуцунаева–Манько сохраняет такое свойство классической задачи Стёрмера, как переход от периодических траекторий к квазипериодическим и нерегулярным. Кроме того, при определённых значениях параметров пространство Гуцунаева–Манько допускает существование семейств периодических траекторий, аналогичных классическим. Однако существуют и такие значения параметров задачи, при которых семейства периодических орбит заметно отличаются от классических.

Ключевые слова: общая теория относительности, задача Стёрмера, периодические орбиты, хаотическое движение.

EDN: ZRKLYA
УДК 517.9

On Approximation Theorems for Solutions to Strongly Parabolic Systems in Anisotropic Sobolev Spaces

Pavel Yu. Vilkov*
Alexander A. Shlapunov†
Siberian Federal University
Krasnoyarsk, Russian Federation

Received 10.10.2025, received in revised form 20.11.2025, accepted 27.12.2025

Abstract. We investigate the problem on Runge pairs for Sobolev solutions of strongly uniformly parabolic systems in non-cylindrical domains of a special kind. We prove that if the coefficients of a parabolic operator are constant, then two domains with sufficiently smooth boundaries, no parts of which are parallel to the plane $t = 0$, form a Runge pair if and only if the complements of any section of the larger domain to the section of the smaller domain by planes $t = const$, have no compact components in the larger section.

Keywords: strongly parabolic equations and systems, approximation theorems, Runge pairs.

Citation: P.Yu. Vilkov, A.A. Shlapunov, On Approximation Theorems for Solutions to Strongly Parabolic Systems in Anisotropic Sobolev Spaces, J. Sib. Fed. Univ. Math. Phys., 2026, 19(2), 260–269. EDN: ZRKLYA.

Approximation theorems for solutions to parabolic operators appeared since 1970-th, see [3, 12], for the heat equation. Actually, these were generalizations of the realated theorems in Complex Analysis see [11, 25, 35] and [2, 17, 19–22, 31, 32] in the theory of (mostly, elliptic) PDE's. Recently, the interest to approximation theorems for general parabolic and elliptical parabolic systems has essentially increased, see, for instance, [5–7, 9, 10, 14, 24, 26, 27, 34]. The main reason for this interest is the following: the classical theory of boundary value problems for parabolic and elliptical parabolic systems was developed in cylinder domains where the method of separating variables allowed to use approximation theorems for elliptic operators instead, see, for instance, [4, 16, 33]. Nowdays, a possibility to consider the boundary problems parabolic for systems in non-cylinder domains becomes very important. For instance, it is the case in Cardiology, because the shape of heart changes over time, see, for instance, [13] where an the ill-posed problem for a parabolic equation was used in the bi-domain model of the myocardium.

In the pioneer papers, Runge considered a pair of domains $D_1 \subset D_2$ of the complex plane and the problem of approximation of holomorphic functions in D_1 by holomorphic functions in D_2 (here the spaces were endowed with the natural Fréchet topology of the space $C(D)$). Various authors used different topologies in the approximation theorems (uniform topology of convergence on compact subsets, toplogies of Lebesgue spaces, Sobolev spaces, etc.). But it turned out that, for elliptic systems, conditions granting for two domains to be a Runge pair are depend essentially on the behaviour of the complement $D_2 \setminus D_1$. For the heat equation, domains $G_1 \subset G_2 \subset \mathbb{R}^{n+1}$ form a Runge pair if and only if the complements $G_2(c) \setminus G_1(c)$ of any section $G_2(c)$ of the larger domain to the section $G_1(c)$ of the smaller domain by hyperplanes $t = c = const$, have no compact components in the larger section.

Actually, as the Faedo-Galerkin method is still very efficient for solving boundary value problems, the consideration of Runge pairs allows to construct series representing a solution to

*pavel_vilkov17@mail.ru
†ashlapunov@sfu-kras.ru

a problem with summands regular at a greater domain. Besides, it is important for applications to have approximation theorems with respect to topologies controlling the behavior of functions up to the boundary of the related domain; see, for instance, Runge type approximation theorems in the Lebesgue space for analytic functions [11], for strongly parabolic operators [27, 34], and approximation theorems in the Sobolev spaces for elliptic operators [31, Ch. 5], [32, Ch. 8].

In this paper we concentrated our efforts on the Runge type approximation theorems for strongly $2m$-parabolic operators with constant coefficients in anisotropic Sobolev spaces. The primary motivation is the systematic use of this type of spaces for solving boundary value problems. We rely essentially on the results of the paper [27] on the Runge type approximation theorems for Lebesgue L^2-solutions to strongly $2m$-parabolic operators keeping the related denotions in the present paper.

1. Preliminaries

Let $\mathbb{R}^n$, $n \geqslant 1$, be the n-dimensional Euclidean space with the coordinates $x = (x_1, \dots, x_n)$ and let $\Omega \subset \mathbb{R}^n$ be a bounded domain (open connected set). As usual, denote by $\overline{\Omega}$ the closure of Ω, and by $\partial\Omega$ its boundary.

We consider functions over $\mathbb{R}^n$ and $\mathbb{R}^{n+1}$. As usual, for $s \in \mathbb{Z}_+$ we denote by $C^s(\Omega)$ and $C^s(\overline{\Omega})$ the spaces of all s times continuously differentiable functions on Ω and $\overline{\Omega}$, respectively. The spaces $C^s(\overline{\Omega})$ are known to be Banach spaces with the standard norms and the $C(\Omega)$ are the Fréchet spaces with the standard semi-norms.

Let also $L^2(\Omega)$ be the Lebesgue space over Ω with the standard inner product $(u, v)_{L^2(\Omega)}$ and let $H^s(\Omega)$, $s \in \mathbb{N}$, be the Sobolev space with the standard inner product $(u, v)_{H^s(\Omega)}$. As usual, we consider the Sobolev space $H^{-s}(\Omega)$, $s \in \mathbb{N}$, as the dual space of $H^s_0(\Omega)$ where $H^s_0(\Omega)$ is the closure of the space $C^\infty_{\rm comp}(\Omega)$ consisting of smooth functions with compact supports in Ω.

Given $m, s \in \mathbb{N}$, we also need the anisotropic Sobolev spaces $H^{2ms,s}(G)$, $s \in \mathbb{Z}_+$, in a domain $G \subset \mathbb{R}^{n+1}$ with the standard inner product,

$$(u, v)_{H^{2ms,s}(G)} = \sum_{|\alpha|+2mj \leqslant 2ms} (\partial_x^\alpha \partial_t^j u, \partial_x^\alpha \partial_t^j v)_{L^2(G)}.$$

Besides, for $\gamma \in \mathbb{Z}_+$, we denote by $H^{\gamma,2sm,s}(G)$ the set of all functions $u \in H^{2sm,s}(G)$ such that $\partial_x^\beta u \in H^{2ms,s}(G)$ for all $|\beta| \leqslant \gamma$. It is convenient to denote by $\mathbf{H}^{2ms,s}_k(G)$ the space of all the k-vector functions with the components from $H^{2ms,s}(G)$, and similarly for the spaces $\mathbf{L}^2_k(G)$, $\mathbf{H}^{\gamma,2ms,s}_k(G)$, etc. These are known to be Hilbert spaces, see [15].

Let L be a $(k \times k)$-matrix differential operator with constant coefficients in $\mathbb{R}^n$ of an even order $2m$:

$$L = \sum_{|\alpha| \leqslant 2m} L_\alpha \partial_x^\alpha$$

where L_α are $(k \times k)$-matrices with real entries such that $L^*_\alpha = L_\alpha$ for all multi-indexes $\alpha \in \mathbb{Z}^n_+$ with $|\alpha| = 2m$. Consider the strongly uniformly (Petrovsky) $2m$-parabolic operator

$$\mathcal{L} = \partial_t - L,$$

see, for instance, [4,28]. More precisely, this additionally means that the operator $(-L)$ is strongly elliptic, i.e. there is a positive constant c_0 such that

$$(-1)^{m+1} w^* \Big(\sum_{|\alpha|=2m} L_\alpha \zeta^\alpha \Big) w \geqslant c_0 |w|^2 |\zeta|^{2mk}$$

for all $\zeta \in \mathbb{R}^n \setminus \{0\}$ and all $w \in \mathbb{C}^k \setminus \{0\}$; here w^* is the transposed and complex adjoint vector for the complex vector $w \in \mathbb{C}^k$.

As usual, we denote by $\mathcal{L}^*$ the formal adjoint operator for $\mathcal{L}$:

$$\mathcal{L}^* = -\partial_t - \sum_{|\alpha|\leqslant 2m} (-1)^{|\alpha|} \partial_x^\alpha (L_\alpha^*(\,\cdot\,).$$

Under these assumptions the operator $\mathcal{L}$ admits a unique fundamental solution $\Phi(x-y, t-\tau)$ of the convolution type, possessing standard estimates [4, formulas (2.16), (2.17)]) and the normality property ([4, Property 2.2]), i.e.

$$\mathcal{L}_{x,t}\Phi(x-y, t-\tau) = I_k\, \delta(x-y, t-\tau), \tag{1}$$

(here the right hand side equals to the unit matrix I_k multiplied by the Dirac distribution at the point (x,t) which is commonly written as $\delta(x-y, t-\tau)$, where δ denotes the Dirac distribution at the origin), and

$$\mathcal{L}^*_{y,\tau}\Phi^*(x-y, t-\tau) = I_k\delta(x-y, t-\tau), \tag{2}$$

where $\Phi^* = (\Phi_{ji})$ is the adjoint matrix for $\Phi = (\Phi_{ij})$.

Let $S_{\mathcal{L}}(G)$ be the set of all the generalized k-vector functions on G, satisfying the (homogeneous) equation

$$\mathcal{L}u = 0 \text{ in } G \tag{3}$$

in the sense of distributions. Also, let the space $S_{\mathcal{L}}(\overline{G})$ be defined as follows:

$$\cup_{U\supset\overline{G}} S_{\mathcal{L}}(U),$$

where the union is with respect to all the domains $U \subset \mathbb{R}^{n+1}$, containing the closure of the domain G.

Then estimates [4, formulas (2.16), (2.17)]) for the fundamental solution imply the standard interior a priori estimates for solutions to (3), see, for instance, [28, §19], or [8, Ch. 4, §2] for the second order operators. This means that the operator $\mathcal{L}$ is hypoelliptic, i.e. all the distributional solutions to equation (3) are C^∞-differentiable on their domain. Then the following embeddings hold true:

$$S_{\mathcal{L}}(\overline{G}) \subset S_{\mathcal{L}}(G) \subset \mathbf{C}^\infty_k(G).$$

Moreover, as the coefficients of $\mathcal{L}$ are constant, the elements of the spaces $S_{\mathcal{L}}(G)$, $S_{\mathcal{L}}(\overline{G})$ are real analytic with respect to the space variable $x \in G(t)$ for all $t \in (T_1, T_2)$, where $T_1 = \inf_{(x,t)\in G} t$, $T_2 = \sup_{(x,t)\in G} t$, and

$$G(t) = \{x \in \mathbb{R}^n : (x,t) \in G\},$$

see, for instance [4]. In particular, the so-called Unique Continuation Property with respect to the space variables x for each fixed t holds true for both the parabolic operator $\mathcal{L}$ and the backwards parabolic operator $\mathcal{L}^*$.

Given a pair of domains $G_1 \subset G_2 \subset \mathbb{R}^{n+1}$, Runge type approximation theorems were proved in [27] for the Fréchet spaces $S_{\mathcal{L}}(G_1) \supset S_{\mathcal{L}}(G_2)$ endowed with the topology of the uniform convergence on compact subsets of G_j and the Hilbert spaces

$$\mathbf{L}^2_{k,\mathcal{L}}(G_1) = S_{\mathcal{L}}(G_1) \cap \mathbf{L}^2_k(G_1) \supset \mathbf{L}^2_{k,\mathcal{L}}(G_2) = S_{\mathcal{L}}(G_1) \cap \mathbf{L}^2_k(G_2).$$

Let us formulate the related result for the spaces $\mathbf{L}^2_{k,\mathcal{L}}(G_j)$ in our particular situation of operators with constant coefficients. With this purpose we need additional regularity assumptions for the domains G_1 and G_2. Namely, we assume that the boundary of domains G_j satisfies the following properties.

(A) The set $G_2(t)$ is a Lipschitz domain in $\mathbb{R}^n$ for each $t \in (T_1, T_2)$ and for any numbers t_3, t_4 such that $T_1 < t_3 < t_4 < T_2$ the set $\Gamma_{t_3,t_4} = \cup_{t\in[t_3,t_4]} \partial G(t)$ is a Lipschitz surface in $\mathbb{R}^{n+1}$;

(A1) For each $t \in [T_1, T_2]$, the sets $G_1(t) = \{x \in \mathbb{R}^n : (x,t) \in G_1\}$, are domains in $\mathbb{R}^n$ with C^{2m}-boundaries if $n \geqslant 2$;

(A2) The boundary ∂G_1 of G_1 is the union $G(T_1) \cup G(T_2) \cup \Gamma$, where

$$\Gamma = \cup_{t \in (T_1, T_2)} \partial G_1(t)$$

is a $C^{2m,1}$-smooth surface without points where the tangential planes are parallel to the coordinate plane $\{t = 0\}$, i.e. we have

$$\sum_{j=1}^{n} (\nu_j(x,t))^2 \geqslant \varepsilon_0 \text{ for all } (x,t) \in \Gamma$$

with a positive number ε_0.

Of course, a cylinder domain $G = \Omega \times (T_1, T_2)$ satisfies assumption (A) if $\partial\Omega$ is a Lipschitz surface and it satisfies assumptions (A1), (A2) if $\partial\Omega$ is a C^{2m}-smooth surface.

Theorem 1. *Let $G_1 \subset G_2$ be domains in $\mathbb{R}^{n+1}$ such that $G_2 \neq \mathbb{R}^{n+1}$. If domain G_2 satisfies assumption* (A) *and bounded domain G_1 satisfies* (A1), (A2) *then $S_{\mathcal{L}}(\overline{G}_2)$ is everywhere dense in the space $\mathbf{L}^2_{k,\mathcal{L}}(G_1)$ if and only for each $t \in (T_1, T_2)$ the set $G_2(t) \setminus G_1(t)$ has no compact (non-empty) components in the set $G_2(t)$.*

Proof. As the Unique Continuation Property with respect to the space variables x for each fixed t holds true for both $\mathcal{L}$ and $\mathcal{L}^*$, the statement follows from [27, Theorems 2.2, 2.4]. □

A similar theorem for the heat equation was obtained in [26] for cylinder domains and in [34] a similar result was proved for the strongly parbolic Lamé type system. Of course, for general strongly $2m$-parabolic operators with variable coefficients the situation is more complicated, but for operators with bounded real analytic coefficients the answer is practically the same, see [27].

We want to extend Theorem 1 to the scale of anisotropic spaces $\mathbf{H}^{\gamma,2ms,s}_{k,\mathcal{L}}(G_j)$, $1 \leqslant j \leqslant 2$, $s \in \mathbb{N}$,

$$\mathbf{H}^{\gamma,2ms,s}_{k,\mathcal{L}}(G) = \mathbf{H}^{\gamma,2ms,s}_{k}(G) \cap S_{\mathcal{L}}(G).$$

Similarly to the space $\mathbf{L}^2_{k,\mathcal{L}}(G)$, by a priori estimates for strongly parabolic operators, the spaces $\mathbf{H}^{\gamma,2ms,s}_{k,\mathcal{L}}(G)$ are closed subspaces of the Hilbert spaces $\mathbf{H}^{\gamma,2ms,s}_{k}(G)$.

Next, denote by $\tilde{\mathbf{H}}^{-\gamma,-2ms,-s}_{k}(G)$ the completion of $\mathbf{C}^\infty_k(\overline{G})$ with respect to the norm

$$\|v\|_{\tilde{\mathbf{H}}^{-\gamma,-2ms,-s}_{k}(G)} = \sup_{\substack{\|\varphi\|_{\mathbf{H}^{\gamma,2ms,s}_{k}(G)} \leqslant 1 \\ \varphi \in \mathbf{H}^{\gamma,2ms,s}_{k}(G)}} \Big|(v,\varphi)_{\mathbf{L}^2_k(G)}\Big|, \ s \in \mathbb{N};$$

here $\tilde{H}$ reflects the fact the usually $H^{-s}(G)$ is reserved for the dual space to $H^s_0(G)$ with slightly different norm. As it is known, the space $\tilde{\mathbf{H}}^{-\gamma,-2ms,-s}_{k}(G)$ is a Banach space, see [1]. The following property is important for the futher exposition.

Lemma 1. *Let G be a bounded domain in $\mathbb{R}^{n+1}$. Then the space $\mathbf{C}^\infty_{0,k}(G)$ is everywhere dense in $\tilde{\mathbf{H}}^{-\gamma,-2ms,-s}_{k}(G)$.*

Proof. Indeed, by the very definition, the space $\mathbf{C}^\infty_k(\overline{G})$ is everywhere dense in $\tilde{\mathbf{H}}^{-\gamma,-2ms,-s}_{k}(G)$. On the other hand, as it is well known that $\mathbf{C}^\infty_{0,k}(\overline{G})$ is everywhere dense in the space $\mathbf{L}^2_k(G)$. Now we note that the norm $\|\cdot\|_{\mathbf{L}^2_k(G)}$ is stronger than the norm $\|\cdot\|_{\tilde{\mathbf{H}}^{-\gamma,-2ms,-s}_{k}(G)}$ on $\mathbf{C}^\infty_k(\overline{G})$ for any $s \in \mathbb{N}$. Thus, the statements of this lemma follows because we may approximate any element of the space $\mathbf{C}^\infty_k(\overline{G})$ by $\mathbf{C}^\infty_{0,k}(G)$-vectors in $\|\cdot\|_{\mathbf{L}^2_k(G)}$-norm. □

2. Approximation in the anisotropic Sobolev spaces

The main result of this paper is the following theorem.

Theorem 2. *Let $s \in \mathbb{N}$, $\gamma \in \mathbb{Z}_+$ $G_1 \subset G_2$ be domains in $\mathbb{R}^{n+1}$ such that $G_2 \neq \mathbb{R}^{n+1}$. If domain G_2 satisfies assumption* (A) *and bounded domain G_1 satisfies* (A1), (A2) *then $S_{\mathcal{L}}(\overline{G}_2)$ is everywhere dense in the space $\mathbf{H}^{\gamma,2ms,s}_{k,\mathcal{L}}(G_1)$ if and only for each $t \in (T_1, T_2)$ the set $G_2(t) \setminus G_1(t)$ has no compact (non-empty) components in the set $G_2(t)$.*

Proof. We begin with the necessity. To prove it we may use the arguments similar to the proof of [27, Theorem 1.2] adapting them for the present situation.

Indeed, as the boundary of the domain G_1 is at least C^1-smooth then the complement $G_2 \setminus \overline{G}_1$ is an open set with Lipschitz boundary. If there is a number $t_0 \in \mathbb{R}$ such that the set $G_2(t_0) \setminus G_1(t_0)$ has a compact non-empty (connected) component $K(t_0)$ in the set $G_2(t_0)$ then $K(t_0)$ is a closure of a domain $D_0 \subset G_2(t_0)$ with C^1-smooth boundary. We have to prove that there is a vector $u \in \mathbf{H}^{2ms,s}_{k,\mathcal{L}}(G_1)$ that can not be approximated by elements of $S_{\mathcal{L}}(\overline{G}_2)$. Now, if a point $y_0 \in K_0$, then (y_0, t_0) is an interior point of $G_2 \setminus \overline{G}_1$ an hence any vector column $U_l(x,t)$, $1 \leqslant l \leqslant k$, of the fundamental matrix $\Phi(x - y_0, t - t_0)$ belongs to the space $\mathbf{H}^{\gamma,2ms,s}_{k,\mathcal{L}}(G_1)$.

Now we may envoke the (second) Green formula for the operator $\mathcal{L}$, see, for instance, [30] for general operators admitting regualar left fundamental solutions or [29] for the second order parabolic operators. Namely, let $\mathcal{G}_L$ be a Green bi-differential operator for the operator L, [30, § 2.4.2]. As it is known, it has order $(2m-1)$ with respect to the space variables x, acting from $\mathbf{C}^{2m,1}_k(\overline{G}_2) \times \mathbf{C}^{2m,1}_k(\overline{G}_2)$ to the space of n-differential forms with coefficients from $C^1(\overline{G}_2)$, i.e.

$$\int_{\partial G_3} \mathcal{G}_L(g,v) = (Lv, g)_{\mathbf{L}^2_k(G_3)} - (v, L^* g)_{\mathbf{L}^2_k(G_3)} \text{ for all } g, v \in \mathbf{C}^{2m,1}_k(\overline{G}_3) \tag{4}$$

and any domain $G_3 \Subset G_2$ with piecewise smooth boundary. As the Green operator of a sum of differential operators can be presented as the sum of the corrresponding Green operators, then for $\mathcal{L}$ we obtain:

$$\mathcal{G}_{\mathcal{L}}(g,v) = g^* v dx - \mathcal{G}_L(g,v),$$

and then the (first) Green formula holds true:

$$\int_{\partial G_3} \mathcal{G}_{\mathcal{L}}(g,v) = (\mathcal{L}v, g)_{\mathbf{L}^2_k(G_3)} - (v, \mathcal{L}^* g)_{\mathbf{L}^2_k(G_3)} \text{ for all } g, v \in \mathbf{C}^{2m,1}_k(\overline{G}_3). \tag{5}$$

Since (y_0, t_0) is an interior point of $G_2 \setminus \overline{G}_1$, we may choose a bounded domain G_3 with a piecewise smooth boundary ∂G_3 such that $(y_0, t_0) \in G_3 \Subset G_2$ and $\partial G_3 \Subset G_1$. If the vector function $U_l(x,t)$ can be approximated in $\mathbf{H}^{\gamma,2ms,s}_k(G_1)$, $s \in \mathbb{N}$, by a sequence $\{u^{(i)}_l\}_{i \in \mathbb{N}}$ from the space $S_{\mathcal{L}}(\overline{G}_2)$ then the sequences of the partial derivatives $\{\partial^\beta_x \partial^\alpha_x \partial^j_t u^{(i)}_l\}$, $|\alpha| + 2mj \leqslant 2ms$, $|\beta| \leqslant \gamma$, converge uniformly on ∂G_3. On the other hand, (the first) Green formula (5) and the normality property (2) of the fundamental solution Φ imply the (second) Green formulas for all $i \in \mathbb{N}$:

$$u^{(i)}_l(x,t) = -\int_{\partial G_3} \mathcal{G}_{\mathcal{L}}(\Phi(x - y, t - \tau), u^{(i)}_l(y,\tau)) \text{ for all } (x,t) \in G_3. \tag{6}$$

Note that there is no need to assume that G_3 is a cylinder domain because this Green formula is a corollary of the *local* reproducing property of the fundamental solution. Now, passing to the limit with respect to $i \to +\infty$ in (6) we obtain

$$U_l(x,t) = -\int_{\partial G_3} \mathcal{G}_{\mathcal{L}}(\Phi(x - y, t - \tau), U_l(y,\tau)) \text{ for all } (x,t) \in G_3 \cap G_1. \tag{7}$$

However, since Φ is a fundamental solution to $\mathcal{L}$ then the right-hand side of formula (7) belongs to $S_{\mathcal{L}}(G_3)$. Therefore the vector function U_l extends as a solution V_l to equation (3) from $G_1 \cap G_3$ to G_3, i.e. to a neighbourhood of the point (y_0, t_0). In particular, since any solution to the operator $\mathcal{L}$ in G_2 is real analytic with respect to the space variables in $G_2(t)$ for each $t \in (T_1, T_2)$, then this extension is unique on $G_3 \setminus (y_0, t_0)$. This means the vector function $V_l \in S_{\mathcal{L}}(G_3)$ coincides with the l-th vector column U_l of the fundamental matrix $\Phi(x - y_0, t - t_0)$ in $G_3 \setminus (y_0, t_0))$. Thus, we obtain a contradiction because for the matrix $V(x,t)$ with columns V_l, $1 \leqslant l \leqslant k$ we have $\mathcal{L}V = 0$ in G_3 but $\mathcal{L}\Phi(x, y_0, t, t_0)$ coincides with the δ-functional concentrated at the point (y_0, t_0) multiplied on $(k \times k)$-unit matrix. The necessity is proved.

Next, we proceed with the sufficiency. Actually we slightly modify the proof from [3] for the solutions to the heat equation, adapting it to the topology of the anisotropic Sobolev spaces, cf. [26, 27] for the approximation in the Lebesgue spaces.

Indeed, let for each $t \in (T_1, T_2)$ the set $G_2(t) \setminus G_1(t)$ have no compact (non-empty) components in the set $G_2(t)$. The Hahn–Banach Theorem implies that G_1, G_2 is a $\mathcal{L}$-Runge's pair in the sense of the present theorem if and only if any continuous linear functional f on $\mathbf{H}^{\gamma, 2ms, s}_{k, \mathcal{L}}(G_1)$ annihilating the space $S_{\mathcal{L}}(\overline{G}_2)$ also annihilates the space $\mathbf{H}^{\gamma, 2ms, s}_{k, \mathcal{L}}(G_2)$.

As we have noted above, the space $\mathbf{H}^{\gamma, 2ms, s}_{k, \mathcal{L}}(G)$ is a closed subspace of the space $\mathbf{H}^{\gamma, 2ms, s}_{k}(G)$. Then any continuous linear functional f on $\mathbf{H}^{\gamma, 2ms, s}_{k, \mathcal{L}}(G_1)$ can be extended as a continuous linear functional F on $\mathbf{H}^{\gamma, 2ms, s}_{k}(G_1)$, i.e. as an element of the Sobolev space $\tilde{\mathbf{H}}^{-\gamma, -2ms, -s}_{k}(G_1)$. In particular, F can be identified as a distrubition ψ on $\mathbb{R}^{n+1}$ supported in $\overline{G}_1$ and having a finite order of singularity:

$$F(u) = \langle u, \psi \rangle \text{ for all } u \in \mathbf{H}^{\gamma, 2ms, s}_{k}(G_1). \tag{8}$$

Let W be the vector function, with components obtained by applying the functional F to the corresponding columns of the matrix $(x,t) \to \Phi(x - y, t - \tau)$:

$$W(y, \tau) = \langle \Phi^*(x, y, t, \tau), \psi(x, t) \rangle.$$

Clearly, it is well-defined outside the support of ψ. By (1), for any vector $\varphi \in \mathbf{C}^{\infty}_{0,k}(\mathbb{R}^{n+1})$ we have

$$\mathcal{L}_{x,t} \langle \Phi^*(x, y, t, \tau), \varphi(y, \tau) \rangle = \varphi(x, t),$$

and then, the hypoellipticity of $\mathcal{L}$ implies that the vector function

$$V_{\varphi}(x, t) = \langle \Phi^*(x, y, t, \tau), \varphi(y, \tau) \rangle$$

belongs to $\mathbf{C}^{\infty}_{k}(\mathbb{R}^{n+1})$. In particular, the vector function W can be extended as a distribution to $\mathbb{R}^{n+1}$ via

$$\langle W, \varphi \rangle = \langle V_{\varphi}, \psi \rangle,$$

because ψ is a (k-vector valued) distribution with compact support.

Next, according to (1), columns of the matrix $\Phi(x, t, y, \tau)$ belong to $S_{\mathcal{L}}(\overline{G}_2)$ with respect to variables (x,t) for each fixed $(y, \tau) \notin \overline{G}_2$. Hence, if $F \in (\mathbf{H}^{\gamma, 2ms, s}_{k}(G_1))^*$ annihilates the space $S_{\mathcal{L}}(\overline{G}_2)$ then we have

$$W(y, \tau) = 0 \text{ for all } (y, \tau) \notin \overline{G}_2. \tag{9}$$

But (2) implies that

$$\mathcal{L}^* W = \psi \text{ in } \mathbb{R}^{n+1}, \tag{10}$$

in the sense of distributions and, in particular,

$$\mathcal{L}^* W = 0 \text{ in } \mathbb{R}^{n+1} \setminus \overline{G}_1. \tag{11}$$

Note that the operator $\mathcal{L}^*$ is backwards-parabolic and, for any solution $v(y, \tau)$ to the equation $\mathcal{L}^* v = 0$, the vector $w(y, \tau) = v(y, -\tau)$ is a solution to the strongly parabolic system of equations

$(\partial_\tau - L_y^*)w = 0$ with constant coefficients. Thus, by the hypoellipticity of such systems, $W(y,\tau) \in \mathbf{C}_k^\infty\big(\mathbb{R}^{n+1} \setminus \overline{G}_1\big)$ and, in particular, it is C^∞-smooth with respect to y in $\mathbb{R}^n \setminus \overline{G}_1(\tau)$ for each $\tau \in \mathbb{R}$ where, as before, $\overline{G}_1(\tau) = \{x \in \mathbb{R}^n : (x,\tau) \in \overline{G}_1\}$.

As the domains $G_1 \subset G_2$ satisfy assumptions (A), (A_1), (A_2) and $G_2 \neq \mathbb{R}^{n+1}$, the components of sets $\mathbb{R}^n \setminus G_2(t) \subset \mathbb{R}^n \setminus G_1(t)$ are either empty sets or closures of Lipschitz domains. Since the set $G_2(t) \setminus G_1(t)$ has no compact components in $G_2(t)$, we see that each bounded component of $\mathbb{R}^n \setminus \overline{G_1(t)}$ intersects with $\mathbb{R}^n \setminus \overline{G_2(t)}$ by a non-empty open set for each $t \in (T_1, T_2)$. Hence, as solutions to the backwards parabolic operator $\mathcal{L}^*$ are real analytic with respect to the space variables x, the vector W vanishes on every bounded component of $\mathbb{R}^n \setminus \overline{G_1(t)}$ for each $t \in (T_1, T_2)$. Next, let $\hat{G}_j(t)$ be the union of $G_j(t)$ with all the components of the set $G_j(t)$ that are relatively compact in $\mathbb{R}^n$. By the discussion above, the closure of $\hat{G}_1(t)$ lies in the closure of $\hat{G}_2(t)$. Then, by De Morgan's Law we have

$$\Big(\mathbb{R}^n \setminus \overline{\hat{G}_1(t)}\Big) \cap \Big(\mathbb{R}^n \setminus \overline{\hat{G}_2(t)}\Big) = \mathbb{R}^n \setminus \Big(\overline{\hat{G}_2(t)} \cup \overline{\hat{G}_1(t)}\Big) = \mathbb{R}^n \setminus \overline{\hat{G}_2(t)}. \tag{12}$$

In particular, this means that the vector W vanishes on unbounded components of the set $\mathbb{R}^n \setminus \overline{G_1(t)}$ for each $t \in (T_1(G_1), T_2(G_1))$, too. Thus, (9) and the real analyticity with respect to the space variables of solutions to the operator $\mathcal{L}^*$ imply that

$$W(y,\tau) = 0 \text{ in } \mathbb{R}^n \setminus \overline{G_1(\tau)} \text{ for all } \tau \in \mathbb{R},$$

i.e. the vector W is supported in $\overline{G}_1$.

Using Lemma 1, we approximate the distribultion $\psi \in \tilde{\mathbf{H}}_k^{-\gamma,-2ms,-s}(G_1)$ by a sequence $\{\psi_i\} \subset \mathbf{C}_{0,k}^\infty(G_1)$ in the space $\tilde{\mathbf{H}}_k^{-\gamma,-2ms,-s}(G_1)$. Then for vectors

$$W_i(y,\tau) = \langle \Phi^*(x,y,t,\tau), \psi_i(x,t)\rangle$$

we have

$$\mathcal{L}^* W_i = \psi_i \text{ in } \mathbb{R}^{n+1}, \tag{13}$$

and, in partucilar, by the hypoellipticity of parabolic operators with constant coefficients, $\{W_i\} \subset \mathbf{C}_k^\infty(\mathbb{R}^{n+1})$. Since $\mathbf{C}_k^\infty(\mathbb{R}^{n+1}) \subset \tilde{\mathbf{H}}_k^{-\gamma,2m(1-s),1-s}(G_1)$, Lemma 1 provides that we may approximate each vector W_i by a sequence $\{V_{i,j}\} \subset \mathbf{C}_{0,k}^\infty(G_1)$ in the space $\tilde{\mathbf{H}}_k^{-\gamma,2m(1-s),1-s}(G_1)$.

Again using Lemma 1 we see that

$$\begin{aligned}
\|\mathcal{L}^*(V_{i,j} - W_i)\|_{\tilde{\mathbf{H}}_k^{-\gamma,-2ms,-s}(G_1)} &= \sup_{\substack{\|\varphi\|_{\mathbf{H}_k^{\gamma,2ms,s}(G_1)} \leqslant 1 \\ \varphi \in \mathbf{C}_{0,k}^\infty(G_1)}} \Big|(\mathcal{L}^*(V_{i,j} - W_i), \varphi)_{\mathbf{L}_k^2(G)}\Big| = \\
&= \sup_{\substack{\|\varphi\|_{\mathbf{H}_k^{\gamma,2ms,s}(G_1)} \leqslant 1 \\ \varphi \in \mathbf{C}_{0,k}^\infty(G_1)}} \Big|(V_{i,j} - W_i, \mathcal{L}\varphi)_{\mathbf{L}_k^2(G)}\Big| = \\
&= \sup_{\substack{\|\varphi\|_{\mathbf{H}_k^{\gamma,2ms,s}(G)} \leqslant 1 \\ \varphi \in \mathbf{C}_{0,k}^\infty(G_1), \mathcal{L}\varphi \neq 0}} \frac{\Big|(V_{i,j} - W_i, \mathcal{L}\varphi)_{\mathbf{L}_k^2(G_1)}\Big|}{\|\mathcal{L}\varphi\|_{\mathbf{H}_k^{\gamma,2m(s-1),s-1}(G_1)}} \|\mathcal{L}\varphi\|_{\mathbf{H}_k^{\gamma,2m(s-1),s-1}(G_1)}.
\end{aligned} \tag{14}$$

On the other hand, the scale of spaces $\mathbf{H}_k^{\gamma,2ms,s}(G)$ is constructed in such way, that any $2m$-parabolic operator $\mathcal{L}$ continuously maps $\mathbf{H}_k^{\gamma,2ms,s}(G)$ to $\mathbf{H}_k^{\gamma,2m(s-1),s-1}(G)$, $s \in \mathbb{N}$, i.e. there exists a positive constant $C(s,\gamma,\mathcal{L},G)$ such that

$$\|\mathcal{L}v\|_{\mathbf{H}_k^{\gamma,2m(s-1),s-1}(G)} \leqslant C(s,\gamma,\mathcal{L},G)\, \|v\|_{\mathbf{H}_k^{\gamma,2ms,s}(G)} \text{ for all } v \in \mathbf{H}_k^{\gamma,2ms,s}(G). \tag{15}$$

Then, taking into the account (14) and (15), we conclude that

$$\|\mathcal{L}^*(V_{i,j}-W_i)\|_{\tilde{\mathbf{H}}_k^{-\gamma,-2ms,-s}(G_1)} \leqslant C(s,\gamma,\mathcal{L},G_1)\|V_{i,j}-W_i\|_{\tilde{\mathbf{H}}_k^{-\gamma,2m(1-s),1-s}(G_1)}, \tag{16}$$

i.e. the sequence $\{\mathcal{L}^*V_{i,j}\}$ converges to $\mathcal{L}^*W_i$ in the space $\tilde{\mathbf{H}}_k^{-\gamma,-2ms,-s}(G_1)$ as $j\to+\infty$.

Hence, it follows from (8), (13), (16) and the contunity of the functional F that for all $u\in\mathbf{H}^{\gamma,2ms,s}_{k,\mathcal{L}}(G_1)$ we have

$$\begin{aligned} F(u) = \langle u,\psi\rangle &= \lim_{i\to\infty}\langle u,\psi_i\rangle = \lim_{i\to\infty}\langle u,\mathcal{L}^*W_i\rangle = \\ &= \lim_{i\to\infty}\lim_{j\to\infty}\langle u,\mathcal{L}^*V_{i,j}\rangle = \lim_{i\to\infty}\lim_{j\to\infty}\langle \mathcal{L}u,V_{i,j}\rangle = 0, \end{aligned} \tag{17}$$

because $\mathcal{L}u=0$ in G_1 in the sense of distributions. Thus, F annihilates $\mathbf{H}^{\gamma,2ms,s}_{k,\mathcal{L}}(G_1)$, too, that was to be proved. □

This work was supported by the Krasnoyarsk Mathematical Center and financed by the Ministry of Science and Higher Education of the Russian Federation (Agreement No. 075-02-2025-1790).

References

[1] R.Adams, J.Fournier, Sobolev Spaces. Pure and Applied Mathematics Series, Vol. 140 (Second ed.), Amsterdam Boston, Academic Press, 2003.

[2] F.E.Browder, Approximation by solutions of partial differential equations, *Amer. J. Math.*, **84**(1962), 134–160.

[3] R.Diaz, A Runge theorem for solutions of the heat equation, *Proc. Amer. Math. Soc.*, **80**(1980), no. 4, 643–646.

[4] S.D.Eidel'man, Parabolic equations, Partial differential equations – 6, *Itogi Nauki i Tekhniki. Ser. Sovrem. Probl. Mat. Fund. Napr.*, 63, VINITI, Moscow, 1990, 201–313.

[5] A.Enciso, D.Peralta-Salas, Existence of knotted vortex tubes in steady Euler flows, *Acta Math.*, **214**(2015), 61–134.

[6] A.Enciso, M.A.García-Ferrero, D.Peralta-Salas, Approximation theorems for parabolic equations and movement of local hot spots, *Duke Math. J.*, **168**(2019), no. 5, 897–939.

[7] A.Enciso, D.Peralta-Salas, Approximation theorems for the Schrödinger equation and Quantum Vortex Reconnection, *Comm. Math. Physics*, **387**(2021), 1111–1149.

[8] A.Friedman, Partial differential equations of parabolic type, Englewood Cliffs, NJ, Prentice-Hall, Inc., 1964.

[9] M.A.García-Ferrero, A.Rüland, W.Zaton, Runge Approximation and Stability Improvement for a Partial Data Calderón Problem for the Acoustic Helmholtz Equation, *Inverse Problems & Imaging*, **16**(2022), 251–281.

[10] P.M.Gauthier, N.Tarkhanov, Rational approximation and universality for a quasilinear parabolic equation, *Journal of Contemporary Mathematical Analysi*, **43**(2008), 353–364.

[11] V.P.Havin, Approximation by analytic functions in the mean, *Dokl. Akad. Nauk SSSR*, **178**(1968), no. 5, 1025–1028.

[12] B.F.Jones, Jr., An approximation theorem of Runge type for the heat equation, *Proc. Amer. Math. Soc.*, **52**(1975), no. 1, 289–292.

[13] V.Kalinin, A.A.Shlapunov, K.Ushenin, On uniqueness theorems for the inverse problem of Electrocardiography in the Sobolev spaces, *Z. Angew. Math. Mech.*, **103**(2023), no. 1, e202100217.

[14] T.Kalmes, An approximation theorem of Runge type for kernels of certain non-elliptic partial differential operators, *Bull. Sci. Math.*, **170**(2021), 103012.

[15] N.V.Krylov, Lectures on elliptic and parabolic equations in Sobolev spaces. Graduate Studies in Math. Vol. 96, AMS, Providence, Rhode Island, 2008.

[16] O.A.Ladyzhenskaya, V.A.Solonnikov, N.N.Ural'tseva, Linear and quasilinear equations of parabolic type, Moscow, Nauka, 1967.

[17] P.D.Lax, A stability theorem for solutions of abstract differential equations, and its application to the study of the local behavior of solutions of elliptic equations, *Comm. Pure Appl. Math.*, no. 9, (1956), 747–766.

[18] J.-L.Lions, Quelques méthodes de résolution des problèmes aux limites non linéare, Dunod/Gauthier-Villars, Paris, 1969.

[19] B.Malgrange, Existence et approximation des solutions des équations aux dérivées partielles et des équations de convolution, *Annales de l'Institut Fourier*, **6**(1955/56), 271–355.

[20] B.Malgrange, Sur les systémes differentiels á coefficients constants, *Colloq. internat. Centre nat. rech. scient.*, **117**(1963), 113–122.

[21] V.G.Maz'ya, V.P.Havin, The solutions of the Cauchy problem for the Laplace equation (uniqueness, normality, approximation), *Tr. Mosk. Mat. Obs.*, **30**(1974), 61–114.

[22] S.N.Mergelyan, Harmonic approximation and approximate solution of the Cauchy problem for the Laplace equation, *Uspekhi Mat. Nauk*, **71**(1956), Issue 5(71), 3–26.

[23] V.P.Palamodov, Linear Differential Operators with Constant, Coefficients, Grundlehren der Mathematischen Wissenschaften 168. Springer, Berlin, 1970.

[24] A.Rüland, M.Salo, Quantitative Runge Approximation and Inverse Problems, *International Mathematics Research Notices*, **20**(2019), 6216–6234.

[25] C.Runge, Zur Theorie der eindeutigen analytischen Funktionen, *Acta Math.*, (1885), no. 6, 229–244.

[26] A.A.Shlapunov, On approximation of solutions to the heat equation from Lebesgue class L^2 by more regular solutions, *Math. Notes*, **111**(2022), no. 5, 778–794.

[27] A.A.Shlapunov, P.Yu.Vilkov, On Runge type theorems for solutions to strongly uniformly parabolic operators, *Siberian Electronic Mathematical Reports*, **21**(2024), no. 1, 383–404.

[28] V.A.Solonnikov, On boundary value problems for linear parabolic systems of differential equations of general form, *Proc. Steklov Inst. Math.*, **83**(1965), 1–184.

[29] A.G.Sveshnikov, A.N.Bogolyubov, V.V.Kravtsov, Lectures on mathematical physics, Moscow, Nauka, 2004.

[30] N.Tarkhanov, Complexes of differential operators, Kluwer Academic Publishers, Dordrecht, NL, 1995.

[31] N.Tarkhanov, The Cauchy Problem for Solutions of Elliptic Equations, Akademie-Verlag, Berlin, 1995.

[32] N.Tarkhanov, The Analysis of Solutions of Elliptic Equations, Kluwer Academic Publishers, Dordrecht, NL, 1997.

[33] R.Temam, Navier-Stokes Equations. Theory and Numerical Analysis, North Holland Publ. Comp., Amsterdam, 1979.

[34] P.Yu.Vilkov, I.A.Kurilenko, A.A.Shlapunov, Approximation of solutions to parabolic Lamé type operators in cylinder domains and Carleman's formulas for them, *Siberian Math. J.*, **63**(2022), no. 6, 1049–1059.

[35] A.G.Vitushkin,, The analytic capacity of sets in problems of approximation theory, *Russian Math. Surveys*, 22(1967), no. 6, 139–200. DOI: 10.1070/RM1967v022n06ABEH003763

Об аппроксимационных теоремах для решений сильно параболических систем в анизотропных пространствах Соболева

Павел Ю. Вилков
Александр А. Шлапунов
Сибирский федеральный университет
Красноярск, Российская Федерация

Аннотация. Мы исследуем задачу о парах Рунге для соболевских решений сильно равномерно параболических систем в нецилиндрических областях специального вида. Мы доказываем, что если коэффициенты параболического оператора постоянны, то две области с достаточно гладкими границами, никакие части которых не параллельны плоскости $t = 0$, образуют пару Рунге тогда и только тогда, когда дополнения любого сечения большей области к сечению меньшей области плоскостями $t = \text{const}$ не имеют компактных компонент в большем сечении.

Ключевые слова: сильно параболические уравнения и системы, аппроксимационные теоремы, пары Рунге.

EDN: ZEIQGO
УДК 54.05

Study of Quasicrystalline Phases Formation in Aluminum Alloy D16

Pavel P. Turchin*
Siberian Federal University
Krasnoyarsk, Russian Federation
Kirensky Institute of Physics
Federal Research Center KSC SB RAS
Krasnoyarsk, Russian Federation
Marina Yu. Chulkova†
Pavel O. Syhodaev‡
Siberian Federal University
Krasnoyarsk, Russian Federation
Maxim S. Molokeev§
Siberian Federal University
Krasnoyarsk, Russian Federation
Kirensky Institute of Physics
Federal Research Center KSC SB RAS
Krasnoyarsk, Russian Federation
Vladimir I. Turchin¶
Siberian Federal University
Krasnoyarsk, Russian Federation

Received 18.05.2025, received in revised form 25.06.2025, accepted 26.07.2025

Abstract. Features of formation and thermodynamic conditions of quasicrystalline phases $Al_{60}Cu_{30}Fe_{10}$ and $Al_{65}Cu_{20}Fe_{15}$ nucleation in alloy D16 are studied. These phases are formed under different annealing conditions by hot isostatic pressing. Phases formation is significantly affected by preliminary mechanical activation of D16 grains and Cu and Fe components added to the alloy.

Keywords: aluminum alloys, quasicrystalline phase, X-ray phase analysis.

Citation: P.P. Turchin, M.Yu. Chulkova, P.O. Syhodaev, M.S. Molokeev, V.I. Turchin, Study of Quasicrystalline Phases Formation in Aluminum Alloy D16, J. Sib. Fed. Univ. Math. Phys., 2026, 19(2), 270–277. EDN: ZEIQGO.

Introduction

Since the discovery of quasicrystalline order in solids [1], a large number of results related to the modification of various alloys with quasicrystals have been obtained. Alloys modification leads to changes and improvements in such properties as strength, creep, microhardness, etc.

*pturchin@sfu-kras.ru https://orcid.org/0000-0002-43716389
†mchulkova@sfu-kras.ru https://orcid.org/0009-0008-1943-8383
‡ https://orcid.org/0000-0003-4748-2249
§ https://orcid.org/0000-0002-8297-0945
¶ https://orcid.org/0000-0001-5584-4794

[2–6]. It is necessary to highlight the studies of aluminum alloys modified with quasicrystalline particles of the composition Al-Cu-Fe. In this case, a more homogeneous transition between the matrix and quasicrystalline particles occurs [3, 5], resulting in improved properties.

Quasicrystals Al-Cu-Fe used for the modification can be obtained by various methods: extreme cooling [7], plasma spraying [8] and solid-phase synthesis [9, 10]. They can be grown to macroscopic sizes [10, 11]. Quasicrystal phases can be formed in an insignificant range of Al, Cu and Fe concentrations [9–12], their production is accompanied by the formation of approximants depending on the thermodynamic conditions of synthesis and concentrations of components [9, 12]. The growth of the quasicrystalline phase is associated with the formation of defects, which dynamics was studied in [13]. And the use of impurity atoms in obtaining quasicrystals can affect approximants' existence. Thus, the addition of Si atoms as impurities makes it possible to avoid the formation of the monoclinic phase $Al_{13}Fe_4$ [9, 10], which is typically formed during Al-Cu-Fe quasicrystals production or phase transformations [7]. The temperature dynamics of the Al-Cu-Fe quasicrystalline phase formation is determined by the chemical energy of the interaction of Al-Cu, Al-Fe and Cu-Fe atom pairs. Two of these reactions are endothermic, and one is exothermic [14], therefore both the annealing process and the sequence of mechanical activation of the initial components are important [15], although the mechanical activation itself leads only to the formation of the approximants of the phase in question [14–15]. The sequence of phase transformations in the Al-Cu-Fe ternary system was studied in [12, 14–15] and is reflected in the three-stage solid-phase synthesis of quasicrystals described in [9–10]. The addition of ready quasicrystals to pure aluminum [3–5] or with various impurities [6] leads to different reactions of solid-phase synthesis on the surface and in the bulk of quasicrystals. Thus, annealing at temperatures of 300°C and 400°C for 250 hours can lead to the disappearance of the QQ phase [16], which does not occur when adding Ni atoms. The conducted studies confirming the improvement of the properties of aluminum alloys by introducing close in composition quasicrystals leave the question of the existence of thermodynamic conditions for the formation of quasicrystallites directly in various aluminum alloys open. Firstly, each alloy contains a specific set and concentration of impurity atoms, leading to the formation of various phases in it and the formation of corresponding properties. Secondly, the melting temperature of the alloy is usually lower than the characteristic temperatures of solid-phase synthesis of the QQ phase in question. And, conversely, as the conducted studies demonstrate, the presence of impurity atoms can simplify the production of the QQ phase by eliminating unnecessary approximants [17].

Therefore, the study investigates various temperature modes of annealing alloy D16 with the addition of Cu and Fe atoms to ensure the concentration composition of the QQ-phase existence in accordance with [10, 17]. To reduce the porosity of the samples, the hot isostatic pressing (HIP) method has been used [18]. Various conditions of mechanical activation of the initial powders of alloy D16, Cu and Fe has been applied. The phase composition of the samples obtained was controlled by the X-ray diffraction (XRD) phase analysis. The annealing temperatures were in the range from the D16 plasticity temperatures where T = 350 – 474°C [19] to the temperatures of the $Al_{63}Cu_{25}Fe_{12}$ QQ-phase nucleation during solid-phase synthesis where T = 600 – 800°C [9–10].

1. Samples acquisition

Aluminum alloy D16 (Al 91-94.7, Cu 3.8-4.9, Fe up to 0.5 wt.%) was pre-crushed to grains of 1–100 μm. Micropowders of high-purity iron and copper were fused in a Pulverisette 6 planetary

Table 1. Sintering modes

Sample	1,2	3	4	5
Annealing conditions				
T, °C	400 - 500 - 600	600 - 650 - 700	700 - 750 - 800	700
t, h	2 - 2 - 1	0.5 - 1 - 1	0.5 - 1 - 1	3

ball mill in an argon atmosphere for 15 hours at 300 rpm in a ratio of 25:12. The particle size of the Cu and Fe powder mixture was 1–150 μm. The crushed D16 powder was mixed with Cu-Fe micropowder in the mill for 1.5 hours at 200 rpm. Then the mechanically activated mixture was pressed at a pressure of 2.2 GPa and annealed using the HIP method. The mass ratio of Al, Cu and Fe atoms corresponded to the stoichiometric ratio $Al_{63}Cu_{25}Fe_{12}$, taking into account the presence of Cu and Fe atoms in the alloy D16. The pressure range during HIP was 13–15 MPa. Tab. 1 demonstrates the parameters of individual annealing modes with annealing times for the specified temperatures. The heating rate during sintering was 120°C/h, the cooling rate was 500°C/h.

Samples 1 and 2 in Tab. 1 differ in the conditions of component preparation and mixing. Sample 1 was mechanically activated by mixing three components at once: D16, Cu, and Fe for 5 hours, unlike the two-stage mechanical activation in other cases. After annealing by the HIP method and conducting microscopic and X-ray phase studies of the samples, samples 1–3 were subjected to additional annealing in vacuum at 600°C for two hours. The dynamics of microscopic and phase changes is analyzed below.

2. Microscopic studies

Microscopic studies of the samples obtained were performed on a Hirox KH - 7700 microscope. Fig. 1 demonstrates the unequal porosity of the samples obtained. It can be concluded that increasing the annealing temperature leads to more homogeneous alloys. Microscopic images also demonstrate the presence of several phases in the samples, the concentration of which differs under various annealing conditions.

The additional annealing of the samples 1–3 (micrographs of the samples are demonstrated in Fig. 2) leads to a change in their microstructure and porosity.

3. X-ray diffraction phase studies

We were interested in the formation of the QQ phase in the obtained alloys and the annealing modes under which it is formed. X-ray diffraction phase analysis was carried out on the prepared surfaces using the standard powder method. The X-ray diffraction phase analysis results for the samples under consideration are demonstrated in Figs. 3, 4, where the estimated concentrations of the crystalline phases for each of the annealing modes are also indicated. The crystalline phases from the ICDD powder database were identified for the obtained X-ray patterns. The intensity difference (the lower graph in Figs. 3, 4), obtained by subtracting the intensities of the identified crystalline phases from the X-ray pattern, was identified using the known X-ray patterns for quasicrystals provided in the same database. It was found that the intensity difference of the

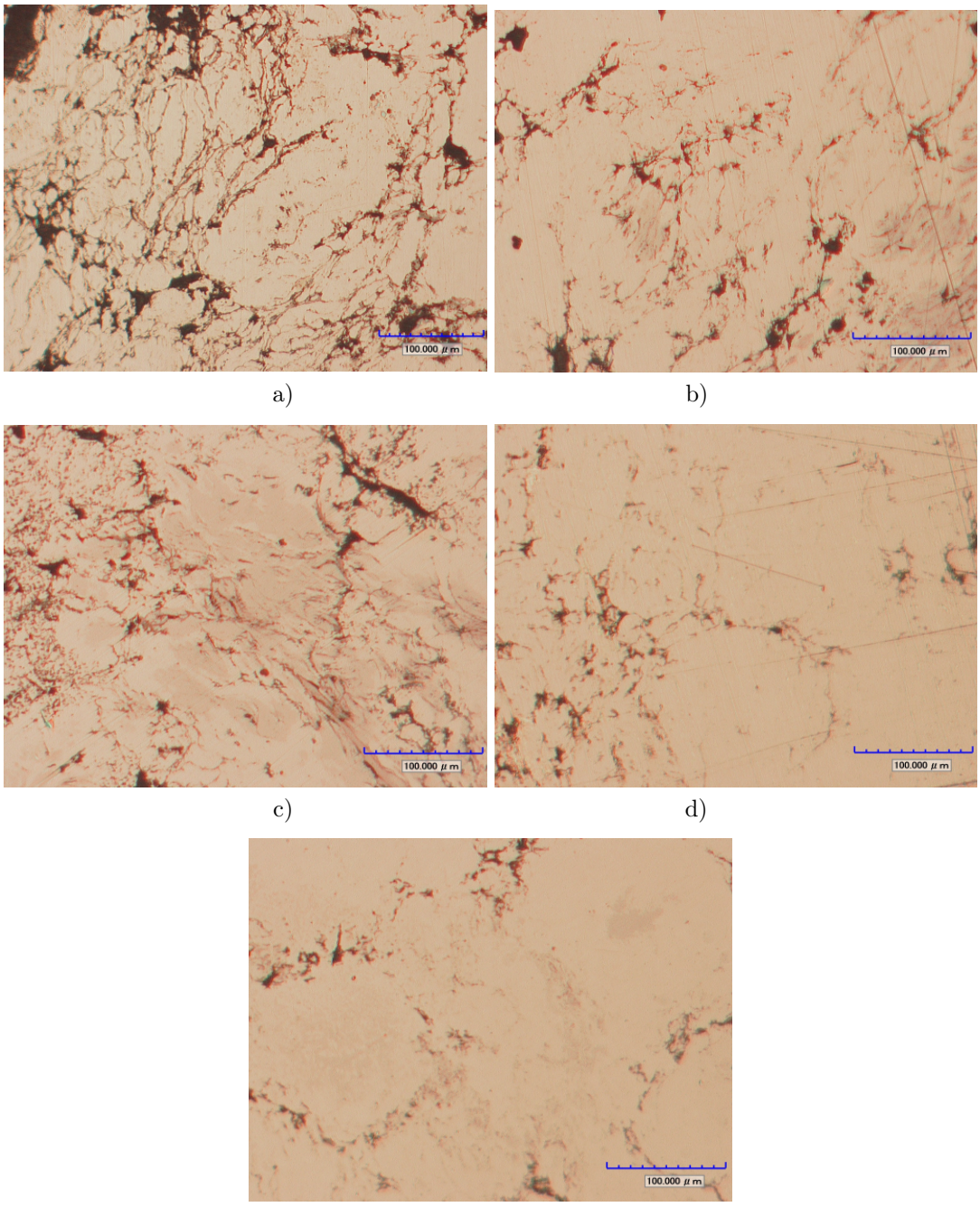

a) b) c) d) e)

Fig. 1. Micrographs of the samples: a - 1, b - 2, c - 3, d - 4, e - 5 (Tab. 1)

X-ray patterns (Figs. 3a and 3d, 4c) is identified with high accuracy by the X-ray patterns of the QQ phases.

Thus, for annealing mode No. 5 (Tab. 1), the intensity difference (Fig. 3d) corresponds to X-ray diffraction pattern No. 49 — 1730 for the $Al_{60}Cu_{30}Fe_{10}$ phase. And for annealing modes No. 1 (Fig. 3a) and No. 3 (Fig. 4c) after additional annealing in vacuum, the intensity difference

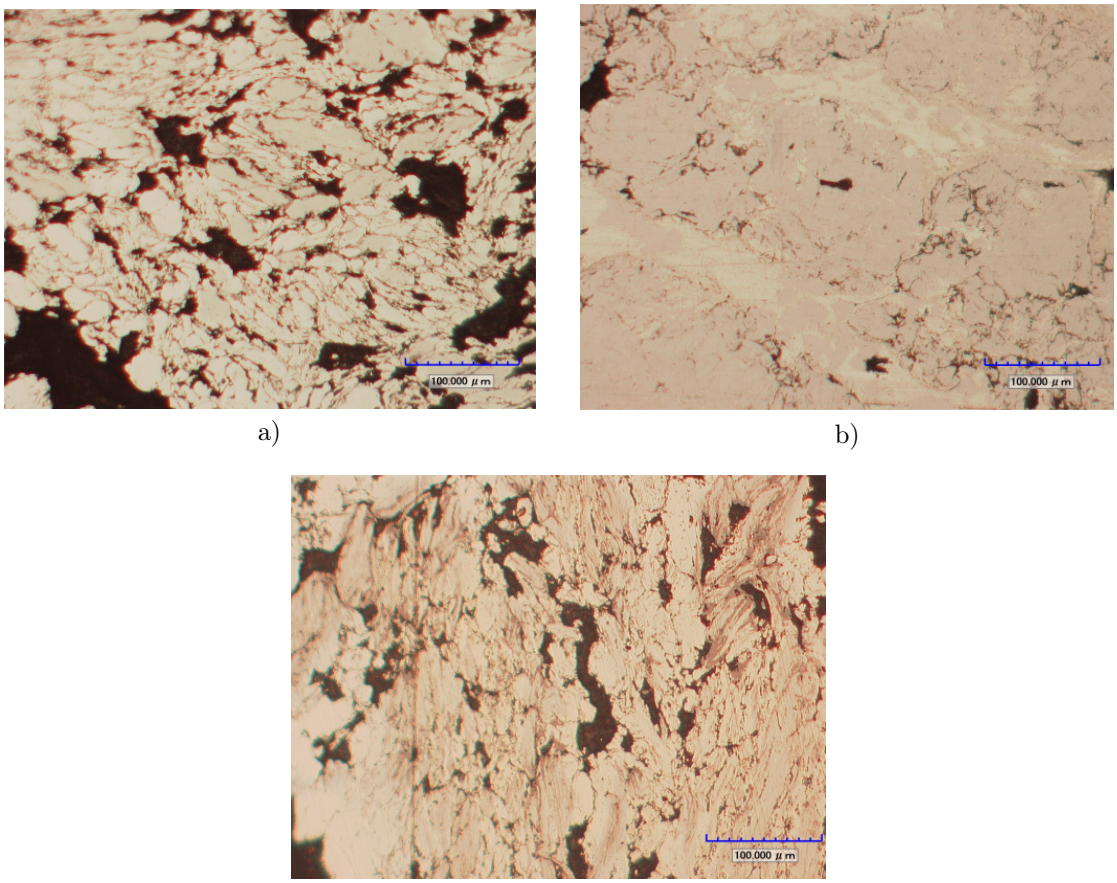

a) b)

c)

Fig. 2. Micrographs of the samples: a - 1, b - 2, c - 3 (Tab. 1) after additional annealing

corresponds to X-ray diffraction pattern No. 49 — 1511 for the $Al_{65}Cu_{20}Fe_{15}$ QQ-phase. The reasons for low QQ phases concentrations in the alloys (units of percent), as well as methods for controlling the QQ phase concentration, require separate study. The data obtained demonstrate that the QQ phase is formed both at temperatures below the melting point of the alloy D16 (sample No. 1) and above this temperature (sample No. 5) without additional annealing. Additional annealing of sample No. 3 also leads to the q-phase formation, which was absent during the primary annealing by the HIP method (Fig. 4c). And in sample No. 1, additional annealing leads to the disappearance of the QQ phase (Fig. 4a).

Conclusion

The performed studies of phase formation in the alloy D16 enriched with Cu and Fe atoms to the concentrations of QQ-phases existence has demonstrated the possibility of $Al_{60}Cu_{30}Fe_{10}$ and $Al_{65}Cu_{20}Fe_{15}$ quasicrystalline phases formation directly in the alloy. For this purpose, various annealing modes by the HIP method can be used in the temperature range from the plasticity temperatures of the alloy D16 to the temperatures of solid-phase synthesis of the $Al_{63}Cu_{25}Fe_{12}$ quasicrystalline phase. Quasicrystalline phases formation is possible both below the alloy D16

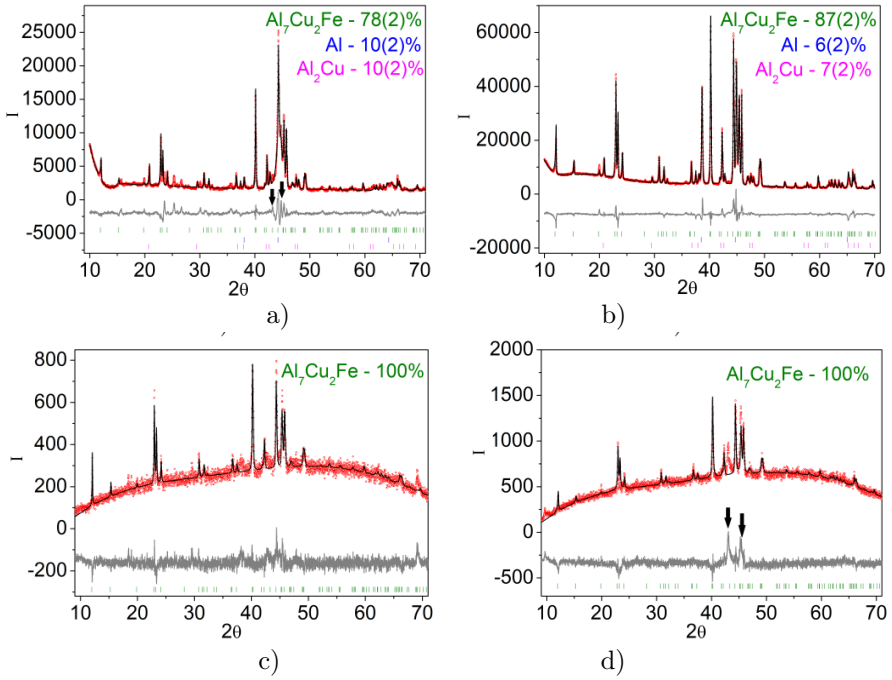

Fig. 3. XRD results for the samples: a – 1, b – 2, c – 4, d – 5. Arrows indicate QQ-phase reflections

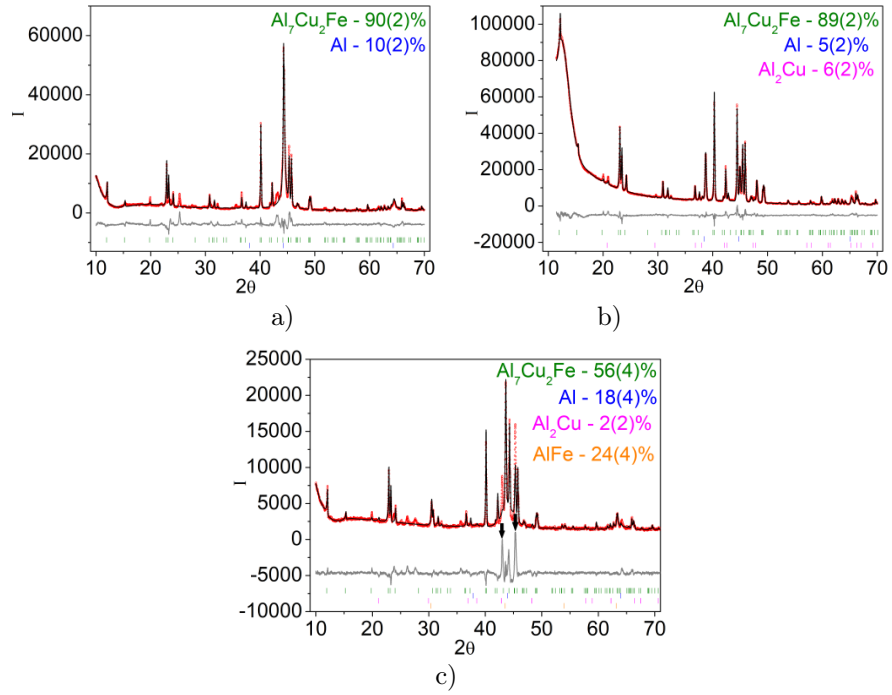

Fig. 4. XRD results for the samples after additional annealing at 600°C: a – 1, b – 2, c – 3. Arrows indicate QQ-phase reflections

melting temperature and above this temperature. Additional annealing can lead to the quasicrystalline phase formation in the alloy, as well as to its destruction.

References

[1] D.Shechtman et al., Metallic phase with long-range orientational order and no translational symmetry, *Physical review letters*, **53**(1984), no. 20, 1951–1953.

[2] M.A.Suarez, et al., Effect of chemical composition on the microstructure and hardness of Al-Cu-Fe alloy, *Materials Characterization*, **62**(2011), no. 9, 917–923. DOI: 10.1016/j.matchar.2011.06.009

[3] J.Bonneville, et al., Al-matrix composite materials reinforced by Al-Cu-Fe particles, *Journal of Physics: Conference Series*, **240**(2010), no. 1, 012013. DOI: 10.1088/1742-6596/240/1/012013

[4] T.El Kabir et al., Hot isostatic pressing synthesis and mechanical properties of Al/Al-Cu-Fe composite materials, *Journal of Materials Research*, **23**(2008), no. 4, 904–910. DOI:10.1557/jmr.2008.0111

[5] F.Tang, I.E.Anderson, S.B.Biner, Microstructures and mechanical properties of pure Al matrix composites reinforced by Al; Cu; Fe alloy particles, *Materials Science and Engineering: A*, **363**(2003), no. 1-2, 20–29. DOI: 10.1016/S0921-5093(03)00433-7

[6] M.Kamalnath, et al., Development of Al1070-Quasicrystal ($Al_{65}Cu_{23}Fe_{12}$) composites using friction stir processing and its mechanical characterization, *Materials Research Express*, **7**(2020), no. 2, 026535. DOI: 10.1088/2053-1591/ab71c5

[7] P.Novak, et al., Thermal stability of Al-Cu-Fe quasicrystals prepared by SHS method, *Materials Engineering*, (2013), no. 20, 77–82.

[8] A.A.Lepeshev, A.V.Ushakov, I.V.Karpov, Modification of the structure and physicomechanical properties of a quasi-crystalline Al-Cu-Fe alloy during plasma sputtering, *Materials Science*, (2012), no. 1, 21–24.

[9] Y.Yokoyama, F.Kenzo, S.Hisakichi, Preparation of large grained $Al_{64}Cu_{23}Fe_{13}$ icosahedral quasicrystal directly from the melt, *Materials transactions JIM*, **41**(2000), no. 6, 668–674. DOI: 10.2320/matertrans1989.41.668

[10] P.P.Turchin, et al., Features of the synthesis of quasicrystalline compounds in the systems $Al_{63}Cu_{25}Fe_{12}$ and $Al_{62}Cu_{20}Co_{15}Si_3$, *Bulletin of KrasGU*, (2006), no. 1, 29–33.

[11] A.P.Tsai, A.Inoue, T.Masumoto, A stable quasicrystal in Al-Cu-Fe system, *Japanese Journal of Applied Physics*, **26**(1987), no. 9A, L1505. DOI: 10.1143/JJAP.26.L1505

[12] E.Huttunen-Saarivirta, Microstructure, fabrication and properties of quasicrystalline Al-Cu-Fe alloys: a review, *Journal of Alloys and Compounds*, **363**(2004), no. 1-2, 154–178. DOI:10.1016/S0925-8388(03)00445-6

[13] E.V.Shalaeva, A.F.Prekul, Structural phase transformations in quasicrystal-forming Al-Cu-Fe alloys and defects of the icosahedral phase, *Physics of Metals and Metallography*, **109**(2010), 424–433. DOI: 10.1134/S0031918X10040137

[14] V.V.Tcherdyntsev, et al., Quasicrystalline phase formation in the mechanically alloyed Al-Cu-Fe system, *Intermetallics*, **13**(2005), no. 8, 841–847.
DOI: 10.1016/j.intermet.2005.01.009

[15] V.V.Tcherdyntsev, et al., Driving forces of redistribution of elements during quasicrystalline phase formation under heating of mechanically alloyed $Al_{63}Cu_{25}Fe_{12}$ powder, *Journal of Physics: Conference Series*, IOP Publishing, **98**(2008), no. 5, 052003.
DOI: 10.1088/1742-6596/98/5/052003

[16] A.Skolakova, et al., Structure and mechanical properties of Al-Cu-Fe-X alloys with excellent thermal stability, *Materials*, **10**(2017), no. 11, 1269. DOI: 10.3390/ma10111269

[17] L.Nascimento, A.Melnyk, Characterization in the Icosahedral Phase of $Al_{63}Cu_{25}Fe_{12}$ System, *Orbital: The Electronic Journal of Chemistry*, (2019), 155–160.
DOI: 10.17807/orbital.v11i3.1381

[18] K.S.Alexandrov, et al., Synthesis by hot pressing and investigation of the physical properties of dielectric ceramics BZT, Advanced materials, technologies, constructions: A collection of scientific papers, 4, 1998, 7–11.

[19] M.Z.Ermanok, V.I.Feygin, A.V.Sukhorukov, Pressing profiles from aluminum alloys, Moscow, Metallurgy, 1977.

Исследование образования квазикристаллических фаз в алюминиевом сплаве Д16

Павел П. Турчин
Сибирский федеральный университет
Институт физики им. Л. В. Киренского ФИЦ КНЦ СО РАН
Красноярск, Российская Федерация
Марина Ю. Чулкова
Павел О. Суходаев
Сибирский федеральный университет
Красноярск, Российская Федерация
Максим С. Молокеев
Сибирский федеральный университет
Институт физики им. Л. В. Киренского ФИЦ КНЦ СО РАН
Красноярск, Российская Федерация
Владимир И. Турчин
Сибирский федеральный университет
Красноярск, Российская Федерация

Аннотация. Исследованы особенности образования и термодинамические условия зарождения квазикристаллических фаз $Al_{60}Cu_{30}Fe_{10}$ и $Al_{65}Cu_{20}Fe_{15}$ в сплаве Д16. Эти фазы образуются при различных режимах отжига методом горячего изостатического прессования. На образование фаз существенно влияет предварительная механоактивация зерен Д16 и добавляемых в сплав компонентов Cu и Fe.

Ключевые слова: алюминиевые сплавы, квазикристаллическая фаза, рентгенофазовый анализ.

EDN: VUGORC
УДК 537.6

Magnetic Ordering and Exchange Interactions of Kotoite $Ni_2Co(BO_3)_2$ from First-principles Calculations

Svetlana Sofronova*
Artem Chernyshev†
Anna Selyanina‡
Aleksandr Krylov§
Timofey Tislenko¶
Kirensky Institute of Physics
Federal Research Center KSC SB RAS
Krasnoyarsk, Russian Federation

Received 08.10.2025, received in revised form 17.11.2025, accepted 19.12.2025

Abstract. The first-principles calculations of the structural and magnetic properties of kotoite $NiCo(BO_3)_2$ have been carried out. The minimization of the lattice parameters shows the values to be in good agreement with the experimental data (the difference is less than 1%). The atomic coordinates have been calculated. Cobalt ions tend to occupy position 2a and nickel ions tend to occupy position $4f$. The same magnetic cell as in $Ni_3B_2O_6$ but quadrupled in size ($2a \times b \times 2c$) has the minimum exchange energy for $Ni_2Co(BO_3)_2$. In $Ni_2Co(BO_3)_2$, the magnetic moments are oriented along the b axis as in $Co_3B_2O_6$.

Keywords: First-principles calculations, exchange interactions, kotoite, magnetic structure

Citation: S. Sofronova, A. Chernyshev, A. Selyanina, A. Krylov, T. Tislenko, Magnetic Ordering and Exchange Interactions of Kotoite $Ni_2Co(BO_3)_2$ from First-principles Calculations, J. Sib. Fed. Univ. Math. Phys., 2026, 19(2), 278–285. EDN: VUGORC.

Introduction

Oxyborates with the general chemical formula $M_{3-x}M'_xB_2O_6$ (where M and M' are Co, Mn, Ni, Mg, Cu, Cd) have long been the object of study up to present. Interesting features have been discovered in these compounds. For example, in $Cu_3B_2O_6$ a complex magnetic structure is observed, with there being two magnetic phases. In the first phase (the singlet one), individual spins interact, while in the second phase (the magnetically ordered one), clusters consisting of several spins coexist [1]. At 10 K, there occurs a magnetic transition to a state representing the superposition of these two phases.

The studies of the crystal lattice dynamics of the antiferromagnet $Ni_3(BO_3)_2$ in the center of the Brillouin zone show that the appearance of several new phonon modes and the anomalous behavior of some "old" phonons at the antiferromagnetic ordering temperature and below, are due to the existence of the structural phase transition associated with the magnetic ordering of $Ni_3(BO_3)_2$ [2]. However, in isostructural $Co_3(BO_3)_2$, this magnetostructural phase transition has not been observed. Recently, $Ni_3(BO_3)_2$ has been found to have great potential as an

*ssn@iph.krasn.ru https://orcid.org/0000 -0003-3486-9874
†Totez_181@mail.ru
‡selyanina.av@iph.krasn.ru https://orcid.org/0000-0002-5461-9277
§shusy@iph.krasn.ru https://orcid.org/0000-0001-8949-0584
¶timtisko@mail.ru https://orcid.org/0009-0004-5599-904X

anode material for sodium-ion batteries. The $Ni_3(BO_3)_2$ electrode has a high reversible capacity of 428.9 mAh·g^{-1} at 200 mA·g^{-1}. The specific capacity of $Ni_3(BO_3)_2$ remains to be high (304.4 mA·h·g^{-1}) even at a very high current density of 2000 mA·g^{-1} [3].

The solid solutions of $Ni_{3-x}Co_x(BO_3)_2$ are known to exist [1, 4, 5], but a detailed study of the physical properties of this compound has not been carried out. In this work, we present a theoretical investigation of the structural and magnetic properties of kotoite $Ni_2Co(BO_3)_2$.

1. Structural properties

According to [1, 4], the $Ni_2Co(BO_3)_2$ compound has a crystal structure of kotoite with the space symmetry group $Pnnm$. In [1, 4], the parameters of the crystal lattice were determined, but information on the coordinates of the atoms was not provided. Using the Wien2K software package, we determined the crystal lattice parameters, atomic coordinates and distribution of transition metal ions over the positions for kotoite $Ni_2Co(BO_3)_2$.

In the Wien2K software package, use is made of the method of linearized augmented plane waves with local orbitals [6, 7, 8]. The exchange-correlation energy is calculated in the LSDA approximation [9] taking into account the density gradient [10], and Hubbard correlation coefficients. In our calculations, we used the potentials U=0.52 Ry and J=0 Ry [11, 12]. In estimating the total energy, a set of 400 k-points in the Brillouin zone was used, and the value R_{mt} K_{max}=7.0. The energy calculation accuracy was 1 μRy. The following radii of atomic spheres were used in the calculations: 2.02 at. units for nickel ions, 2.02 at. units for cobalt ions, 1.30 at. units for boron and oxygen ions. The modified Blochl tetrahedral method was applied to calculate the total density of the states [13].

Since X-ray diffraction cannot distinguish between nickel and cobalt ions due to the fact that these ions have the same electronic configuration, it is impossible to determine the distribution of transition metal ions over crystallographic positions. In order to reveal how nickel and cobalt ions are distributed over the positions, we calculated the energies of various cation-ordered configurations. The unit cell of kotoite contains 6 transition metal ions, which occupy two crystallographic positions: $2a$ and $4f$. In Fig. 1, the transition metal ions are indicated by the blue circles numbered 1 to 6. Ions 1 and 2 occupy position $2a$, while ions 3-6 occupy position$4f$.

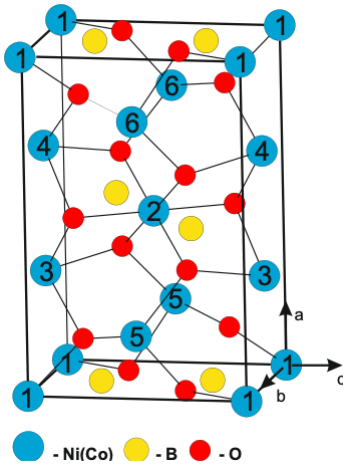

Fig. 1. The crystal structure of kotoite

The experimental values of the lattice parameters of $Ni_2Co(BO_3)_2$ and the experimental atomic coordinates for kotoite $Ni_3(BO_3)_2$ were the starting points for calculating the energy and

minimizing the structural parameters for various cation-ordered configurations.

The results of minimizing the lattice parameters and atomic coordinates for the most preferred type of cationic ordering are given in Tab. 1. The minimization of the lattice parameters showed the values to be in good agreement with the experimental data (the difference is less than 1%).

Table 1. The calculated structural parameters of $Ni_2Co(BO_3)_2$

Lattice parameters Calculations [1]		a=Å	b=Å	c=Å
		4.48	5.46	8.42
		4.48	5.42	8.35
Ion	Site	Ion coordinates		
		x/a	y/b	z/c
Ni	4f	1/2	0	0.3086
Co	2a	1/2	1/2	1/2
O_1	8h	0.7096	0.1811	0.1367
O_2	4g	0.2420	0.3087	0
B	4g	0.5403	0.2370	0

2. Magnetic properties

There is no information on the magnetic properties of kotoite $Ni_2Co(BO_3)_2$. The compounds $Co_3(BO_3)_2$ and $Ni_3(BO_3)_2$ are known to be antiferromagnets, and the easy magnetization axis in these compounds is oriented along the crystallographic directions b and c, respectively [14]. The magnetic structure of kotoites $Co_3(BO_3)_2$ and $Ni_3(BO_3)_2$ was solved using the neutron diffraction method [15, 16]. It was not possible to completely solve the magnetic structure and determine the magnetic moment of each magnetic ion in the cell. However, the authors assumed the magnetic cell of both compounds to be 4 times larger than the elementary crystallographic cell ($2a \times b \times 2c$). The magnetic moments of the transition metal ions in $Co_3(BO_3)_2$ form ribbons. The magnetic moments inside the ribbon are oriented ferromagnetically, while the magnetic moments of different ribbons are oriented antiferromagnetically (Fig. 2).

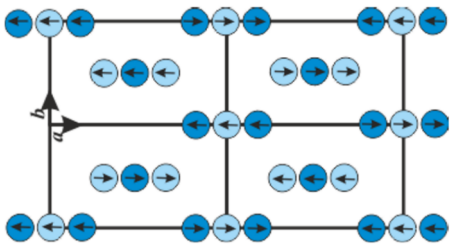

Fig. 2. The magnetic structure of $Co_3(BO_3)_2$

In one of our previous works, we determined the exchange interaction parameters of kotoite $Ni_3(BO_3)_2$ and showed the exchange interactions of the second coordination sphere to be important for the formation of magnetic order and we also observed an increase of the magnetic cell [17]. The exchange interaction parameters were determined from the calculation of the total energies of different magnetically ordered structures. Using the same technique, we calculated the exchange interaction parameters for kotoite $Ni_2Co(BO_3)_2$.

The exchange interaction parameters were estimated from the calculated energy values for a number of different spin configurations, both for the magnetic cell coinciding with the crystallographic one, and for the magnetic cells doubled along the a and c axis (Tab. 2). Since only

the spin configuration changed upon calculating the energies, and the other parameters of the crystal structure remained unchanged, the total energy can be written as a sum of the exchange contribution (the first term) and the constant value (e_0):

$$E_m = -\frac{1}{2}\sum_{ij} J_{ij} \ \ \langle \mathbf{s}_i \cdot \mathbf{s}_j \ \rangle + e_0 \tag{1}$$

where J_{ij} is the exchange interaction parameters between the i and j atoms.

Table 2. The orientation of the magnetic moments on atoms, expressions of the exchange contribution to the energy through the exchange interaction parameters and calculated energy values of different magnetically-ordered structures for the magnetic cells coinciding with the crystallographic one

Configuration	**Ni$_1$**	**Ni$_2$**	**Ni$_3$**	**Ni$_4$**	**Ni$_5$**	**Ni$_6$**
a	u	u	d	d	d	d
b	d	u	d	d	u	u
c	d	d	d	u	u	u
d	d	u	d	u	u	d
e	d	u	d	u	d	d
f	d	d	d	d	d	u
g	d	u	u	u	d	d
h	u	u	u	u	u	u
i	d	u	u	d	d	u
j	d	u	d	u	d	u
k	d	d	d	d	u	u
l	u	d	u	u	u	u

Configuration	**The exchange part of energy**	**(at.units)**
a	$8J_1 + 8J_2 - 8J_4 - 2J_3 - 2J_5 - 4J_6 - 4J_7 - 4J_8 - e_0$	**-19741.869304**
b	$8J_1 - 8J_2 + 8J_4 - 2J_3 - 2J_5 + 4J_6 + 4J_7 + 4J_8 - e_0$	-19741.868375
c	$4J_1 + 4J_2 - e_0$	**-19741.869382**
d	$4J_1 - 4J_2 - e_0$	-19741.868996
e	$-4J_1 + 4J_2 - e_0$	**-19741.869311**
f	$-4J_1 - 4J_2 - e_0$	-19741.869064
g	d$-8J_1 + 8J_2 + 8J_4 - 2J_3 - 2J_5 + 4J_6 + 4J_7 + 4J_8 - e_0$	-19741.868399
h	$-8J_1 - 8J_2 - 8J_4 - 2J_3 - 2J_5 + 4J_6 - 4J_7 - 4J_8 - e_0$	-19741.868703
i	$-2J_3 - 8J_4 + 2J_5 + 4J_6 - 4J_7 - 4J_8 - e_0$	-19741.867484
j	$2J_3 - 8J_4 + 2J_5 - 4J_6 + 4J_7 + 4J_8 - e_0$	-19741.867662
k	$-2J_3 - 8J_4 + 2J_5 - 4J_6 + 4J_7 + 4J_8 - e_0$	-19741.868790
l	$-2J_3 - 8J_4 - 2J_5 - 4J_6 - 4J_7 - 4J_8 - e_0$	-19741.868945

Next, for description we use the exchange interaction parameters depicted in Fig. 3, where J_1 are the parameters of the exchange interaction between atoms 1-5, 1-6, 2-3, 2-4; J_2 are the parameters of the exchange interaction between atoms 1-3, 1-4, 2-5, 2-6; J_3 are those for atoms 3-4 and 5-6 and J_4 are those for atoms 3-5 and 4-6, J_5 are the parameters of the exchange interaction of the second coordination sphere between ions 3-4 (5-6), J_6 are those for ions 1-1, J_7 are those parameters for 1-6(5) or 2-3(4) and J_8 are those for 3-3, 4-4, 5-5, 6-6. The remaining parameters of the exchange interaction are assumed to equal to zero.

Tab. 3 shows the directions of the magnetic moments, expressions of the exchange contribution to the energy through the exchange interaction parameters and calculated energy values of

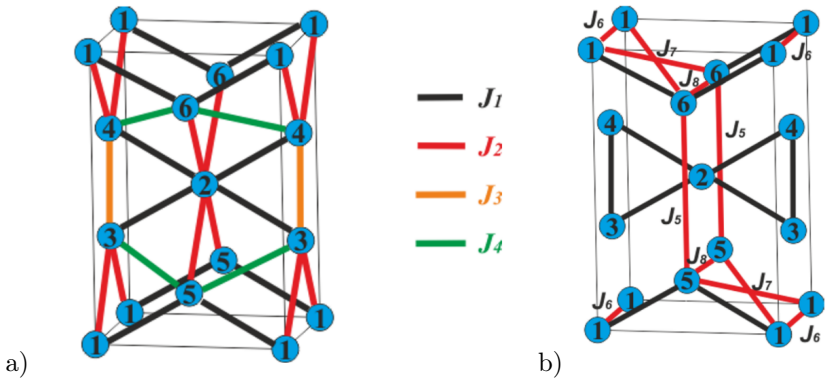

Fig. 3. The exchange interactions of the first (a) and second (b) coordination spheres

Table 3. The orientation of the magnetic moments on atoms, expressions of the exchange contribution to the energy through the exchange interaction parameters and calculated energy values of different magnetically-ordered structures for the magnetic cells doubled along the a and c axes

Magnetic cells doubled along the a axis													
1	1’	2	2’	3	3’	4	4’	5	5’	6	6’	The exchange part of energy	E (at.units)
u	d	u	d	u	d	d	u	u	d	d	u	$-4J_3 - 4J_5 - 8J_6 - 4J_8 - e_0$	–39483,735147
u	u	u	d	u	u	d	d	u	d	d	u	$-4J_3 - 4J_5 - e_0$	–39483.735186
d	u	d	u	d	u	d	u	u	d	u	d	$4J_3 + 4J_5 - 8J_6 - 4J_8 - e_0$	–39483.737539
u	u	u	d	u	d	u	d	d	d	d	d	$4J_3 + 4J_5 - 8J_7 - e_0$	–39483.737646
d	u	d	u	u	d	u	u	d	d	d	u	$-8J_6 - e_0$	–39483.736265
Magnetic cells doubled along the c axis													
1	1’	2	2’	3	3’	4	4’	5	5’	6	6’	The exchange part of energy	E (at. units)
d	d	d	u	u	u	d	d	d	u	d	d	$-4J_3 - e_0$	–39483.735098
u	d	d	d	d	u	d	d	d	d	u	d	$4J_3 - e_0$	–39483.735187
d	u	u	u	u	d	d	u	d	d	u	d	$-4J_5 - e_0$	–39483.739076
d	d	d	u	u	u	u	d	u	d	u	u	$4J_5 - e_0$	–39483.738125

different spin configurations for the magnetic cells coinciding with the crystallographic one and for the doubled magnetic cells. The calculated values of the exchange interaction parameters for $Ni_2Co(BO_3)_2$ are given in Tab. 4. The exchange interaction parameters of $Ni_3B_2O_6$ are also presented for comparison [17].

Table 4. The exchange interaction parameters obtained taking into account the contributions to the exchange interaction energy of the second coordination sphere

The exchange interactions (K)	J_1	J_2	J_3	J_4	J_5	J_6	J_7	J_8
$Ni_3B_2O_6$	–2.67	–6.36	–0.11	8.36	2.45	–2.14	–3.48	2.80
$Ni_2CoB_2O_6$	–1.39	–7.63	1.73	5.64	–18.79	–2.82	1.36	3.63

As can be seen from Tab. 4, three exchange parameters change significantly: J_3, J_5 and J_7. In contrast to $Ni_3B_2O_6$, in $Ni_2Co(BO_3)_2$ the strongest exchange interactions (J_5) are antiferromagnetic and they occur between the spins in the second coordination sphere. The exchange interactions inside the triangular ribbons (J_1, J_3) do not compete with each other, despite the different nature of the interaction, whereas the exchange interactions between the ribbons (J_2 and J_4) in the first coordination sphere compete with each other.

In the case of the magnetic cell coinciding with the crystallographic one (Tab. 2), three magnetic configurations have close energy values, two of them being ferrimagnetic and one being antiferromagnetic due to a strong competition between the ferromagnetic and antiferromagnetic exchange interactions in the magnetic system of $Ni_2Co(BO_3)_2$.

We used the calculated exchange interaction parameters to determine the magnetic structure with the lowest exchange energy for the magnetic cell quadrupled in size ($2a \times b \times 2c$). The magnetic structure shown in Fig. 4 has the lowest exchange energy per cell. This type of the magnetic structure was proposed as a result of studying the magnetic structure of $Ni_3B_2O_6$ using the neutron diffraction method.

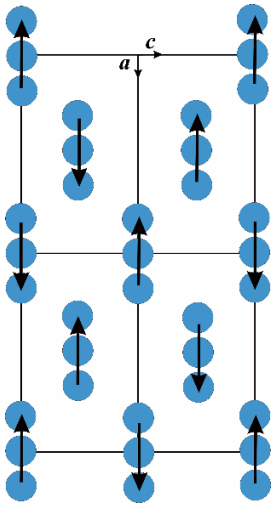

Fig. 4. The magnetic structure with the lowest exchange energy for the magnetic cell quadrupled in size ($2a \times b \times 2c$)

In order to determine the orientation of the magnetic moments relative to crystallographic directions, the total energies of the ferromagnetic state were calculated taking into account spin-orbit interactions with the magnetic moments oriented along the crystallographic directions. Tab. 5 shows the difference between the energy of the ferromagnetic state with the magnetic moments oriented along the crystallographic axis [uvw] and the energy of the ferromagnetic state with the magnetic moments oriented along the crystallographic axis c ($E_{[uvw]} - E_{[001]}$) for $Ni_2Co(BO_3)_2$ and for $Ni_3B_2O_6$ for comparison. As follows from the calculations performed,

Table 5. The calculated energies of the ferromagnetic state, depending on the orientation of the magnetic moments

The orientation of the magnetic moments	$E_{[uvw]} - E_{[001]}$ (Ry) $Ni_2CoB_2O_6$	$E_{[uvw]} - E_{[001]}$ (Ry) $Ni_3B_2O_6$ [16]
[100]	$6.1*10^{-5}$	$9.2*10^{-5}$
[010]	**$-1.0*10^{-5}$**	$9.2*10^{-5}$
[001]	0	**0**

the magnetic moments in Ni2Co$(BO_3)_2$ are directed along the b axis. The magnetic moments in $Co_3B_2O_6$ are oriented in the same direction, while in $Ni_3B_2O_6$ the magnetic moments are oriented along the c axis. The calculated magnetic moments of nickel and cobalt atoms in $Ni_2Co(BO_3)_2$

are given in Tab. 6. For both magnetic ions, the calculated magnetic moments are close to the nominal ones, corresponding to the high-spin state with the spin S = 3/2 for cobalt ions and S = 1 for nickel ions.

Table 6. The calculated magnetic moments of nickel and cobalt atoms for $Ni_2Co(BO_3)_2$

Atom	**Magnetic moments (μ_B)**
Co	2.82
Ni	1.78
O	0.02
O	0.07

Conclusion

In this work, we performed a theoretical study of the structural and magnetic properties of kotoite $Ni_2Co(BO_3)_2$. The calculated values of the crystal lattice parameters are in good agreement with the experimental data. The study of cationic ordering show that cobalt ions tend to occupy the 2*a* position. Despite the fact that the exchange interaction parameters of $Ni_2Co(BO_3)_2$ differ from those of $Ni_3B_2O_6$, the same magnetic cell as in $Ni_3B_2O_6$ has the minimum exchange energy. However, the direction of the magnetic moments changes. While in $Ni_3B_2O_6$ the magnetic moments are oriented along the c axis, in $Ni2Co(BO_3)_2$ the magnetic moments are oriented along the b axis, as well as in $Co_3B_2O_6$. It would be interesting to obtain crystals of kotoite $Ni_2Co(BO_3)_2$ and study their structural and magnetic properties in order to evaluate whether the calculations using the Wien2K software package can well predict the properties of the compounds.

The research was supported by the Russian Science Foundation and Krasnoyarsk Regional Science Foundation, project no. 23-12-20012 (https://rscf.ru/en/project/23-12-20012/).

References

[1] B.Tekin, H.Güler, Synthesis and crystal structure of dicobalt nickel orthoborate, $Co_2Ni(BO_3)_2$, *Materials Chemistry and Physics*, **108**(2008), 88–91.

[2] R.V.Pisarev, M.A.Prosnikov, V.Y.Davydov, et al., Lattice dynamics and a magnetic-structural phase transition in the nickel orthoborate $Ni_3(BO_3)_2$, *Physical Review B*, **93**(2016), 134306.

[3] B.Xu, Ya.Liu, J.Tian, X.Ma, Q.Ping, B.Wang, Yo.Xia, $Ni_3(BO_3)_2$ as anode material with high capacity and excellent rate performance for sodium-ion batteries, *Chemical Engineering Journal*, **363**(2019), 285.

[4] H.Güler, B.Tekin, Synthesis and crystal structure $CoNi_2(BO_3)_2$, *Inorganic Materials*, **45**(2009), 538–542.

[5] S.Sofronova, E.Moshkina, A.Chernyshev, et al., Crystal growth and cation order of $Ni_{3-x}Co_xB_2O_6$ oxyborates, *Cryst. Eng. Comm*, **26**(2024), 2536–2543.

[6] E.Sjostedta, L.Nordstrцma, D.Singhb, An alternative way of linearizing the augmented plane-wave method, *Solid State Communications*, **114**(2000), 15–20.

[7] P.Blaha, K.Schwarz, G.Madsen, D.Kvasnicka, J.Luitz, An Augmented Plane Wave + Local Orbitals Program for Calculating Crystal Properties, Vienna: Vienna University of Technology Inst. of Physical and Theoretical Chemistry, 2015.

[8] P.Baha, K.Schwarz, F.Tran, R.Laskowski, G.Madsen, L.Marks, WIEN2k: An APW+lo program for calculating the properties of solids, *J. Chem. Phys.*, **152**(2020), 074101.

[9] J.Perdew, Y.Wang, Accurate and simple analytic representation of the electron-gas correlation energy, *Physical Review B*, **45**(1992), 13244.

[10] J.P.Perdew, K.Burke, M.Ernzerhof, Generalized Gradient Approximation Made Simple, *Physical Review Letters*, **77**(1996), no. 18, 3865.

[11] V.I.Anisimov, J.Zaanen, O.K.Andersen, Band theory and Mott insulators: Hubbard U instead of Stoner I, *Physical Review B*, **44**(1991), 943.

[12] V.I.Anisimov, I V.Solovyev, M.A.Korotin, M.T.Czy?yk, G.A.Sawatzky, Density-functional theory and NiO photoemission spectra, *Physical Review*, **48**(1993), 16929.

[13] P.E.Blöchl, O.Jepsen, O.K.Andersen, Improved tetrahedron method for Brillouin-zone integrations, *Physical Review B*, **49**(1994), 16223.

[14] L.N.Bezmaternykh, S.N.Sofronova, N.V.Volkov, E.V.Eremin, O.A.Bayukov, I.I.Nazarenko, D.A.Velikanov, Magnetic properties of$Ni_3B_2O_6$ and $Co_3B_2O_6$ single crystals, *Physica Status Solidi b*, **249**(2012), no. 8, 1628–1633.

[15] R E.Newnham, R.P.Santoro, P.F.Seal, G.R.Stallings, Antiferromagnetism in $Mn3B_2O_6$, $Co_3B_2O_6$, and$Ni_3B_2O_6$, *Physica Status Solidi (b)*, **16**(1966), K17–K19.

[16] R.Newnham, M.Redman, R.Santoro, Neutron-diffraction study of $Co3B_2O_6$, *Zeitschrift für Kristallographie. Crystalline Materials*, **121**(1965), 418–424.

[17] S.N.Sofronova, I.I.Nazarenko, Super-Superexchange Influence on Magnetic Ordering in$Ni_3B_2O_6$ Kotoite, *Physica Status Solidi (B) Basic Research*, **256**(2019), 1900060.

Магнитное упорядочение и обменные взаимодействия в $Ni_2Co(BO_3)_2$ со структурой котоита на основе расчетов первых принципов

Светлана Софронова
Артем Чернышев
Анна Селянина
Александр Крылов
Тимофей Тисленко
Институт физики им. Л. В. Киренского
Федеральный исследовательский центр КНЦ СО РАН
Красноярск, Российская Федерация

Аннотация. Проведены расчеты структурных и магнитных свойств $Ni_2Co(BO_3)_2$ со структурой котоита с помощью программного пакета Wien2K. Минимизация параметров кристаллической решетки показывает, что полученные значения находятся в хорошем согласии с экспериментальными данными (разница составляет менее 1%). Из расчета энергий разных магнитоупорядоченных состояний оценены параметры обменных взаимодействий. Оценка энергии обменного вклада показала, что в $Ni_2Co(BO_3)_2$ минимальной энергией обмена обладает та же магнитная структура, что и в $Ni_3B_2O_6$. Однако в отличие от $Ni_3B_2O_6$ в $Ni_2Co(BO_3)_2$ магнитные моменты ориентированы вдоль оси b, как в $Co_3B_2O_6$.

Ключевые слова: первопринципные расчеты, обменные взаимодействия, котоиты, магнитная структура.